Mechanical modelling of the source of glacial earthquakes in polar regions

Pauline Bonnet

Thèse préparée à
l'Institut de Physique du Globe de Paris
Université de Paris

École doctorale Sciences de la Terre et de l'environnement
et physique de l'Univers STEP'UP n° 560

Equipe sismologie

Mechanical modelling of the source of glacial earthquakes in polar regions

par Pauline Bonnet

Thèse de doctorat de Sciences de la Terre et de l'environnement

- dirigée par
  Anne Mangeney, Olivier Castelnau

- présentée et soutenue publiquement le
  (7 juin 2021)

- devant un jury composé de
  Anne Mangeney, Professeur, Institut de Physique du Globe de Paris (directrice de thèse)
  Olivier Castelnau, Directeur de recherche CNRS, Arts et Métiers Paris (directeur de thèse)
  Fabian Walter, Professeur, ETH Zurich (rapporteur)
  Angelika Humbert, Professeur, Alfred-Wegener-Institut, Bremerhaven (rapporteur)
  Vladislav Yastrebov, Chargé de recherche CNRS, Mines Paris, invité (co-encadrant)
  Julie Deshayes, Chargée de recherche CNRS, LOCEAN, Paris, examinatrice
  Guilhem Barruol, Directeur de recherche CNRS, Institut de physique du globe de Paris, examinateur
  Jérôme Weiss, Directeur de recherche CNRS, ISTerre, Grenoble, examinateur (comité)

Scientific Context

This PhD was conducted in the Seismology team of IPG Paris (Université de Paris) and in the Centre des Matériaux of Mines Paris, Evry, under the supervision of Anne Mangeney (IPGP), Olivier Castelnau (PIMM, ENSAM) and Vladislav Yastrebov (Mines Paris). This work was mainly focused on mechanical modelling of iceberg capsize, however, for the seismology aspects of the PhD we collaborated with Eleonore Stutzmann (IPGP) and Jean-Paul Montagner (IPGP). This work follows the work conducted by A. Sergeant during her PhD in the seismology team of IPGP (Sergeant, 2016).

To improve our understanding of the fluid motion during capsize, a collaboration was initiated at the beginning of the PhD with Alban Leroyer and Patrick Queutey from LHEEA, in Centrale Nantes, France. This team develops and runs the ISIS-CFD solver for fluid-structure simulations. Thanks to the ISIS-CFD simulations we could better understand the complexe fluid motion during capsize and also validate and improve a semi-analytical model. Then, we investigated the response of a deformable visco-elastic glacier to the capsize of an iceberg, with tunable basal friction laws. We used the finite element Z-set software developed by the Centre des Matériaux of Mines Paris and by ONERA, Chatillon. The Z-set software allows to model materials with complexe rheologies and dynamic interactions between solids. We simulated a glacier with a model geometry and a glacier with the geometry of the Helheim glacier. In order to initiate properly our model, we collaborated with Martin Rueckamp and Angelika Humbert, in the Alfred Wegener Institute, Bremerhaven, Germany. This team develops and runs an ISSM model and has put in place the modelling of the steady-state behaviour of the Helheim glacier.

This PhD was funded by a DGA-MRIS scholarship and the doctoral school STEP'UP (Université de Paris). In addition, a teaching contract with the PIMM laboratory (ENSAM) was established with 80 hours of tutorial classes in structural mechanics for Master students given during the two first years of the PhD.

Peer-reviewed publications

1. Sergeant, A., Mangeney, A., Yastrebov, V.A., Walter, F., Montagner, J.P., Castelnau, O., Stutzmann, E., **Bonnet, P.**, Ralaiarisoa, V.J.L., Bevan, S. and Luckman, A. (2019). Monitoring Greenland ice sheet buoyancy-driven calving discharge using glacial earthquakes. *Annals of Glaciology, 60*(79), 75-95.

2. **Bonnet, P.**, Yastrebov, V.A., Queutey, P., Leroyer, A., Mangeney, A., Castelnau, O., Sergeant, A., Stutzmann, E. and Montagner, J.P. (2020). Modelling capsizing icebergs in the open ocean. *Geophysical Journal International, 223*(2), 1265-1287.

3. **Bonnet P.**, Yastrebov V. A., Mangeney A., Castelnau O., Rueckamp M., Queutey P., Leroyer A., Sergeant A., Stutzmann E., Montagner J-P., Modelling of the response of glaciers to capsizing icebergs, ***in prep.***

Conferences

Orals

1. Mechanical modelling of iceberg capsize constrained by seismic inversion, P Bonnet, A. Sergeant, V. Yastrebov, A. Mangeney, P. Queutey, A. Leroyer, O. Castelnau, E. Stuzmann, J.-P. Montagner, **POLAR 2018 SCAR/IASC Open Science Conference**, Davos, Switzerland, 15 – 26 June, 2018.

2. Mechanical modelling of iceberg capsize constrained by seismic inversion, P. Bonnet, A. Sergeant, V. Yastrebov, A. Mangeney, P. Queutey, A. Leroyer, O. Castelnau, E. Stuzmann, J.-P. Montagner, **4th TIDES Advanced Training School 2018**, Prague, CZ, 2 – 6 July, 2018.

3. Estimating the Volume of Capsizing Icebergs with Seismic Data, P. Bonnet, A. Sergeant, V. Yastrebov, A. Mangeney, P. Queutey, A. Leroyer, O. Castelnau, E. Stuzmann, J.-P. Montagner, **AGU Fall meeting 2018**, Washington, USA, 10 – 14 December, 2018.

4. Estimating the Volume of Capsizing Icebergs with Seismic Data, P. Bonnet, A. Sergeant, V. Yastrebov, A. Mangeney, P. Queutey, A. Leroyer, O. Castelnau, E. Stuzmann, J.-P. Montagner, **EGU General Assembly 2019**, Vienna, Austria, 7 – 12 April, 2019, (talk given by Anne Mangeney).

5. Estimation des volumes d'icebergs qui se retournent : modélisation mécanique et analyse des signaux sismiques, P. Bonnet, V. Yastrebov, A. Mangeney, O. Castelnau, P. Queutey, A. Leroyer, A. Sergeant, E. Stuzmann, J.-P. Montagner, Talk, **CFM, Congrès Français de Mécanique 2019**, Brest, 26-30 August 2019.

Posters

1. Mechanical modelling of iceberg capsize constrained by seismic inversion, P Bonnet, A. Sergeant, V. Yastrebov, A. Mangeney, P. Queutey, A. Leroyer, O. Castelnau, E. Stuzmann, J.-P. Montagner, **Congrès des doctorants de STEP'UP 2018**, Paris, FRANCE, 26 – 30 March, 2018, poster (best poster of the day).

2. Estimating volumes of capsizing iceberg : mechanical modeling of capsize constrained by seismic signals, P. Bonnet, A. Sergeant, V. Yastrebov, A. Mangeney, P. Queutey, A. Leroyer, O. Castelnau, E. Stuzmann, J.-P. Montagner, **Congrès des doctorants de STEP'UP 2019**, Paris, FRANCE, 25 – 29 March, 2019.

3. Modelling the source of glacial earthquakes for a better understanding of the impact of iceberg capsize on glacier stability, P. Bonnet, V. Yastrebov, P. Queutey, A. Leroyer, A. Mangeney, O. Castelnau, E. Stuzmann, J.-P. Montagner, A. Sergeant, Online Presentation, **EGU online conference** 2020, 3-6 May 2020.

Seminar

1. Mechanical modelling of iceberg capsize, the source of glacial earthquakes, P. Bonnet, V. Yastrebov, A. Mangeney, O. Castelnau, P. Queutey, A. Leroyer, A. Sergeant, E. Stuzmann, J.-P. Montagner, **Seismology team, IPGP**, January 28th, 2020.

2. Modelling glacial earthquakes: ocean/iceberg/glacier/earth interaction, P. Bonnet, V. Yastrebov, A. Mangeney, O. Castelnau, P. Queutey, A. Leroyer, A. Sergeant, E. Stuzmann, J.-P. Montagner, **Centre des Matériaux, Mines ParisTech**, online, November 3rd, 2020.

Outreach

1. Facilitator for a seismology workshop, **Cité des Sciences et de l'Industrie for the landing of Insight**, November 26th, 2018.

2. Facilitator for a seismology workshop, **Institut de Physique de Globe de Paris for the Fête de la Science**, October 10th, 2018.

3. Webinar for pupils on Polar glaciers for **Semaine polaire, APECS - FRANCE**, May 15th, 2020.

4. Article for children on glaciers and climate change in **Les romans de Je lis déjà**, January-March, 2021.

Acknowledgements

Merci à toutes les personnes, qui de près ou de loin, ont participé à ce projet, et m'ont aidé à mener à bien ce doctorat.

Merci à mes trois encadrants Anne, Vlad et Olivier pour les nombreuses réunions ensemble, à l'IPGP, ou bien sur zoom. Merci de m'avoir partagé vos connaissances, votre expérience et votre passion pour la mécanique des solides, la tribologie, la glaciologie, la sismologie, les simulations numériques, et la géophysique en général. Merci pour votre temps, vos conseils, et votre confiance. C'était un grand plaisir de travailler avec vous, et j'espère avoir encore l'occasion d'échanger avec vous dans le futur.

Merci aux rapporteurs et aux membres du Jury de thèse, Fabian Walter, Angelika Humbert, Julie Deshayes, Guilhem Barruol et Jérôme Weiss pour votre expertise et vos retours précieux sur le manuscrit et la soutenance.

Merci à Jérôme Weiss et Jean-Louis Dufresne, pour votre participation aux réunions annuelles du comité de thèse, et pour vos remarques et conseils utiles.

Merci à nos collaborateurs, Patrick Queutey et Alban Leroyer qui ont accepté de rejoindre le projet et ont largement contribué à la compréhension des processus d'interaction fluide-structure lors du retournement d'icebergs. Merci à notre collaborateur Martin Rückamp pour les nombreuses simulations de l'écoulement du Helheim glacier qui ont aidé à initialiser nos simulations à temps courts de la réponse du glacier à un retournement d'iceberg.

Merci à la DGA, INRA, Cost-Eu, et ERC SlideQuakes d'avoir permis mon inscription à plusieurs conférences et workshop scientifiques internationaux.

Merci à la DGA et à l'Ecole Doctorale Step'Up pour le financement de ce projet de thèse. Merci également à la DGA pour l'organisation de l'évènement d'acceuil avec la présentation de l'ensemble des activitiés de recherche financées par les bourses DGA. Merci à l'Ecole Doctorale Step'Up pour les formations sur l'éthique et l'intégrité scientifique, et sur la pédagogie.

Merci à l'Equipe Sismologie de l'IPGP, Eléonore, Jean-Paul, Guilhem, Jean-Philippe, Claudio, Martin, Anne, et Nobu, pour le cadre de travail exceptionnel, pour les séminaires hebdomadaires, pour le séminaire d'équipe en Normandie, pour les pauses café chaleureuses dans la salle de convivialité ainsi que pour le financement de la prolongation de la thèse. Merci également à Sylvie pour son aide précieuse pour les ordres de mission et les nombreuses démarches administratives. Merci aussi à Michel pour les conseils et solutions techniques en informatique.

Merci au Centre des Matériaux des Mines pour l'acceuil lors de mes visites ponctuelles. Merci à Jamel, Basile et Laurent pour leur aide sur le code Z-set.

Merci au PIMM de l'Ensam, pour les moments agréables lors de l'HCERES du laboratoire. Merci également à Katell Derrien de m'avoir permis de donner des TD et TP en Sciences des Matériaux pendant mes deux premières années de thèse.

Merci à tous les collègues de l'IPGP (Marina, Nassima, Ssu-Ting, Shipra, Thaïs, Allister, Julian, Manon, Océane, Hugo, Marc, Aline, Alexia, Angèle, Emilie, Gaspard, Laetitia, Tara, Delphine, Martin, Edith) pour les pauses chocolat, les Beer Party, les joggings du vendredi midi, les trajets du retours en vélo, l'organisation collective du CDD et des évènements du groupe Egalité et GreenGlobe. Merci aux doctorants du bureau 321 pour les échanges et les conseils quotidiens. Merci à Hekla pour les évènements scientifiques, artistiques, culinaires et sportifs entre doctorants de l'IPGP.

Merci à Grégoire de rendre le quotidien plus doux.

Merci à ma famille, ma mère, mon père, mes grands parents, ma soeur, mon frère, mon oncle et ma tante, pour votre écoute, vos encouragemnets, et votre soutien tout au long de mes études.

Et enfin, merci aux amis d'enfance, aux amis de l'ENSTA, à la danse, la musique, la poésie et la montagne pour les évasions ressourcantes.

Pour faire le portrait d'un iceberg (inspiré de Jacques Prévert, *Pour faire le portrait d'un oiseau*)

Pour faire le portrait d'un iceberg,
Peindre d'abord un glacier,
Peindre ensuite
quelque chose de joli,
quelque chose de simple,
quelque chose de beau,
quelque chose d'utile,
un sismomètre ou un GPS,
sur le glacier.
Placer ensuite l'ordinateur dans un bureau,
un appartement,
ou bien au Svalbard.
Se cacher derrière l'écran,
sans rien dire,
en tapant sur le clavier.
Parfois l'iceberg arrive vite
Mais il peut aussi bien mettre de longues années avant de se décider
Ne pas se décourager
Attendre
Attendre s'il le faut pendant des années
La vitesse ou la lenteur de l'arrivée de l'iceberg n'ayant aucun rapport avec la qualité du tableau
Quand l'iceberg arrive,
s'il arrive,
Observer le plus profond silence
Attendre que l'iceberg se détache totalement du glacier pousser doucement l'ice-mélange à l'aide du modèle d'interaction fluide-structure
puis mettez le fluide en mouvement,
en ayant soin de ne pas perturber la faune et la flore,
faire ensuite le portrait du Sermilik fjord,
en choisissant la plus belle de ses falaises, pour l'iceberg.
Peindre aussi la géométrie du Helheim glacier et la loi de frottement basal,
la rhéologie visco-élastique, et la langue flottante.
Et puis attendre que l'iceberg se décide à chavirer.
Si l'iceberg ne chavire pas c'est mauvais signe,
signe que le tableau est mauvais
mais s'il chavire c'est bon signe,
signe que vous pouvez signer.
Alors vous arrachez tout doucement
un des cristaux du glacier
et vous écrivez votre nom dans un coin du tableau.

French summary

Introduction

L'estimation du bilan de masse des calottes polaires est un enjeu actuel pour appréhender l'évolution rapide de ces masses glaciaires sous l'effet du changement climatique. Le vêlage d'iceberg représente une part importante de la perte de masse des glaciers au Groenland. Certains icebergs sont instables lorsqu'ils se détachent du terminus glaciaire, et en se retournant, exercent une force sur ce terminus qui est retransmise à la terre solide. Il en résulte des séismes (de magnitude de l'ordre de 5 détectable à des distances télé-sismiques) et une déformation du glacier proche du terminus.

Quelles informations sur la rhéologie du glacier, les lois de frottement basales, la géométrie du glacier et de l'iceberg, et le type de retournement d'iceberg pouvons-nous extraire des données sismiques et GPS ?

Pour répondre à cette question, nous proposons de modéliser le retournement d'iceberg et la réponse du glacier à ce retournement à l'aide d'un modèle mécanique multi-paramétrique. La modélisation de la dynamique du système glacier-iceberg-lit-rocheux-océan requiert un couplage entre des équations de la mécanique des solides déformables, de la dynamique du contact et de la dynamique des fluides. Pour répondre au compromis entre précision et rapidité d'implémentation d'un tel modèle, nous utilisons un modèle complet de dynamique des solides déformables et de dynamique du contact (basé sur le code Eléments Finis Zset développé à l'Ecole des Mines de Paris et à l'ONERA) et un modèle simplifié (nommé SAFIM) pour l'interaction hydrodynamique iceberg-océan.

Le travail de cette thèse consiste à comprendre la complexité du retournement d'icebergs et l'interaction avec l'océan grâce à des calculs numériques complets de dynamique des fluides (code ISIS-CFD) en collaboration avec le LHEEA de NANTES, améliorer et valider le modèle simplifié de retournement d'iceberg SAFIM, étendre la modélisation au système complet glacier-iceberg-lit-rocheux-océan en intégrant une loi de frottement entre le glacier et le lit rocheux ainsi qu'une rhéologie plus précise de la glace, étudier la sensibilité de la déformation du glacier pendant le retournement d'iceberg aux paramètres de friction, de la rhéologie et de la géométrie, contraindre les simulations éléments finis à l'aide des mesures GPS pour estimer les paramètres physiques du modèle.

Nous résumons ci-dessous les quatre chapitres du manuscrit ainsi que la conclusion.

Modélisation du retournement d'iceberg : l'interaction iceberg-océan

Le modèle de référence ISIS-CFD pour l'interaction fluide-structure a permis de quantifier le mouvement important en terme de vitesses et de vortex de l'eau autour de l'iceberg pendant son retournement. Cependant, ISIS-CFD ne permet pas de reproduire les efforts de contact entre un iceberg et un terminus marin. Ainsi, nous proposons un modèle qui permet le contact entre un iceberg et un glacier et qui reproduit de manière simplifiée les interactions iceberg-océan.

Ce modèle SAFIM (Semi-Analytical Floating Iceberg Modèle) pour la modélisation du retournement d'iceberg reproduit la dynamique d'un iceberg rectangulaire, 2D, rigide soumis à la force de contact avec le glacier, aux forces de gravité, de pression hydrostatique et à des efforts hydrodynamiques. Les efforts hydrodynamiques dans SAFIM sont : une force de traînée qui reprend celle proposée dans (Sergeant et al., 2018) en lui ajoutant un coefficient de traînée ajustable, et des masses ajoutées extrapolées à partir de formules de la littérature avec des coefficients ajustables. Nous avons montré que la dynamique de l'iceberg est invariante par rapport à la hauteur de l'iceberg, ce qui permet de faire le lien entre les expériences de laboratoire et les événements à l'échelle du terrain (iceberg de l'ordre du km3). Ces coefficients ont été optimisés par minimisation de l'erreur entre SAFIM et ISIS-CFD pour plusieurs rapports d'aspect d'icebergs instables. Les performances (en terme d'amplitude des efforts fluides

sur l'iceberg) du modèle SAFIM sont les meilleures lorsque l'on considère un coefficient de traînée qui augmente linéairement avec le rapport d'aspect de l'iceberg et aucune masse ajoutée. Par contre, pour reproduire correctement la durée du retournement, l'usage des masses ajoutées est suggéré. D'autres modèles de traînée (avec coefficient variable sur la surface de l'iceberg en fonction du signe de la pression) et de masses ajoutées (matrice complète de masses ajoutées calculée avec un modèle de mécanique des fluides) ont été étudiées pour améliorer SAFIM, sans que cela ne mène à de meilleurs résultats. On montre le fort impact de la densité de la glace et de l'eau dans la dynamique du retournement, et donc probablement dans le signal sismique généré. Les calculs CFD montrent aussi des mouvements fluides très significatifs même loin (plusieurs km) de l'iceberg qui doivent engendrer un mélange important des couches dans l'océan (température, salinité, etc), et probablement affecter aussi la biosphère marine. Les simulations ISIS-CFD montrent que les efforts du fluide sur l'iceberg sont fortement liés aux tourbillons formés dans le fluide. Ainsi, une représentation plus précise des efforts fluides locaux sur l'iceberg ne semble pas possible sans invoquer les équations de la mécanique des fluides. La dynamique de l'iceberg donnée par ISIS-CFD et SAFIM est en accord avec les expériences disponibles. Ce travail fait l'objet de l'article publié (Bonnet et al., 2020).

En complément de l'article, dans ce chapitre nous avons également présenté des résultats obtenus avec le code ISIS-CFD. Nous montrons que le champs de pression sur les bords de l'iceberg ne sont pas corrélés au champ de vitesses, ce qui soutient l'observation donnée précédemment sur la forte dépendance des efforts hydrodynamiques locaux sur les mouvements tourbillonaires et la déformation de la surface libre.

Lors du retournement d'un iceberg, plusieurs phénomènes sont susceptibles d'émettre des ondes sismiques et il est nécessaire de connaître la signature sismique de ces différents phénomènes pour interpréter ensuite le signal sismique mesuré. Le modèle ISIS-CFD a permis d'estimer les efforts sur le fond marin pendant le retournement. Nous discutons la potentielle source de signaux sismiques en comparant l'intégrale de ces efforts filtrés aux efforts hydrodynamiques sur l'iceberg.

Calcul de la force de contact iceberg-glacier

Nous avons ensuite modélisé le mouvement d'un iceberg se retournant en contact avec un glacier rigide ou élastique. Pour cela nous avons utilisé les efforts hydrodynamiques de SAFIM paramétrés dans la partie précédente. Nous avons utilisé plusieurs méthodes pour traiter le contact (par pénalisation et force d'un ressort élastique) entre l'iceberg et un terminus rigide ou une langue flottante. Les résultats obtenus avec ce modèle semi-analytique SAFCIM ont été validés par comparaison des résultats avec un modèle de référence pour le contact entre des solides, le modèle Z-set. L'avantage du modèle analytique est la rapidité des calculs par rapport au modèle Z-set (plus de 10 fois plus rapide).

Nous avons ici montré la faible influence de la rigidité de la langue flottante sur la force transmise par l'iceberg au glacier. Ceci permet de justifier l'application d'une force pré-calculée. De plus, ce modèle a permis d'estimer les efforts horizontaux pour différents rapports d'aspect de l'iceberg et pour les deux styles de capsize (sens de retournement opposés): bottom-out (le bas de l'iceberg s'éloigne du front) et top-out (le haut de l'iceberg s'éloigne du front). De plus, ceci a permis de calculer la zone d'application de la force pour les deux types de capsize, qui sera utilisée dans les simulations de la réponse du glacier au retournement d'iceberg effectuée dans les chapîtres suivants.

Modélisation de la réponse du glacier sur lit-rocheux au retournement d'iceberg: cas d'une géométrie simple avec une pente constante

Dans la littérature, il existe de nombreuses études présentant des modèles d'écoulement de glaciers visqueux à temps longs (sans retournement d'iceberg), ou des modèles simple de retournement d'icebergs contre un glacier rigide ou élastique (sans comportement visqueux ni lois de frottement basales). Nous proposons ici un modèle novateur de la réponse d'un glacier à un retournement d'iceberg en contact avec un glacier visco-élastique et avec deux lois de frottement basales (loi visqueuse Weertman et loi de Coulomb). Ce modèle de mécanique des solides permet de calculer la réponse visco-élastique à temps courts d'un glacier au retournement d'iceberg. En accord avec la littérature, nous utilisons comme lois de frottement: la loi de Weertman loin de la ligne d'échouage, et la loi de Coulomb proche de la ligne d'échouage. La lois de friction de Weertman, récemment développée dans Z-set, a été validée. Pour cela, nous avons comparé les résultats du modèle Eléments finis Z-set avec une solution analytique d'écoulement d'un glacier avec une loi de Weertman. Cette comparaison a permis de corriger une erreur présente en amont dans l'implémentation de la loi de Weertman. Bien que le modèle Z-set soit capable de modéliser la dynamique d'un iceberg chavirant, il est difficile de libérer l'iceberg après un temps d'initiation. Ainsi, nous utilisons la force de contact pré-calculée dans le chapître précédent.

Dans ce chapître, nous nous sommes intéressés à un glacier avec une géométrie avec une pente constante: lit rocheux incliné de quelques degrés, et glacier parallélépipédique. La mise en place du calcul a nécessité d'introduire une phase d'initialisation pendant laquelle le glacier se met en mouvement jusqu'à atteindre un régime permanent. Notons cependant que ce modèle ne prétend pas modéliser le comportement du glacier à temps longs. En effet, dans ce cas il serait nécessaire de prendre en compte l'accumulation et la fonte de la glace. Ces effets sont négligeables pendant la durée du retournement d'iceberg.

A l'aide de ce modèle, nous cherchons à estimer la signature des paramètres du modèles (géométrie, rhéologie de la glace, lois de frottement basales, type de retournement) sur la réponse du glacier.

Ainsi, dans un premier temps, nous avons ajusté la valeur des paramètres selon les résultats de la littérature, et de manière à reproduire les vitesses en surface typiquement observées sur le terrain. Ensuite, nous avons analysé la sensibilité de la dynamique du glacier aux paramètres du modèle. Nous observons une forte influence du module d'Young de la glace, de la longueur de la langue flottante, de la taille de l'iceberg et du type de retournement sur l'amplitude des déplacements. De plus, le comportement visco-élastique du glacier permet d'expliquer un déplacement résiduel à la fin du retournement qu'un modèle avec un comportement purement élastique ne permet pas de reproduire.

De plus, il s'agît d'analyser l'influence de ces paramètres sur les mouvements en surface du glacier et les efforts transmis au lit rocheux, et de discuter la possibilité de contraindre ces paramètres à l'aide de mesures sur le terrain (GPS et signaux sismiques). Grâce à ce modèle nous pouvons reproduire le mouvement du glacier dans toute son épaisseur pendant le retournement d'iceberg, ce que ne permettent pas les mesures GPS exclusivement localisée en surface. Nous soulignons en particulier que l'amplitude du mouvement du glacier pendant le retournement est différent à la surface libre et à la surface basale. Le rapport de l'amplitude des déplacements horizontaux sur l'amplitude des déplacements verticaux est égal à 2 pour un retournement bottom-out et à 1 pour un retournement top-out, en raison de la différence dans la zone d'application de la force sur le terminus. L'amplitude relative des déplacements en surface et à la base dépend du type de retournement (du fait d'un changement de la zone d'application de la force sur le terminus).

Nous observons que la force appliquée sur le terminus et directement transmise à la surface basale pendant le

retournement, sans modification. En effet, ceci est cohérent avec l'estimation, par un calcul analytique de l'inertie du glacier pendant le retournement, qui est négligeable. Néanmoins, la distribution des contraintes basales est affectée par le retournement d'iceberg et est sensible aux paramètres de friction basale. Ceci suggère la possibilité de détecter un signal sismique contenant une information sur la loi de friction basale, à l'aide d'une station locale.

Modélisation de la réponse du Helheim glacier au retournement d'iceberg

Afin de reproduire des évènements réels pertinents, nous avons sélectionné des évènements de retournements d'icebergs bien documentés, i.e. pour lesquels il existe des observations d'un changement transitoire dans l'écoulement du glacier (avec des mesures GPS) et des enregistrements de signaux sismiques. Ces évènements se sont déroulés au Helheim glacier, un des trois plus gros glaciers du Groenland, sur la côte Sud-Est. Pour modéliser proprement ces évènements, nous avons engagé une collaboration avec l'Alfred Wegener Institut en Allemagne. Martin Rueckamp de cet institut, nous a fourni des données de référence de la topographie, des vitesses d'écoulement. Grâce à une inversion utilisant un modèle de référence en écoulement des glaciers à long terme, il a calculé le champs de viscosité dépendante de la température. L'implémentation des données du glacier réel a nécessité d'adapter le calcul Z-set pour y introduire une géométrie ajustable et un champs de viscosité hétérogène.

La rhéologie et la géométrie sont donc fixées. Les paramètres ajustables restant sont: le module d'Young, la longueur de la langue flottante ainsi que les paramètres de la loi de friction. Pour cette géométrie complexe, nous utilisons dans un premier temps, une loi de friction de Coulomb sur toute la surface basale.

Par ailleurs, la longueur de la langue flottante pendant les évènements est peu documentée. Ainsi, nous avons ajusté la géométrie du glacier Helheim pour y modifier la longueur de la partie flottante.

Une simulation avec une langue flottante de 4.5 km et un module d'Young réduit à 3 GPa permet de reproduire qualitativement l'amplitude des déplacements en surface mesurés pendant un évènement.

Ces simulations novatrices de la réponse du glacier visco-élastique au retournement d'iceberg font l'objet d'un article en préparation.

Conclusion et Perspectives

Nous avons amélioré la compréhension physique des processus en jeu lors du retournement d'un iceberg en pleine mer. Le modèle ISIS-CFD a mis en évidence le mouvement intense du fluide autour de l'iceberg qui se retourne, ainsi que l'effet de l'échelle sur la force normalisée, en particulier pour les grands rapports d'aspect de l'iceberg. Les simulations ISIS-CFD ont également montré l'impact d'un changement dans les densités d'eau et de glace sur les forces hydrodynamiques modélisées sur l'iceberg chavirant. Nous avons validé un modèle semi-analytique pour les forces hydrodynamiques agissant sur l'iceberg.

Nous avons ensuite étendu le modèle SAFIM pour inclure le contact entre l'iceberg et un terminus rigide ou une langue glaciaire élastique. Avec ce modèle SAFCIM, nous avons montré le faible impact de la flexibilité de la langue glaciaire sur la force de contact. Cette observation implique que nous pouvons utiliser une force de contact iceberg-glacier pré-calculée dans le modèle Z-set. Nous suggérons également une paramétrisation possible de la force de contact qui permettrait de décrire cette force sans nécessité la résolution numérique des équations de la dynamique.

Nous avons ensuite modélisé la réponse d'un glacier visco-élastique bidimensionnel au retournement d'un iceberg au front du glacier en utilisant le logiciel éléments finis Z-set et la force de contact de l'iceberg précalculée avec

SAFCIM. Nous avons étudié l'impact des paramètres de la géométrie, de la rhéologie de la glace, des lois de friction (Weertman et Coulomb) et du type de retournement sur la réponse du glacier à une force de retournement au niveau du terminus. Nous avons analysé le comportement d'un glacier avec deux géométries: une géométrie modèle (un glacier avec une hauteur constante, un socle rocheux avec une pente constante, et une langue de glacier de forme rectangulaire horizontale), et une géométrie d'un glacier réel (le glacier Helheim avec et sans langue flottante). La déformation transitoire du glacier pendant le retournement est essentiellement due à une compression élastique de la glace. Le comportement visqueux de la glace explique le décalage observé dans les déplacements à la fin du retournement par rapport aux déplacements obtenus en absence de retournement. Nos simulations suggèrent que la force de retournement d'iceberg appliquée sur le terminus est transmise dans le lit rocheux sans être affectée par la réponse du glacier visco-élastique bidimensionnel. Nous avons montré une forte dépendance de l'amplitude du mouvement horizontal au coefficient de friction de Coulomb : lorsque le coefficient de friction de Coulomb diminue de 0.4 à 0.2, l'amplitude du mouvement inverse est plus de deux fois supérieure. Par ailleurs, nous suggérons que le rapport des déplacements à la surface du glacier et à différentes distances du terminus peut aider à estimer la longueur de la langue flottante. Nous avons montré que l'amplitude des déplacements horizontaux à la surface du glacier qui ont été mesurés sur le glacier de Helheim sont bien prédits dans le cas d'un glacier avec une langue flottante d'une longueur de 4 km et avec un module de Young de 3 GPa.

Ce travail a ouvert divers perspectives de travail. Du côté de la mécanique du glacier, il s'agirait d'inclure la loi de frottement de Weertman dans les simulations avec la géométrie du glacier Helheim pour mieux initialiser le calcul. Une telle implémentation présente des défis numériques (le calcul est instable pour des valeurs suffisemment faibles du coefficient de Weertman). Par ailleurs, les simulations produisent un mouvement vertical vers le haut de la langue glaciaire. Or, un mouvement vertical vers le bas est observé sur le terrain. Ceci suggère l'importance des efforts de dépression sous la langue glaciaire, comme mentionné dans la littérature. Ainsi, il s'agirait d'appliqué sous la langue flottante des efforts hydrodynamiques qui soient représentatifs de la baisse de pression hydrodynamique produite par le mouvement de l'iceberg. Dans ce sens, des développements sont en cours pour calculer de telles pressions sur la langue flottante pendant le retournement, à l'aide du modèle ISIS-CFD. Par ailleurs, pour améliorer notre compréhension de la réponse d'un glacier au retournement d'un iceberg, un modèle analytique unidimensionnel d'un glacier avec une force de friction de Coulomb ou une force de friction de Weertman a été développé récemment par Vladislav Yastrebov (co-directeur de cette thèse).

Les résultats obtenus avec les simulations de la réponse d'un glacier au retournement d'iceberg, avec le modèle éléments finis Z-set, ainsi que les résultats des modèles analytiques font l'object de deux articles en préparation.

Contents

CHAPTER 1

Introduction

1.1 Motivations

Due to greenhouse gas emissions in recent decades, the physical and chemical properties of our planet's water bodies have been modified: increase in the average temperature of the atmosphere and oceans, ocean acidification, increase in extreme weather events. This brutal and sustained *climate change* is threatening life on earth and risks triggering irreversible changes in the climate (tipping points) (Hoegh-Guldberg et al., 2018). The globally averaged temperature in 2020 was $+1.02° \pm 0.1°$ C higher than the globally averaged temperature in the 1951-1980 period Lenssen et al. (2019). The global warming is more intense in the Arctic region than in the rest of the world: between 2000 and 2020 the increase in the temperatures above latitude 60° has doubled the increase of the globally averaged temperatures (Ballinger et al., 2020).

In this context, a main concern in climate sciences and glaciology is to understand and predict the rapid evolution of ice sheets and their contribution to sea level rise. Greenland ice sheet is a major contributor to sea level rise in recent years (Zwally et al., 2011; King et al., 2020; Mouginot et al., 2019). With a total of 3902 ± 342 GT of ice losses between 1992 and 2018, it has caused a rise of the mean sea level of 10.8 ± 0.9 mm (Shepherd et al., 2020). The melting of Greenland and Antarctic ice sheets has multiple dramatic consequences: the drowning of low elevation lands (Hoegh-Guldberg et al., 2018), the possible modification of the circulation of water masses in the ocean due to the release of low density freshwater (Deshayes et al., 2014; Lenaerts et al., 2015), the reduction of the albedo in the polar regions producing a further increase (*positive feedback*) of the warming (Golledge et al., 2019).

Ice losses occur inland through surface melting and runoff and at marine terminating glaciers through frontal melting and iceberg calving which are modulated by dynamic processes (e.g. Enderlin et al., 2014). Unstable icebergs, which have a short alongflow dimension compared to the height of the iceberg (MacAyeal and Scambos, 2003), capsize at the front of marine terminating glaciers. The capsize event generates seismic waves that are recorded at teleseismic distances (e.g. Ekström et al., 2003; Ekström, 2006; Amundson et al., 2008; Nettles and Ekström, 2010, Walter et al., 2012; Veitch and Nettles, 2012; Sergeant et al., 2016; Olsen and Nettles, 2017, 2019). The number of these events has increased between 1993 and 2013 (Veitch and Nettles, 2012; Olsen and Nettles, 2017). Moreover, Nettles et al. (2008), Nettles and Ekström (2010), Murray et al. (2015a), Murray et al. (2015b) observed a change in the surface velocities at the surface of the Helheim glacier during the capsize of cubic-kilometer icebergs at a glacier front. Veitch and Nettles (2012) showed that glacial earthquakes occurence coincides with changes in the glacier dynamics: thinning, retreat and acceleration. This suggests the importance of analysing the dynamic processes at play during the capsize of an iceberg at the terminus of a marine terminating glacier.

Understanding the physical processes occuring during capsize requires, *a priori*, to describe: (1) the glacier behaviour which depends on the glacier and ice tongue temperature, anisotropy, geometry, roughness, crevasses, ice microscopic structure, glacier height and bathymetry (2) the iceberg's dynamics which is a function of its volume, shape, roughness, and ice and water densities (3) the interactions between the glacier and the bedrock - the friction law - which depend on the bathymetry and roughness of the interface, the till deformation, the ice and till temperature, the basal hydrology. Field data can help constrain this information: remote sensing data gives insights on the glacier elevation, the bedrock elevation, and the surface velocities (e.g. Rosenau et al., 2015; Morlighem et al., 2017), GPS campaigns allow to monitor the short time changes in surface velocities (e.g. Nettles et al., 2008; Nettles and Ekström, 2010; Murray et al., 2015a,b), ground penetrating radar campaigns or active-source seismic imaging can constrain the bedrock elevation and the water content (e.g. Veitch et al., 2021), terrestrial pictures and videos can help estimate iceberg velocity and geometry (e.g. Sergeant et al., 2016), seismic measurements give information on the dynamic processes that generate the seismic waves, after deconvolution

from the propagation effects (see reviews by Podolskiy and Walter, 2016; Aster and Winberry, 2017). However, extracting information on the dynamics of the glacier-iceberg-water-bedrock from these field measurements is not straightforward. Therefore, it is necessary to develop a mechanical model, with adjustable parameters, that is able to reproduce these observations.

Extensive developments in ice flow modelling in recent years allow a more precise description of the long term behaviour of glaciers and ice sheets (see model benchmarks presented by Payne et al., 2000; Pattyn et al., 2008; Gagliardini and Zwinger, 2008; Pattyn et al., 2012). In a shorter time scale, a few studies have analysed the response of glaciers to calving (without the capsize of an iceberg) such as **?**, Wagner et al. (2016). Only few studies have modelled the interaction between a rigid glacier and a capsizing iceberg (Tsai et al., 2008; Amundson et al., 2010; Sergeant et al., 2018, 2019). The reverse horizontal motion at the surface has been interpreted as being mainly an elastic process dependent on the length of the glacier tongue and the Young's modulus of ice (Murray et al., 2015a). Other aspects of the system, may influence these deformations: the ice viscosity (such as for tidal flexure Robel et al., 2017), the basal friction laws (stick-slip behaviour can occur at the basal surface of glaciers e.g. Wiens et al., 2008; Winberry et al., 2011, 2020), the geometry of the basal surface (e.g. Durand et al., 2011) and the geometry of the floating tongue (e.g. Wagner et al., 2016). To our knowledge, no model describes the response of a visco-elastic glacier with adjustable friction laws, to the capsize of an iceberg at the glacier terminus.

Seismic analysis and mechanical modelling studies showed that the main source of seismic waves during capsize is the force of the capsizing iceberg on the glacier front (Tsai et al., 2008; Nettles et al., 2008; Olsen and Nettles, 2017; Sergeant et al., 2016, 2018, 2019). However, other dynamic phenomena occuring during the calving and capsize may also generate recordable seismic waves such as the friction force between the accelerating glacier and the bedrock (e.g. Winberry et al., 2020), the dynamic pressure force on the seafloor below the capsizing iceberg (such as observed for small calvings e.g. Bartholomaus et al. (2012) or for microseisms e.g. Longuet-Higgins, 1950), the oscillations of the glacier tongue (similarly to a tidal forcing e.g. Podolskiy et al., 2016), the reflexions of the ocean waves on the fjord lateral boundaries (e.g. Walter et al., 2013; Sergeant et al., 2016). To extract information from the seismic signals, one needs to understand these different source processes and the type of seismic signals they may produce.

The questions that we will address in this work are:

- What are the physical processes governing the response of a glacier to the capsize of an iceberg at the terminus?
- What information can we extract from the observed displacements at the surface of the glacier and the recorded seismic signals?
- Can the motion of the glacier on the bedrock or the fluid pressure on the seafloor be a source of glacial earthquakes?

1.2 Ice sheets and glaciers

The Antarctic and Greenland ice sheets are enormous volumes of ice with a maximum height of ≈ 3 km lying on a bedrock which has negative elevations in the central part Morlighem et al. (2017). The amount of ice of these ice sheets represents a global sea level rise of 7.42 ± 0.05 m for the Greenland ice sheet (Morlighem et al., 2017), and $\approx +58.3$ m for the Antarctic ice sheet (Fretwell et al., 2013).

Snow accumulates at high altitude -in the central region- of ice sheets; then forms packed firn and ice. This ice is convected towards the low altitude regions through channelized high velocity glaciers terminating in the ocean

(Greve and Blatter, 2009). On Fig. 1.1, we show the ice velocities at the surface of Greenland (a) and Antartica (b), in km/year (1 km/year= 2.739 m/day), adapted from Mouginot et al. (2017).

The temporal evolution of the mass of the Greenland and Antartic ice sheets is quantified by the *ice mass balance* (MB) i.e. the difference between accumulation (snowfalls) and ice losses (melt, avalanches and calving of icebergs). Ice is lost through surface melting and *dynamic losses*, i.e. frontal erosion (surface and subglacial melting and iceberg calving). It is usually estimated by the difference between *surface masse balance* (SMB, accumulations minus surface melting) and solid ice discharge at the glacier fronts (SD). The average values for Greenland ice sheet in the 1991-2015 period are 306 ± 120 Gt.yr^{-1} for SMB, and 477 ± 51 Gt.yr^{-1} for SD. The difference gives the MB of -171 ± 171 Gt.yr^{-1} (Van Den Broeke et al., 2016). These values increase with a trend of -10.2 ± 2.3 Gt.yr^{-1} for the SMB, 6.6 ± 0.4 Gt.yr^{-1} for the SD, and in total 16.8 ± 2.8 Gt.yr^{-1} for the MB. The evolution of Greenland Ice sheet SMB correlates, to some extent, with atmospheric forcings: North atlantic oscillation, Greenland blocking index, and Atlantic multidecadal oscillation. In the last decades, the warmer phases of these periodical atmospheric forcings have been amplified (Catania et al., 2020).

Glacier ice is convected towards lower altitudes due to gravity through two processes: viscous flowing of the ice and basal sliding. The viscous flowing is dependent on the ice temperature: a warm ice will flow faster than a colder ice. The temperature of the ice increases with depth and towards lower altitudes in general. Basal sliding is governed by various processes: the viscous flow around bedrock asperities (Weertman, 1957), the effective pressure (glaciostatic minus hydrostatic pressure) (Iken, 1981; Budd et al., 1979), and the till viscous deformation (Tulaczyk et al., 2000; Truffer et al., 2001; Gagliardini et al., 2007). These processes vary in space and time and are not well constrained.

The lateral friction of the glacier tongue on the fjord sides and the friction of the glacier tongue on pinning points (submarine mounts in contact with the floating tongue) induce resisting forces which have a stabilising effect (*buttressing*) on the glacier flow (Gudmundsson, 2013). In some cases, a slight retreat (due to iceberg calving or melting) beyond a pinning point can produce a dramatic dynamic change in the glacier stability referred as *Marine ice sheet instability* (Favier et al., 2014).

1.3 Calving

Polar glaciers usually have a floating part (between the grounding line and the terminus) that can be of various types (Copland and Mueller, 2017): ice shelves in Antarctica extend on hundreds of kilometers seaward, glacier tongues are narrow relative to their length, tide-water glaciers are near-grounded and are sensitive to the change in tide levels, sea-ice ice shelf, and composite ice shelves (*sikussak*). Tide-water glaciers have a short floating tongue, which extends from the grounding line to the terminus position. Thus the height of a terminus is similar to that of the grounded part of the glacier (≈ 1 km high for Greenland glaciers). At the grounding line, the glacier experiences a combination of stresses: a horizontal shear due to basal friction in the grounded part and longitudinal streching and lateral shearing in the floating part (Pattyn, 2003) and an upwards buoyancy force modulated by tides (Oerlemans and Nick, 2005).

Calving at near-grounded glacier fronts ranges from avalanches of small icebergs to calving of full-glacier-height icebergs. The latter are either stable tabular icebergs, or thinner and unstable icebergs that capsize close to the glacier front. The capsize of these cubic kilometer icebergs lasts a few minutes and generates an earthquake of magnitude $M_{SW} \approx 5$ calculated the range of $35 - 150$ s (Ekström et al., 2003; Ekström, 2006). The loss of potential energy (from the vertical to the horizontal floating position) is converted into the kinetic energy of the iceberg and

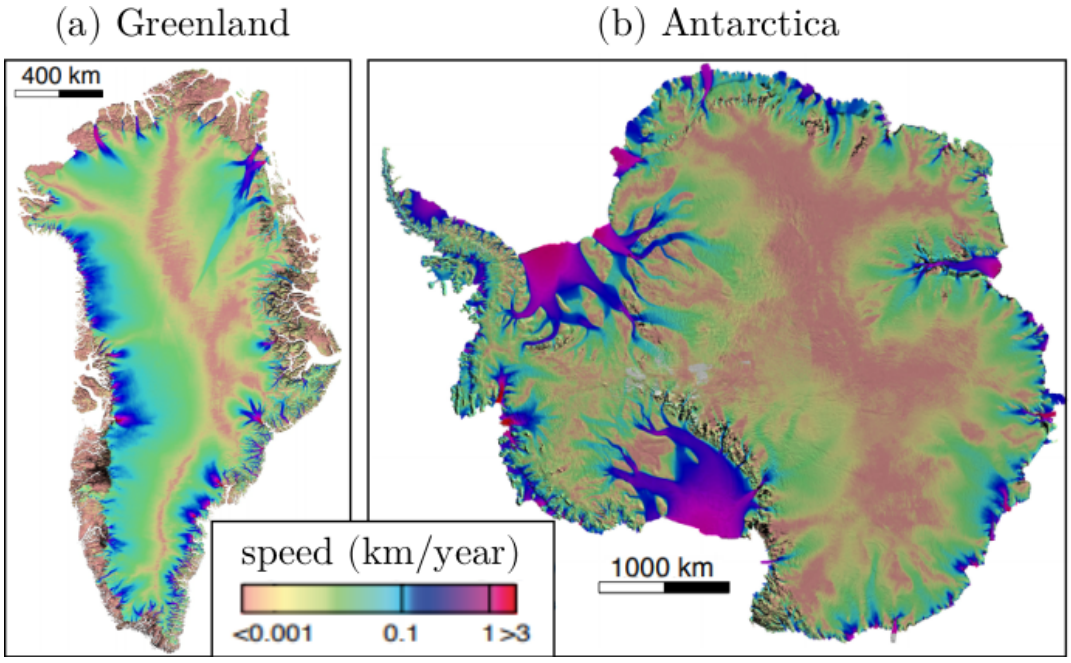

Figure 1.1: Surface velocity of the Greenland ice sheet (a) and the Antarctic ice sheet (b) in km/yr, adapted from Mouginot et al. (2017).

the water (and the glacier) (Burton et al., 2012), and is eventually dissipated through turbulence, basal friction and viscous deformation.

The calved icebergs and sea ice in the fjord form the *ice-mélange* that behaves as a dense viscous material, with a stabilising effect on the terminus (Amundson et al., 2010; Peters et al., 2014; Cassotto et al., 2015). The ice-mélange in less dense in the summer than in the winter due to higher temperatures (Cassotto et al., 2015). A capsizing iceberg can rotate either with the top of the iceberg moving away from the glacier (top-out) or with the bottom of the iceberg moving away from the glacier (bottom-out). In presence on ice-mélange, the bottom-out capsize is preferred over the top-out capsize because of the resisting forces applied by the ice-mélange on the top part of the iceberg (Amundson et al., 2010).

In Greenland, buoyancy-driven iceberg capsize can cause a horizontal and vertical movement of the glacier tongue (Murray et al., 2015a), potentially destabilizing or restabilizing the ice tongue depending on the glacier's flotation state (Cassotto et al., 2019). Iceberg capsize can also trigger ice-shelf break-off as observed in Antarctica (MacAyeal and Scambos, 2003; Burton et al., 2013). Capsizing icebergs can slowly push ice-mélange away from the glacier front (Amundson et al., 2010) or squeeze it and rigidify it (Peters et al., 2014), this can affect the stabilizing effect produced by ice-mélange at the calving front (Todd and Christoffersen, 2014). Note that during iceberg capsize, important volumes of fjord water are mixed (Burton et al., 2012), which can affect fauna and flora (Moon et al., 2016). We shematically represent the different components of a glacier front that are involved during capsize in Fig. 1.2, adapted from Hulbe (2017).

1.4 Seismic data

In the early 2000's, earthquakes located at Greenland glacier fronts were discovered by Ekström et al. (2003). The authors used a non traditional detection technique that focuses on the energy at higher periods (≈ 35 s$< T <\approx 150$ s) compared to the typical tectonic earthquake period range 1 s$< T <$ 30 s. Similarly to landslides (Kawakatsu, 1989),

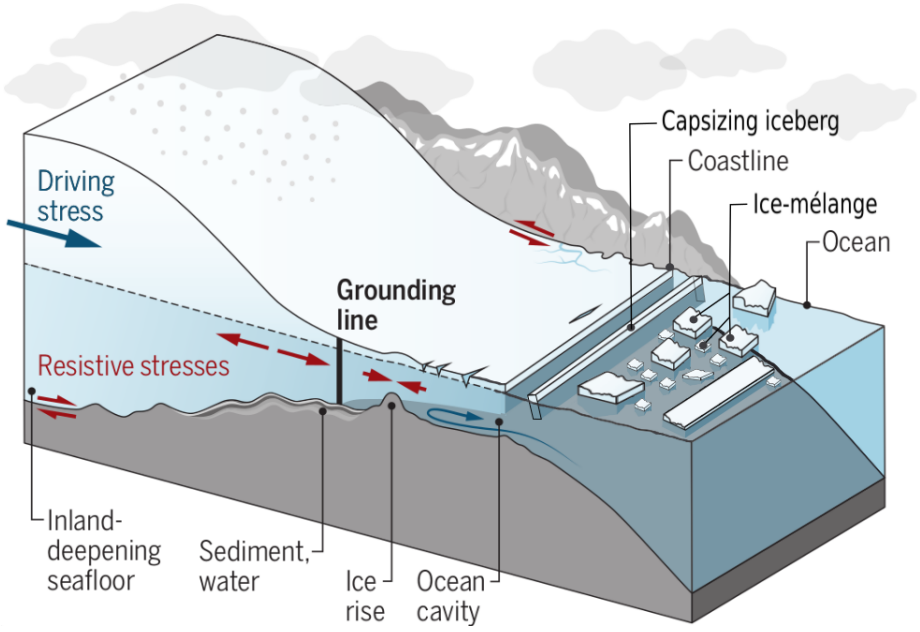

Figure 1.2: Schematic view of a glacier front, adapted from Hulbe (2017)

the source of these events is well represented by a horizontal centroid single force (positive boxcar followed by a negative boxcar) applied in the direction of the glacier flow (Ekström, 2006; Tsai and Ekström, 2007; Veitch and Nettles, 2012; Olsen and Nettles, 2017, 2019). Tsai et al. (2008) proposed different possible sources for the measured glacial earthquakes: the acceleration of the glacier without the inclusion of calving (such as a landslide), and the capsize of an iceberg against a glacier front. The authors argue that the second process better describes the source of glacial earthquakes in terms of amplitude and timescale. Later, field observations have confirmed that the source of glacial earthquakes is related to an event of iceberg capsize (Nettles et al., 2008; Nettles and Ekström, 2010). Further seismic analysis and modelling studies have argued that the source of the seismic signal is the force of the iceberg on the glacier (Nettles et al., 2008; Nettles and Ekström, 2010; Walter et al., 2012; Veitch and Nettles, 2012; Sergeant et al., 2016, 2018, 2019). During the capsize of an iceberg, the dynamics of the whole system glacier-bedrock-water-iceberg-ice-mélange is involved. Therefore, several other source forces may generate seismic waves (Podolskiy and Walter, 2016):

- Considering a rigid glacier fixed to the bedrock, the force of the iceberg on the glacier front will be completely transmitted to the bedrock, and seismic waves will only be produced at the iceberg-glacier interface. However, in the case where the glacier moves during capsize, there may be an additional source of seismic waves: the force applied by the moving glacier on the bedrock. For several recorded seismic events, a motion of the glacier was observed during and after an event of iceberg capsize (reverse motion and step-like change in the velocities). There may be a seismic signature of the motion of the glacier during capsize, e.g. due to a stick-slip motion (Wiens et al., 2008; Winberry et al., 2020). To our knowledge, no mechanical modelling of the sliding of a glacier during iceberg capsize has been done in the literature.

- The drop of hydrodynamic pressure below a glacier tongue during a capsize may produce a vertical force on the glacier that could generate seismic waves (Murray et al., 2015a). This might have similarities with the response of a glacier tongue to tidal forcing (flexure of the tongue) for which icequakes have been measured which the same time variability as the tides (Winberry et al., 2009; Podolskiy et al., 2016).

- The pressure force on the seafloor due to the motion of the water during the capsize may be a source of seismic waves recorded at teleseismic distances. Such hypothesis has not yet been investigated in the literature, to our knowledge. This has similarities with other geophysical phenomena which produce seismic waves: the impact of calving of small iceberg in the water (Bartholomaus et al., 2012), and the wave-wave interactions that produce microseisms (Longuet-Higgins, 1950).

- Icebergs usually capsize at near grounded glacier front, thus where the sea floor is shallow. Therefore, another possible source of seismic waves is the scraping of the iceberg on the fjord bottom (Amundson et al., 2008)

- The reflexions of the ocean waves on the fjord lateral boundaries produce a seismic tremor, known as *seiche* (e.g. Walter et al., 2013; Sergeant et al., 2016).

Seismic waves are elastic waves produced by a source force (or a double couple in case of tectonic events) that propagate in the earth. If the propagation effects are well known (velocities of elastic waves well constrained), the seismic signals emitted during the capsize of an iceberg can shed light on the source mechanism (e.g. Amundson et al., 2010; Walter et al., 2012; Olsen and Nettles, 2017, 2019; Sergeant et al., 2016). If the seismic signals produced by different sources are different (in frequency, start time, duration and location), then the physical processes at play for each source phenomena can be decoupled by analysing various parts of the seismic spectrum (Sergeant et al., 2016). There is a good seismic coverage in Greenland thanks to the GLISN network (Clinton et al., 2014). This network of about 33 seismic stations has been deployed since 2006 on ice and land in Greenland and closeby islands, for the purpouse of studying earthquakes produced in this region.

(Sergeant et al., 2018, 2019) inverted the volumes of capsizing icebergs by comparing the seismic source force (calculated using the seismic data) and a mechanical model (Sergeant et al., 2018) for the contact force of the capsizing iceberg on the glacier front. This study estimated the dynamic losses at Greenland glacier fronts between 1993 and 2003, and discussed the temporal and spatial variation of this buoyancy driven discharge. We present a slight correction in the calculation of the source force from the seismic data in appendix A. Although the error implied by this correction was not estimated, it should not change the results, because it only affects one seismic station.

1.5 Surface measurements

On top of seismic signals, there are complementary (and more traditional) measurement techniques. GPS measurements at the surface of the glacier gives insights on the motion of the glacier during capsize (Nettles et al., 2008; Nettles and Ekström, 2010; Murray et al., 2015a,b). We describe these measuremnets in the next section 1.6. Such data have a good temporal resolution (≈ 1 second), but they are not continuous because data are only available for few events that occured during a GPS campaign. Satellite and terrestrial images, underwater imaging, and ground penetrating radar (GPR) campaings (e.g. Chauché, 2016; Kehrl et al., 2017; Joughin et al., 2018) give information on velocities at the surface of the glacier and the geometry of the glacier. Such measurements have a temporal resolution of several hours or days which is too long for monitoring capsize events. However, this data give valuable information on the longer time behaviour of the glacier such as the observed acceleration, retreat and thinning of Greenland glaciers, which are correlated to the calving processes (Veitch and Nettles, 2012).

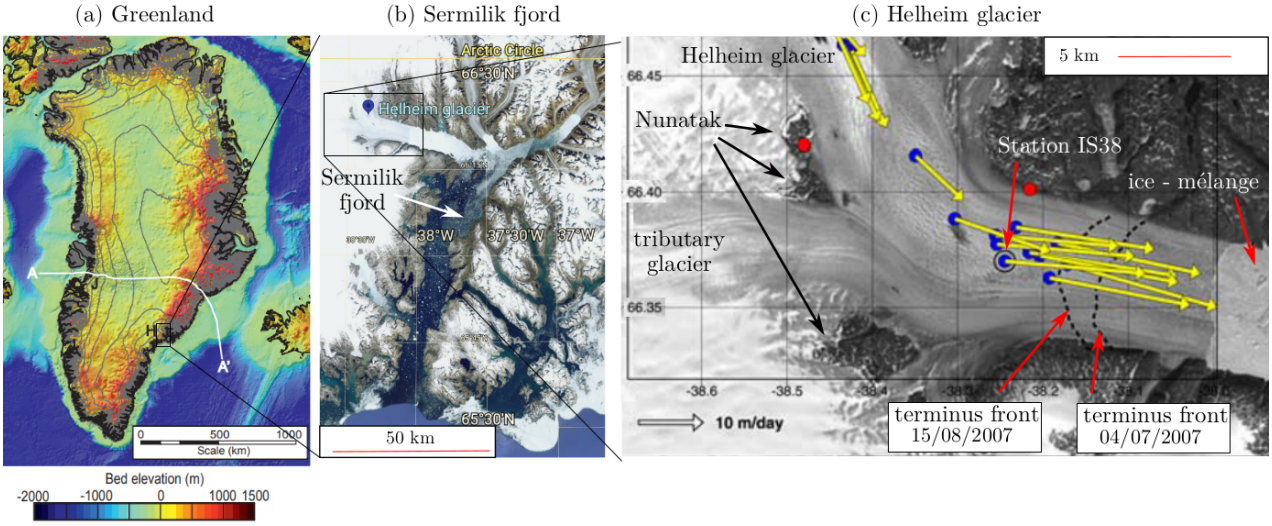

Figure 1.3: Greenland bathymetry adapted from Vaughan et al. (2014) (a), the Sermilik fjord (Google maps view) (b) and the Helheim glacier, the yellow arrows show the direction and the amplitude of the averaged velocities in July-August 2007, adapted from Nettles et al. (2008) (c).

1.6 Well documented capsize events at the Helheim glacier

Due to the difficulty of instrumentation, there are only a few well documented capsize events. To our knowledge, there are only two campaigns that observed horizontal displacements of a glacier during an event of iceberg capsize. Both campaigns took place at the Helheim glacier (Fig. 1.3 a), one of the two biggest tide water glaciers in Southeast Greenland together with Kangerdlugssuaq glacier. For these events, seismic waves were recorded at seismic stations.

In the summer 2007, Nettles et al. (2008); Nettles and Ekström (2010) observed that the glacier response to the capsize of an iceberg was a step-like acceleration. In the summer 2013, the glacier reversed its motion during a few seconds during the several capsize events (Murray et al., 2015a,b).

To shed light on the physical processes at play during these events, it is neccesary to describe and understand the basal geometry, the recent evolution of the glacier geometry, velocities, and other measured or inferred physical properties of the glacier.

Helheim glacier geometry

Due to variations in external forcings (seasonal and yearly weather variations, and longer term climate change) there is a temporal variation of the geometry (surface elevation, submarine geometry, and terminus position) and the thermo-dynamical properties (velocities and temperatures). Because of harsh field conditions, we do not have continuous measurements. To estimate the glacier geometry and physical properties at a certain time and location, it is possible to do an interpolation on various datasets or an inversion using glacier modelling to estimate the mechanical behaviour of the glacier.

A top view of the Helheim glacier terminus at the end of the Sermilik fjord is shown in Fig 1.3 b, and the basal elevations and surface velocities are shown in Fig. 1.4. Helheim glacier flowlines (e.g. red dashed line in Fig. 1.4) rotate from a NW-SE orientation to a W-E orientation about 15km upstream from the terminus. A smaller ice stream (tributary glacier) joins the main Helheim glacier just dowstream from a Nunatak (glacial island) and after the turn in the flowlines (Fig 1.3 c). Moving towards the terminus, along the flowline the basal elevation of the Helheim glacier decreases, except between 20 and 10 km upstream from the terminus, where it increases thus there

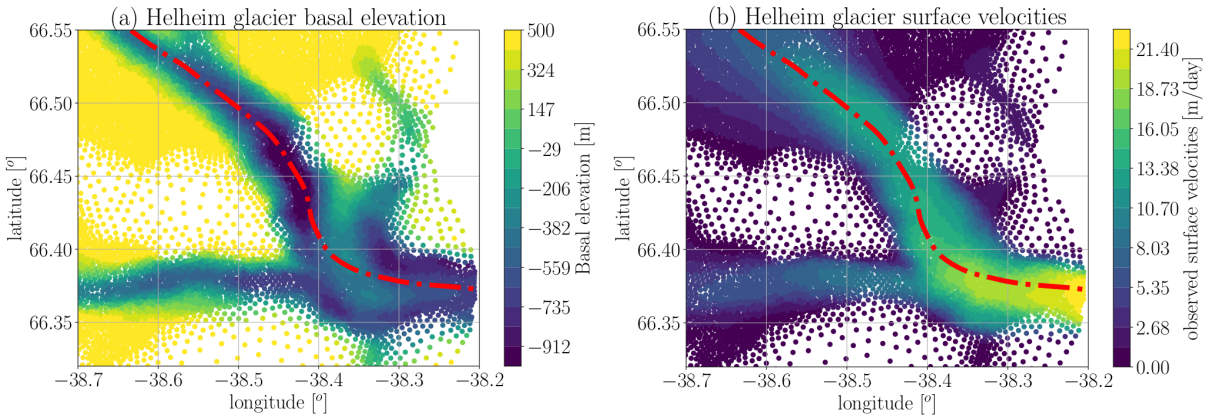

Figure 1.4: Bedrock elevation at the Helheim glacier (a) (Morlighem et al., 2017), and observed velocities at the Helheim glacier (Joughin et al., 2016, 2018) (b).

is a bowl shape followed by a hill shape bathymetry.

Surface measurements did not allow to determine precisely this glacier-water interface of the floating tongue. (Kehrl et al., 2017) inferred that a zone of the Helheim glacier was grounded (resp. floating) during the 2011-2015 period when its surface remained more than 5m above (resp. bellow) the flotation threshold. The flotation line is the glacier surface elevation for the case where the glacier would be at hydrostatic equilibrium and still in contact with the bedrock (the submarine height equals the bedrock depth). The flotation threshold is located at $(1-\frac{\rho_w}{\rho_i})H_w$ above sea level, with H_w the height of the submarine part of the glacier. Note that the 5m uncertainty accounts for the error on the bedrock of ±50m and the vertical motion of the glacier with the tides. The authors infer a tongue of length $3-5$ km long and narrower than the glacier terminus (Kehrl et al., 2017, fig. 5d).

Thinning or thickening rates can be inferred from surface velocities which have a high temporal resolution (≈ 130 measurements on the 2008-2016 period) using the flux gate method (Kehrl et al., 2017). At the Helheim glacier, thickening rates peaked in January - March, and glacier thinning rates peaked in August, September, with values exceeding 15cm/d during 2010, 2013 and 2015 summers and around $5-10$ cm/d during 2011, 2012, and 2014 summers.

Seasonal pattern and capsize events

Helheim glacier exhibits two types of seasonal pattern. The first type is: a large summer retreat with non tabular iceberg calving, followed by a winter advance of >3 km that stopped when the terminus reached the top of the reverse bed slope (hill), where it became floating and calved tabular icebergs. In this case the ice mélange was less rigid (2010/2011 and 2013/2014). In the second type there is no clear advance or retreat (2008/2009, 2009/2010, 2011/2012, 2012/2013, 2014/2015, 2015/2016).

Since two well documented iceberg capsize events mentioned above occurred on 25 and 31 July 2013. The glacier retreated by 2.8 km down the reverse bed slope between March and mid-August reaching a terminus position 5 km upstream of the mean terminus position on the 2008-2016 period. During this retreat, the glacier sped up by 1.9 km/yr (32 %), reached a maximum velocity in September and thinned by ≈ 20 m. 20 km upstream it sped up by 0.3 km/yr (6 %) and reached its maximum velocity in late November (Kehrl et al., 2017).

Helheim glacier 2007 event: brutal acceleration

(Nettles et al., 2008; Nettles and Ekström, 2010) observed the event that occurred on DOY 225 (August 25) in 2007 at Helheim glacier using twelve GPS sensors on the glacier in the last 20 km from the terminus (blue dots in Fig. 1.3 c) and a seismic station located in the Isortoq settlement, about 100 km from the glacier. The GPS data are measured with a 15 s interval. Here, we summarize their observations:

- the mean horizontal velocities during the campaign was 25 m/day close to the calving front, and 12 m/day further upstream (yellow arrows in Fig. 1.3 c)
- a brutal acceleration of the glacier, with a step-like change in the velocity during capsize, in the last 15 km before the terminus was observed during and after the capsize.
- for a GPS sensor (IS38) located ≈ 3 km from the terminus front, the glacier accelerates from a mean velocity of 21.7 m/day before the capsize to a mean velocity of 23 m/day just after the capsize and slowly decelerates to 22.7 m/day about 12 hours after the capsize, see detrended horizontal displacements in Fig. 1.5 (a).
- a small glacial earthquake occured about 30 min before the speedup and another larger glacial earthquake occured 80 min after the small one, see detrended horizontal displacements in Fig. 1.5 (b).

According to the authors (Nettles et al., 2008), the observed step-like change in the velocity corresponds to an acceleration too small to explain the observed seismic radiation.

In Fig. 1.5 (c), we show the vertical displacements at station SFJD, located ≈ 542 km from the Helheim glacier front, to the West. The spectrogram (middle) shows that the energy is higher in the $\approx 0.001 - 0.07$ Hz frequency band. We observe several events with durations of ≈ 10 min.

Helheim glacier 2013 event: transitory reverse motion

(Murray et al., 2015b,a) monitored the Helheim glacier using nineteen GPS sensors between July 11 and August 28 2013, five cameras on the bedrock with an hourly time resolution, and seismic stations from the GSN network. A series of capsizing events occurred on DOY 206 (July 25) producing glacial earthquakes and a transitory reverse motion of the glacier surface. We report specific observations here:

- the pre earthquake flow speed was 29 m/day
- the terminus was ungrounded on a few kilometers, as explained above and in (Kehrl et al., 2017, fig. 5d)
- a vertical downwards motion of 12 cm occurred during ≈ 3 minutes and then a vertical upwards motion of 16 cm occurred during ≈ 2 minutes
- a reverse horizontal motion of 40 m/day occurred during 200 s, that is about 9 cm in total

We adapted the figure 2.A and 2.B by (Murray et al., 2015a) in Fig. 4.8 (Chapter 4).

1.7 Modelling glaciers

Most ice flow models in the literature focus on long time scales and aim at reproducing the evolution of ice sheets and glaciers with past and future climate change, (e.g. Calov et al., 2018; Rückamp et al., 2018; Goelzer et al., 2020; Rückamp et al., 2020). Using inverse approaches, these models also allow to retrieve physical properties

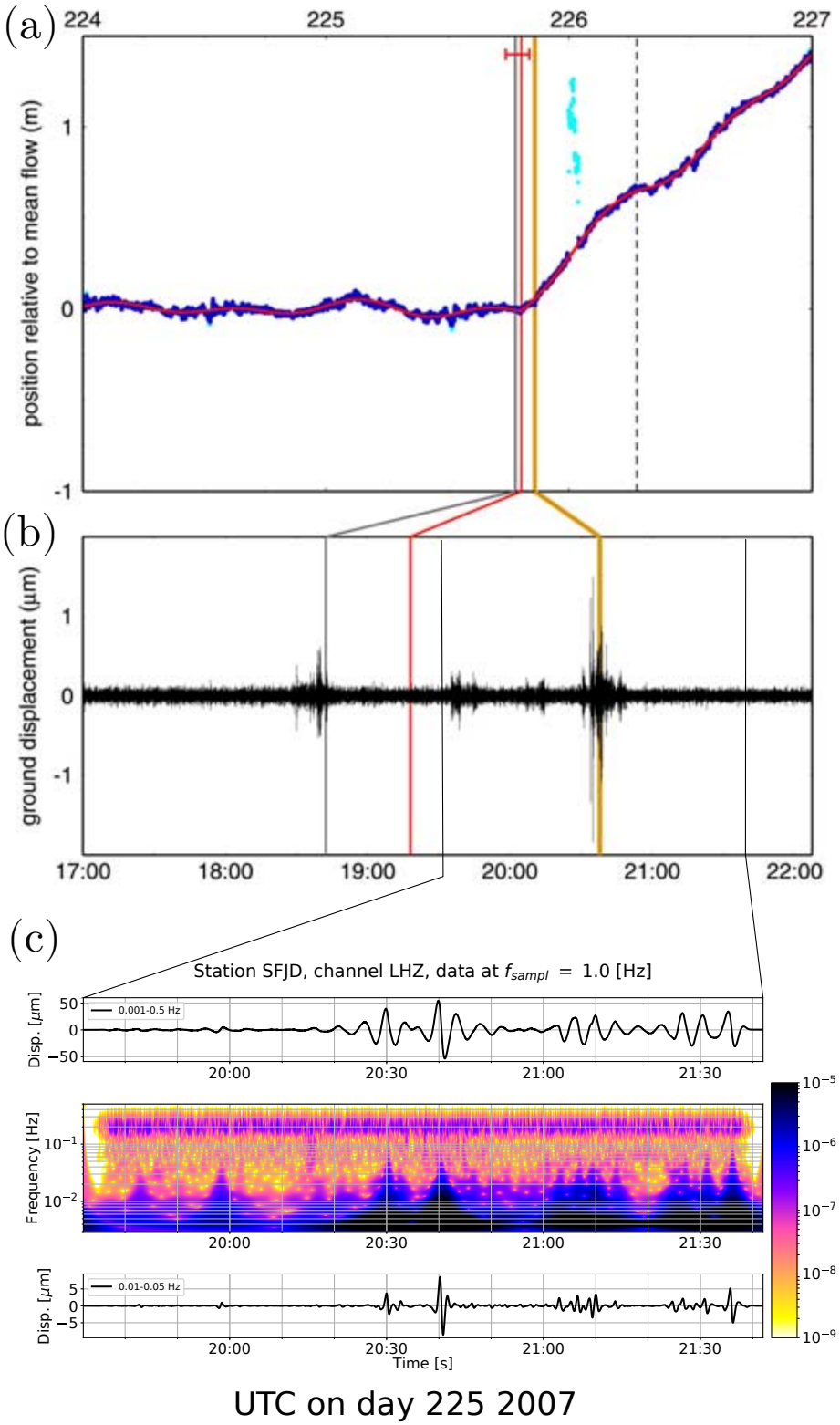

Figure 1.5: Along-flow position of GPS station IS38 (Fig.1.3 a) (a), seismic data from a station located at ≈ 100 km (Nettles et al., 2008) (b), and LHZ component from SFJD GLISN station located at ≈ 542 km from the glacier front (c). The plots of the SJFD station represent from top to down: the displacement filtered between 0.001 and 0.5 Hz, the spectrogram and the displacement filtered between 0.01 and 0.05 Hz.

of the glacier (ice rheology and basal friction), from the available field measurements, that is surface topography, surface velocities, and bathymetry (e.g Macayeal, 1992; Gudmundsson and Raymond, 2008; Morlighem et al., 2010; Arthern et al., 2015). The surface velocity and surface elevation are directly related to the flow properties and the basal motion, although these two effects are difficult to decouple. In these models, the flow is usually assumed to be purely viscous (no elasticity), with temperature dependent viscosity and additional enhancement factors that account for the ice microstructure (preferred orientation of ice grains and damage) or more advanced anisotropic rheological laws (e.g. Mangeney et al., 1997; Castelnau et al., 1998; Mangeney and Califano, 1998).

At a shorter time scale, some models describe the response of a elastic or visco-elastic floating tongue to tidal forcing (e.g. Vaughan, 1995; Rosier et al., 2017). Krug et al., 2014b modelled the ice fracture and implemented a damage criteria to include calving process using the finite element Elmer/Ice model (Gagliardini et al., 2013). Tsai et al. (2008) use a one-dimensional glacier with Glen's rheology with a friction law to reproduce the seismic waves emitted at a glacier front during an acceleration of the glacier (but no iceberg capsize). Tsai et al. (2008); Amundson et al. (2012); Sergeant et al. (2018) give semi-analytical models for the capsize of an iceberg in contact with a glacier terminus using a drag force and/or an added-mass effect to model the motion of the fluid.

1.8 Manuscript Outview

In this PhD we investigated the physical processes at play during the capsize of an iceberg at the front of tide-water glaciers. The processes are governed by fluid dynamics with a free surface, solid mechanics of a visco-elastic material, fluid-structure interactions, contact mechanics, thermo-dynamics and wave propagation in a heterogeneous medium. Because of the complexity of the system, no model has yet been designed to couple all the equations related to these processes. Our methodology is use a state-of-the-art model for solid mechanics and contact mechanics (Z-set) and a semi-analytical model for fluid-structure interactions (SAFIM). This work follows the previous work by A. Sergeant in her PhD (Sergeant, 2016) which was published in (Sergeant et al., 2016, 2018, 2019).

In Chapter 2 we tackle the modelling of a rectangular iceberg capsizing in the open ocean. We use results of a reference model in fluid-structure interactions (ISIS-CFD) to analyse the motion of the capsizing iceberg as well as the hydrodynamic effects. However, ISIS-CFD does not yet model the dynamics of an iceberg in contact with a glacier front. Therefore, we use a semi-analytical model (SAFIM) that accounts for the fluid forces using parametrized forces. We validate and improve the semi-analytical model against the reference model in the case of an iceberg capsizing in the open ocean. This work is the published article (Bonnet et al., 2020). We add a complement to this article describing the hydrodynamic pressure computed by the reference model during the capsize of a field scale iceberg. We analyse the hydrodynamic pressure on the sea floor during the capsize and its integrated force as a potential source of seismic waves. We compare the hydrodynamic pressure on the surface of the iceberg with a local quadratic or linear drag.

In Chapter 3, we tackle the modelling of a two-dimensional iceberg in contact with a rigid or an elastic glacier front. Compared to the work conducted by Sergeant (2016), we use an adjustable drag coefficient (validated in Chapter 4) and we include the elasticity of the glacier. We present several contact laws for the iceberg-glacier contact problem, and their limitations, in particular relative to the elasticity of the glacier. We investigate the impact of the glacier elasticity on the glacier-iceberg horizontal and vertical contact force. With this work, we obtain the capsize force that will be applied on the terminus of a visco-elastic glacier in the next Chapters.

In Chapter 4 we assess the response of a two-dimensional visco-elastic glacier to the capsize of an iceberg. We build the numerical setup in the finite element Z-set software. As a first step to investigate the importance of the

model parameters, the chosen geometry is a glacier with a parallelogram shape on a smooth and inclined bedrock. We study a glacier with a grounded terminus and a glacier with a horizontal and rectangular floating tongue. As suggested by literature studies, we implement two friction laws: a Weertman viscous law upstream and a Coulomb friction law close to the terminus. We observe that the force applied on the terminus front is fully transmitted to the bedrock and discuss this by estimating, with an analytical calculation, the negligible inertia of the glacier during capsize. We show the deformation of the glacier during the two types of capsize for both a grounded glacier and a glacier with a floating tongue, and we compare it qualitatively to displacements measured in the field. In addition to the effect of the elasticity, we discuss the effect of ice viscosity and the friction coefficients on the surface and basal displacements of the glacier during the capsize.

In Chapter 5 we extend the setup used in the previous Chapter 4 to the geometry of a field glacier in Greenland for which there are well documented capsize events. We chose the Helheim glacier and assess two different geometries: a grounded geometry and a geometry with a floating tongue (both geometries are supported by different field observations). To initiate our model we use results from an ISSM inversion, a reference model for long time simulations of glaciers and ice sheets, developed and run by collaborators. For this complex geometry, the Weertman law is not yet included in the Z-set model. Thus, we apply the Coulomb friction law on all the basal interface and we focus on the response of the last kilometres before the terminus. We discuss the similarities of the results obtained with the geometry of a Helheim glacier and the results obtained with a geometry on a constant slope. To investigate the effect of the length of the Coulomb and Weertman zone, we use the constant slope geometry (with a height similar to the height of the Helheim glacier). Finally, we compare the results obtained with the Helheim geometry with the displacements measured by Murray et al. (2015a).

CHAPTER 2

Modelling capsizing icebergs in open ocean

In this chapter we present results on the physical understanding and the mechanical modelling of the motion of a capsizing in the open ocean using a reference model for fluid-structure interactions (ISIS-CFD) and a semi-analytical model (SAFIM). The first part of this Chapter is the published paper Bonnet et al. (2020). In addition, we show other results that were obtained with the ISIS-CFD model and that give insights into the hydrodynamic pressure on the sea floor and on the iceberg during the capsize in section 2.11 and section 2.12.

Geophysical Journal International

Geophys. J. Int. (2020) **223,** 1265–1287
Advance Access publication 2020 July 25
GJI General Geophysical Methods

doi: 10.1093/gji/ggaa353

Modelling capsizing icebergs in the open ocean

P. Bonnet,[1,2,3] V.A. Yastrebov,[3] P. Queutey,[4] A. Leroyer,[4] A. Mangeney,[1,5,6] O. Castelnau,[2] A. Sergeant,[7,*] E. Stutzmann[1] and J-P Montagner[1]

[1] *Institut de Physique du Globe de Paris, Sorbonne Paris Cité, Seismology Group, CNRS UMR* 7154, *Paris, France. E-mail: pbonnet@ipgp.fr*
[2] *ENSAM, CNAM, Laboratoire Procédés et Ingénierie en Mécanique et Matériaux, CNRS UMR 8006, Paris, France*
[3] *MINES ParisTech, PSL University, Centre des Matériaux, CNRS UMR* 7633, *Evry, France*
[4] *Laboratoire en Hydrodynamique Energétique et Environnement Atmosphérique (LHEEA), METHRIC Team, CNRS UMR* 6598, *Centrale Nantes, France*
[5] *Université de Paris, France*
[6] *Inria, Lab. J.-L. Lions, ANGE team, CNRS, France*
[7] *Laboratory of Hydraulics, Hydrology and Glaciology, ETH Zurich, Zurich, Switzerland*

Accepted 2020 July 12. Received 2020 June 17; in original form 2019 December 20

SUMMARY

At near-grounded glacier termini, calving can lead to the capsize of kilometre-scale (i.e. gigatons) unstable icebergs. The transient contact force applied by the capsizing iceberg on the glacier front generates seismic waves that propagate over teleseismic distances. The inversion of this seismic signal is of great interest to get insight into actual and past capsize dynamics. However, the iceberg size, which is of interest for geophysical and climatic studies, cannot be recovered from the seismic amplitude alone. This is because the capsize is a complex process involving interactions between the iceberg, the glacier and the surrounding water. This paper presents a first step towards the construction of a complete model, and is focused on the capsize in the open ocean without glacier front nor ice-mélange. The capsize dynamics of an iceberg in the open ocean is captured by computational fluid dynamics (CFD) simulations, which allows assessing the complexity of the fluid motion around a capsizing iceberg and how far the ocean is affected by iceberg rotation. Expressing the results in terms of appropriate dimensionless variables, we show that laboratory scale and field scale capsizes can be directly compared. The capsize dynamics is found to be highly sensitive to the iceberg aspect ratio and to the water and ice densities. However, dealing at the same time with the fluid dynamics and the contact between the iceberg and the deformable glacier front requires highly complex coupling that often goes beyond actual capabilities of fluid-structure interaction softwares. Therefore, we developed a semi-analytical simplified fluid-structure model (SAFIM) that can be implemented in solid mechanics computations dealing with contact dynamics of deformable solids. This model accounts for hydrodynamic forces through calibrated drag and added-mass effects, and is calibrated against the reference CFD simulations. We show that SAFIM significantly improves the accuracy of the iceberg motion compared with existing simplified models. Various types of drag forces are discussed. The one that provides the best results is an integrated pressure-drag proportional to the square of the normal local velocity at the iceberg's surface, with the drag coefficient depending linearly on the iceberg's aspect ratio. A new formulation based on simplified added-masses or computed added-mass proposed in the literature, is also discussed. We study in particular the change of hydrodynamic-induced forces and moments acting on the capsizing iceberg. The error of the simulated horizontal force ranges between 5 and 25 per cent for different aspect ratios. The added-masses affect the initiation period of the capsize, the duration of the whole capsize being better simulated when added-masses are accounted for. The drag force mainly affects the amplitude of the fluid forces and this amplitude is best predicted without added-masses.

Key words: Fracture and flow; Glaciology; Numerical modelling.

* Now at: Aix Marseille Univ, CNRS, Centrale Marseille, LMA, France

1 INTRODUCTION

A current concern in climate science is the estimation of the mass balances of glaciers and ice sheets. The Greenland ice sheet mass balance contributes significantly to sea level rise, accounting for about 15 per cent of the annual global sea level rise between 2003 and 2007 (Zwally *et al.* 2011). However, it is difficult to draw conclusions on general trends given the high uncertainties (Lemke *et al.* 2007) in these estimations, notably due to difficulties in estimating and partitioning the ice-sheet mass losses (Van den Broeke *et al.* 2009). Ice mass balance can be determined by calculating the difference between the (i) surface mass balance, mainly determined by inland ice gains minus ice losses and (ii) dynamic ice discharge, mainly made up of submarine melting and iceberg calving (Van Den Broeke *et al.* 2016). One third to one half of the ice mass losses of the Greenland ice sheet are due to dynamic ice discharge (Enderlin *et al.* 2014). Note that dynamic ice discharge is a complex phenomenon, influenced by ocean and atmospheric forcing and by glacier geometry and dynamics (Benn *et al.* 2017).

When a marine glacier terminus approaches a near-grounded position, calving typically occurs through the capsize of glacier-thickness icebergs. Such buoyancy-driven capsize occurs for icebergs with a width-to-height ratio below a critical value (MacAyeal & Scambos 2003). When drifting in the open ocean, icebergs deteriorate through various processes such as break-up, wave erosion and solar or submarine convection melting (Job 1978; Savage 2001), and release freshwater that can potentially affect overturning ocean circulation (Marsh *et al.* 2015; Vizcaino *et al.* 2015). Wagner *et al.* (2017) explain that icebergs mainly melt through wind-driven wave erosion that leads to lateral thinning and thus eventually a buoyancy driven capsize of the icebergs. Moreover, iceberg drift simulations have shown that capsizing icebergs live longer and drift further than non-capsizing icebergs (Wagner *et al.* 2017) .

When they capsize right after calving, icebergs exert an almost horizontal transient contact force on the glacier front. This force is responsible for the generation of up to magnitude $M_w \approx 5$ earthquakes that are recorded globally (Ekström *et al.* 2003; Podolskiy & Walter 2016; Aster & Winberry 2017) and can be recovered from seismic waveform inversion (Walter *et al.* 2012; Sergeant *et al.* 2016). The study of iceberg calving and capsizing with such glacial earthquakes data is a promising tool, complementary to satellite imagery or airborne optical and radar sensors as it can provide more insights into the physical calving processes and iceberg–glacier–ocean interaction (Tsai *et al.* 2008; Winberry *et al.* 2020) as well as it can track ice losses almost in real time. However, there is no direct link between the size of an iceberg and the generated seismic signal (Tsai *et al.* 2008; Amundson *et al.* 2012; Walter *et al.* 2012; Sergeant *et al.* 2016, 2018). Sergeant *et al.* (2018, fig. 6d) showed that a given centroid single-force (CSF) amplitude, which is usually used to model the relevant signal, can be obtained with icebergs of different volumes (their fig. 6d). Olsen & Nettles (2019, fig. 9) found a weak correlation between the seismic data (CSF amplitude) and the dimensions of the iceberg, the authors also suggested that taking into account hydrodynamics and iceberg shape could improve this correlation. Different processes involving the interactions between the iceberg, glacier, bedrock, water and ice mélange contribute to the type of calving, earthquake magnitude and seismic waveform (Tsai *et al.* 2008; Amundson *et al.* 2010, 2012).

To investigate in detail the link between iceberg volume, contact force and the generated seismic signals, the use of a hydrodynamic model coupled with a dynamic solid mechanics model is required. The iceberg-ocean interaction governs the iceberg capsize dynamics and thus controls the time-evolution of the contact force which is responsible for the seismic waveform and amplitudes. Full modelling of the glacier / ocean / bedrock / iceberg / ice-mélange system is beyond capabilities of most existing models because it requires complex and costly coupling between solid mechanics, contact dynamics and fluid dynamics. Simplified models of capsizing icebergs proposed in the literature approximate icebergs by 2-D rectangular rigid solids subject to gravity and buoyancy force, iceberg-glacier contact force and simplified hydrodynamic effects using either added-masses (Tsai *et al.* 2008) and/or pressure drag (Amundson *et al.* 2012; Burton *et al.* 2012; Sergeant *et al.* 2018, 2019). These models have been proposed to describe a specific aspect of the capsize: its vertical and rotational motion (Burton *et al.* 2012) validated against laboratory experiments, or the horizontal force that icebergs exert on the glacier fronts (Tsai *et al.* 2008; Sergeant *et al.* 2018). To build a complete catalogue of seismogenic calving events that can be used for seismic inversion and iceberg characterization, the model must accurately describe the interactions between the iceberg, the glacier and the ocean. At the same time, its formulation should either remain sufficiently simple to enable fast simulations of numerous events or, alternatively be based on the interpolation of the response surface constructed on numerous full-model simulations. In particular, the horizontal force and the torque exerted by the fluid on the iceberg should be modelled as accurately as possible, since it controls the horizontal contact force (Tsai *et al.* 2008; Amundson *et al.* 2012; Burton *et al.* 2012; Sergeant *et al.* 2018).

This paper aims (i) to provide insights in the complex interactions between a capsizing unconstrained iceberg and the surrounding water in 2-D using a reference fluid dynamics solver and (ii) to reproduce the main features of this interaction using a simplified model formulation suitable for being integrated in a more complete model. For this, we use a computational fluid dynamics solver (ISIS-CFD Software for Numerical Simulations of Incompressible Turbulent Free-Surface Flows) to generate reference results for the capsizing motion. This model solves Reynolds Averaged Navier–Stokes Equations (RANSE) and handles interactions between rigid solids and fluids with a free surface, but is not yet validated for modelling contacts between solids. This state-of-the-art solver has been extensively validated on various marine engineering cases (Visonneau 2005; Queutey *et al.* 2014; Visonneau *et al.* 2016) but not yet applied to kilometre-size objects subject to fast and big rotations like capsizing icebergs in the open ocean, which give rise to high vorticity. Before applying ISIS-CFD to the field-scale iceberg capsize, we evaluate how well it can reproduce small-scale laboratory experiments (typical dimension of 10 cm). We compare here ISIS-CFD simulations to the laboratory experiments conducted by Burton *et al.* (2012).

To obtain a model that can be easily coupled with a solid mechanics model, we propose a simplified formulation (SAFIM, for Semi-Analytical Floating Iceberg Model) for the interactions between iceberg and water. In this model, the introduced hydrodynamic forces account for water drag and added-masses, these two effects being considered uncoupled and complementary. Such a description was initially proposed for modelling the effect of waves on vertical piles (Morison *et al.* 1950) and has been widely used for modelling the effect of waves and currents on bulk structures (Tsukrov *et al.* 2002; Venugopal *et al.* 2009). The SAFIM's hydrodynamic forces involve some coefficients that need to be calibrated to represent as accurately as possible the effects of the hydrodynamic flow on the capsize motion. These coefficients were calibrated on the reference results provided by ISIS-CFD.

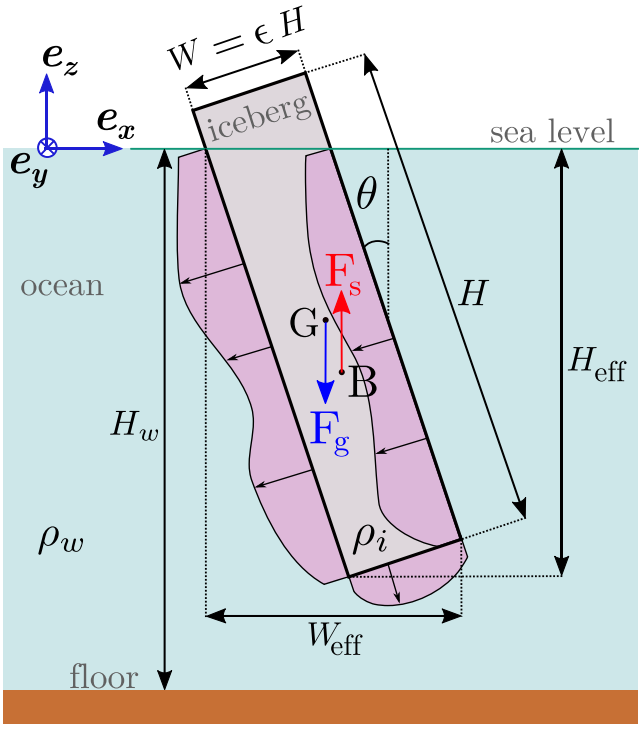

Figure 1. Simplified iceberg's geometry: the centre of gravity is G and the centre of buoyancy is B. The forces acting on the moving iceberg are: the gravity force $\boldsymbol{F}_g$, the hydrostatic fluid force $\boldsymbol{F}_s$ and the hydrodynamic pressure sketched by the pink shaded area, the forces from the added mass are not indicated; these efforts also induce a torque on the iceberg.

The paper is organized as follows. Section 2 presents the reference ISIS-CFD fluid dynamics model and its results are compared with those of laboratory experiments from Burton *et al.* (2012). The complexity of the fluid motion surrounding the iceberg and the pressure on the iceberg are then discussed. The similarities between the laboratory-scale and field-scale simulations are also presented. In Section 3, we present the SAFIM model and discuss the differences with other models from the literature. In Section 4, ISIS-CFD and SAFIM are compared for different case-studies, the error quantification and fitting of parameters are discussed. Section 5 is an overall discussion: comparison of previous models, the new SAFIM model and the reference ISIS-CFD model, followed by a discussion of different drag and added-mass models, which is concluded by a sensitivity analysis with respect to physical properties of geophysical systems.

2 CFD SIMULATIONS OF ICEBERG CAPSIZE

2.1 Problem set-up

In this paper, we investigate the capsize of unstable 2-D icebergs in the open ocean, that is away from the glacier front, other icebergs and in absence of ice-mélange. Water and ice densities are noted ρ_w and ρ_i. In our numerical simulations, for the field scale, we take the typical values of $\rho_w = 1025\,\mathrm{kg\,m^{-3}}$ and $\rho_i = 917\,\mathrm{kg\,m^{-3}}$. For the laboratory experiments, the densities are set to $\rho_w = 997\,\mathrm{kg\,m^{-3}}$ and $\rho_i = 920\,\mathrm{kg\,m^{-3}}$, which would enable a direct comparison with Burton *et al.* (2012). A typical geometry is shown in Fig. 1. The out-of-plane dimension L of the iceberg (i.e. along $\mathbf{e}_y$) is assumed to be sufficiently large compared to the height and the width such that the problem can be considered essentially 2-D. This assumption is discussed in Section 5.6.

In this 2-D set-up, icebergs are assumed to be rectangular with in-plane dimensions H and W and an aspect ratio denoted by $\varepsilon = W/H$. Rectangular icebergs in a vertical position are unstable, that is will capsize spontaneously, for aspect ratios smaller than a critical value (MacAyeal & Scambos 2003):

$$\varepsilon < \varepsilon_c = \sqrt{6\,\rho_i\,\frac{\rho_w - \rho_i}{\rho_w^2}}.$$

This critical aspect ratio is $\varepsilon_c \approx 0.75$ for the field densities and $\varepsilon_c \approx 0.65$ for the laboratory densities. For $\varepsilon > \varepsilon_c$, icebergs are vertically stable and will not capsize unless initially tilted sufficiently (Burton *et al.* 2012).

The iceberg is assumed to be homogeneous and rigid, that is it does not deform elastically. The mass of an iceberg per unit of thickness along $\mathbf{e}_y$ is given by $m = \rho_i H^2 \varepsilon$. Points G and B are the centre of gravity of the iceberg and the centre of buoyancy, respectively. The iceberg position is described by the horizontal and vertical positions of G, denoted x_G and z_G, respectively, and by the inclination θ with respect to the vertical axis, which is collinear with the vector of the gravity acceleration. H_w is the water depth.

2.2 ISIS-CFD solver

The ISIS-CFD solver, developed by LHEEA in Nantes (France), is a state-of-the-art solver for the dynamics of multiphase turbulent flows (Queutey & Visonneau 2007; Leroyer *et al.* 2011; Guilmineau *et al.* 2017, 2018), interacting with solid and/or flexible bodies (Leroyer & Visonneau 2005; Hay *et al.* 2006; Durand *et al.* 2014), and with a free surface. Today, it is one of very few available software products capable of solving problems as complex as interactions between solids and fluids with a free surface (water and air interface). The target applications of ISIS-CFD are in the field of marine engineering, for example modelling the dynamic interactions between a ship and surface waves (Visonneau 2005; Queutey *et al.* 2014; Visonneau *et al.* 2016) or the complex flows and interactions involved in the global hull-oars-rower system in Olympic rowing (Leroyer *et al.* 2012). ISIS-CFD solves the Reynolds Averaged Navier-Stokes Equations (RANSE, Robert *et al.* 2019) and also disposes few other turbulence models.

For the specific application of iceberg capsize (Fig. 1), two different turbulence equations were tested and were found to give very similar results: *k-w* (Menter 1993) and Spalart-Allmaras (Spalart & Allmaras 1992). The code uses an adaptive grid refinement (Wackers *et al.* 2012) or an overset meshing method (mandatory to deal with large amplitude body motion close to a wall for example) to connect two non-conforming meshes. The mesh used here is a converged mesh with $n = 43\,000$ elements. An example of a typical mesh is illustrated in Fig. 2. The coupling between the solid and the fluid is stabilized with a relaxation method based on the estimation of the periodically updated added-mass matrix (Yvin *et al.* 2018). The lateral sides of the simulation box are put far from the capsizing iceberg, and include a damping region, so that the reflected waves do not interfere with the flow near the iceberg for the duration of the simulation.

In the field of application of the ISIS-CFD flow solver, the typical range of Reynolds numbers (Re) extends from 10^6 for model-scale ship flow to 10^9 for full-scale ship flow (Visonneau *et al.* 2006), and the local viscous contribution to the hydrodynamic force is as high

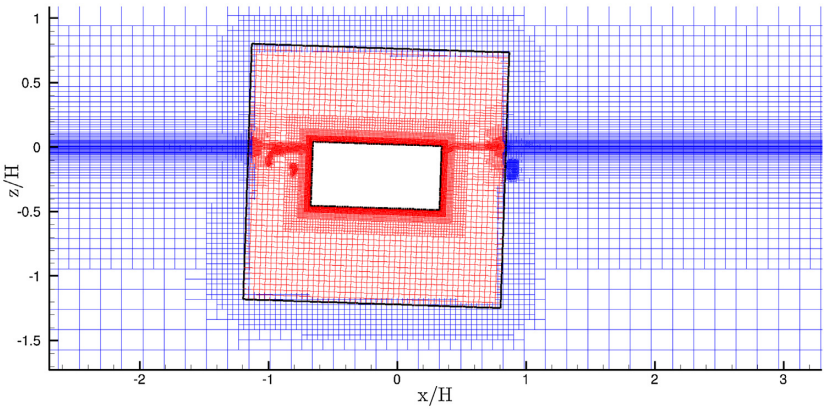

Figure 2. A portion of a typical mesh used for the simulation of iceberg capsize with ISIS-CFD. The two axes represent the dimensionless horizontal position x/H and the dimensionless vertical position z/H. The iceberg $\varepsilon = 0.5$ (in white) is in the centre of a squared domain (fine mesh in red) moving and rotating with the iceberg over a background domain (coarser mesh in blue). The mesh is automatically refined around the air-water interface (a finely meshed horizontal zone) and also around the solid/fluid interface.

as ≈50 per cent of the total drag force. Here, the ISIS-CFD solver is applied to a significantly different geometry (rectangular shape of iceberg instead of streamlined shape of ship), type of motion (big rotations instead of translational motion) and dimensions (km-scale icebergs instead of tens of metres long ships). This application provides new challenges for the ISIS-CFD solver: high vorticity and free surface motion, greater lengths and velocities together with massive separations due to the sharp corners of the iceberg.

2.3 Laboratory experiments

Since ISIS-CFD simulations are compared with laboratory data (Section 2.4), we briefly summarize here the technical details of the corresponding experiments conducted by Burton *et al.* (2012). The laboratory experiments consist in the capsize of parallelepipedic plastic icebergs of density $\rho_i = 920 \pm 1\,\mathrm{kg\,m^{-3}}$ in a long and narrow fjord-like tank 244 cm long, 28 cm wide and 30 cm tall, filled with water at room temperature ($\rho_w \approx 997\,\mathrm{kg\,m^{-3}}$). To assess the effect of water depth H_w on iceberg-capsize dynamics, two types of experiments were conducted in which the water height was varied from 11.4 to 24.3 cm. The iceberg height was $H = 10.3$ cm, ($H < H_\mathrm{w}$) and the width varied between $W = 2.5$ cm and $W = 10.2$ cm, corresponding to aspect ratios ranging between 0.25 and 1. The length of the iceberg was $L = 26.6$ cm, which is slightly smaller than the tank width to reduce edge effects so that the flow can be considered as 2-D. The plastic icebergs were initially placed slightly tilted with respect to the vertical position and were held by hand close to hydrostatic equilibrium. When the surface of the water became still, several drops of dye were introduced around the plastic iceberg to visualize the water flow. Then the icebergs were released to capsize freely. The capsizes were recorded by a camera located outside the tank. Snapshots are shown in Fig. 3(top row). Further experimental details can be found in Burton *et al.* (2012). A selection of four experiments are presented here, corresponding to aspect ratios $\varepsilon = 0.246$, 0.374, 0.496 and 0.639.

Laboratory experiments show, to some extent, the fluid motion using dye at some specific locations. The ISIS-CFD computational fluid dynamics model makes a valuable contribution to the understanding of the complex motion of the fluid surrounding a capsizing iceberg since it computes the whole velocity field in the fluid. Fluid velocity colour maps computed with ISIS-CFD are qualitatively compared with the images of the laboratory experiments in Figs 3(a)–(f), the maps of the iceberg's surface velocity computed using the calibrated SAFIM model (see Section 3) are also shown in Figs 3(g), (h) and (i). All results are shown at the identical time moments centred at the time when $\theta = 90^\circ$.

Results for the capsize of an iceberg of aspect ratio $\varepsilon = 0.496$ are shown for three different times: in Figs 3(a), (d) and (g) during capsize; in Figs 3(b), (e) and (h) when the iceberg reaches the horizontal position for the first time ($\theta = 90^\circ$); and in Figs 3(c), (f) and (i) some time later. The arrows represent the dimensionless velocity $|u'| = |\boldsymbol{u}|/\sqrt{gH}$, where $\boldsymbol{u}$ is the velocity field of the fluid. We observe a good qualitative agreement between the position and inclination of the iceberg obtained by ISIS-CFD and the laboratory experiments. Note that the iceberg is submarine when it reaches $\theta \approx 90^\circ$ for the first time (Figs 3b and e). The motion of the fluid—initially almost at rest—is visible all around the capsizing iceberg. Large vortices, associated with the iceberg motion, are clearly visible throughout the capsize in Fig. 3 (top and middle row). The intense fluid motion represents an important amount of kinetic energy that is eventually dissipated; this energy is transmitted by the motion of the iceberg, and this slows down the iceberg. Note also that the iceberg moves leftwards during the capsize.

2.4 Comparison of simulations with experiments

Here, we compare ISIS-CFD with the laboratory experiments by Burton *et al.* (2012). In Fig. 4, results are provided for three different unstable icebergs: a thin $\varepsilon = 0.246$ iceberg, a medium $\varepsilon = 0.374$ iceberg and a thick $\varepsilon = 0.639$ iceberg. The horizontal position x_G, vertical position z_G and tilt angle θ are plotted against time. As the plastic icebergs were initially positioned by hand, some variability in the results are observed. To provide an estimate of the variability of the protocol, three experiments with identical plastic icebergs and the same (nominal) initial conditions were conducted for each aspect ratio. We selected these three aspect ratios because of the consistency of the experimental results. The initial conditions in ISIS-CFD were chosen to fit the average values of the laboratory experiments. In ISIS-CFD simulations, the icebergs were tilted by a small angle of 0.5° for the thin and medium iceberg (black curves in Figs 4g and h) and a larger angle of 15° for the thicker iceberg (black curves in Fig. 4i). The icebergs were initially placed in a hydrostatic equilibrium. The water level in the tank $H_\mathrm{w} = 11.4$ or 24.3 cm was found to have a negligible effect on the iceberg motion:

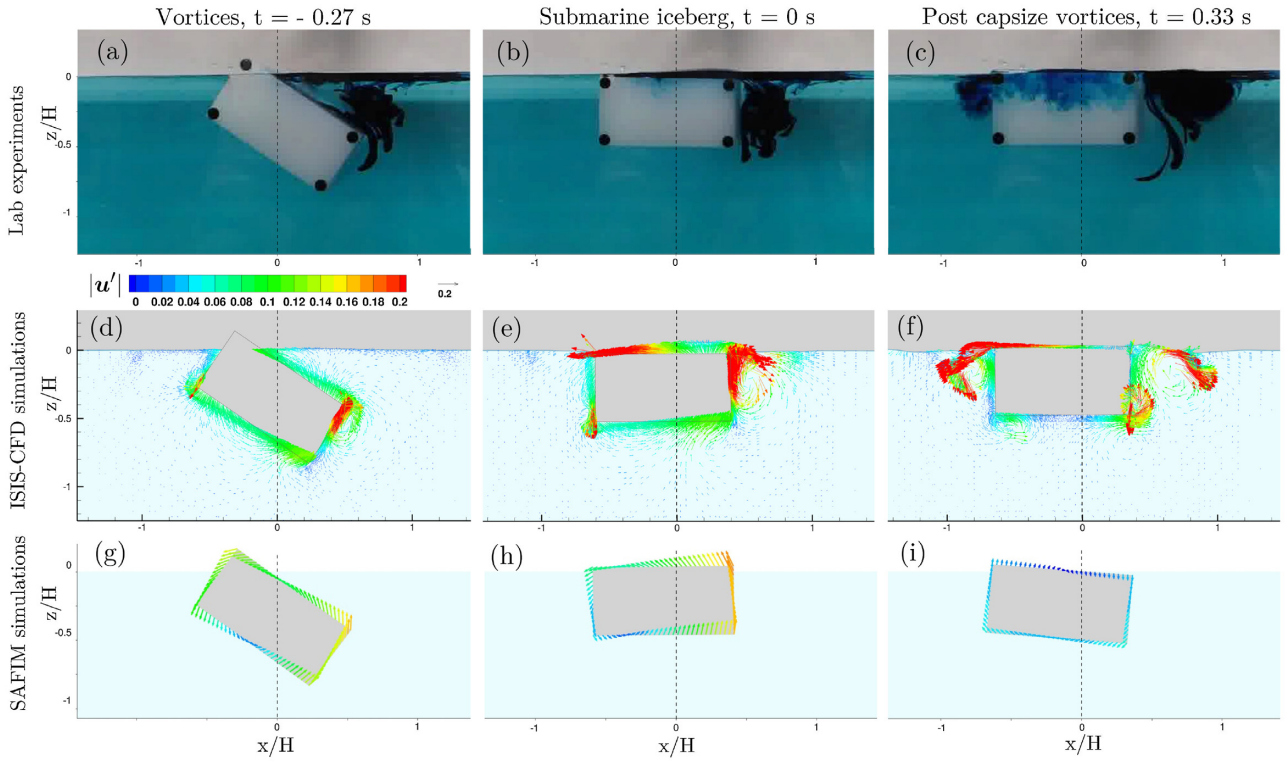

Figure 3. Side view of experiments from Burton *et al.* (2012) (a, b, c); colour map of the dimensionless velocity $\boldsymbol{u}' = \boldsymbol{u}/\sqrt{gH}$, where $\boldsymbol{u}$ is the velocity field in the water computed with ISIS-CFD (d, e, f); dimensionless velocity along the surface of the iceberg with SAFIM (g, h, i). Three time moments of the capsize (indicated on top of each column) are shown. The timescale is calibrated such that $t = 0$ s corresponds to the first time when the iceberg reaches $\theta = 90°$, as in Burton *et al.* (2012). The iceberg aspect ratio is $\varepsilon = 0.496$. The floor and walls are not shown in the snapshots. The corresponding animation of ISIS-CFD simulation is available in supplementary material [S1].

results are within the data variability shown in Fig. 4. Therefore, the experiments with a constant water depth $H_w = 24.3$ cm are compared with the ISIS-CFD simulations carried out for the same water depth.

We first analyse the motion of the iceberg during capsize. Once released, it tilts to reach the horizontal position with associated upward and sideward motion. It then rises out of the water in a rocking motion superimposed with a continuous horizontal displacement (Fig. 4). The thinner the iceberg, the faster it moves in the horizontal direction with a quasi constant velocity at least for the first 1.5 s. This horizontal motion is an important aspect of the iceberg capsize on which we would like to focus here. Note that, besides gravity and buoyancy which cannot cause horizontal motion, the only external force acting on the capsizing iceberg is due to the relative motion of water around the iceberg (the air has a negligible effect here). These hydrodynamic forces are responsible for the horizontal iceberg motion. They need to be captured accurately by the model as they contribute considerably to the contact force generated between the iceberg and the glacier front when a just-calved iceberg capsizes (Tsai *et al.* 2008; Sergeant *et al.* 2018).

Fig. 4 shows that ISIS-CFD results are in very good agreement with the laboratory data especially in terms of the evolution of the tilt angle. The slight discrepancy on the vertical and rotational motion computed by ISIS-CFD could be due to differences between the laboratory and simulation set-ups with regards to the 2-D approximation and the initial conditions as discussed above. Another reason for this slight discrepancy could be related to the turbulence model treated by the RANS approach. The generation of large vortices and separations are not initially induced by turbulent phenomena. We observed that Euler approach (perfect fluid with no viscosity and thus no possible dissipation of energy in turbulence phenomenon) captures similar flow topologies. However, the evolution of these vortices and separations can be affected by turbulent effects for which the RANS approach is not specifically designed for. Simulations using methods such as DES (detached eddy simulation) or LES (large eddy simulation) could improve the accuracy but would require high computational costs.

2.5 From the laboratory to the field scale

In the previous section, ISIS-CFD simulations were shown to fit laboratory experiments very well. However, our aim is to reproduce the dynamics of the capsize of field-scale icebergs with dimensions of several hundred metres, that is four orders of magnitude larger than for the laboratory scale. Also, as pointed out by Sergeant *et al.* (2018), the laboratory-scale Reynolds number $Re = LU/\nu \approx 10^3$, is six orders of magnitude smaller than the characteristic Reynolds number $Re \approx 10^9$ for the field scale (with L the typical length, U the typical speed and ν the dynamic viscosity of the fluid). Global viscous effects are expected to be more pronounced for laboratory-scale than for the field-scale capsize. Therefore, the question is whether laboratory-scale experiments can be used to understand the kinematics of the field-scale iceberg capsize.

We compare the horizontal force induced by the water to the iceberg during its capsize computed by ISIS-CFD for the two cases: (1) a field-scale iceberg of height $H = 800$ m and (2) a laboratory-scale iceberg of height $H = 0.103$ m, all other parameters being the same: the aspect ratio $\varepsilon = 0.25$, infinite water pool, same densities

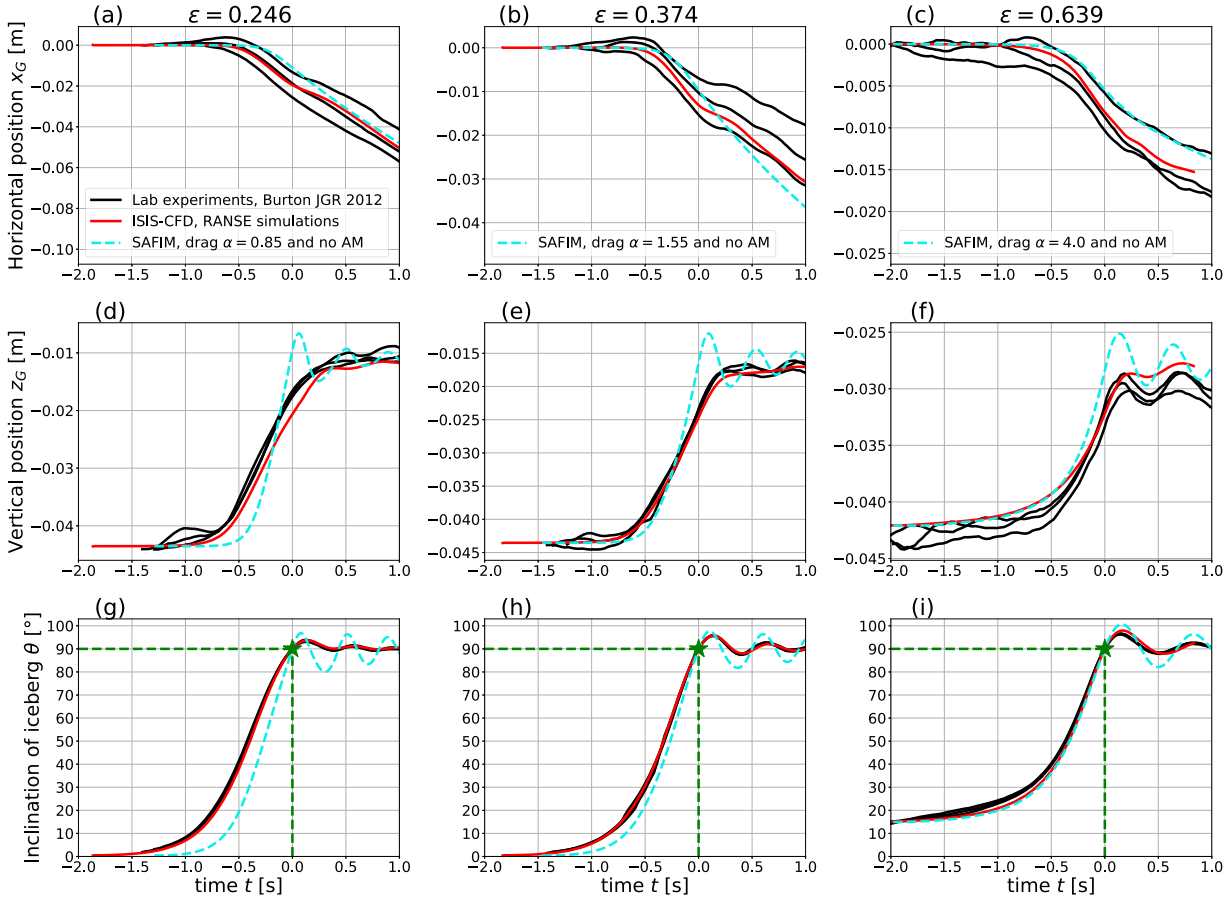

Figure 4. Horizontal position x_G (a, b, c), vertical position z_G (d, e, f) and tilt angle θ (g, h, i) of icebergs of height $H = 10.3$ cm for $\varepsilon = 0.246$ (a, d, g), $\varepsilon = 0.374$ (b, e, h) and $\varepsilon = 0.639$ (c, f, i). Data are provided for three laboratory experiments (solid black), ISIS-CFD simulations (solid red) and SAFIM simulations (dashed blue). The origin of the time axis in all experiments and simulations is set to the time at which the iceberg reaches the horizontal position for the first time, that is when $\theta = 90^\circ$ (green stars and dashed lines), as in Burton *et al.* (2012).

of the water and the ice, taken to be equal to the field densities (Section 2.1). Results are given in Fig. 5 using dimensionless variables, that is a dimensionless horizontal force $F'_x = F_x/(mg)$ acting on the capsizing iceberg and a dimensionless time $t' = t/\sqrt{H/g}$. Note that this horizontal force F'_x acting on the iceberg is the hydrodynamic force. However, in the case of iceberg-glacier interaction a similar hydrodynamic force will contribute to the total contact force between a glacier and a capsizing iceberg. We observed that the two curves corresponding to the two scales are very similar from the beginning of the movement until $t' \approx 15.6$, which corresponds to $\theta \approx 90^\circ$. This similarity between the forces at the laboratory and field scales can be explained using the Vaschy-Buckingham π theorem, assuming that the effect of viscosity is negligible, as detailed in Appendix A. For times larger than $t' \approx 15.6$, the discrepancy between laboratory and field scales is larger and dimensions start to play a more important role. This discrepancy probably originates from the fact that after the buoyancy driven capsize, the iceberg motion is driven by the evolution of complex vortices and different gravity-waves dynamics.

The other variables of the system (vertical force and torque acting on the iceberg and horizontal and vertical displacement and inclination of the iceberg) are also similar for the laboratory and field scales.

Since it was demonstrated that the laboratory and field scales produce the same horizontal dimensionless force, in the remaining simulations we will present only the dimensionless quantities obtained from simulations of the laboratory-scale iceberg with $H = 0.103$ m, for densities corresponding to field values, and in absence of sea floor. The laboratory scale was chosen because numerical convergence is easier to achieve in ISIS-CFD for the laboratory scale than for the field scale. The sensitivity of the capsize to the densities will be discussed in Section 5.5. Also, the depth of the sea floor was observed to have no significant effect on the capsize dynamics. Results for icebergs of different heights (but of the same aspect ratio) can be deduced with a factor of proportionality given by the normalizations from Table 1.

In ISIS-CFD simulations and laboratory experiments, we observe five stages during the capsize:

(i) In the *initial* phase ($0 < t' < 6$), the horizontal force F'_x oscillates around zero with a negligible amplitude (about 1 per cent of its extremum amplitude). This stage is the initiation of the capsize with buoyancy and gravity forces making the iceberg rotate and rise.

(ii) Then the absolute value of F'_x increases, first slowly and then faster until the first extremum at $t' \approx 12.2$. This is explained by the

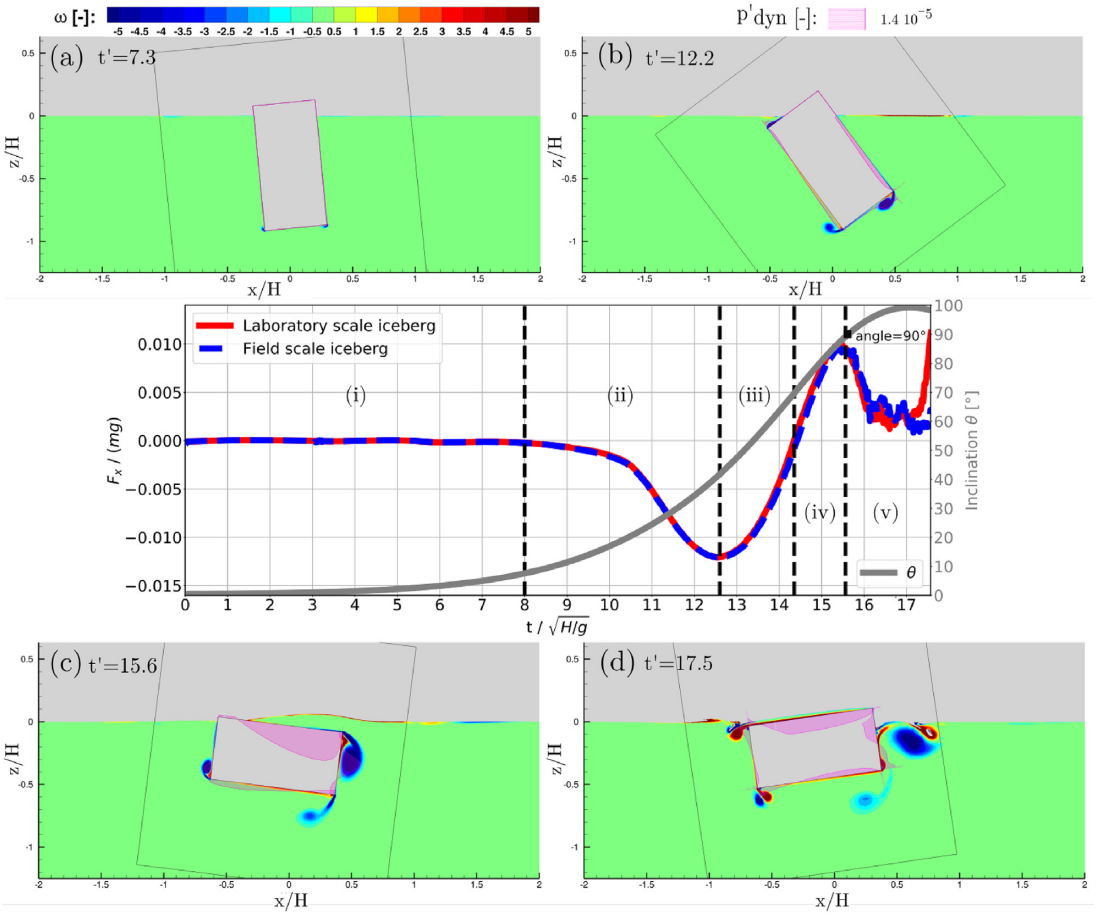

Figure 5. The horizontal dimensionless force $F^{'} = F_x/(mg)$ that the water exerts on the iceberg ($\varepsilon = 0.5$) is plotted against a dimensionless time $t^{'} = t/T_H$ with the characteristic time $T_H = \sqrt{H/g}$ for both laboratory ($H = 0.103$ m, $T_H = 0.102$ s, in red) and field ($H = 800$ m, $T_H = 9.03$ s, in blue) scales. The iceberg inclination θ (grey curve with scale on the right) is plotted against dimensionless time $t^{'}$, the curve is the same for the lab scale and the field scale. The vorticity fields around the iceberg at four different times are also shown: (a) initial phase of iceberg's motion $t^{'} \approx 7.3$, (b) time of maximal force in the left direction $t^{'} \approx 12.2$, (c) time of maximal force in the right direction $t^{'} \approx 15.6$ and (d) corresponds to the oscillations of the iceberg at later time $t^{'} \approx 17.1$. The pink shaded area represents the local hydrodynamic pressure. The colour maps are discussed in Section 5.3 and the phases (i) to (v) are discussed in 2.5.

Table 1. Table of dimensionless variables, with $N^{'}$ denoting the dimensionless variable related to N and with the iceberg linear mass density $m = \rho_i\, H^2\, \varepsilon$, G the centre of gravity of the iceberg and the characteristic time $T_H = \sqrt{H/g}$. Note that the dimensionless forces and torques can also be written through a normalization by the characteristic mass m, length H and time T_H with the following formulas: $F_x' = F_x\, T_H^2/(m\, H)$, $F_z' = F_z\, T_H^2/(m\, H)$ and $M_\theta' = M_\theta\, T_H^2/(m\, H^2)$. See Section. 5.5 for a discussion on a non-dimensionalization with a dimensionless time $T_{\rho,\,H}$ that depends on the densities.

Variable name	Dimensionless variable
Forces	$F^{'} = F/(mg)$
Torque	$M_\theta' = M_\theta/(mgH)$
Positions	$r^{'} = r/H$
Time	$t' = t\sqrt{g/H}$
Velocity	$u' = u/\sqrt{Hg}$

fact that the induced vertical and rotational velocities and accelerations of the iceberg produce a hydrodynamic force that has a non-zero horizontal component, which is the only horizontal force acting on the iceberg. It induces a horizontal motion of the iceberg towards the left for the anti-clock wise iceberg rotation considered here.

(iii) The absolute value of F_x' decreases to $F_x' = 0$ before $t^{'} \approx 14.4$, which corresponds to $\theta \approx 70°$ (Fig. 5). The horizontal motion of the iceberg triggers a horizontal resisting fluid force.

(iv) The force F_x' becomes positive and increases to an extremum at $t^{'} \approx 15.6$, where the iceberg is horizontal $\theta \approx 90°$. Its amplitude is of the same order of magnitude than the first negative force but the duration is shorter. Therefore, it decelerates the iceberg leftward motion, but does not cancel it.

(v) At the later stage (after $t^{'} \approx 15.6$), F_x' oscillates around zero and is slowly damped. The iceberg rocks around $\theta = 90°$ and drifts to the left while slowly decelerating.

The highest water velocities in the surrounding ocean are reached when the iceberg is close to $\theta = 90°$. Dimensionless velocities are shown in Fig. 6. We observe that for an iceberg of height H (here 800 m):

- high velocities in the fluid $\approx 0.5\sqrt{g\,H}$ (here $\approx 42\,\mathrm{m\,s^{-1}}$) are reached between times $t^{'} = 10$ (here ≈ 90 s) and $t^{'} = 34$ (here ≈ 307 s), see dark red regions in Figs 6(b), (c) and (d).
- at a distance of about H from the iceberg, the water flows at a maximum speed of $\approx 0.01\sqrt{g\,H}$ (here $\approx 88\,\mathrm{cm\,s^{-1}}$).
- at a distance of about $3.5\,H$ from the iceberg, the water flows at a maximum speed of $\approx 0.0005\sqrt{g\,H}$ (here $\approx 4.4\,\mathrm{cm\,s^{-1}}$).

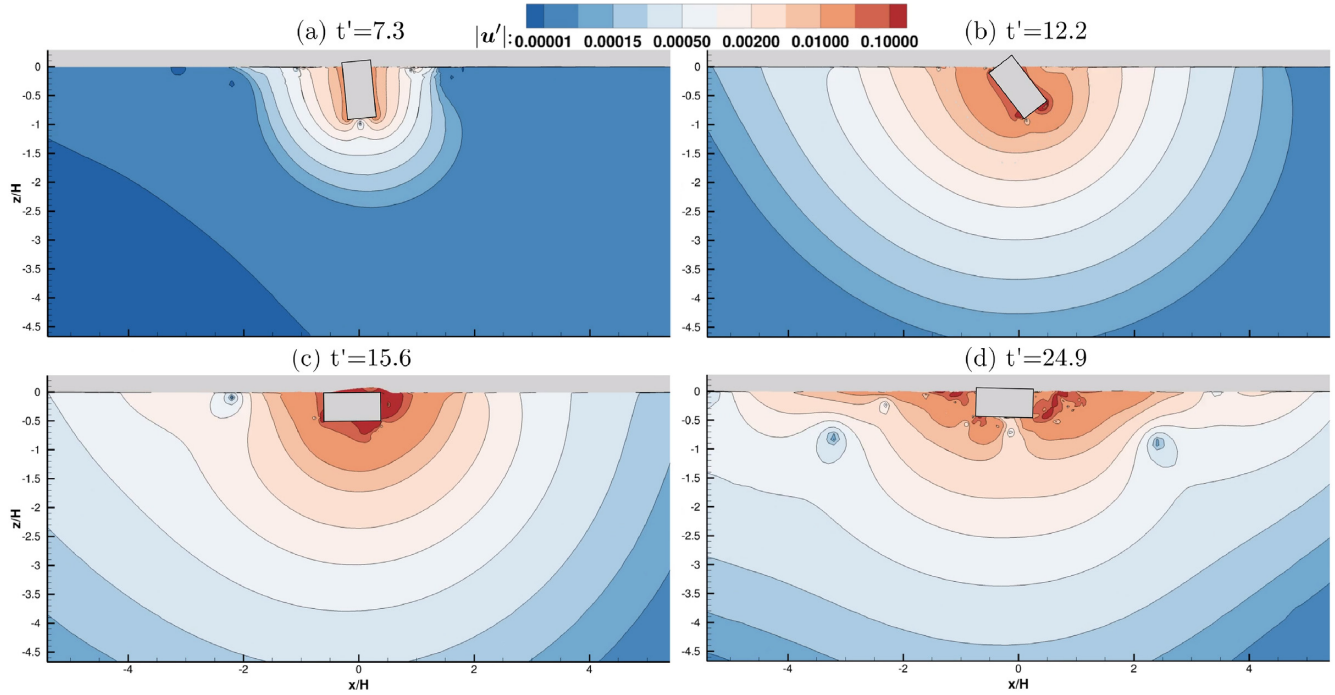

Figure 6. Iso-lines of the absolute value of the dimensionless velocity $|u'| = |u/\sqrt{gH}|$ in the fluid surrounding the iceberg with aspect ratio $\varepsilon = 0.5$ (grey rectangle). Captions (a), (b) and (c) correspond to the same times as in Figs 5(a)–(c). Panel (d) at time $t' = 24.9$ shows the vanishing fluid motion. An animated figure is available in supplementary material [S2].

Note that the maximum plume velocities measured in (Mankoff *et al.* 2016; Jouvet *et al.* 2018) are horizontal velocities at the surface ≈ 3 m/s.

Moreover, we observe that the iso-lines for the velocities are roughly semi-circles centred on the iceberg, with a radius slightly higher in the horizontal direction.

3 EMPIRICAL MODEL SAFIM

3.1 General formulation

The reference ISIS-CFD model has the advantage of being very accurate for fluid-structure interactions but it cannot readily model contacts between deformable solids. As explained in the introduction, we aim to construct a simpler fluid-structure interaction model that can be more easily coupled with dynamic solid-mechanics models. Thus we propose a simple empirical model that can be used to estimate the horizontal force applied to a capsizing iceberg. This model was initiated in (Sergeant *et al.* 2018, 2019) and is extended and validated in this study.

As proposed by Tsai *et al.* (2008), Burton *et al.* (2012) and Sergeant *et al.* (2018), one possible way to construct such a simple model of a capsizing iceberg consists in solving equations of a rigid iceberg motion subject to relevant forces and torque while discarding water motion. The general equations of iceberg motion for such simplified models can be written in two dimensions as:

$$(m + m_{xx})\ddot{x}_G + m_{xz}\ddot{z}_G + J_{x\theta}\ddot{\theta} = \boldsymbol{F}_d \cdot \boldsymbol{e}_x \tag{1}$$

$$m_{xz}\ddot{x}_G + (m + m_{zz})\ddot{z}_G + J_{z\theta}\ddot{\theta} = \left(\boldsymbol{F}_g + \boldsymbol{F}_s + \boldsymbol{F}_d\right) \cdot \boldsymbol{e}_z \tag{2}$$

$$J_{x\theta}\ddot{x}_G + J_{z\theta}\ddot{z}_G + (I + I_{\theta\theta})\ddot{\theta} = (\boldsymbol{M}_s + \boldsymbol{M}_d) \cdot \boldsymbol{e}_y \tag{3}$$

where $I = \rho_i H^4 \varepsilon(1 + \varepsilon^2)$ is the moment of inertia of the iceberg with respect to its centre of gravity G and around an axis parallel to $\mathbf{e}_y$ (multiplying I by the iceberg thickness along $\mathbf{e}_y$ gives the inertia for the 3-D case). Such a formulation accounts for the hydrostatic force $\boldsymbol{F}_s$ and the corresponding torque $\boldsymbol{M}_s$ computed at G, the gravity force $\boldsymbol{F}_g$, overall hydrodynamic effects expressed by the force $\boldsymbol{F}_d$ and the associated torque $\boldsymbol{M}_d$ at G and so-called added-masses m_{xx}, m_{zz}, $I_{\theta\theta}$, m_{xz}, $J_{z\theta}$ and $J_{x\theta}$ that account for the mass of water that must be accelerated during the iceberg motion.

Hydrodynamic forces that oppose the motion of the iceberg are commonly called *drag forces* $\boldsymbol{F}_d$. The corresponding drag torque $\boldsymbol{M}_d$ accounts for a particular distribution of the drag pressure along the iceberg surface. The drag force usually scales with the squared relative velocity between the water and the solid with a factor of fluid density and it acts in the opposite direction of this velocity. Note that the friction drag can be neglected here, as shown in Appendix A.

When the water motion is not computed, the added-mass (AM) should also be included in the model. Added-masses introduce some additional inertia to the moving iceberg. This effect is known to be significant when the density of the fluid is comparable or bigger than the density of the solid, such as for ice and water. The matrix of added-masses, which is symmetrical (Molin 2002; Yvin *et al.* 2018), has the following form:

$$[m_{AM}] = \begin{bmatrix} m_{xx} & m_{xz} & J_{x\theta} \\ m_{xz} & m_{zz} & J_{z\theta} \\ J_{x\theta} & J_{z\theta} & I_{\theta\theta} \end{bmatrix} \tag{4}$$

Added-mass effects are of two types: a force associated with an added-mass can arise in a given direction due to (1) an acceleration in that direction, which corresponds to the *diagonal* terms m_{xx}, m_{zz} and $I_{\theta\theta}$ in eqs (1–3), and (2) an acceleration in another direction, which is accounted for by the *coupled* terms m_{xz}, $J_{z\theta}$, $J_{x\theta}$.

Within this framework, models proposed by Burton *et al.* (2012) and Tsai *et al.* (2008), summarized in Table 2, differ in the way they account for the drag and the added-mass. In the formulation proposed by Tsai *et al.* (2008), pressure drag and the associated torque are not considered and only some of diagonal terms are taken into account in the added-mass matrix. In the formulation by Burton *et al.* (2012), added-mass effects are neglected. As for the drag effects, they are assumed to depend only on individual components of the velocity of G and on the angular velocity, for example the drag along $\boldsymbol{e}_x$ only depends on the velocity $\dot{x}_G$. As a consequence, both models predict that an iceberg initially at rest ($\dot{x}_G = 0$) will not experience any horizontal movement along $\boldsymbol{e}_x$ during its capsize. As discussed above, this result contradicts experimental and ISIS-CFD results.

3.2 SAFIM

To better reproduce the motion of capsizing icebergs, we have developed a new model along the lines of previous propositions by our group (Sergeant *et al.* 2018, 2019). The model is referenced as SAFIM. In addition to the previously used drag formulation, this new model uses a drag coefficient varying with the aspect ratio and integrates a tunable added-mass effect. As will be shown, SAFIM reproduces the main results of ISIS-CFD. For example, it predicts the horizontal movement of capsizing icebergs initially at rest.

A particular feature of the drag model in SAFIM is that it is based on the *local* velocity of the iceberg's surface through which the drag pressure could be approximated as $p = \rho_w v_n \text{sign}(v_n)/2$, where $\boldsymbol{v}$ is the local velocity of the iceberg surface, $v_n = |\boldsymbol{v} \cdot \boldsymbol{n}|$ is the corresponding normal velocity, and $\boldsymbol{n}$ is the local normal to the surface of the iceberg. Therefore, the total drag force and the drag torque are evaluated as integrals of local pressure over the submerged part of the iceberg Γ_s:

$$\boldsymbol{F}_d = -\alpha \frac{1}{2} \int_{\Gamma_s} \rho_w v_n^2 \text{sign}(v_n) \boldsymbol{n} \, d\Gamma, \tag{5}$$

$$\boldsymbol{M}_d = -\alpha \frac{1}{2} \int_{\Gamma_s} \rho_w v_n^2 \text{sign}(v_n) (\boldsymbol{r} - \boldsymbol{r}_G) \wedge \boldsymbol{n} \, d\Gamma, \tag{6}$$

where, $\boldsymbol{r}$ is the local position vector and $\boldsymbol{r}_G$ is the position vector of the iceberg's centre of mass; the wedge sign $\wedge$ denotes a vector cross product. We consider here a quadratic dependence of the local drag force on the normal velocity, this is discussed in Section 5.3. The integral expressions for the drag force and torque are given in Appendix B. The factor α of the order of unity is the only adjustable parameter of the drag model. It can be adjusted with respect to the reference CFD simulations or experiments. We recall that in the original papers of Sergeant *et al.* (2018, 2019), this factor was set to $\alpha = 1$ by default. However, due to the complexity of the fluid flow, the optimal value of α may change with the geometry of the iceberg.

This formulation, rather than attempting to describe the local pressure accurately, which is difficult based on geometrical considerations only (Section 5.3; Sergeant *et al.* (2018)), aims at providing a good approximation of the global forces and torques acting on the rotating iceberg. As opposed to the simplified drag model of Burton *et al.* (2012) - in which the drag force and torque depend only on the velocity of the centre of gravity - the hydrodynamic forces $\boldsymbol{F}_d$ and the torque $\boldsymbol{M}_d$ depend here on the iceberg's current configuration z_G, θ (which determines the submerged part), and on the three velocities $\dot{x}_G$, $\dot{z}_G$, $\dot{\theta}$, (which together with the inclination angle θ determine the local normal velocity). This makes it possible to produce a horizontal force acting on the iceberg during capsize even for icebergs initially at rest. Another advantage is that a unique fit-parameter α is required to represent the drag effect, contrary to three independent fit parameters used in Burton *et al.* (2012). This makes it possible to easily generalize the model to more complex iceberg geometries.

As for the added-masses in SAFIM, we will consider two possibilities: *simplified* added-masses and *computed* added-masses. The simplified added-masses option is based on analytical formulas for the diagonal terms of the added-mass matrix. The coupled terms of added-mass are taken to be equal to zero: $m_{xz} = 0$, $J_{z\theta} = 0$, $J_{x\theta} = 0$. The formulas used are taken from (Wendel 1956) for fully or partly submerged solids and were adapted to a capsizing body. The horizontal and vertical added-masses take the following forms:

$$m_{xx} = \frac{1}{4} C_x \pi \rho_w H_{\text{eff}}^2(z_G, \theta) \tag{7}$$

$$m_{zz} = \frac{3}{16} C_z \pi \rho_w W_{\text{eff}}^2(z_G, \theta) \tag{8}$$

where H_{eff} and W_{eff} are the effective height and width defined as the projection of the submerged part of the iceberg along the horizontal and vertical axes, respectively (see Fig. 1 and Appendix B2) which depend on the vertical and angular positions of the iceberg. Therefore, the added masses m_{xx} and m_{zz} evolve during the capsize. On the other hand, the added moment of inertia $I_{\theta\theta}$ is assumed to depend only on the height of the iceberg, so it remains constant during the capsize:

$$I_{\theta\theta} = 0.1335 \, C_\theta \pi \rho_w \left(\frac{H}{2}\right)^4. \tag{9}$$

In order to adjust the added-mass effect used in SAFIM to reproduce the reference ISIS-CFD results, we introduce three calibration factors in the above equations: C_x, C_z and C_θ (see Section 4 for calibration).

Computed added-masses are calculated using a computational fluid dynamics solver. This is done by applying a unit acceleration on the iceberg for the considered degree of freedom, which leads to a simplified expression of the Navier-Stokes equations (eq. (16) in (Yvin *et al.* 2018)). Then we obtain an equation for the pressure (the eq. (18) in (Yvin *et al.* 2018)) which can be solved on the fluid domain using a numerical method such as the finite element, boundary element method or finite-volume method (used in this study (Queutey & Visonneau 2007)). The integration of the induced pressure on the emerged part of the iceberg in response to a unit acceleration along x, z or rotation around y gives the corresponding column of the symmetrical added-mass matrix including both diagonal and coupled entries. Similarly to the simplified added-mass, the values of the computed added-mass also depend on the iceberg position and they therefore evolve during the capsize. For the computed added-masses, the coupled terms are non-zero, giving rise to a coupling between horizontal, vertical and rotational accelerations.

To solve the motion eqs (1–3) with SAFIM, the Störmer-Verlet integration scheme is used. Since SAFIM has only three degrees of freedom, the integration over time is very fast, only a few seconds compared to few hours for ISIS-CFD on a single CPU. The time step in SAFIM that ensures a sufficiently accurate results is $\Delta t = 0.1$ s in the field scale and $\Delta t = 0.001$ s in the laboratory scale. In both cases, this step corresponds to a dimensionless time step of $\Delta t' = \Delta t / \sqrt{H/g} \approx 0.01$.

Table 2. Dynamic fluid forces proposed by Tsai & Ekström (2007) and Burton *et al.* (2012) for iceberg capsize modelling.

Ref.	Added-mass (AM):	Drag:
(Tsai *et al.* 2008)	$m_{xx_T} = \frac{3\pi\rho_w L}{8}\left(H^2\cos(\theta)^2 + W^2\sin(\theta)^2\right)$ $m_{zz_T} = 0$ $I_{\theta\theta_T} = \frac{\rho_w}{24}(H^2 - W^2)^2$ $m_{xz} = 0, J_{x\theta} = 0, J_{z\theta} = 0$	$\boldsymbol{F}_d = 0$ $\boldsymbol{M}_d = 0$
(Burton *et al.* 2012)	$m_{xx} = 0$ $m_{zz} = 0$ $I_{\theta\theta} = 0$ $m_{xz} = 0, J_{x\theta} = 0, J_{z\theta} = 0$	$\boldsymbol{F}_{d_B}\cdot\boldsymbol{e}_x = \nu_x\lvert\dot{x}\rvert^2\mathrm{sign}(\dot{x})$ $\boldsymbol{F}_{d_B}\cdot\boldsymbol{e}_z = \nu_z\lvert\dot{z}\rvert^2\mathrm{sign}(\dot{z})$ $\boldsymbol{M}_{d_B}\cdot\boldsymbol{e}_y = \nu_\theta\lvert\dot{\theta}\rvert^2\mathrm{sign}(\dot{\theta})$

4 PERFORMANCE AND LIMITATIONS OF SAFIM

4.1 SAFIM's calibrations

The validation of the proposed model should be suited to the final objectives: (1) an accurate reproduction of the forces exerted by the water on the iceberg during capsize; (2) the ease of implementation in a finite element solver for simulation of the whole iceberg–glacier–bedrock–ocean system (left for future work), (3) suitability of the model for the entire range of possible geometries of icebergs encountered in the field. In this context, we consider 2D icebergs with rectangular cross-sections (Fig. 1). We use typical densities observed in the field. As discussed in Section 5, the considered density has a non-negligible effect on the calving dynamics. We apply SAFIM to the same four geometries as described in Section 2.3, with initial tilt angles given in Section 2.4 and Table C1.

To compare SAFIM and ISIS-CFD results, we compute the mismatch in the time-evolution of the horizontal forces F_x ($\mathcal{L}^2$ norm) during the capsize. The phases of the capsize that we focus on are phases (ii) and (iii) (defined in Section 2.5). The reason we do not seek to perfectly model the initial phase (i) with SAFIM is discussed in Section 5.2. Also, SAFIM is designed to model the capsize phase but cannot model the very end of the capsize ($\theta > 80°$), that is phase (iv), nor the post-capsize phase (v). In these phases, forces induced by complex fluid motion, which are difficult to parametrize, are expected to dominate gravity and buoyancy forces.

For SAFIM with a drag force and no added-masses, the mismatch is defined as:

$$E_1 = \frac{\int_{t_1}^{t_2}\left|F_{x_{\mathrm{ISIS}}}(t) - F_{x_{\mathrm{SAFIM}}}(t-\Delta t)\right|^2 \mathrm{d}t}{\int_{t_1}^{t_2}|F_{x_{\mathrm{ISIS}}}(t)|^2\mathrm{d}t} \tag{10}$$

with F_x being the total horizontal force acting on the iceberg, t_1 such that $F_x(t_1) = 1/6F_{\min}$ and $t_1 < t_{\min}$ and t_2 such that $F_x(t_2) = 1/6F_{\min}$ and $t_2 > t_{\min}$, with $F_{\min}$ being the first extremum of the force and $t_{\min}$ the time at which it occurs. In Fig. 5, $t_1' = 10.3$ and $t_2' = 14.2$. This time interval is within phases (ii) and (iii). Since without added-mass the initial phase of capsize cannot be accurately reproduced, for the comparison purpose, the SAFIM response is shifted artificially in time so that the first extremum of the curve fits that of ISIS-CFD. This time shift Δt is discussed in Section 5.2.

For the SAFIM model with a drag force and *added-masses*, a more demanding mismatch is used, which reads as:

$$E_2 = \frac{\int_0^{t_3}\left|F_{x_{\mathrm{ISIS}}}(t) - F_{x_{\mathrm{SAFIM}}}(t)\right|^2 \mathrm{d}t}{\int_0^{t_3}|F_{x_{\mathrm{ISIS}}}(t)|^2\mathrm{d}t} \tag{11}$$

where $t = 0$ is the beginning of the simulation and t_3 the first time for which the horizontal force crosses zero $F_x(t_3) = 0$ after $t_{\min}$, which corresponds to $t_3' = 14.4$ in Fig. 5. This time interval includes phases (i), (ii) and (iii). The force is not shifted in time as for E_1. Errors (10) and (11) are computed for a parametric space of drag and added-mass coefficients as detailed in Appendix C. The optimized values of the coefficients α, C_x, C_z and C_θ are chosen such that the errors E_1 and E_2 are minimized.

4.2 Effect of drag and added-mass

We analyse the horizontal force produced by SAFIM in order to understand the effects of the drag force and added-masses on the dynamics of the iceberg capsize. To do so, the dynamics of an iceberg with an aspect ratio $\varepsilon = 0.246$ were simulated by SAFIM with and without drag and with and without added-masses and compared to the results of ISIS-CFD (Fig. 7):

case 0: no drag and no coupled terms in the added-mass matrix: the horizontal force predicted by SAFIM is equal to zero $F_x' = 0, \forall\, t$, as expected. For the sake of clarity, this case is not plotted in Fig. 7.
case 1: drag and no added-mass (no AM) is shown in Fig. 7 for two values of the drag coefficient $\alpha = 1$ (purple curve) and $\alpha = 0.85$ (blue curve). The value $\alpha = 0.85$ is the optimized value of α obtained by minimizing the error E_1. The force has a slightly higher amplitude (around $t' \approx 8.5$) and duration with $\alpha = 1$ than with the optimized drag coefficient $\alpha = 0.85$. Even though the amplitude and shape of the SAFIM horizontal force are very similar to the ISIS-CFD results, the full capsize occurs earlier with SAFIM. When the SAFIM curves are shifted in time by $\Delta t' = 2.7$ (cyan curve in Fig. 7), the previous SAFIM force fits well ISIS-CFD. The shape is the same and the error on the waveform is $E_1 = 5.2$ per cent, with a relative error on the first force extremum of 4 per cent. A comparison of SAFIM with the optimized α-factor, SAFIM with $\alpha = 1$, and ISIS-CFD is given in Appendix D, for the four aspect ratios.
case 2: drag and simplified added-mass: when coefficients for the drag and added-masses are taken all equal to 1 the horizontal force is very different from the reference ISIS-CFD results (orange curve in Fig. 7). The duration of the capsize is largely overestimated and the amplitude is strongly underestimated. The optimized drag and added-mass coefficients that give a minimum error E_2 are $\alpha = 1.1$ for the drag, $C_\theta = 0.75$ for the added moment of inertia and zero factors $(C_x, C_z) = (0, 0)$. The corresponding results (yellow curve in Fig. 7) are in a very good agreement with the reference results ($E_2 = 10$ per cent) both for the shape and for the time corresponding to the force extremum $t' \approx 11.45$. The added moment of inertia (coefficient C_θ) slows down the initial rotation of the iceberg. However, the amplitude of the force extremum is slightly underestimated by

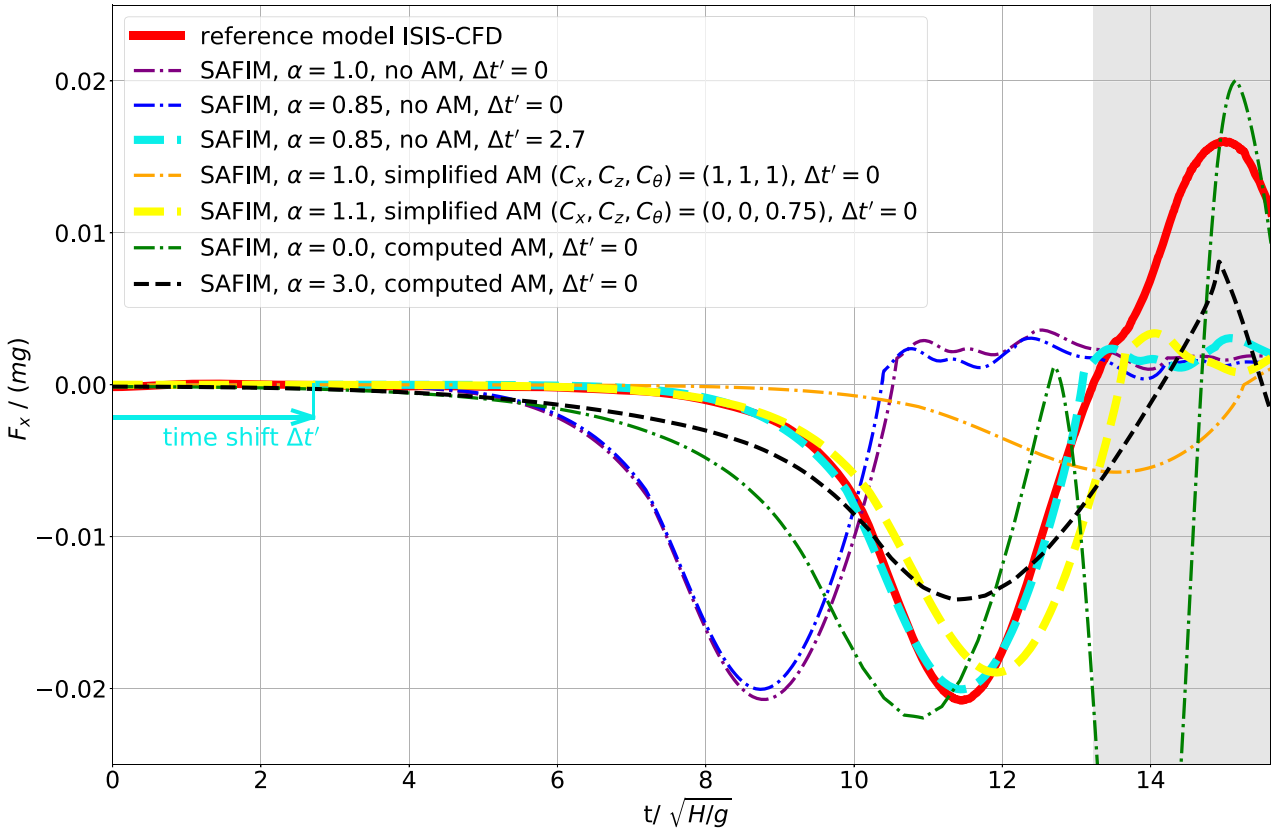

Figure 7. Computed horizontal force $F'_x = F_x/(mg)$ applied on the iceberg versus dimensionless time $t' = t/\sqrt{H/g}$ for a reference ISIS-CFD simulation and for SAFIM simulations with different drag and added-mass parameters.

8 per cent. The accuracy of the formula of the simplified added-masses with coefficients equal to 1 is discussed in Section 5.4.
case 3: no drag and computed added-masses: SAFIM (dark green curve in Fig. 7) fits the reference results quite well in amplitude but not in time and predicts a huge second minimum.
case 4: drag and computed added-masses: when correcting the drag coefficient to $\alpha = 3.0$, which minimizes the error E_2, SAFIM fits better in time, reproducing the initial slow change of the force, but the amplitude and the shape still do not fit ISIS-CFD (black curve in Fig. 7). Similarly to the simplified added-masses, the computed added-masses slow down the initial rotation of the iceberg.

This analysis suggests that the drag force has mainly an effect on the amplitude of the first force extremum and that the added-masses have an effect on the duration of the initiation of the capsize. Also, optimized coefficients of drag and added-masses improve the model significantly compared with the case with all coefficients set to 1. Further discussions on the pros and cons of the SAFIM models are given in Section 5.1.

4.3 Effect of the iceberg's aspect ratio

We will now analyse the forces and the torque acting on the four selected geometries of icebergs computed by ISIS-CFD and SAFIM. The evolution of the dimensionless horizontal force F'_x, vertical force F'_z, torque M'_θ, horizontal displacement x'_G, vertical displacement z'_G and inclination θ obtained by ISIS-CFD and SAFIM are plotted in Fig. 8 for SAFIM best-fitted results obtained with drag and without added-masses and in Fig. 9 for SAFIM results with drag and simplified added-masses. SAFIM models use optimized parameters indicated in Table C1 for each aspect ratio.

We will first discuss the sensitivity of the forces computed with the reference model ISIS-CFD to the aspect ratios ε. We observe that the amplitude of the first extremum of both the horizontal force F'_x and the vertical force F'_z decreases with increasing aspect ratio. Consequently, the amplitude of the horizontal acceleration $\ddot{x}_G = F_x/m = gF'_x$, also decreases with increasing aspect ratio. This is consistent with the observed slower horizontal displacement of icebergs with larger aspect ratios as reported in Section 2.4. Also, the durations of the capsize do not differ much in the four cases.

drag and no added-masses (case 1): The minimal error E_1 increases with the aspect ratio (from 5 per cent for $\varepsilon = 0.246$ and up to 24 per cent for $\varepsilon = 0.639$). The optimal drag coefficient α increases in an approximately affine way with the aspect ratio (Fig. 10a) as:

$$\alpha_{\text{opt}}(\varepsilon) \approx -1.6 + 8.8\varepsilon$$

with the coefficient of determination equal to $R^2 = 0.98$. This linear regression is valid within the range of studied aspect ratios $0.246 \leq \varepsilon \leq 0.639$. Note that this formula should not be used for $\varepsilon < 0.18$ for which the drag coefficient would be negative, which is physically meaningless.

drag and simplified added-masses (case 2): The minimal errors E_2 for SAFIM with drag and simplified added-masses are greater than the errors E_1 with drag and no added-masses Fig. 10(b). As for E_1, the error E_2 increases with the aspect ratio (from 10 per cent for $\varepsilon = 0.246$ up to 26 per cent for $\varepsilon = 0.639$). Note that for all the

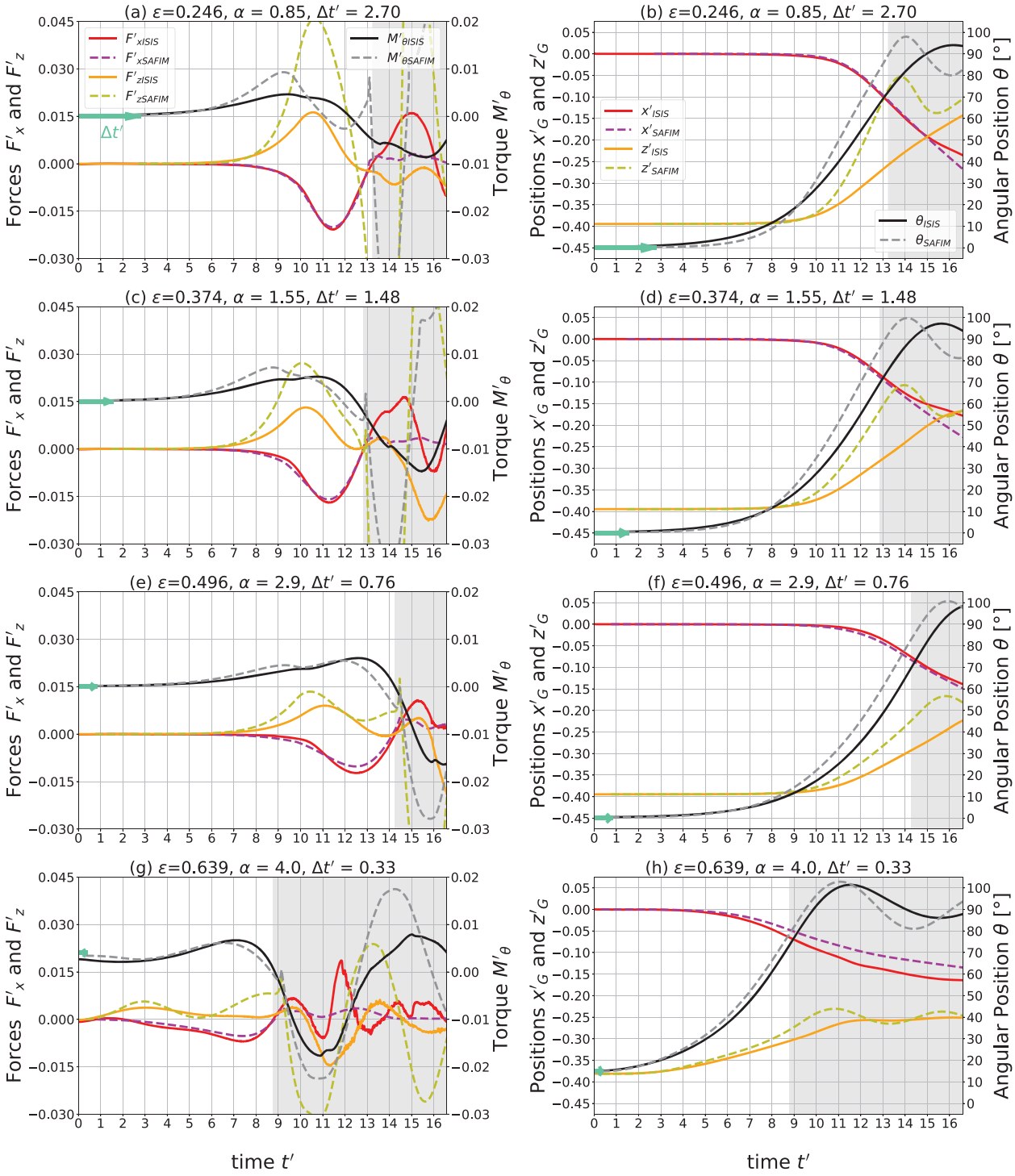

Figure 8. Capsize simulations for SAFIM with drag, without added-masses and with time-shifts, and for ISIS-CFD: evolution of the dimensionless total horizontal force F'_x, vertical force F'_z and torque M'_θ on the iceberg (a, c, d, e), of the horizontal x'_G and vertical z'_G positions of G and of the inclination θ of the iceberg (b, d, f, g). Results are given for icebergs with $\varepsilon = 0.246$ (a, b), $\varepsilon = 0.374$ (c, d), $\varepsilon = 0.496$ (e, f) and $\varepsilon = 0.639$ (g, h). SAFIM curves were shifted (green arrow) by the dimensionless time $\Delta t' = \Delta t \sqrt{g/H}$. The SAFIM drag coefficient α and time $\Delta t'$ are indicated in the titles.

four studied cases, optimization of the error requires keeping only one non-zero added-mass coefficient, namely the added moment of inertia coefficient. The simplified added-masses allows a slow initiation of rotation, which can be explained by an added moment of inertia of the surrounding fluid.

drag and computed added-masses (case 4): In that case, SAFIM predicts the time and amplitude of the extremum of the force and the torque less accurately than the two previous cases: the error $E_2 > 34$ per cent for all the four studied cases (Fig. 10b). The corresponding results are not shown here.

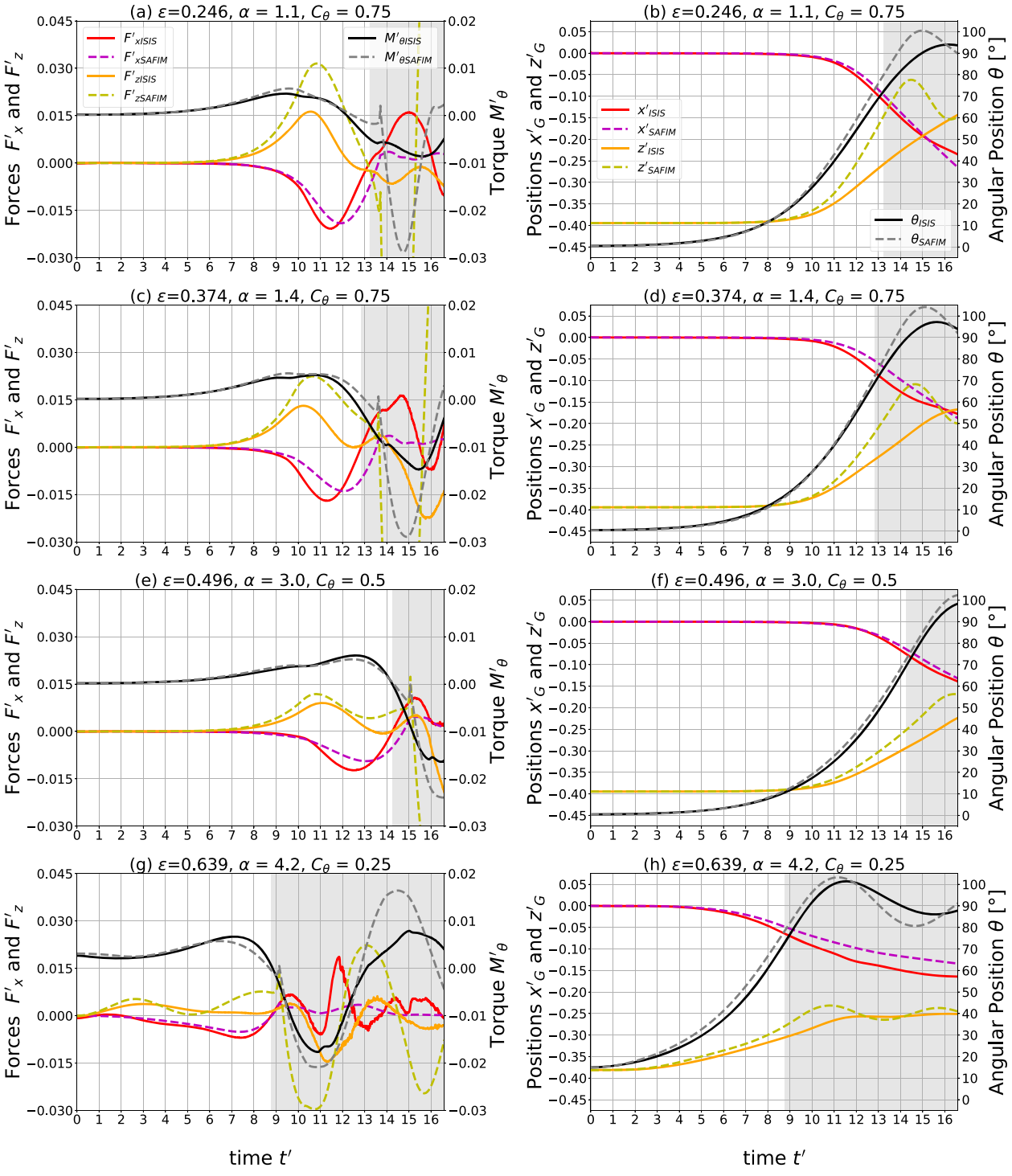

Figure 9. Same as in Fig. 8 but for SAFIM with drag, simplified added-masses and no time shift ($\Delta t'$). SAFIM drag coefficient α and added-mass coefficient C_θ are indicated in the titles.

5 DISCUSSION

First we will discuss the performance of SAFIM in Sections 5.1 and 5.2, then the modelling choices in Sections 5.3 and 5.4 and finally the sensitivity of the model results to geophysically meaningful variations of parameters in Sections 5.5, 5.6 and 5.7.

5.1 SAFIM performance and comparison with existing models

The advantages of the formulated and validated SAFIM model with drag and without added-masses is that (1) it can be readily implemented in a finite element model like the one in (Sergeant

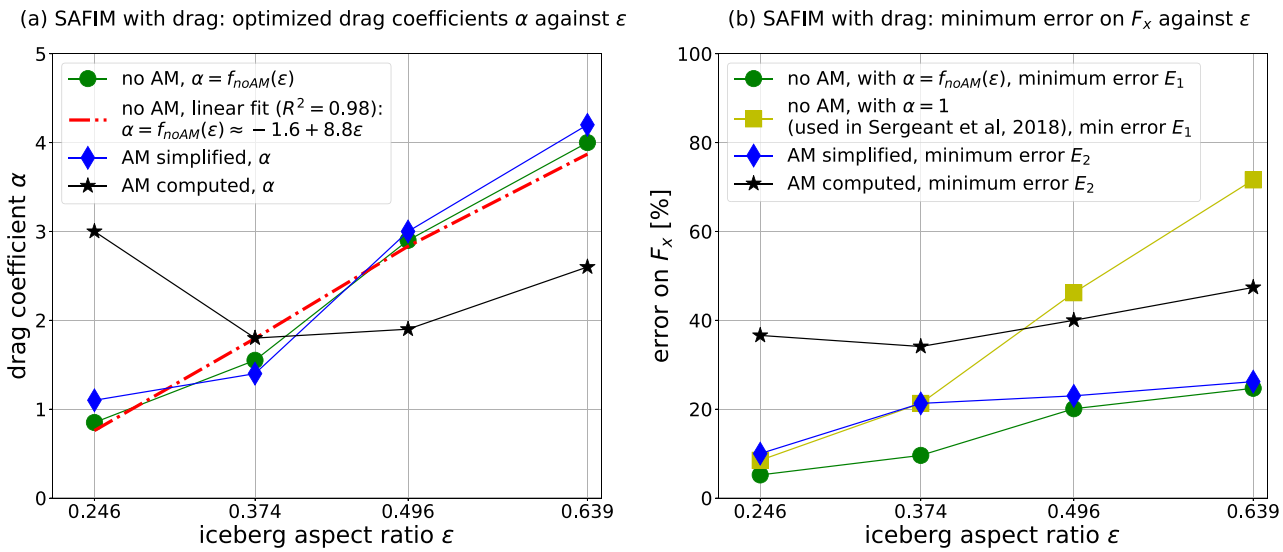

Figure 10. (a) Optimized values of the drag coefficient α for different iceberg's aspect ratios, which were determined for SAFIM with and without added-mass, only added moment of inertia was used in the simplified added-mass model, and a full added-mass matrix was used for the computed added-mass; (b) the minimal error of the horizontal force corresponding to different models for different iceberg's aspect ratios. The optimal parameters and corresponding minimal errors are also given in Table C1.

et al. 2018), (2) it requires only one parameter, the drag coefficient $\alpha_{\text{opt}}(\varepsilon) \approx -1.6 + 8.8\varepsilon$, (3) it quite accurately reproduces the shape and amplitude of the horizontal force. The drawback of this model is that it does not correctly simulate the kinematics of the iceberg capsize, especially the time needed to reach the peak force (see discussion in Section 5.2). In addition, the evolution of the torque and vertical force is not well reproduced.

The advantage of SAFIM with drag and simplified added-masses is that it correctly reproduces the time of the force extremum (no shift in time is needed) and it reproduces the torque and the vertical force better than SAFIM with drag and no added-masses. Its drawback is that it underestimates the amplitude of the first extremum of the horizontal force by ≈10 per cent.

SAFIM with drag and computed added-masses gives less accurate results than the two other versions. Assuming that the computed added-masses are physical and accurate (Yvin *et al.* 2018), the drag model in SAFIM is not suitable with that added-mass formulation since it does not make it possible to reproduce the dynamics of the iceberg.

The proposed SAFIM model well predicts the first part of the horizontal force applied by the fluid on the iceberg, either when using a drag force only (i.e. no added-masses) and shifting the curve in time or when using a drag force and simplified added-masses (and no shift in time). However, the evolution of the force after the capsize ($\theta > 80°$) is not well modelled. This is probably due to the fact that the evolution of the local fluid pressures is governed by a complex fluid motion around the iceberg (see Section 5.3) which is hard to parametrize without full fluid dynamics computations. The duration and amplitude of the positive peak in the force is however comparable to that of the first minimum of the force (see e.g. for $\epsilon = 0.374$ Fig. 8).

An advantage of SAFIM over previous models (Tsai *et al.* 2008; Burton *et al.* 2012) is that, thanks to a special form of the drag force, it can describe the horizontal movement of a capsizing iceberg triggered by its rotation. As shown in Sergeant *et al.* (2018), SAFIM can distinguish between a top-out and bottom-out capsize, when used to simulate the contact force between a capsizing iceberg and a rigid glacier front. A qualitative explanation of the emerging non-zero horizontal force given by the drag force is given in Appendix B.

We calculate the error in SAFIM with a drag coefficient $\alpha = 1$ for all aspect ratios and without added-mass (Fig. 10). Exactly the same model was used in Sergeant *et al.* (2018, 2019), but for modelling an iceberg capsizing in contact with a glacier front. The error E_1 is about two times greater than when taking the optimum value of the α coefficient for each aspect ratio, and the amplitude and duration of the first negative part of the force is underestimated—except for the thinnest iceberg with $\varepsilon = 0.246$, for which the opposite is true. Note that this error is only relevant for a freely capsizing iceberg. In future work, the errors for an iceberg capsizing in contact with a glacier front should be estimated but this will require a reference model for fluid-structure interactions that can track the contact between solids, which is a challenging problem (Mayer *et al.* 2010).

5.2 Initiation of the capsize

In the previous sections, the drag parameter for SAFIM without added-masses was optimized by implementing an artificial time shift of the SAFIM force curve with respect to ISIS-CFD. This was done because, as already mentioned, SAFIM without added-masses is not able to predict the accurate duration of the initiation of the capsize, where the motion is slow and the horizontal force is close to zero.

Various reasons suggest that this initial phase may not be relevant in the global context of the ultimate objective of the project, that is estimation of the short time-scale volume loss on marine-terminating icebergs. To achieve this objective, we need to compare the modelled contact force with the inverted seismic source force. The very beginning of the seismic force has a too small signal-to-noise ratio, therefore it is the first peak of the force that is used as a reference to compare the seismic force and the modelled force. Also, because this force evolves very slowly at the beginning, it will not be responsible for the generation of seismic waves with a period of 50 s that is predominantly observed on glacial earthquake seismograms (Ekström *et al.* 2003; Tsai & Ekström 2007; Tsai *et al.*

2008; Sergeant *et al.* 2018). Another reason for ignoring the beginning of the capsize is that the duration of the initial slow rotation [phase (i)] of the iceberg is strongly dependent on the initial angle of inclination of the iceberg which is hard to constrain in the field data and, when it is sufficiently small, has little effect on the capsize [phases (ii), (iii), (iv)]. The initiation phase of the capsize may also depend on the asymmetrical geometry of the iceberg, its surface roughness and the 3-D effects (see Sections 5.6 and 5.7).

Nevertheless, if we consider a complete glacier / ocean / bedrock / iceberg / ice-mélange system, the initial detachment of the iceberg can result in various other effects such as basal sliding or vertical oscillations of the glacier tongue, which can produce a seismic signal. Therefore the superposition of these phenomena can be erroneous if the timing is not well reproduced. To solve this issue, simulations of the complete glacier / ocean / bedrock / iceberg / ice-mélange system with a full fluid dynamics model coupled with a model for dynamics of deformable solids would seem to be unavoidable, however, as already discussed, it lies beyond actual computational possibilities of the softwares that we dispose.

5.3 Drag force and local pressure field

Following Burton *et al.* (2012), a linear drag model with a local pressure proportional to the normal velocity $|v_n|$ was also tested in SAFIM. It results in the following modification to eqs (5) and (6):

$$\boldsymbol{F}_d = -\alpha \frac{1}{2} \int_{\Gamma_s} \rho_w |v_n| \text{sign}(v_n) \boldsymbol{n} \, \mathrm{d}\Gamma, \tag{12}$$

$$\boldsymbol{M}_d = -\alpha \frac{1}{2} \int_{\Gamma_s} \rho_w |v_n| \text{sign}(v_n) (\boldsymbol{r} - \boldsymbol{r}_G) \wedge \boldsymbol{n} \, \mathrm{d}\Gamma. \tag{13}$$

Such a drag model yields worse results than the original model with quadratic dependency when compared with the reference ISIS-CFD model. In addition, other drag models were tested with linear and quadratic pressure dependency on the velocity, with a non-uniform parameter α on the surface of the iceberg and with drag depending on the sign of the local normal velocity v_n. Of all drag models tested, the most accurate was the model with quadratic dependency on the normal velocity and with a constant α-factor over the whole surface of the iceberg. However, to better fit the reference results, the α-factor was made dependent on the iceberg's aspect ratio, which is an important difference with the original model presented in Sergeant *et al.* (2018).

To go further in our understanding of the forces generated by the fluid, we analyse the hydrodynamic pressure distribution on the sides of the iceberg, computed by ISIS-CFD and defined as $p_{dyn} = p_{tot} - p_{sta}$, with p_{tot} the total fluid pressure and p_{sta} the hydrostatic pressure computed for the reference still water level ($z = 0$). In particular, we attempted to establish a link between the spatial distribution of the hydrodynamic pressure on the iceberg and the local features of the fluid flow, notably with the normalized vorticity (see Fig. 5) which is defined as: $\omega = -\sqrt{H/g}\, \boldsymbol{e}_y \cdot (\nabla \wedge \boldsymbol{u})$, with a negative value (blue) accounting for a vortex rotating clockwise and a positive (red) value for a counter-clockwise vortex. On the four snapshots presented in Fig. 5, we also plot the dimensionless hydrodynamic pressure $p'_{dyn} = p_{dyn}/(\rho_i H g)$. The hydrodynamic pressure is plotted as a shaded pink area outside the iceberg for a negative pressure and inside the iceberg for a positive pressure. Note that these values are about two orders of magnitude lower than the average hydrostatic pressure. The dynamic pressure is higher at locations where there is a vortex close to the surface of the iceberg such as on the corner furthest right in Figs 5(b) and (c), on the bottom part of the left side and in the middle on the right side of the iceberg. This observation suggests that the dynamic pressure field is highly dependent on the vortices in the fluid. Such an evolution of complex vortex motion cannot be reproduced within SAFIM and requires the resolution of the equations of fluid motion as in ISIS-CFD. Note that the high values of the pressure on the top side of the iceberg in Figs 5(c) and (d) are due to an additional hydrostatic pressure produced by the wave that is above the reference sea level.

Using ISIS-CFD simulations, we made an attempt to correlate the local hydrodynamic pressure p_{dyn} with the normal velocity v_n via a power law as it is the case in SAFIM:

$$|p_{\text{dyn}}| = b|v_n|^a. \tag{14}$$

in order to optimize the drag law used here (in SAFIM, the coefficients are $a = 2$ and $b = -\alpha \, \text{sign}(v_n) \, \rho_w/2$). This attempt was not successful. We observed that the values of a and b vary significantly along the sides of the iceberg and with time particularly on the top part of the long sides of the iceberg and close to the corners. Also, we tried to correlate the dynamic pressure for $a = 2$, as in SAFIM, without success. Nevertheless, the choices made in SAFIM ensures rather accurate overall drag forces and torques acting on the iceberg due to dynamic pressure.

5.4 Accuracy of the added-mass

The simplified added-masses, defined by eqs (7), (8) and (9), with only diagonal terms in the added-mass matrix, will now be compared with the reference computed added-masses. Both added-mass matrices depend on the current iceberg position, and therefore they should be updated at every time step. These matrices are calculated for the iceberg's motion computed by ISIS-CFD. We show the time evolution of the added-masses and the added moment of inertia, for the capsize of a laboratory-scale iceberg with $H = 0.103$ m and $\varepsilon = 0.246$ in Figs 11(a)–(c) and $\varepsilon = 0.496$ in Figs 11(d)–(f).

The simplified horizontal and vertical added-masses are in very good agreement with the corresponding computed added-masses: relative error (with the $\mathcal{L}^2$ norm) of 21 per cent on m_{xx} for $\varepsilon = 0.246$ and 23 per cent for $\varepsilon = 0.496$; relative error of 11 per cent on m_{zz} for $\varepsilon = 0.246$ and 13 per cent for $\varepsilon = 0.496$. The simplified added moment of inertia $I_{\theta\theta}$ is assumed to be constant in our model whereas the computed one varies in time and has a smaller value: relative error of about 30 per cent.

For the aspect ratio $\varepsilon = 0.246$, the horizontal added-mass m_{xx} decreases from ≈ 2.5 m at the beginning down to ≈ 0.2 m, where m is the iceberg mass, whereas, symmetrically, the vertical added-mass m_{zz} increases from ≈ 0.2 m at the beginning up to ≈ 2.5 m at the end of the capsize. The horizontal added-mass m_{xx} measures the resistance of the fluid to a horizontal acceleration $\ddot{x_G}$ of the iceberg. The iceberg has a longer submerged vertical extension (of the order of H) at the beginning than at the end (of the order of W) of the capsize, thus it needs to displace a greater volume of fluid in a horizontal motion at the beginning than at the end of the capsize ($\theta > 90°$). Therefore, a greater added-mass m_{xx} is expected at the beginning of the capsize. The vertical added-masses m_{zz}, sensitive to the horizontal extension of the iceberg, experience the opposite variations in time. The computed added moment of inertia is equal to the moment of inertia of the iceberg I at the beginning. Then it increases to 1.25 I and decreases below the iceberg's moment of inertia to 0.9 I (see Fig. 11).

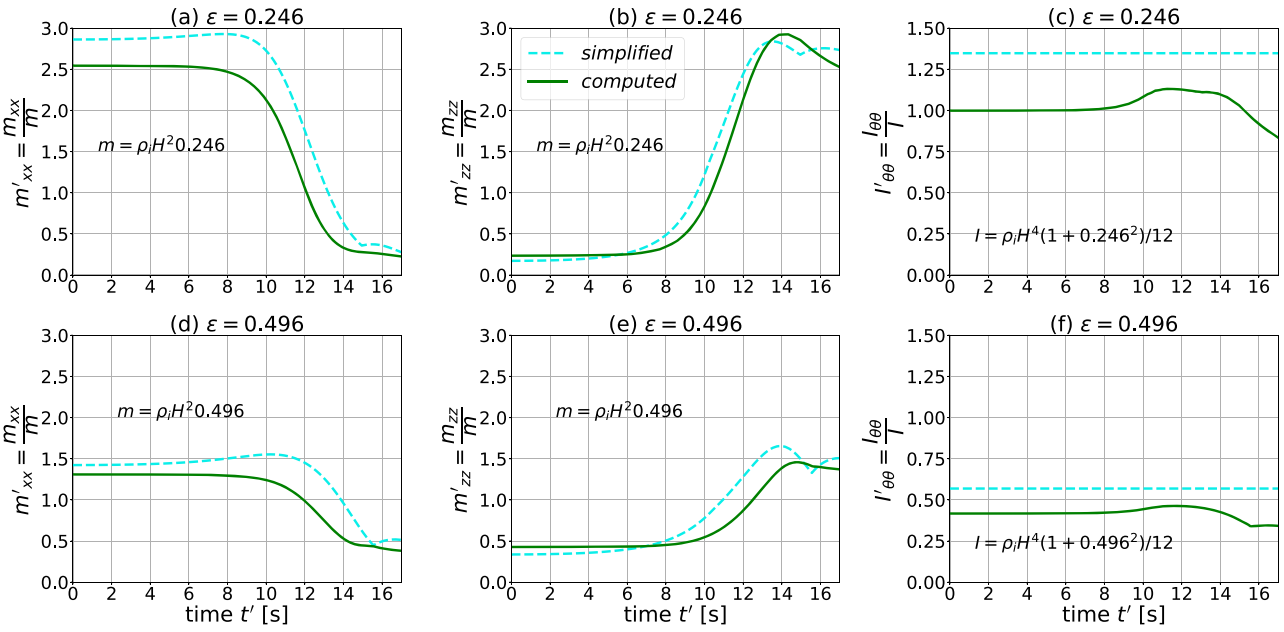

Figure 11. Time evolution of dimensionless horizontal added-masses (a) and (d), vertical added-masses (b) and (e), added moment of inertia (c) and (f). The dashed cyan curves are the simplified added-masses and moment of inertia and the solid green curves are the computed added-masses and moment of inertia. Values are given for a laboratory-scale iceberg ($H = 0.103$ m) with field densities and aspect ratio $\varepsilon = 0.246$ in (a), (b) and (c) and $\varepsilon = 0.496$ in (d), (e) and (f). For each aspect ratio ε, the values are normalized by the mass of the iceberg $m = \rho_i H^2 \varepsilon$ and the inertia of the iceberg $I = \rho_i H^4(1 + \varepsilon^2)/12$. The non-constant added-masses are given for the positions of the iceberg in the ISIS-CFD simulations. The values of the simplified added-masses are plotted for all coefficients equal to 1: $C_x = C_z = C_\theta = 1$.

For the aspect ratio $\varepsilon = 0.496$, the variations of the dimensionless added-masses are different in amplitude but with rather similar evolutions.

For other geometries, the added-masses (resp. inertia) are also of the same order of magnitude as the masses (resp. inertia) of the iceberg as found here for rectangular icebergs. For example, in the case of a 2-D thin ellipse with an aspect ratio of b/a, with a the along-flow dimension and b the cross-flow dimension, Newman (1999) gives the added-masses and added moment of inertia. For $b/a = 0.2$, the transverse added-mass is equal to 0.9 times the mass of the *displaced volume of fluid* (i.e. the submerged volume of the solid times the density of the fluid) and the added moment of inertia is equal to 0.7 times the inertia of the displaced volume of fluid. For similar densities for the fluid and the solid, the added-masses and the added moment of inertia are close to those of the solid. The optimized values of the coefficients for the simplified added-masses and moment of inertia in SAFIM are given in Table C1. These values are not in agreement with the reference computed added-masses. However, as discussed in Section 5.1, the SAFIM model with the simplified added-mass matrix gives better results than SAFIM with the computed added-mass matrix. For $\varepsilon = 0.246$, note that the optimized simplified added moment of inertia ($C_\theta = 0.75$) is close to the computed one. However, the simplified added moment of inertia is not in agreement with the computed one for higher ε.

The optimized value $C_z = 0$ is consistent with the choice of $m_{zz} = 0$ in Tsai *et al.* (2008) even though it is not equal to the computed vertical added-mass. The optimized coefficient $C_x = 0$ gives $m_{xx} = 0$. The horizontal added-mass m_{xx} from Tsai *et al.* (2008) varies similarly to the computed added-mass. The added moment of inertia $I_{\theta\theta}$ with the formula in Tsai *et al.* (2008) is constant throughout the capsize and different from the optimized added moment of inertia. However, the formula for added-masses and added moment of inertia from Tsai *et al.* (2008) were given for the simulation of an iceberg capsizing in contact with a wall, which may significantly affect the values of the added-masses.

5.5 Effect of water/ice densities

The laboratory experiments discussed in Section. 2.3 were conducted with water and ice densities slightly different from those in the field (see Section. 2.1).

As shown in Fig. 12, the dynamics of the iceberg computed by ISIS-CFD with field densities is significantly different from those obtained with laboratory densities: the amplitude, duration and initiation of the capsize are very sensitive to changes in densities. This sensitivity is also very well reproduced by SAFIM with drag and no added-masses. Note that no change in the drag coefficient α is needed to accurately reproduce this effect with SAFIM.

In Section 2.5, we pointed out the similarity between laboratory scale and field scale simulations if the same water and ice densities were used in both. To obtain the dimensionless variables, we used the timescale $T_H = \sqrt{H/g}$, length scale H and mass scale m (see Table 1). However, as shown in Fig. 12, using different densities yields great differences in the horizontal force. Here, we explain how a simulation of a laboratory-scale iceberg with laboratory densities can be related to a simulation of a field-scale iceberg with field densities. We use the same approach as in Section 2.5, with length scale H and mass scale m but we introduce a timescale depending on the densities as proposed by Tsai *et al.* (2008) (ignoring the factor 2π):

$$T_{\rho,H} = \sqrt{\frac{H\rho_i}{g(\rho_w - \rho_i)}}. \tag{15}$$

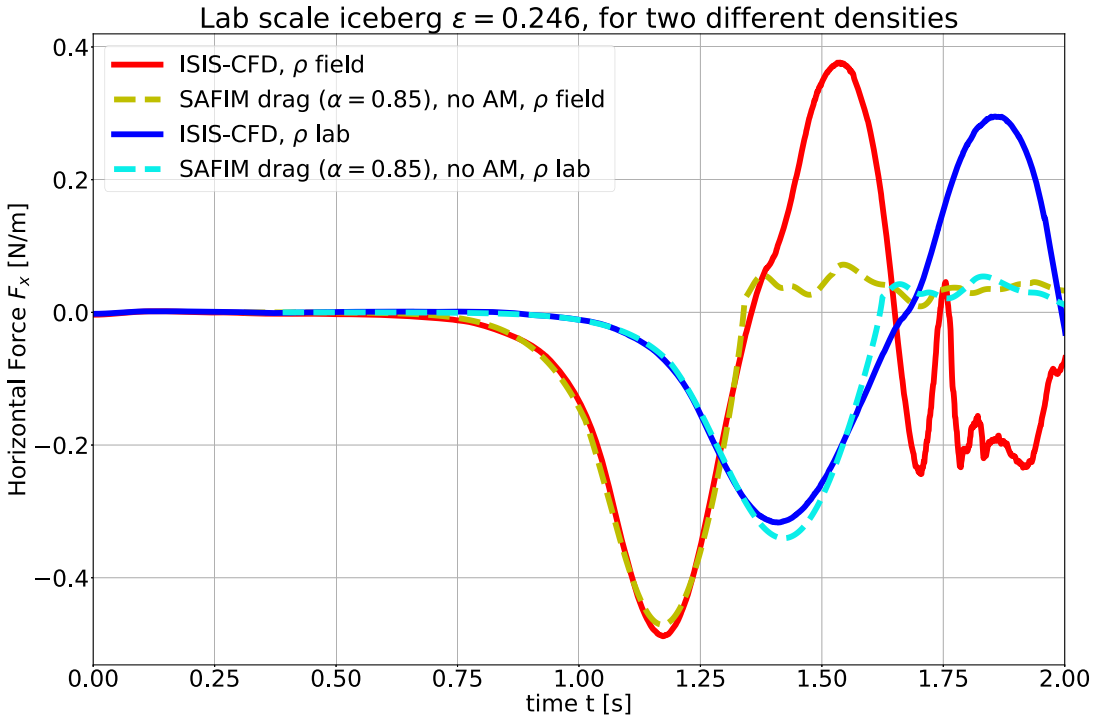

Figure 12. Horizontal force acting on a capsizing iceberg ($H = 0.103$ m and $\varepsilon = 0.246$) computed by ISIS-CFD and SAFIM for two different sets of densities: laboratory densities (blue and cyan curves) $\rho_w = 997\,\mathrm{kg\,m^{-3}}$ and $\rho_i = 920\,\mathrm{kg\,m^{-3}}$ and field densities (red and yellow curves) $\rho_w = 1025\,\mathrm{kg\,m^{-3}}$ and $\rho_i = 917\,\mathrm{kg\,m^{-3}}$.

In Fig. 13, we plot the dimensionless horizontal force $F_x' = F_x\,T^2/(m\,H)$ with respect to the dimensionless time $t' = t/T$ for timescale $T = T_H$ and for timescale $T = T_{\rho,H}$ and for three aspect ratios $\varepsilon = 0.25$, 0.375 and 0.5. For the timescale T_H which does not involve densities, the dimensionless curves differ considerably whereas for $T_{\rho,H}$, which takes the densities into account, the agreement is improved, especially for small aspect ratios.

Using a shift in time, the fit can be improved even further. Therefore, to upscale the laboratory-scale experiments to the field scale, a dimensionless timescale $T_{\rho,H}$ should be used rather than a simple scaling T_H.

As densities have a large impact on capsize dynamics, more realistic water and ice densities, including their spatial heterogeneity, should be considered in future capsize models. Water density depends on salinity and temperature. For example, in the fjord of the Bowdoin glacier (northwest Greenland), water density may change in the range between 1015 and 1028 $\mathrm{kg\,m^{-3}}$ (Sejr *et al.* 2017; Middelbo *et al.* 2018; Holding *et al.* 2019; Ohashi *et al.* 2019). Ice density is more difficult to evaluate as in situ measurements are rare. It depends on the volume fraction of air bubbles, which is for example around 20−30 per cent for firn at ≈ 40 m in depth (Herron & Langway 1980). The density of the iceberg may then be heterogeneous and can probably range between ≈ 600 and $\approx 930\,\mathrm{kg\,m^{-3}}$ (the density of pure ice at -10 °C being about $918\,\mathrm{kg\,m^{-3}}$). With these ranges of ice and water field densities, the factor $\sqrt{\rho_i/(\rho_\mathrm{w} - \rho_i)}$ varies between the extreme values ≈1.18 and ≈3.31, which corresponds to an even greater spread than in our lab/field comparison (3.46 for lab densities, 2.92 for field values). Therefore consideration of the effect of density and its variability has to be integrated in the inverse problem for iceberg volume estimation based on the seismic signal inversion.

5.6 3-D effects

Capsizing icebergs have the following typical dimensions: full-glacier-height 500 m $\lessapprox H \lessapprox$ 1000 m, width in the glacier's flow direction $W \lessapprox 0.75H$ (MacAyeal & Scambos 2003), width along the glacier's coast line generally greater than the iceberg's height $H \lessapprox L$, with the upper limit equal to the glacial fjord width. However, as discussed above, in our modelling we neglect the effect of the third dimension on the dynamics of the capsizing iceberg. The first argument to support this simplification is that iceberg capsizing in a narrow fjord-like tank [laboratory experiments of Burton *et al.* (2012)] is very well reproduced with the 2-D ISIS-CFD model (Section 2). In the field, icebergs capsize in fjords with much more complex geometries. For example, the fjord may be much wider than the iceberg which would yield a truly 3-D motion of the fluid. Real capsizing iceberg should induce vortices on each side of the iceberg which may have an effect on the motion of the iceberg that has not yet been evaluated.

5.7 Effect of the iceberg geometry

This study was conducted with the assumption that the icebergs have a perfectly rectangular (parallelepipedic) shape and smooth surface. However, icebergs in the field have much more complex shapes. The freeboard of an iceberg has irregularities that can range from a scale larger than 100 m down to a scale less than 0.1 m (Landy *et al.* 2015). The roughness of the submerged part of icebergs is poorly documented because of the difficulty in conducting suitable measurements. In future work, we could estimate the roughness of some well documented icebergs, such as the PII-B-1 tabular iceberg in Northwest Greenland scanned with a Reson 8125 multibeam

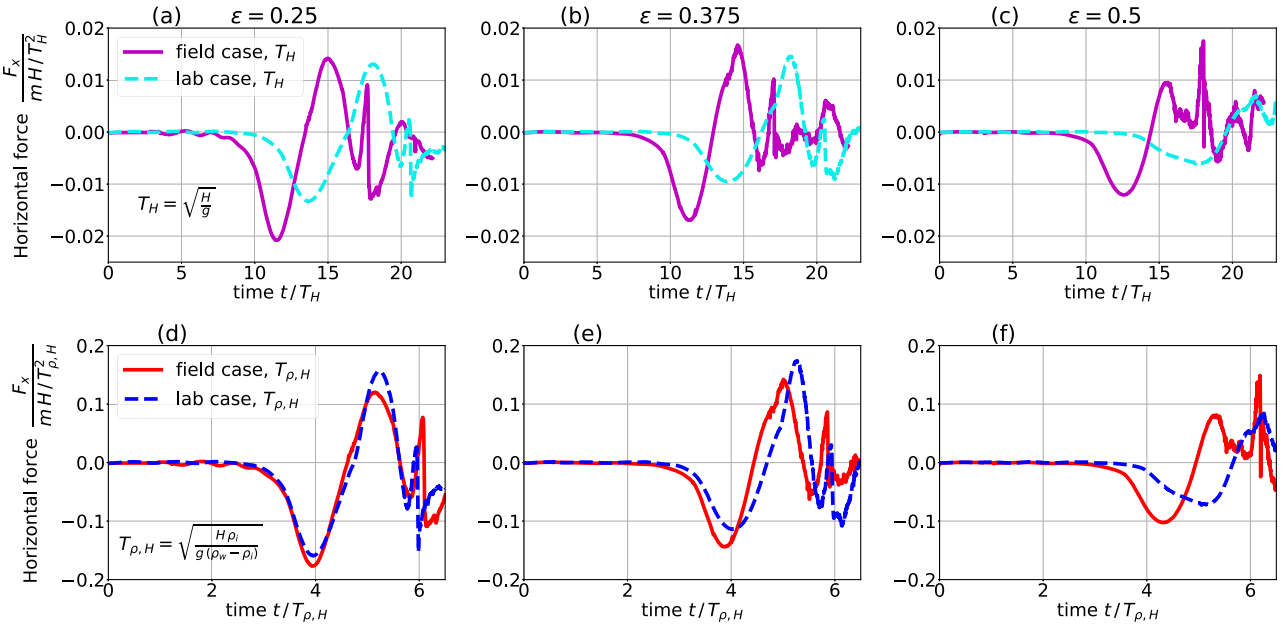

Figure 13. Dimensionless horizontal force acting on a capsizing iceberg computed by ISIS-CFD for a field-scale iceberg with field densities $\rho_w = 1025\,\mathrm{kg\,m^{-3}}$ and $\rho_i = 917\,\mathrm{kg\,m^{-3}}$ (solid lines) and for a laboratory-scale iceberg with laboratory densities $\rho_\mathrm{w} = 997\,\mathrm{kg\,m^{-3}}$ and $\rho_i = 920\,\mathrm{kg\,m^{-3}}$ (dashed lines). The top row (a, b, c) is for timescale $T_H = \sqrt{H/g}$ and the bottom row (d, e, f) is for timescale $T_{\rho,H} = \sqrt{H/g}\,\sqrt{\rho_i/(\rho_\mathrm{w}-\rho_i)}$. The first, second and third columns correspond to $\varepsilon = 0.25, 0.375$ and 0.5, respectively.

sonar by Wagner *et al.* (2014). In fluid mechanics modelling, surface features have a great impact on the boundary layer close to the surface and in some cases also on the whole flow (Krogstad & Antonia 1999). A sensitivity analysis would be needed to assess the influence of the surface features and surface roughness on the dynamics of capsizing icebergs.

Furthermore, in our simulations, icebergs were initially in hydrostatic equilibrium. In Sergeant *et al.* (2018), the effect of hydrostatic imbalance of the iceberg at the initiation of the capsize was assessed by varying the vertical position of the iceberg with respect to the water level. Hydrostatic imbalance results in a different evolution of the contact force with the glacier front and different dominant frequencies of generated seismic waves. This is supported by seismic observations of calving events.

6 CONCLUSION

In this study, we have improved the understanding of free iceberg capsize in open water through fluid-dynamics simulations (ISIS-CFD solver) validated against laboratory experiments (Burton *et al.* 2012). In particular, we have shown the complexity of the fluid motion and the dynamics of the iceberg during capsize: vortices around the iceberg during and after capsize, motion of the fluid around the iceberg (velocity of $\approx$88 cm s^{-1} for a $H = 800$ m high iceberg at a distance H from the iceberg), wave generation, iceberg submergence when reaching the horizontal position and a significant horizontal displacement of the iceberg during capsize. Moreover, we have shown that the non-dimensionalized horizontal force $F'_x = F_x/(\rho_i H^2 \varepsilon g)$ is invariant with the height H of the iceberg. The horizontal force acting on the iceberg while its capsize changes its sign after the full capsize. Depending on the iceberg dimensions, this reverse force could be as high and last as long as the one acting during the capsize. Extrapolating these results to iceberg capsize against the glacier terminus would suggest that the force applied by the rotating iceberg on the glacier could be followed by a purely hydrodynamic force of opposite sign, once the contact is lost. This could possibly be compatible with the boxcar force shape assumed by (Olsen & Nettles 2017, 2019) even though the filtering of the contact force itself, with a constant sign, would also lead to a changing sign filtered force as explained by (Sergeant *et al.* 2018, fig. 7). This hypothesis should be however clarified by a full scale CFD analysis including contact and glacier terminus.

We have presented here a Semi-Analytical Floating Iceberg Model (SAFIM) and demonstrated its accuracy for various geometries as well as for different water and ice densities by comparing the results with direct numerical CFD simulations. Our simple model is slightly more complex but more accurate than the one used in our previous study (Sergeant *et al.* 2018): the new feature is that the drag parameter depends on the iceberg aspect ratio (affine function) to minimize the error with the reference CFD simulations. SAFIM's error is of 5 to 20 per cent (about half the maximum error made with the Sergeant *et al.* (2018) model) on the horizontal force F_x (without added-masses) during the capsize phase for different aspect ratios. An extension of this model to more complex iceberg shapes and to three dimensions is relatively straightforward. Different options are offered by SAFIM. For accurate modelling of the amplitude of the fluid forces, SAFIM should be used with drag but without added-masses. For accurate modelling of the time of the peak force and the torque, it should be used with a drag force and an added moment of inertia. In the global context of estimations of iceberg volume by analysis of seismic signals generated during iceberg capsize in contact with a glacier front, based on the discussion on the time-shift in Section 5.2, SAFIM should be used with an optimized drag coefficient and no added-masses. However, for today this model has been validated only for the case of the capsize of an iceberg in the open ocean. Further validation will be conducted for the simulation of the capsize of an iceberg in contact with a glacier. In the geophysical context of modelling seismogenic iceberg capsize, further studies

would help improve the model accuracy. Examples of such studies include (i) modelling of the full glacier / ocean / bedrock / iceberg / ice-mélange system, which is computationally very challenging and (ii) sensitivity analysis of the iceberg dynamics to the iceberg shape, surface roughness and fjord geometry, which may be also very complex.

ACKNOWLEDGEMENTS

The authors acknowledge funding from ANR (contract ANR-11- BS01-0016 LANDQUAKES), ERC (contract ERC-CG-2013-PE10-617472 SLIDEQUAKES), DGA-MRIS and IPGP - Université de Paris ED560 (STEP'UP), which has made this work possible. The authors acknowledge Justin Burton for providing us with the data from laboratory experiments. The authors are also very grateful to François Charru, Emmanuel de Langre and Evgeniy A. Podolskiy for fruitful discussions, and the reviewers (Jason M. Amundson and Bradley P. Lipovsky) for helpful comments.

This is IPGP contribution number 4157.

REFERENCES

Amundson, J.M., , Fahnestock, M., Truffer, M., Brown, J., Lüthi, M.P. & Motyka, R.J., 2010. Ice mélange dynamics and implications for terminus stability, Jakobshavn Isbrae, Greenland, *J. geophys. Res.,* **115**(1), F01005.

Amundson, J.M., Burton, J.C. & Correa-Legisos, S., 2012. Impact of hydrodynamics on seismic signals generated by iceberg collisions, *Ann. Glaciol.,* **53**(60), 106–112.

Aster, R.C. & Winberry, J.P., 2017. Glacial seismology, *Rep. Prog. Phys.,* **80**(12), 126801.

Benn, D.I., Cowton, T., Todd, J. & Luckman, A., 2017. Glacier calving in Greenland, *Curr. Clim. Change Rep.,* **3**(4), 282–290.

Burton, J.C. *et al.*, 2012. Laboratory investigations of iceberg capsize dynamics, energy dissipation and tsunamigenesis, *J. geophys. Res.,* **117**(1), 1–13.

Durand, M., Leroyer, A., Lothodé, C., Hauville, F., Visonneau, M., Floch, R. & Guillaume, L., 2014. FSI investigation on stability of downwind sails with an automatic dynamic trimming, *Ocean Eng.,* **90**(2013), 129–139.

Ekström, G., Nettles, M. & Geoffrey, A.A., 2003. Glacial earthquakes, *Science,* **622**(2003), 10–13.

Enderlin, E.M., Howat, I.M., Jeong, S., Noh, M.-J., van Angelen, J.H. & van den Broeke, M.R., 2014. An improved mass budget for the Greenland ice sheet, *Geophys. Prospect.,* **41**(9), 3307–3314.

Guilmineau, E., Deng, G.B., Leroyer, A., Queutey, P., Visonneau, M. & Wackers, J., 2017. Numerical simulations for the wake prediction of a marine propeller in straight-ahead flow and oblique flow, *J. Fluids Eng., Trans. ASME,* **140**(2), doi:10.1115/1.4037984.

Guilmineau, E., Deng, G.B., Leroyer, A., Queutey, P., Visonneau, M. & Wackers, J., 2018. Wake prediction of a marine propeller: the role of the turbulence closures, *ERCOFTAC Ser.,* **24,** 251–256.

Hay, A., Leroyer, A. & Visonneau, M., 2006. H-adaptive Navier-Stokes simulations of free-surface flows around moving bodies, *J. Mar. Sci. Technol.,* **11**(1), 1–18.

Herron, M.M. & Langway, C.C., 1980. Firn densification: an empirical model, **25**(93), 373–385.

Holding, J.M., Markager, S., Juul-Pedersen, T., Paulsen, M.L., Møller, E.F., Meire, L. & Sejr, M.K., 2019. Seasonal and spatial patterns of primary production in a high-latitude fjord affected by Greenland Ice Sheet run-off, *Biogeosciences,* **16**(19), 3777–3792.

Job, J., 1978. Numerical modelling of iceberg towing for water supplies: a case study, *J. Glaciol.,* **20**(84), 533–542.

Jouvet, G., Weidmann, Y., Kneib, M., Detert, M., Seguinot, J., Sakakibara, D. & Sugiyama, S., 2018. Short-lived ice speed-up and plume water flow captured by a VTOL UAV give insights into subglacial hydrological system of Bowdoin Glacier, *Rem. Sens. Environ.,* **217,** 389–399.

Krogstad, P.Å. & Antonia, R.A., 1999. Surface roughness effects in turbulent boundary layers, *Exp. Fluids,* **27**(5), 450–460.

Landy, J.C., Isleifson, D., Komarov, A.S. & Barber, D.G., 2015. Parameterization of centimeter-scale sea ice surface roughness using terrestrial LiDAR, *IEEE Trans. Geosci. Rem. Sens.,* **53**(3), 1271–1286.

Lemke, P. *et al.*, 2007. Observations: changes in snow, ice and frozen ground, climate change 2007: the physical science basis, in *Contribution Of Working Group to the Fourth Assessment Report of the Intergovernmental Panel on Climate Change,* 337–383, Cambridge Univ. Press.

Leroyer, A. & Visonneau, M., 2005. Numerical methods for RANSE simulations of a self-propelled fish-like body, *J. Fluids Struct.,* **20**(7), 975–991.

Leroyer, A., Wackers, J., Queutey, P. & Guilmineau, E., 2011. Numerical strategies to speed up CFD computations with free surface—application to the dynamic equilibrium of hulls, *Ocean Eng.,* **38**(17–18), 2070–2076.

Leroyer, A., Barré, S. & Kobus, J.-M., 2012. Experiments and simulations: approach and steps towards a better knowledge of the hydrodynamics of rowing blades, *Movement Sport Sci.,* **75** (2012/1 (75)), 85–96.

MacAyeal, D.R. & Scambos, T.A., 2003. Catastrophic ice-shelf break-up by an ice-shelf-fragment-capsize mechanism, *J. Glaciol.,* **49**(164), 22–36.

Mankoff, K.D., Straneo, F., Cenedese, C., Das, S.B., Richards, C.G. & Singh, H., 2016. Structure and dynamics of a subglacial discharge plume in a Greenlandic fjord, *J. geophys. Res.: Oceans,* **121**(8), 1–14.

Marsh, R. *et al.*, 2015. NEMO-ICB (v1.0): interactive icebergs in the NEMO ocean model globally configured at eddy-permitting resolution, *Geoscient. Model Dev.,* **8**(5), 1547–1562.

Mayer, U.M., Popp, A., Gerstenberger, A. & Wall, W.A., 2010. 3D–fluid-structure-contact interaction based on a combined XFEM FSI and dual mortar contact approach, *Comput. Mech.,* **46**(1), 53–67.

Menter, F., 1993. Zonal two equation kw turbulence models for aerodynamic flows, in *Proceedings of the 23rd AIAA Fluid Dynamics, Plasmadynamics, and Lasers Conference,* AIAA-93-2906.

Middelbo, A.B., Sejr, M.K., Arendt, K.E. & Møller, E.F., 2018. Impact of glacial meltwater on spatiotemporal distribution of copepods and their grazing impact in Young Sound NE, Greenland, *Limnol. Oceanogr.,* **63**(1), 322–336.

Molin, B., 2002. *Hydrodynamique des Structures Offshore,* Guides Pratiques sur Les Ouvrages En Mer. TECHNIP.

Morison, J., Johnson, J. & Schaaf, S., 1950. The force exerted by surface waves on piles, *J. Petrol. Technol.,* **2**(05), 149–154.

Newman, J.N., 1999. *Marine Hydrodynamics,* The MIT Press.

Ohashi, Y., Aoki, S., Matsumura, Y., Sugiyama, S., Kanna, N. & Sakakibara, D., 2019. Water mass structure and the effect of subglacial discharge in Bowdoin Fjord, northwestern Greenland, *Ocean Sci. Discuss.,* 1–30, doi:10.5194/os-2019-33.

Olsen, K.G. & Nettles, M., 2017. Patterns in glacial-earthquake activity around Greenland , 2011–13, *J. Glaciol.,* **63,** 1077–1089.

Olsen, K.G. & Nettles, M., 2019. Constraints on terminus dynamics at Greenland glaciers from small glacial earthquakes, *J. geophys. Res.,* **124**(7), 1899–1918.

Podolskiy, E.A. & Walter, F., 2016. Cryoseismology, *Rev. Geophys.,* **54**(4), 708–758.

Queutey, P. & Visonneau, M., 2007. An interface capturing method for free-surface hydrodynamic flows, *Comput. Fluids,* **36**(9), 1481–1510.

Queutey, P., Wackers, J., Leroyer, A., Deng, G., Guilmineau, E., Visonneau, M., Hagesteijn, G. & Brouwer, J., 2014. Dynamic behaviour of the loads of podded propellers in waves: experimental and numerical simulations, in *Proceedings of the 33rd International Conference on Ocean, Offshore and Artic Engineering, OMAE*.

Robert, Y., Leroyer, A., Barré, S., Queutey, P. & Visonneau, M., 2019. Validation of CFD simulations of the flow around a full-scale rowing blade with realistic kinematics, *J. Mar. Sci. Technol.,* **24**(4), 1105–1118.

Savage, S., 2001. Aspects of Iceberg deterioration and drift, in *Lecture Notes in Physics,* **582,** 279–318.

Sejr, M.K., Stedmon, C.A., Bendtsen, J., Abermann, J., Juul-Pedersen, T., Mortensen, J. & Rysgaard, S., 2017. Evidence of local and regional freshening of Northeast Greenland coastal waters, *Sci. Rep.,* **7**(1), 13183.

Sergeant, A., Mangeney, A., Stutzmann, E., Montagner, J.P., Walter, F., Moretti, L. & Castelnau, O., 2016. Complex force history of a calving-generated glacial earthquake derived from broadband seismic inversion, *Geophys. Res. Lett.,* **43**(3), 1055–1065.

Sergeant, A., Yastrebov, V., Mangeney, A., Castelnau, O., Montagner, J. & Stutzmann, E., 2018. Numerical modeling of iceberg capsizing responsible for glacial earthquakes, *J. geophys. Res.,* **123**(11), 3013–3033.

Sergeant, A. *et al.*, 2019. Monitoring Greenland ice-sheet buoyancy-driven calving discharge using glacial earthquakes, *Ann. Glaciol.,* **60**(79), 75–95.

Spalart, P.R. & Allmaras, S.R., 1992. A one-equation turbulence model for aerodynamic flows, in *Proceedings of the 30th Aerospace Sciences Meeting and Exhibit,* Reno, NV, USA.

Tsai, V.C. & Ekström, G., 2007. Analysis of glacial earthquakes, *J. geophys. Res.,* **112**(3), 1–13.

Tsai, V.C., Rice, J.R. & Fahnestock, M., 2008. Possible mechanisms for glacial earthquakes, *J. geophys. Res.,* **113**(3), 1–17.

Tsukrov, I., Eroshkin, O., Fredriksson, D., Swift, M.R. & Celikkol, B., 2002. Finite element modeling of net panels using a consistent net element, *Ocean Eng.,* **30**(2), 251–270.

Van den Broeke, M., Bamber, J., Ettema, J., Rignot, E., Schrama, E., van De Berg, W.J., van Meijgaard, E., Velicogna, I. & Wouters, B., 2009. Partitioning recent Greenland mass loss, *Science,* **326**(5955), 984–986.

Van Den Broeke, M.R., Enderlin, E.M., Howat, I.M., Kuipers Munneke, P., Noël, B.P.Y., Van De Berg, W.J., Van Meijgaard, E. & Wouters, B., 2016. On the recent contribution of the Greenland ice sheet to sea level change, *Cryosphere,* **10**(5), 1933–1946.

Venugopal, V., Varyani, K. & Westlake, P., 2009. Drag and inertia coefficients for horizontally submerged rectangular cylinders in waves and currents, *J. Eng. Maritime Environ.,* **223**(1), 121–136.

Visonneau, M., 2005. A step towards the numerical simulation of viscous flows around ships at full scale - recent achievements within the European Union Project Effort, in *Proceedings of the Marine CFD 2005,* Southampton, UK.

Visonneau, M., Queutey, P. & Deng, G., 2006. Model and full-scale free-surface viscous flows around fully-appended ships, in *Proceedings of the European Conference on Computational Fluid Dynamics, ECCOMAS CFD 2006*.

Visonneau, M., Deng, G.B., Guilmineau, E., Queutey, P. & Wackers, J., 2016. Local and Global Assessment of the Flow around the Japan Bulk Carrier with and without energy saving devices at model and full scale, in *Proceedings of the 31st Symposium on Naval Hydrodynamics,* Monterey, CA.

Vizcaino, M., Enderlin, E.M., van den Broeke, M.R., Lenaerts, J. T.M., Le Bars, D. & van Kampenhout, L., 2015. Representing Greenland ice sheet freshwater fluxes in climate models, *Geophys. Res. Lett.,* **42**(15), 6373–6381.

Wackers, J., Deng, G., Leroyer, A., Queutey, P. & Visonneau, M., 2012. Adaptive grid refinement for hydrodynamic flows, *Comput. Fluids,* **55,** 85–100.

Wagner, T.J., Wadhams, P., Bates, R., Elosegui, P., Stern, A., Vella, D., Abrahamsen, E.P., Crawford, A. & Nicholls, K.W., 2014. The "footloose" mechanism: Iceberg decay from hydrostatic stresses, *Geophys. Res. Lett.,* **41**(15), 5522–5529.

Wagner, T.J., Stern, A.A., Dell, R.W. & Eisenman, I., 2017. On the representation of capsizing in iceberg models, *Ocean Modell.,* **117,** 88–96.

Walter, F., Amundson, J.M., O'Neel, S., Truffer, M., Fahnestock, M. & Fricker, H.A., 2012. Analysis of low-frequency seismic signals generated during a multiple-iceberg calving event at Jakobshavn Isbr, Greenland, *J. geophys. Res..,* **117**(1), 1–11.

Wendel, K., 1956. Hydrodynamic Masses and Hydrodynamic Moments of Inertia, *PhD thesis*, Hamburg, Translated in English by Labouvie, E.N. & Borden, A., Available online at http://hdl.handle.net/1721.3/51294.

Winberry, J.P., Huerta, A.D., Anandakrishnan, S., Aster, R.C., Nyblade, A.A. & Wiens, D.A., 2020. Glacial Earthquakes and Precursory Seismicity Associated With Thwaites Glacier Calving, *Geophys. Res. Lett.,* **47**(3), e2019GL086178.

Yastrebov, V.A. & Bonnet, P., 2020. SAFIM: Semi-Analytical Floating Iceberg Model, Zenodo. Software. https://doi.org/10.5281/zenodo.3583022.

Yvin, C., Leroyer, A., Visonneau, M. & Queutey, P., 2018. Added mass evaluation with a finite-volume solver for applications in fluid–structure interaction problems solved with co-simulation, *J. Fluids Struct.,* **81,** 528–546.

Zwally, J.H. *et al.*, 2011. Greenland ice sheet mass balance: distribution of increased mass loss with climate warming; 2003-07 versus 1992-2002, *J. Glaciol.,* **57**(201), 88–102.

SUPPORTING INFORMATION

Supplementary data are available at *GJI* online.

Figure animated_figure_online_S1_review.mp4
animated_figure_online_S2.mp4

Please note: Oxford University Press is not responsible for the content or functionality of any supporting materials supplied by the authors. Any queries (other than missing material) should be directed to the corresponding author for the paper.

APPENDIX A: DIMENSIONAL ANALYSIS

The Vashy–Buckingham - π theorem states that the problem can be written with $n - p$ dimensionless ratios obtained by a combination of the n characteristic variables. The integer p is the number of independent physical dimensions in the iceberg capsize system, which is 3 (time, length and mass). The characteristic variables of the system are the dimensions, H and W, the densities ρ_i and ρ_w, the water viscosity μ_w and gravity g, so $n = 6$.

The $n - p = 3$ dimensionless ratios are chosen here to be:

$$\varepsilon, \quad \frac{\rho_w}{\rho_i}, \quad \frac{\mu_w}{\rho_w H^{3/2} g^{1/2}}$$

The calculation of the horizontal force $F_x(t)$ from the $n = 6$ independent characteristic variables of the problem can be written as:

$$F_x = f(H, W, \rho_i, \rho_w, \mu_w, g)$$

The Vashy-Buckingham - π theorem states that the problem can be written as:

$$\frac{F_x}{mg} = \mathcal{G}\left(\varepsilon, \frac{\rho_w}{\rho_i}, \frac{\mu_w}{\rho_w H^{3/2} g^{1/2}}\right) \tag{A1}$$

To estimate the effect of viscosity, we compare the pressure and viscous forces. The fluid force on the surface of the iceberg calculated by ISIS-CFD is the sum of a friction-induced force (locally tangent to the fluid/solid interface) and a pressure-induced force (normal to this interface). In the case of an iceberg with aspect ratio $\varepsilon = 0.25$, the friction force is found to be $\approx$300 times smaller than the pressure force for the field-scale case ($H = 800\,\mathrm{m}$) and $\approx$10 times smaller for the laboratory case ($H = 0.103\,\mathrm{m}$) as illustrated in Fig. A1. Therefore, viscous effects can be reasonably neglected in both scales. This leads to the following approximation for eq. (A1):

$$\frac{F_x}{mg} \approx \mathcal{G}\left(\varepsilon, \frac{\rho_w}{\rho_i}\right), \tag{A2}$$

that is for similar initial conditions and boundary conditions, the evolution with time of the dimensionless force $F_x' = F_x/(mg)$ only depends on the aspect ratio ε and the density ratio ρ_w/ρ_i. However, the function f remains unknown and is investigated in Sections 2.5 and 5.5.

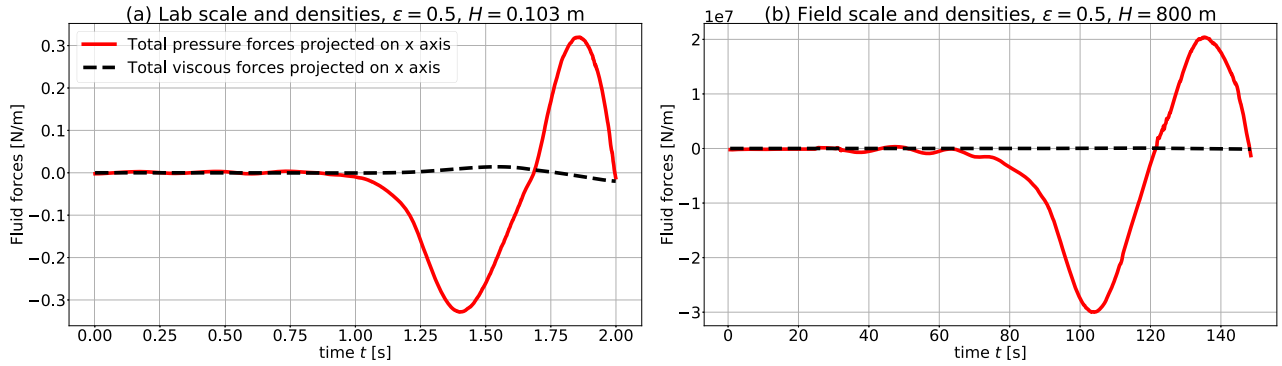

Figure A1. Viscous forces and pressure forces for (a) a laboratory-scale and (b) a field-scale iceberg capsize, computed by ISIS-CFD.

APPENDIX B: SAFIM FORCES AND TORQUES

The integrated expressions for hydrostatic and drag forces and the associated torques are given below for SAFIM and for a rectangular iceberg as in Fig. 1. All these expressions are implemented in the Python code available online at (Yastrebov & Bonnet 2020).

The effect of the hydrostatic pressure is given by the following integral: $\boldsymbol{F}_s = -\rho_w g \int_{\Gamma_s} z\boldsymbol{n}\, d\Gamma$, where $\boldsymbol{n}$ is the outward surface normal and Γ_s is the submerged part of the iceberg. The torque induced by this pressure distribution with respect to the centre of gravity G at position $\boldsymbol{r}_G$ is given by: $\boldsymbol{M}_s = -\rho_w g \int_{\Gamma_s} (\boldsymbol{r} - \boldsymbol{r}_G) \wedge \boldsymbol{n}\, d\Gamma$

The drag force is given by eq. (5), and the drag torque with respect to G by eq. (6). The calculation of the integral of the pressure drag is split into integration over all submerged or partly submerged sides of the rectangular iceberg. Consider a partly submerged side $S = AB$ and let us assume that corner A is a submerged corner and B is a corner outside the water. Then the velocity $\boldsymbol{v}_M$ of a point $M \in [AB]$ is:

$$\boldsymbol{v}_M = \boldsymbol{v}_G + \dot{\theta}\boldsymbol{e}_y \wedge (\boldsymbol{r}_M - \boldsymbol{r}_G), \tag{B1}$$

where $\boldsymbol{v}_G$ is the velocity of G, $\boldsymbol{r}_M = \boldsymbol{r}_A + \xi(\boldsymbol{r}_B - \boldsymbol{r}_A)$ with $\xi \in [0, \xi_i]$ and ξ_i defining the intersection between$[AB]$ and the water surface. Thus, for the side AB, the contribution of the drag force is given by

$$F_d^{AB} = \frac{1}{2}\alpha\rho_w \boldsymbol{n} \|\boldsymbol{r}_B - \boldsymbol{r}_A\| \int_0^{\xi_i} |v_n|^2 \mathrm{sign}(v_n)\, \mathrm{d}\xi,$$

where $v_n = \boldsymbol{v}_M \cdot \boldsymbol{n}$. For the case of a totally submerged side, $\xi_i = 1$. For the case of a side totally outside the water, the contribution to the drag force is zero.

B1 Horizontal motion of capsizing iceberg

With the formulation of the drag force given above, we can reproduce the horizontal motion of a freely capsizing iceberg, which is observed experimentally and reproduced with the accurate ISIS-CFD simulations. Obtaining a closed form solution of SAFIM equations eqs (1), (2) and (3) is out of reach. We wish to give here some intuitive explanation of the horizontal motion of the iceberg. The resultant of the buoyancy and gravity forces moves the iceberg upwards and makes it rotate: these two effects initiate the vertical and rotational motion of the iceberg. The induced velocity produces a force with a non-zero horizontal component.

We now explain why these two initial motions -upwards and rotation-, together generate a horizontal drag force, in the framework of SAFIM. We draw the velocity $\boldsymbol{v}$ (triple red arrow) of several points on the surface of the iceberg and its normal component $v_n\boldsymbol{n}$ (dashed red arrow). In SAFIM, the elementary drag force $d\boldsymbol{F}_d$ (solid black arrow) is collinear with $\boldsymbol{n}$ and opposes the normal velocity $v_n\boldsymbol{n}$. The projection of the elementary drag forces on the horizontal axis $d\boldsymbol{F}_{d_x} = (d\boldsymbol{F}_d \cdot \boldsymbol{e}_x)\boldsymbol{e}_x$ is shown by a dashed green arrow if it is leftward and dashed blue arrow if it is rightward. The integral of these horizontal elemental forces results in the global horizontal force $\boldsymbol{F}_d \cdot \boldsymbol{e}_x$.

For the case of upward motion Fig. B1(a), the vertical local velocity is constant along the iceberg surface. The horizontal drag force on the two long sides of the iceberg is leftward whereas on the submerged side CD, it is rightward with a smaller amplitude. The iceberg thus moves to the left.

For the case of rotational motion around G, with no motion of G (Fig. B1b), the velocity increases with the distance to the centre of rotation. The further away the point is, the more it contributes to the drag force. Two points located at the same distance from G, but with opposite normal velocity $v_n\boldsymbol{n}$ (i.e. one point on the blue line and one point on the green line) have the same absolute contribution to the drag force but in opposite directions. Thus the drag force on the part of the surface coloured by solid green lines compensates the drag force on the part coloured blue. The remaining part of the surface coloured by dashed green lines at the iceberg bottom, induces a leftward total horizontal force. Therefore, by superposing vertical and rotation motion, we obtain a net drag force in the direction of the initial tilt of the iceberg, here to the left.

B2 Simplified added-masses

The calculation of the simplified added-masses given in eqs (7) and (8), requires the calculation of the effective height H_{eff} and effective width W_{eff} of the submarine part of the iceberg (see Fig. 1). To calculate them, we use the positions of the four corners: C, D, E, F (Fig. B1). The coordinates of a corner $P \in \{C, D, E, F\}$ have the general expression:

$$x_P = x_G + \delta_1^P \frac{H}{2}\sin(\theta) + \delta_2^P \frac{L}{2}\cos(\theta)$$
$$z_P = z_G + \delta_3^P \frac{H}{2}\cos(\theta) + \delta_4^P \frac{L}{2}\sin(\theta)$$

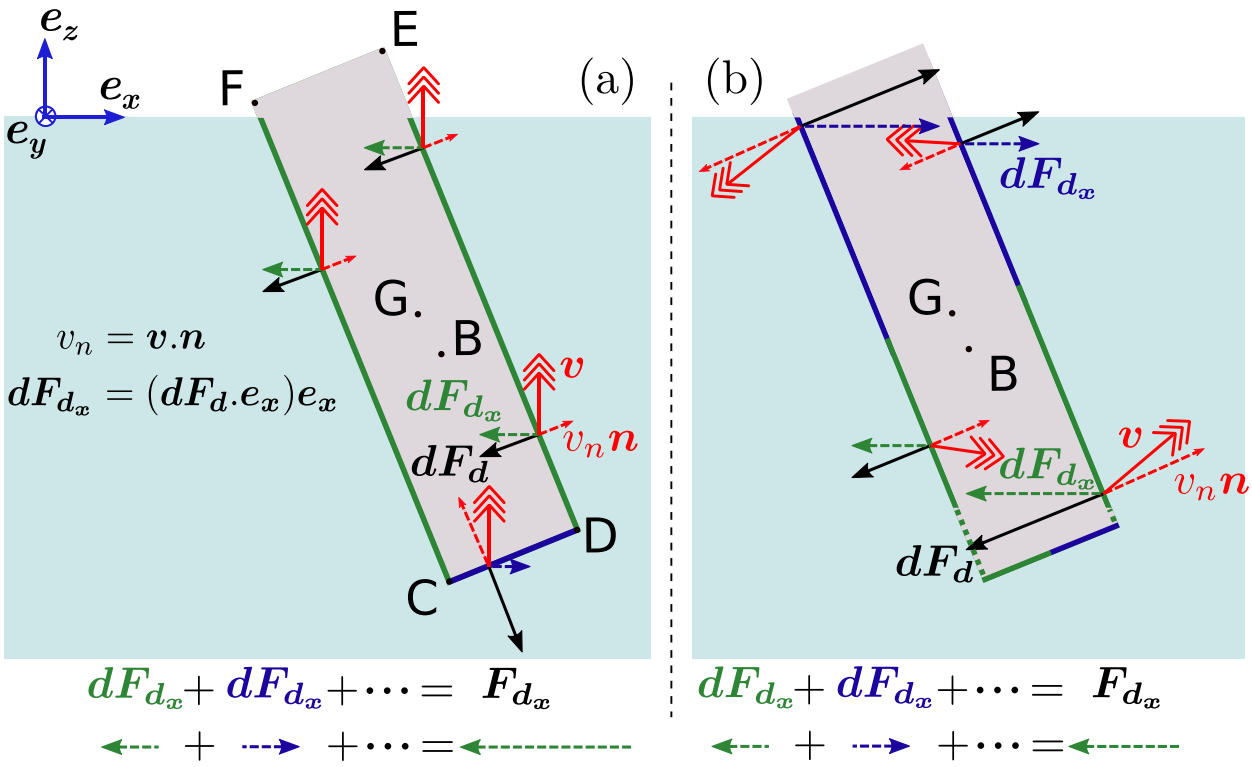

Figure B1. Schematic explanation of the horizontal force induced by the formulation of the drag force in SAFIM for (a) a vertical upward motion of the iceberg, and (b) a rotation of the iceberg.

with $(\delta_1^P, \delta_2^P, \delta_3^P, \delta_4^P)$ defined as follows for the four corners

$$\{\delta_1^C, \delta_2^C, \delta_3^C, \delta_4^C\} = \{1, -1, -1, -1\},$$
$$\{\delta_1^D, \delta_2^D, \delta_3^D, \delta_4^D\} = \{1, 1, -1, 1\},$$
$$\{\delta_1^E, \delta_2^E, \delta_3^E, \delta_4^E\} = \{-1, 1, 1, 1\},$$
$$\{\delta_1^F, \delta_2^F, \delta_3^F, \delta_4^F\} = \{-1, -1, 1, -1\}.$$

The effective height can be calculated with the following expressions:

$$H_{\text{eff}} = \max\left((z_w - z_C);\ (z_w - z_D);\ (z_w - z_E);\ (z_w - z_F)\right)$$

where z_w is the water level.

The effective width, defined as the distance between the leftmost and the rightmost points of the submerged part of the iceberg, is calculated similarly, but after checking which are the submerged corners and the geometrical intersection between the water surface and the iceberg sides.

APPENDIX C: OPTIMAL PARAMETERS

We summarize in Table C1 the errors of SAFIM computed with respect to the ISIS-CFD results for a quadratic drag model and the three options for added-masses (no added-masses, simplified or computed added-masses). These errors correspond to the minimal possible errors obtained by the minimization procedure. The step used for the drag coefficient α was 0.05 and the step for the added-masses factors was 0.25.

APPENDIX D: COMPARISON OF SAFIM WITH MODEL IN SERGEANT *ET AL.* (2018, 2019)

We compare SAFIM model with optimised α-factor, SAFIM model with $\alpha = 1$ (as used in Sergeant *et al.* (2018, 2019)) and ISIS-CFD in Fig. D1. The optimisation of the drag coefficient α improves the horizontal force F_x' and torque M_θ', in particular for the three biggest aspect ratios (Figs D1c–h).

Table C1. First two columns: geometrical characteristics and initial conditions of the studied icebergs. Laboratory-scale iceberg simulations have height $H = 0.1$ m and field-scale iceberg simulations have height $H = 800$ m. The density of the water is $\rho_w = 1025$ kg m^{-3} and the density of the ice is $\rho_i = 917$ kg^{-3}. Next columns: parameters minimizing the error on F_x and the corresponding error for SAFIM without added-masses, SAFIM with computed added-masses and SAFIM with simplified added-masses.

		No AM		Computed *AM*		Simplified *AM*				
ε	θ_0 [°]	Error E_1	α	Error E_2	α	Error E_2	α	C_x	C_z	C_I
0.246	0.5	5.2%	0.85	36.6%	3	10.0%	1.1	0.	0.	0.75
0.374	0.5	9.6%	1.55	34.1%	1.8	21.3%	1.4	0.	0.	0.75
0.496	0.5	20.1%	2.9	40.0%	1.9	23.0%	3.0	0.	0.	0.5
0.639	15	24.7%	4.0	47.4%	2.6	26.2%	4.2	0.	0.	0.25

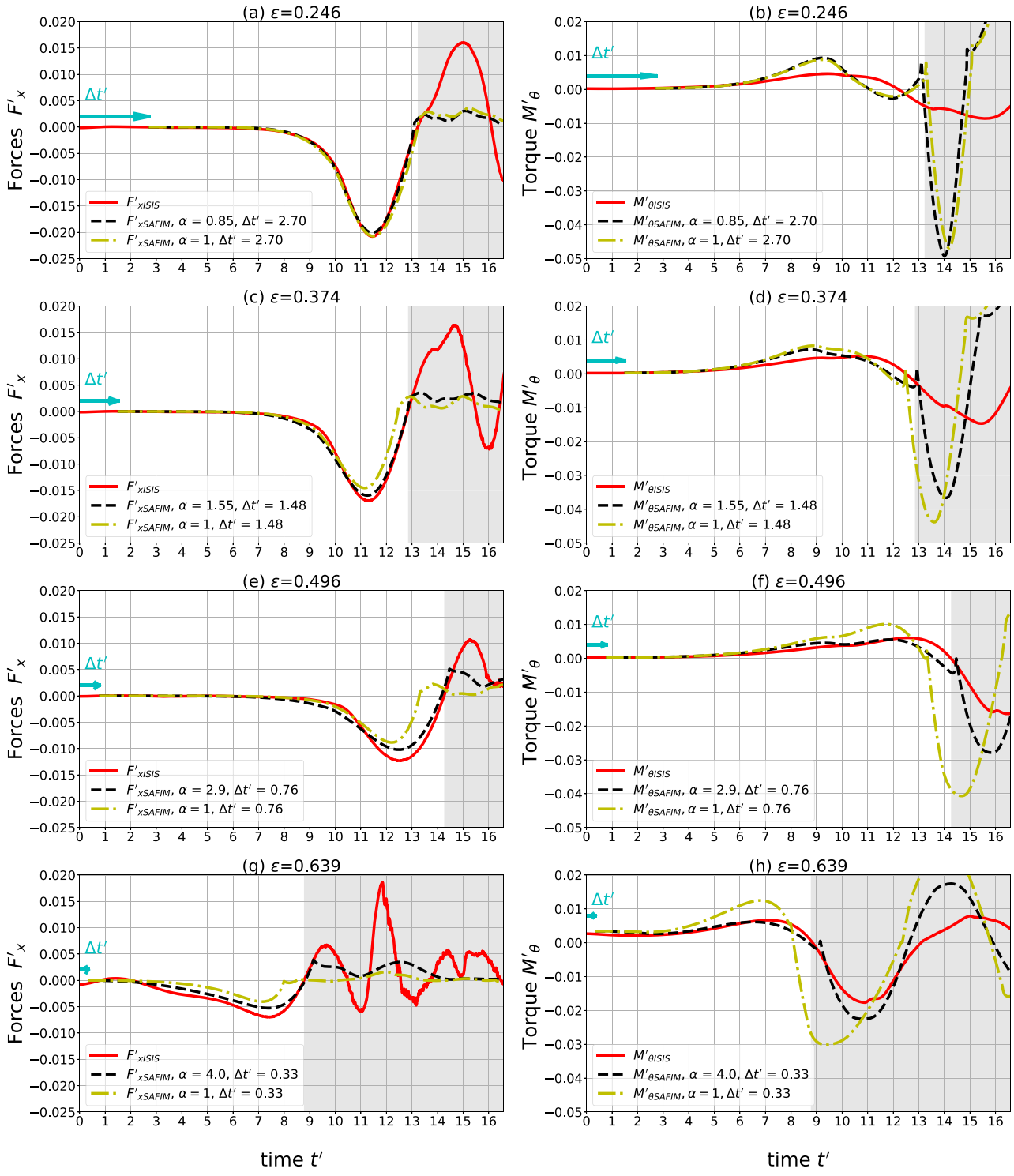

Figure D1. Capsize simulations for SAFIM with optimized drag without added-masses and with time shifts (black lines), for SAFIM with drag coefficient $\alpha = 1$ without added-masses and with time shifts (yellow lines), and for ISIS-CFD (red lines): evolution of the dimensionless total horizontal force F'_x on the iceberg (a, c, d, e), and torque M'_θ (b, d, f, g). Results are given for icebergs with $\varepsilon = 0.246$ (a, b), $\varepsilon = 0.374$ (c, d), $\varepsilon = 0.496$ (e, f) and $\varepsilon = 0.639$ (g, h). SAFIM curves were shifted (blue arrow) by the dimensionless time $\Delta t' = \Delta t \sqrt{g/H}$. The SAFIM α-factor and time $\Delta t'$ are indicated in the legends.

2.11 Complements on hydrodynamic pressure on the sea floor

Sergeant et al., 2018, 2019 showed that the seismic signal emitted during capsize contains precious information on the iceberg capsize, in particular the iceberg volume. This work showed that the source of the seismic waves is consistent with the modelled contact force between the capsizing iceberg and the glacier terminus. This was also supported by the fact that the volume of the inverted iceberg (by comparison between the inverted seismic source and the modelled force) was consistent with the estimation of the volume made using available pictures (for a well documented event). However, other dynamic interactions between the ocean / ice-mélange / iceberg / glacier / sea floor / bedrock may produce seismic waves during capsize (e.g. Tsai et al., 2015; Sergeant et al., 2016; Podolskiy and Walter, 2016).

In order to extract physical information from the seismic waves, it is crucial to investigate the various possible sources of seismic waves. Here, we analyse the source force due to the pressure forces on the sea floor, calculated with the ISIS-CFD software.

Using seismic stations located at less than 2 km from the terminus front, Bartholomaus et al. (2012) have recorded seismic signals emitted during the calving of small icebergs falling into the water. The seismic signals have a typical duration of $5-2$ s and have maximum amplitudes in the $0.5-5$ Hz frequency range. The authors interpret the seismic signals as being emitted by the interaction between the falling icebergs and the sea-surface. The authors support this hypothesis by the fact that such phenomenon is similar to a cavitation process which can generate seismic waves in other geophysical fields (e.g. Chouet et al., 1997). In the field of ambient noise seismology, the following source mechanisms have been proposed: the interactions of ocean waves with a continental slope (primary microseisms) and ocean wave-wave interactions (secondary microseisms). These mechanism produce pressure forces on the sea floor that generate seismic waves (e.g. Longuet-Higgins, 1950; Hasselmann, 1963; Ardhuin et al., 2011, 2015). Similarly, we make the hypothesis that the pressure forces exerted on the sea floor below a capsizing iceberg may be the source of seismic waves. In order to separate the source of the seismic signals, it is crucial to investigate if this seismic signal emitted by the pressure variations on the floor has a negligible amplitude or has different characteristics (in location, component, start time, duration, frequency range) compared to the signal emitted by the iceberg-glacier contact force. The typical frequency band where glacial earthquakes have been observed is $\approx 0.01-0.2$Hz that is $\approx 5-100$s (Ekström et al., 2003; Ekström, 2006; Walter et al., 2012; Sergeant et al., 2016). As a first step in this study, we investigate the variations in time of the pressure on a horizontal sea floor below a capsizing iceberg in the open ocean for a field scale capsize.

The geometry of the simulation is that of a typical field scale event (Murray et al., 2015a): the iceberg height is $H = 790$ cm and aspect ratio $\varepsilon = 0.23$, with ice density $\rho_i = 917$ kg/m^3, water density $\rho_w = 1025$ kg/m^3 and a water depth at rest $H_{depth} = 1.5$ km. The limits of the domain in the horizontal direction are set to ± 15.8 km on all sides of the iceberg's initial position (at $x = 0$ m), with damping conditions to avoid reflexions.

The total local pressure on the sea floor $p_{tot}(t)$ is:

$$p_{tot}(x,t) = p_{sta} + p_{dyn}(x,t) \tag{2.1}$$

with $p_{sta} = \rho_w g z$ the hydrostatic pressure at rest (horizontal sea level) and at the water depth z, and $p_{dyn}(x,t)$ the hydrodynamic pressure, that is the perturbation of the pressure around the hydrostatic pressure due to the fluid motion and the oscillations in the water level. The hydrostatic pressure at rest at the bottom of the tank is $p_{sta}(0) = 1.9\ 10^7$N/m^2 here.

We plot the local dynamic pressure $p_{dyn}(t)$ in Fig. 2.1 for time $t = 21$ s to time $t = 221$ s and in Fig. 2.2 for time $t = 231$ s to time $t = 431$ s. We show one figure every 10 s to see the *slowly* evolving patterns (we show the variations with a time step of 2s in Fig. 2.3 a). The colors change from yellow to red to black with time. The black horizontal line represents the sea floor, the cyan horizontal line is the sea level, and the black rectangle is the position of the iceberg during the capsize.

We observe that, until time $t \approx 271$ s, the pressure on the sea floor increases and the maximum amplitude is located approximately below the iceberg. Then the amplitude decreases and the location of the maximum of amplitude of the pressure shifts in the direction of displacement of the iceberg (towards the left here). During the whole simulation, we calculated that the highest value of the hydrodynamic pressure p_{dyn} is a negative pressure of 1.02 10^4N/m^2 at time $t =\approx 271$ s and at $x = 158$ m.

In Fig. 2.3 (a) we plot the values of the pressure on the sea floor at $x = 0$ m (at the vertical below the center of gravity of the iceberg initially), and at $x = \pm 1000$ m, $x = \pm 5000$ m and $x = \pm 10000$ m. We observe that the pressure is higher below the iceberg ($x = 0$ m) until time $t \approx 300$ s. Then the pressure is higher further away (at $x \approx -1000$ m until time $t \approx 355$ s) and then it is higher even further (at $x \approx -5000$ m). This is consistent with the observations on Fig. 2.1 and Fig.2.2. The curves of the variation of pressure below the iceberg (at $x = 0$ and $x \pm 1000$ m) are noisy. Numerically, such calculation is challenging because of the proximity of the iceberg to the floor (due to the overlapping of the refined mesh around the iceberg and floor).

In Fig. 2.3 (b), we plot the force on the sea floor, $F_z(t) = \int p_{dyn}(x,t)dx$. This integration is done on the total sea floor which extends over a length of 31.6 km centred on the initial position on the iceberg (black curve on Fig. 2.3 b). This is a force in N/m since it is not integrated in the third dimension. This force has an amplitude lower than 0.4 10^7 N/m during the capsize of the iceberg ($0^o < \theta < 90^o$). In the context of the generation of seismic waves, it is interesting to compare the amplitude of the pressure force on the sea floor to the amplitude of the horizontal contact force of the iceberg on the glacier front. For an iceberg with the current geometry, the contact force has an amplitude of 3.3 10^7 N/m and lasts for $t \approx 200$ s (Bonnet et al., 2020). Therefore the amplitude of the force on the sea floor is about 10% of the amplitude of the contact force. This simulation is done in open ocean, so there is no contact force in this case. However, we can expect that the hydrodynamic forces acting on the iceberg during capsize are of the same order of magnitude than the forces acting on an iceberg in contact with a glacier. We show the horizontal hydrodynamic force $F_x^{iceberg}$ (purple curve in Fig. 2.3 b) and vertical hydrodynamic force $F_z^{iceberg}$ (green curve in Fig. 2.3 b) acting on the iceberg during the capsize in free ocean. The aim is here to qualitatively compare the amplitude, duration and period of these forces to that on the sea floor. The force on the seafloor is < 10 % of the amplitude of the force during capsize, that is when the iceberg inclination is $\theta < 90^o$, (yellow curve on the y-axis on the right). In the case of capsize in contact with the terminus front, this corresponds approximately to the time when there is a contact between an iceberg and the glacier front. However, after the capsize ($\theta < 90^o$), the amplitude of the force on the seafloor is comparable to the force acting on the iceberg.

The force on the sea floor is a vertical force. Tsai and Ekström (2007); Sergeant et al. (2016) observed that the source force inverted from the seismic signal has a vertical component with an amplitude typically $< 20\%$ of the amplitude of the horizontal component. Part of this vertical component can be explained by the friction between the glacier front and the capsizing iceberg (Sergeant et al., 2018), or by a vertical motion of the glacier tongue (Murray et al., 2015a) due to a drop of hydrodynamic pressure below the glacier tongue during a bottom-out capsize. Our results suggest that the pressure force on the sea floor can also explain part of the observed vertical component of the force inverted from the seismic signals, in particular towards the end of the capsize and after the capsize.

We also show in Fig. 2.3 (b), the force on the part of the sea floor on the left $15.8 < x < 0$ km and the part

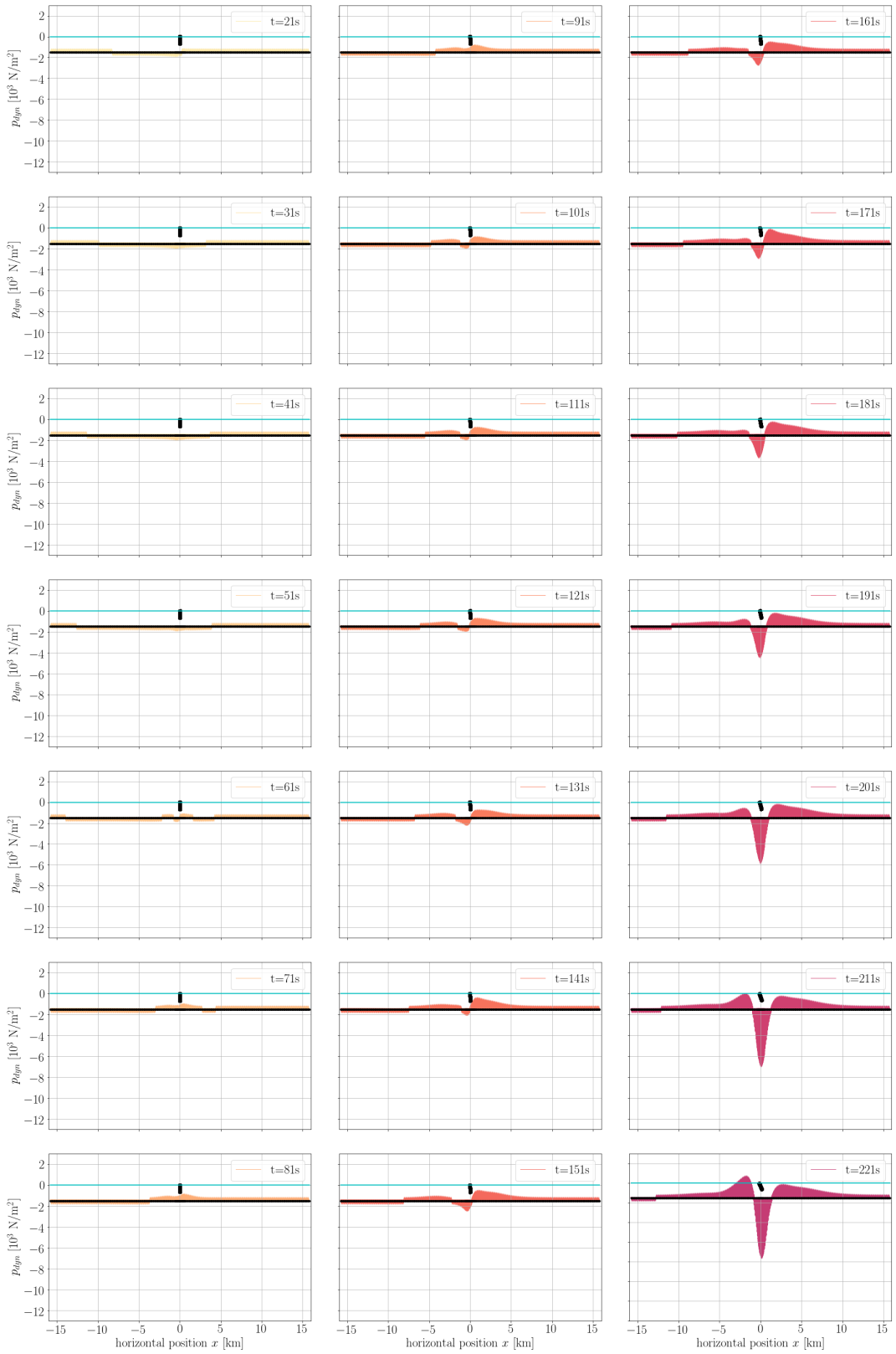

Figure 2.1: Pressure distribution p_{dyn} on the sea floor below a field scale capsizing iceberg from time 21 s to 211 s, every 10 s. The position of the seafloor and the iceberg are shown in black. The sea level at equilibrium is shown with the cyan horizontal line.

on the right $0 < x < 15.8$ km. We can expect similarities in the water motion on the sea floor between the current simulation in open ocean and a simulation with a glacier tongue. However, it would be speculative to say that the

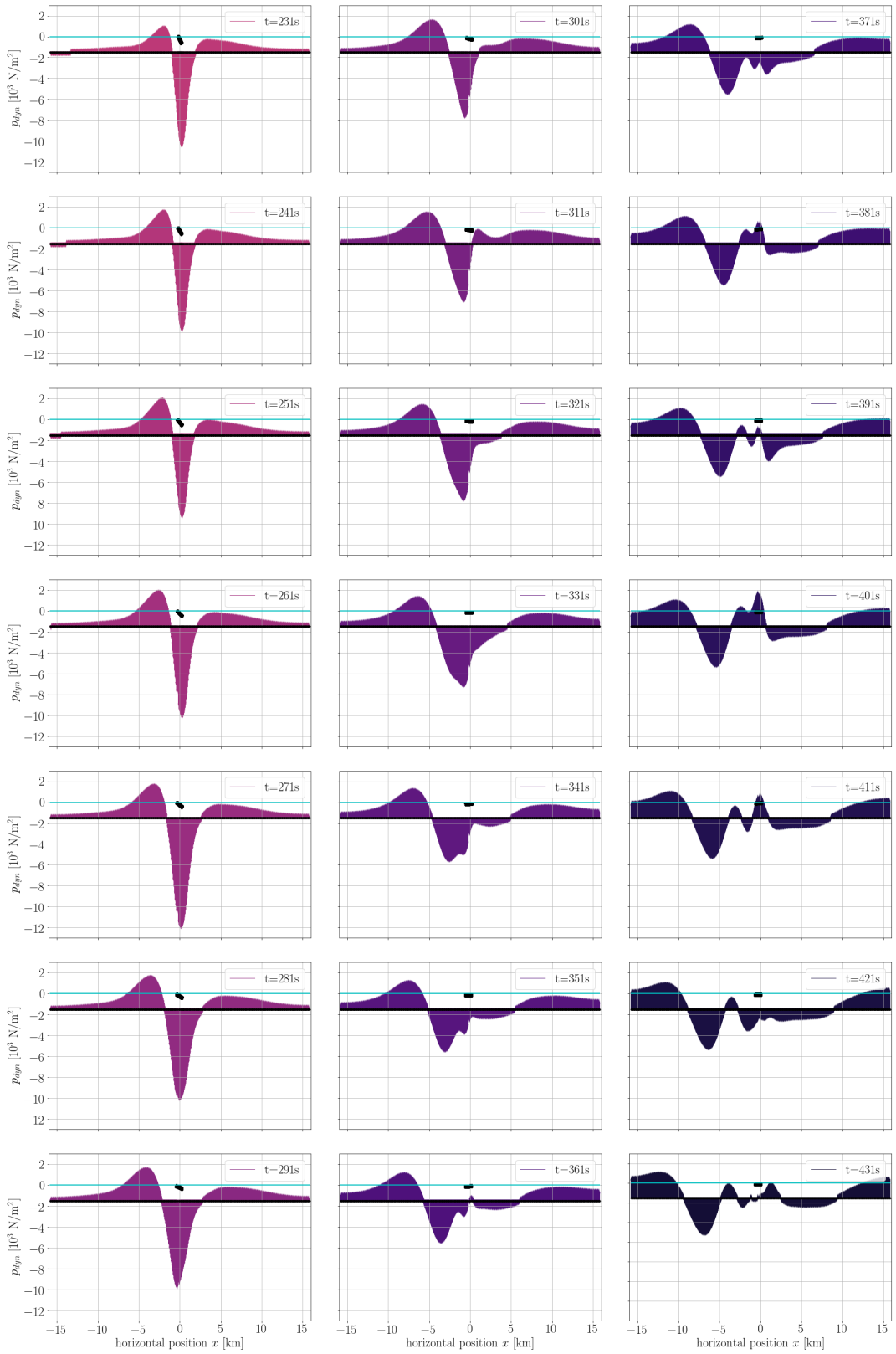

Figure 2.2: Same as Fig 2.1 from time 213 s to 431 s.

pressure field on the sea floor is unchanged between a simulation in open ocean and a simulation with a glacier tongue. Nevertheless, with such a hypothesis, we investigate the possible implications our results in the open ocean would have on simulations with a glacier tongue.

In the current simulation, the iceberg rotates anti-clockwise. Therefore, in the case of a top-out capsize, the glacier would be located on the right side of the iceberg, and in the case of a bottom-out capsize, the glacier would be located on the left side of the iceberg. Thus the integrated force on the part of the sea floor on the left $x < 0$ gives an estimate of the pressure field below the glacier for a bottom-out capsize (red curve on Fig. 2.3 b), and on the right $0 < x$ of a top-out capsize (cyan curve on Fig. 2.3 b). At the beginning of the simulation $t < 200$ s, the pressure on the left is negligible compared to that on the right (cyan curve on Fig. 2.3 b). After the end of the capsize when $t > 200$ s, the amplitude on each part increases and decreases alternatively with a period of ≈ 80s (see change of the signs at $t = 220$s, $t = 300$s, $t = 380$s). This suggests that the variations in time of the generated pressure field below the glacier tongue during the capsize is sensitive to the type of capsize, with a higher pressure on the sea floor (thus maybe on the glacier tongue) during a bottom-out capsize compared to a top-out capsize.

In Fig. 2.3 (c) we show the same forces filtered in between 0.01 and 0.1 Hz, which suggests the negligible impact of the force on the seafloor compared to the hydrodynamic forces within the bandwidth during capsize. However for lower frequencies the pressure on the sea floor becomes preponderant on the forces on the iceberg.

In future work, it would interesting to extend this study to a more realistic geometry: an iceberg capsizing close to the glacier tongue, with a sea floor with more realistic bathymetry. Such changes are expected to affect the hydrodynamic effects and the pressure on the sea floor, however it is difficult to guess how much. Moreover, in the case where this pressure on the seafloor is significative (e.g. at low frequencies, and for sea floor at a lower depth), it would be interesting to assess what type of seismic waves are generated by such an extended pressure on the sea floor to help with the interpretation of measured seismic signals (using models in the literature such as the spectral elements method).

2.12 Complements on hydrodynamic pressure on the iceberg

In Bonnet et al. (2020) we suggested that the spatial variation of the hydrodynamic pressure on the surface of the iceberg is closely linked with the formation of vortices in the fluid (based on results of the ISIS-CFD solver). From this we concluded the difficulty to calculate the local pressure forces without modelling the whole fluid motion. When not modelling the whole fluid motion, the strategy is to give a parametrized fluid force.

As explained in Bonnet et al. (2020), there are two different types of parametrised laws that allow to reproduce the total hydrodynamic forces and that are widely used: the drag forces and moments (proportional to a power of the local velocities) and the added-mass forces and moments (proportional to the local accelerations). The parametrised drag law given in Bonnet et al. (2020) is based on the integration of a local drag pressure as a function of the normal velocity. To investigate the validity of this local drag, we compare the local pressure at the surface of the iceberg computed by ISIS-CFD, and the normal local velocity at the surface of the iceberg. Although this pressure is linked to complex vortices Bonnet et al. (2020)[Fig. 5], we investigate whether there is a local drag effect or added-mass effect that may describe this pressure field. ISIS-CFD is able to compute the hydrodynamic pressure due to the local added-mass effect. This local pressure due to the added-mass effect was initially implemented in ISIS-CFD for stabilising the numerical resolution (Yvin et al., 2018), as explained in Bonnet et al. (2020)(section 2.2).

Therefore, we propose to separate the local pressure p_{dyn} into two contributions: the contribution from the added-mass effect p_{am} and the contribution from other effects $p_{dyn} - p_{am}$. To investigate whether these other effects are well described by a local drag, we compare the local velocity field with the field $p_{dyn} - p_{am}$ (the total local pressure minus the local pressure due to added-mass effects).

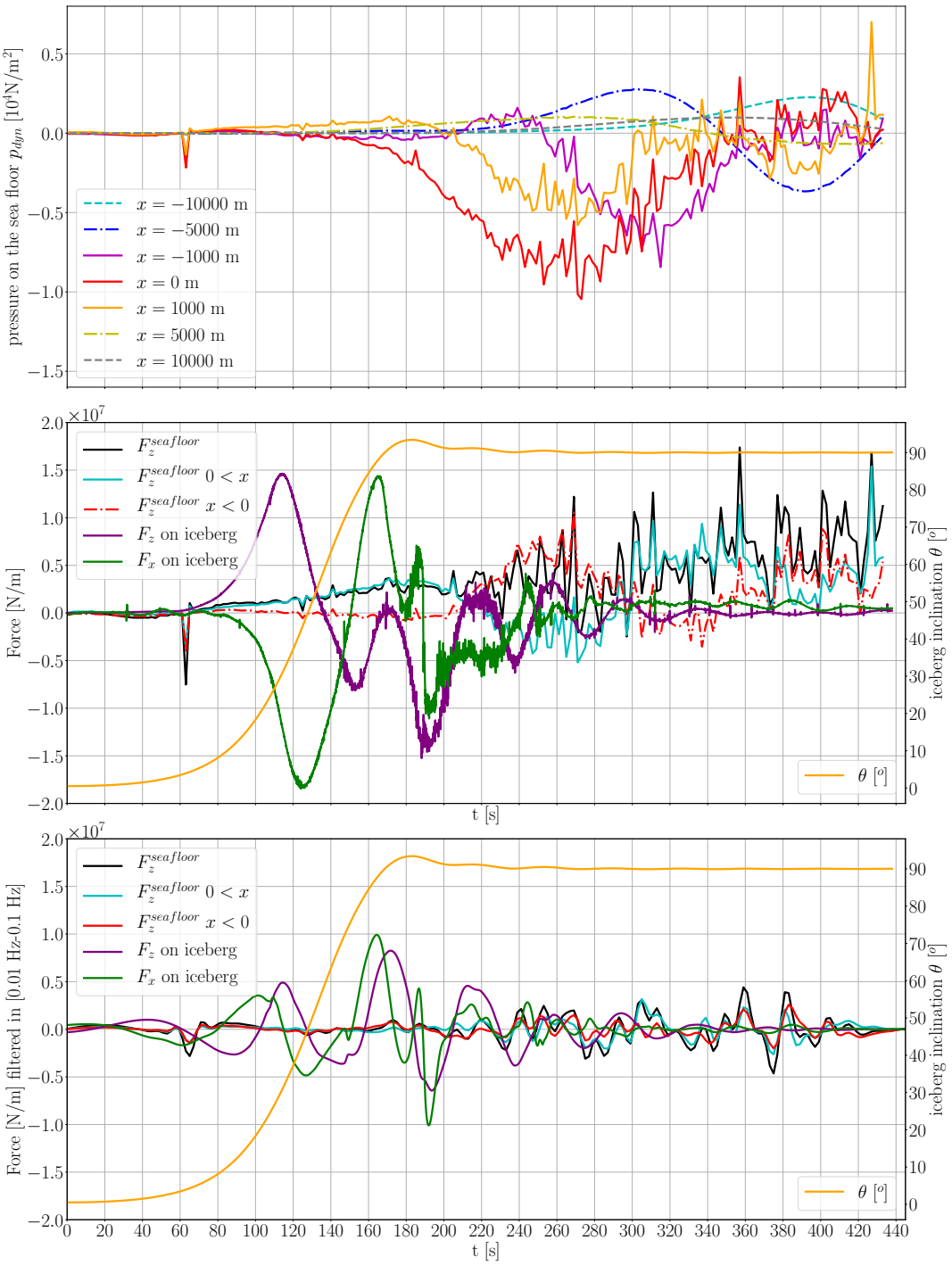

Figure 2.3: Hydrodynamic Pressure at seven locations on the sea floor (a), total force on the sea floor (black curve), force on the part of the sea floor on the left ($x < 0$ cyan curve) and on the right ($x > 0$ red curve), vertical hydrodynamic forces on the iceberg (purple curve) and horizontal hydrodynamic forces on the iceberg (green curve) non filtered (b), and filtered in [0.01-0.1] Hz (c) during the capsize of a field scale iceberg. The angle of inclination of the iceberg θ during capsize is shown in orange (on the y-axis on the right) in (b) and (c)

We show the results for a laboratory scale iceberg (as used in Bonnet et al., 2020), of height $H = 10.3$ cm, and aspect ratio $\varepsilon = 0.25$. We select various times during the capsize.

First we discuss the difference between the total dynamic pressure p_{dyn} and the local dynamic pressure minus the local added-mass pressure $p_{dyn} - p_{am}$, then we compare these pressures with a local quadratic drag and a local linear drag. The aim here is to qualitatively assess whether there is a correlation between the pressures p_{dyn} or

$p_{dyn} - p_{am}$ and the drag.

For an iceberg of aspect ratio $\varepsilon = 0.25$, we plot the hydrodynamic pressure p_{dyn} (gray curve), the local dynamic pressure minus the local added-mass pressure $p_{dyn} - p_{am}$ (blue curve), and the local quadratic drag $-1/2\rho_w|v_n|v_n$ (in cyan, red, yellow and magenta for each of the four sides of the iceberg) in Fig. 2.6 during the capsize (time and angle of inclination of the iceberg are indicated in the title). The x-axis is the position along the surface of the iceberg, $\beta[^o]$ as defined in Fig. 2.5. In Fig. 2.4 for each of these times, we show the position of the iceberg. We plot the sides of the iceberg in cyan, red, yellow and magenta as in Fig. 2.6.

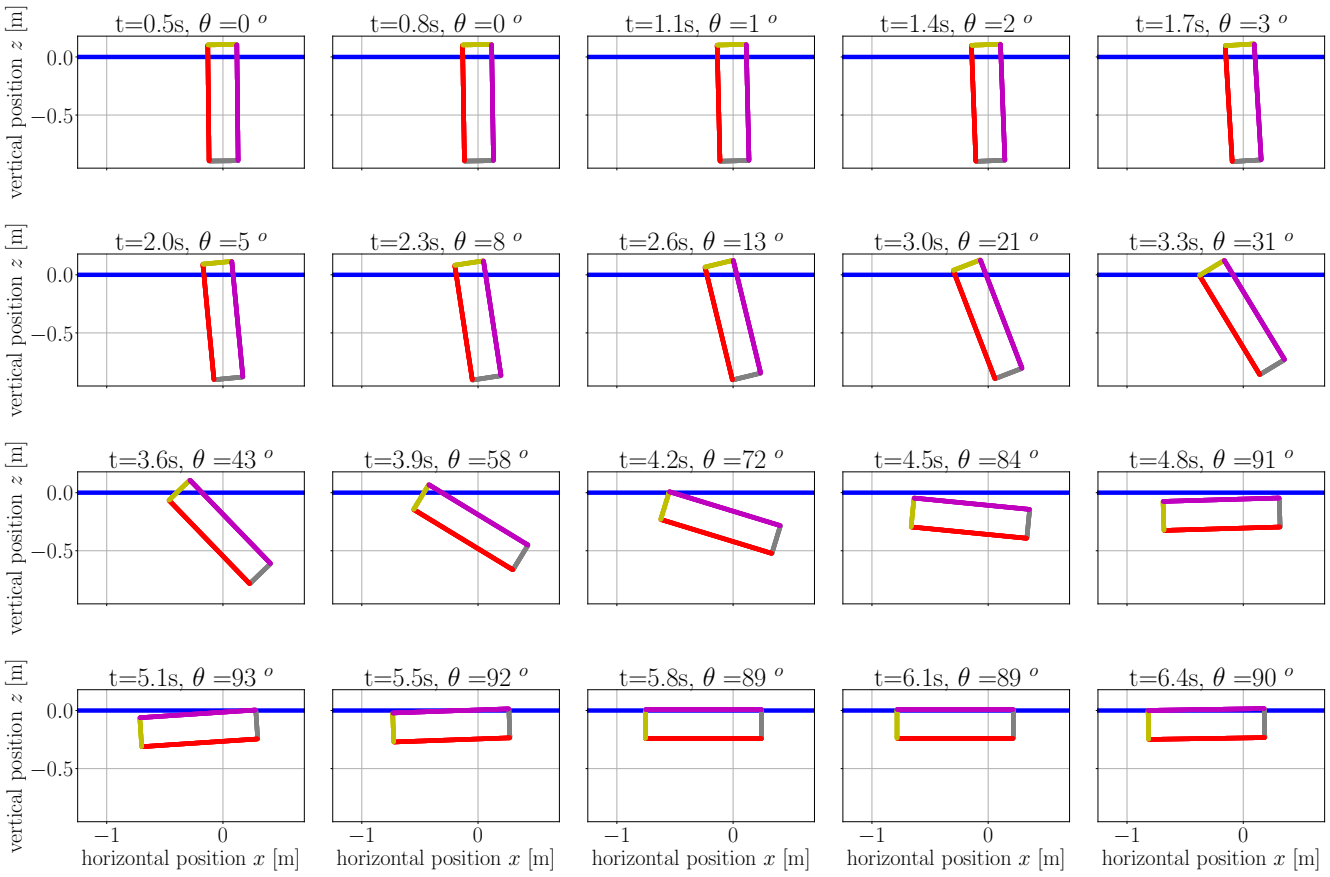

Figure 2.4: Iceberg position at the snapshots showed in Figs. 2.6 and 2.7.

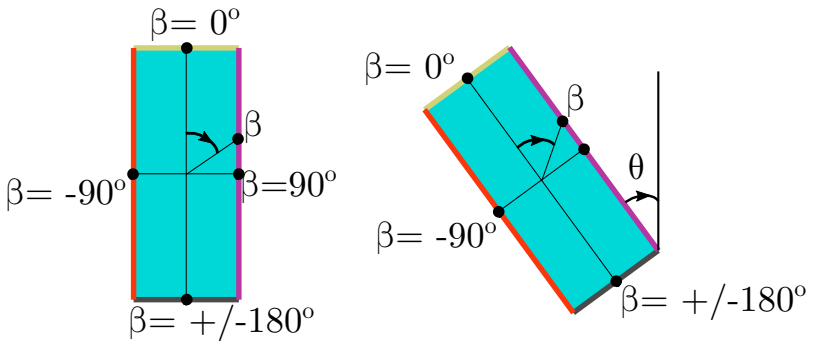

Figure 2.5: Definition of the angular position along the surface of the iceberg β.

We observe that p_{dyn} and $p_{dyn} - p_{am}$ are similar between time $t = 3.3$ s (angle of inclination $\theta = 31°$) and time $t = 4.5$ s (angle of inclination $\theta = 31°$). As explained in Bonnet et al. (2020), this is the part of the capsize that

we aim to reproduce (in the context of iceberg capsizing against a glacier front). However, at the beginning of the capsize ($t < 3.3$ s) p_{dyn} and $p_{dyn} - p_{am}$ differ significatively, thus the local added-mass effect is significative, in particular in the upper and lower parts of the iceberg ($\beta \approx 0°$ and $\beta \approx \pm 180$). This is consistent with the discussion in Bonnet et al. (2020)(section 5.2) on the importance of the added-mass effect in the duration of the initiation of the capsize.

We observe that the local quadratic drag $-1/2\rho_w|v_n|v_n$ is much smaller than the pressures p_{dyn} and $p_{dyn} - p_{am}$. Here, we fixed the drag coefficient to $\alpha = 1$. With $\alpha = 0.85$ which is the optimized value calculated in Bonnet et al. (2020) for $\epsilon = 0.25$, it is even smaller. A much higher value of the drag coefficient $\alpha = 5$ allows to reproduce similar amplitudes of the local pressure. However, such a law allows a correct overall representation of the hydrodynamic forces. We investigate whether, locally a linear drag would match better the hydrodynamic pressure. We show the linear drag $-1/2\rho_w v_n$ on a similar plot (Fig. 2.7). We now observe a good correlation between the local linear drag on the long sides of the iceberg (red and magenta curves), and the pressure p_{dyn} (in cyan). Again, we did not add a multiplication factor (drag coefficient α). However, the total force integrated from a local linear drag does not fit the reference force (according to the study we did to minimize the error on this force). Such observations suggest that it is not possible to reproduce the local hydrodynamic forces using a quadratic or linear local drag formulation. Nevertheless, the integration of the local quadratic drag forces on the surface of the iceberg fits the reference hydrodynamic forces on the iceberg (as shown in Bonnet et al., 2020) with one single drag coefficient α for the horizontal and vertical forces and the torque.

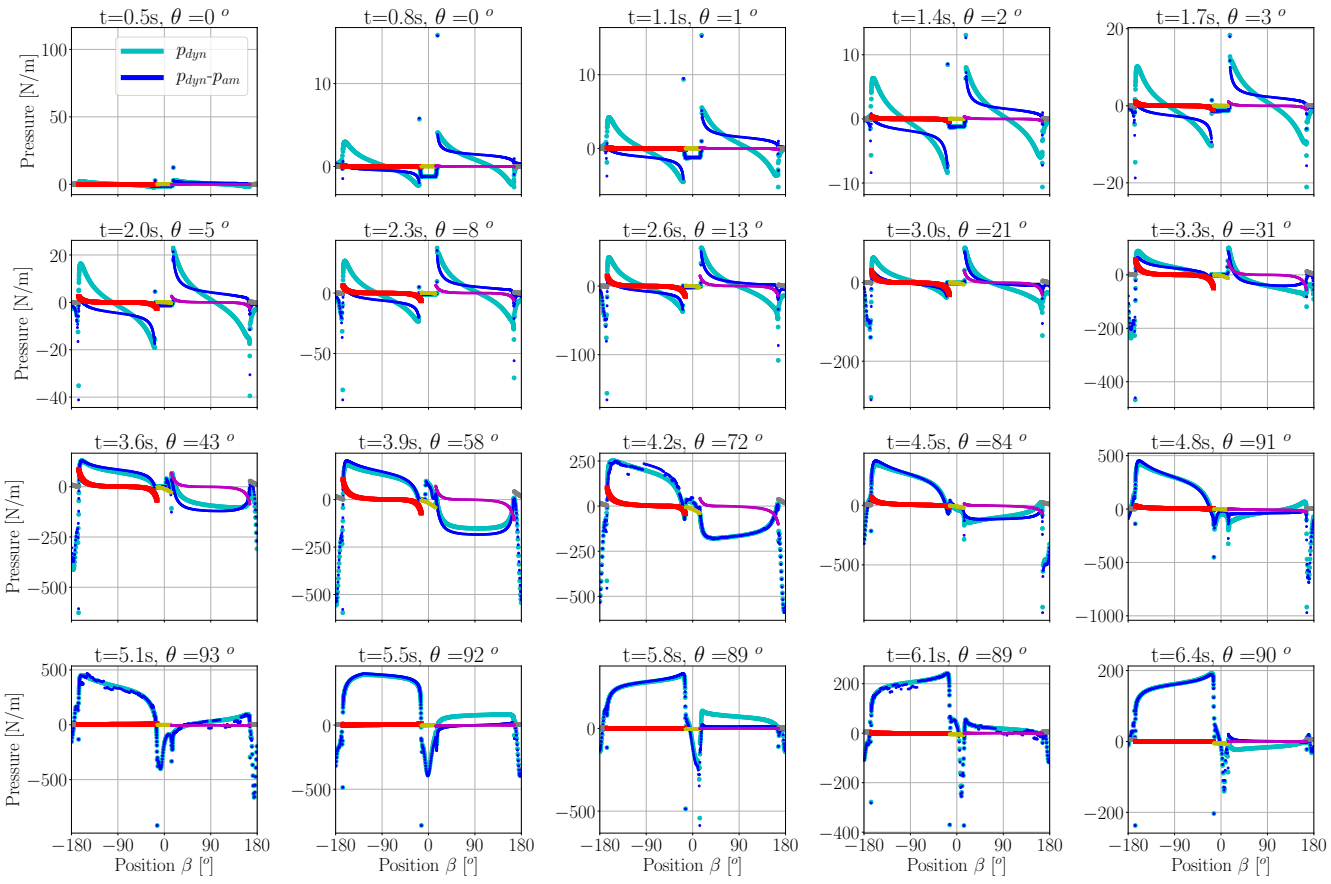

Figure 2.6: Local dynamic pressure p_{dyn} (cyan) and local dynamic pressure minus the local added-mass pressure $p_{dyn} - p_{am}$ (blue) and local drag force $-1/2\rho_w|v_n|v_n$ (in gray, red, yellow and magenta), along the surface of the iceberg (x-axis). The position along the surface of the iceberg is given by the angular position of this point, increase clockwise, and such that angular position 0° corresponds to the middle of the yellow side of the iceberg (that is initially horizontal and above sea level). To help with the visualisation, the curve $-1/2\rho_w abs(v_n)v_n$ is shown in four different colors for each side of the iceberg. The position of the iceberg at each time is shown in Fig 2.4

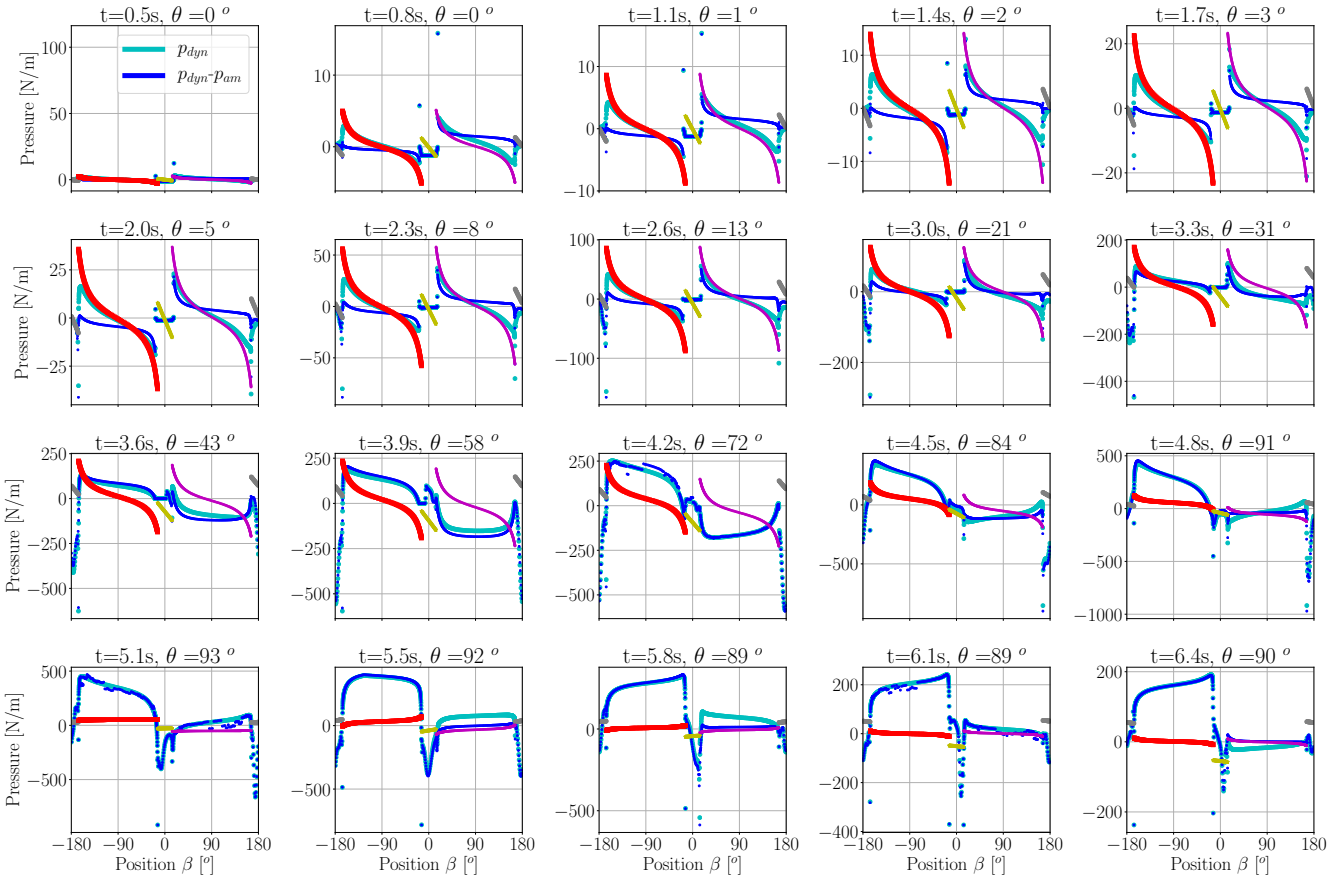

Figure 2.7: Same as in Fig 2.6 but with $-1/2\rho_w v_n$ instead of $-1/2\rho_w abs(v_n)v_n$

CHAPTER 3

Semi-analytical model for an iceberg capsizing against a glacier

3.1 Introduction

The dynamics of an iceberg capsizing close to a glacier terminus, is governed by the hydrodynamic forces (Chapter 2) but also by the contact force with the glacier front.

In the literature, one of the first attempts to model iceberg capsize was done by MacAyeal and Scambos (2003). The authors analysed how one iceberg capsize can trigger a chain of capsize leading to the break-up of a whole ice shelf such as the Larsen B in Antarctica. As a first approximation, they assumed that the capsize of an iceberg between two tabular icebergs is quasi-static. Later Burton et al. (2012) modelled the capsize of an iceberg in open ocean and ran laboratory experiments that show the importance of hydrodynamics (see Chapter 2). Burton et al. (2013) extend the laboratory experiments to multiple adjacent capsizing icebergs with a quasi-static energetic analysis. (Tsai et al., 2008) propose a model with rigid iceberg capsizing against a rigid and static terminus, and with a horizontal contact force, that is no friction between the terminus front and the iceberg. The motion of the iceberg is governed by the Newton's second law with adjustable added-masses on the horizontal axis accounting for the resistance of the water and the ice-mélange, and an added-inertia. Amundson et al. (2012) also modelled a rigid iceberg capsizing against a rigid static wall, with a horizontal contact force. The authors do not take into account added-masses but the drag forces with one coefficient per degree of freedom (horizontal displacements, vertical displacements, and inclination angle). Murray et al. (2015a) conducted laboratory experiments with plastic icebergs against a rigid wall. Using force measurements on the wall during the capsize of the laboratory iceberg and field measurements of the glacier surface displacements, and assuming that the response of the glacier is purely elastic with a Young's modulus of $E = 1$ GPa, the authors were able to estimate the length of the glacier tongue of the Helheim glacier on DOY 212 in 2013: $L \approx 4.9$ km.

In the literature, the Young's modulus of ice was estimated through laboratory experiments with extension or compression of ice samples, or with seismic velocity measurements. These experiments yield values of the Young's modulus of ice ranging from $E \approx 3$ GPa to $E \approx 10$ GPa (e.g. Langleben, 1962; Rist et al., 1996). The value of the Young's modulus has been estimated for the floating tongues of tide water glaciers using measurements of surface displacements (and the glacier geometry) and mechanical models of the tidal ice shelf flexure. Depending on the simplifying assumption in the mechanical models, the Young's modulus is an *effective* value that incorporates various physical phenomenon such as the ice viscosity, fractures, heterogeneous density. Vaughan (1995) assume that the response of tide-water glaciers to tidal forcing is purely elastic (as in our SAFCIM model), and estimated the Young's modulus to be 0.88 ± 0.35 GPa for a number of ice shelves in Antarctica. When using a model that includes the viscous behaviour of ice the inverted Young's modulus is bigger (we refer to literature on this topic in section 4.2.3).

In this Chapter, we propose a model for the capsize of an iceberg against a rigid and an elastic tongue. The tongue is a one dimensional spring whose stiffness is a function of the Young's modulus and the length of the glacier tongue. We extend the SAFIM model (presented in Chapter 2 by adding a rigid glacier front and an elastic glacier tongue. We investigate the effect of a Coulomb friction law between the iceberg and the glacier front. Finally, we propose a possible parametrization of the contact force with four parameters.

3.2 Equations for the iceberg motion

Here we model the dynamics of a rigid iceberg in contact with a glacier tongue. In the continuity of the SAFIM model for iceberg capsizing in open ocean presented in the Chapter 2, we call this model the SAFCIM model for

Semi-Analytical Floating in Contact, Iceberg Model. As in the SAFIM model, the three degrees of freedom of the iceberg are: the horizontal coordinate of the center of gravity x_G, the vertical coordinate of the center of gravity z_G and the angle of inclination of the iceberg θ. The forces and moments (calculated at the center of gravity) that act on the iceberg during its capsize are the gravity force $\boldsymbol{F}_g$, the hydrostatic force $\boldsymbol{F}_s$ and moment $\boldsymbol{M}_s$, the hydrodynamic force $\boldsymbol{F}_d$ and moment $\boldsymbol{M}_d$. Compared to the equations for an iceberg capsizing in free ocean, there is an additional contact force $\boldsymbol{F}_c$ and moment $\boldsymbol{M}_c$. We represent the setup schematically in Fig 3.1.

$$m\,\ddot{x}_G = (\boldsymbol{F}_d + \boldsymbol{F}_c)\cdot \boldsymbol{e}_x \tag{3.1}$$

$$m\,\ddot{z}_G = (\boldsymbol{F}_g + \boldsymbol{F}_s + \boldsymbol{F}_d + \boldsymbol{F}_c)\cdot \boldsymbol{e}_z \tag{3.2}$$

$$I\,\ddot{\theta} = (\boldsymbol{M}_s + \boldsymbol{M}_d + \boldsymbol{M}_c)\cdot \boldsymbol{e}_y \tag{3.3}$$

For an iceberg capsizing in free ocean, a formula for the hydrodynamic effects with a drag coefficient function of the aspect ratio, and no added-masses was given in (Bonnet et al., 2020). We assume that this formula is also valid for the case of an iceberg capsizing in contact with a glacier. In future work, more precise hydrodynamic forces could be used: (i) by using a Computational Fluid Dynamics model able to solve contacts between solids, or (ii) by improving the formula for hydrodynamic forces acting on an iceberg capsizing in contact with a wall (by comparison against a computational fluid dynamics model), in the same way it was done in (Bonnet et al., 2020) for an iceberg in free ocean. In the scope of this study, no such Computational Fluid Dynamics solver able to model such a phenomenon was found.

We recall here the hydrodynamic force and moment:

$$\boldsymbol{F}_d = -\alpha\frac{1}{2}\int_{\Gamma_s} \rho_w v_n^2 \mathrm{sign}(v_n)\boldsymbol{n}\,d\Gamma, \tag{3.4}$$

$$\boldsymbol{M}_d = -\alpha\frac{1}{2}\int_{\Gamma_s} \rho_w v_n^2 \mathrm{sign}(v_n)(\boldsymbol{r}-\boldsymbol{r}_G)\wedge\boldsymbol{n}\,d\Gamma, \tag{3.5}$$

with the drag coefficient α depending on the iceberg aspect ratio ϵ, according to the following formula:

$$\alpha = \alpha_0 + \frac{b\varepsilon}{(1+\frac{c}{\varepsilon^5})} \tag{3.6}$$

with $\alpha_0 = 0.85$, $b = 5.576$ and $c = 0.012$ three non-dimensional parameters. We plot the value of α with respect to the aspect ratio ε in Fig 3.2.

3.2.1 Contact force between the iceberg and the glacier

In this model, the glacier is assumed to be a homogeneous rectangular bloc of ice behaving as an elastic spring fixed on one side and with no inertia. The stiffness of this spring is determined by the length L_t, the Young's modulus of ice E, and the height H_t equal to the iceberg height H. We consider that the left side of the glacier is fixed, the right side of the glacier is the terminus front, and the iceberg is located further on the right. We assume that the effect of the downflow velocity of the glacier is neglectable during the time of the capsize. The horizontal contact force of the glacier on the iceberg is positive (contact) or zero (no contact), cf Fig 3.1. Sergeant et al. (2016, 2018) explain that the inverted force at the source of glacial earthquakes can be approximated as horizontal. We investigate the

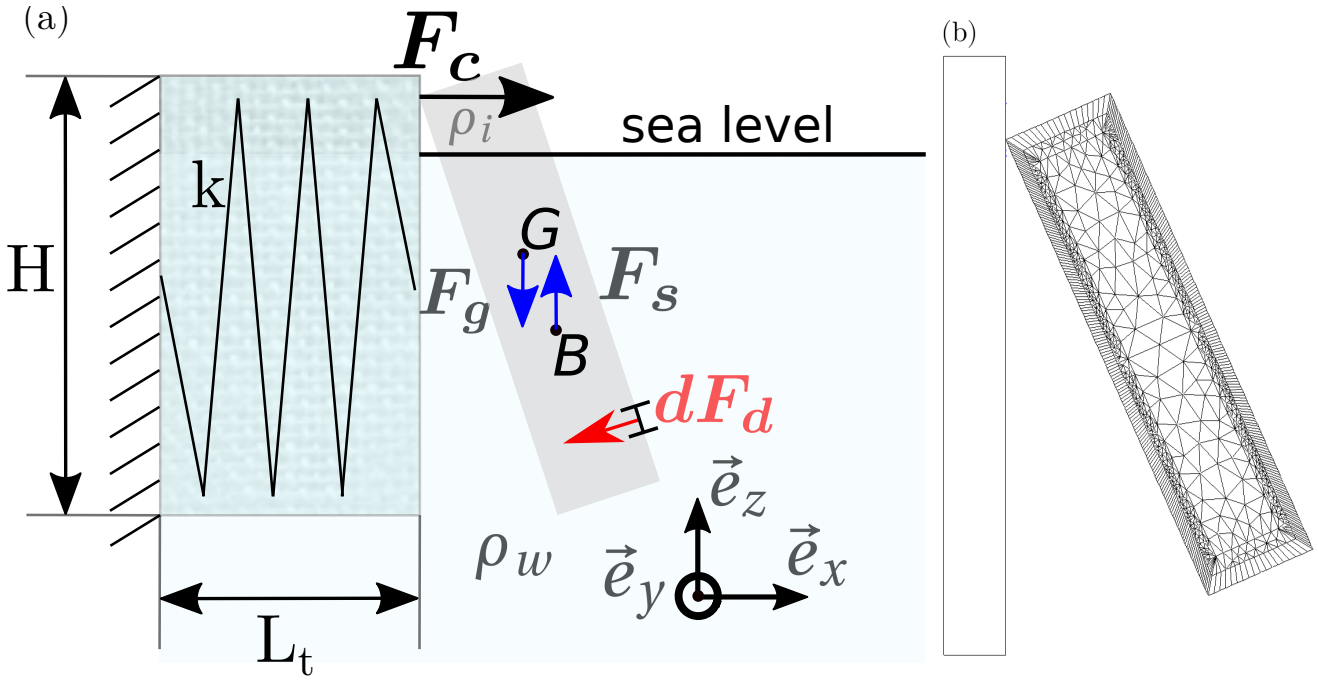

Figure 3.1: Schematic view of the capsizing iceberg in contact with an elastic glacier tongue (a), and mesh for the reference finite element simulation (b)

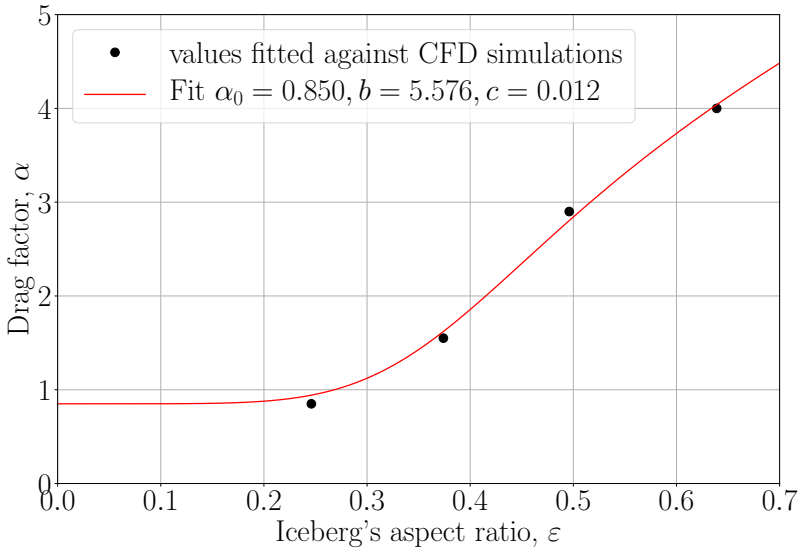

Figure 3.2: Drag coefficient $\alpha(\varepsilon)$. The four black dots correspond to values inverted in Chapter 2 and the red line is given by equation 3.6.

effect of a Coulomb friction between the iceberg and the glacier in section 3.3.3.

The contact force between a rigid iceberg and an elastic spring with no inertia and no flexion writes:

$$\boldsymbol{F}_c(t) = (x_t^0 - x_t(t))\frac{HE}{L_t}\boldsymbol{e}_x \tag{3.7}$$

with H the iceberg and glacier height, E the Young's modulus of the glacier ice, L_t the length of the glacier floating tongue, x_t the horizontal position of the glacier front, x_t^0 the initial position of the glacier front. The glacier front is

assumed to be initially at rest and the iceberg is close to the vertical position (inclined by 0.06°). The contact force is transmitted at the point of contact between the glacier and the iceberg corner. When the iceberg is pushing the wall, that is $x_c \leq x_t^0$ (with x_c the horizontal position of the iceberg corner) the glacier front position is assumed to be equal to the horizontal position of the iceberg corner $x_c = x_t$, and $\boldsymbol{F}_c$ is given by the *stiffness force* eq. 3.7. At the end of the capsize, the iceberg corner moves away from the wall and the contact is lost: $x_c > x_t^0$, the contact force is zero $\boldsymbol{F}_c = \boldsymbol{0}$ and the wall is back to its initial position $x_t = x_t^0$. We assume that the glacier is only in compression or at rest and never in tension.

The numerical integration is sensitive to the stiffness $k = (HE)/L_t$ of the glacier tongue. We provide details in the next section on the implementation of this contact model, starting with the case of a rigid terminus front.

3.2.2 Implementation of the contact force in SAFCIM

In this work, we aim at modelling the dynamics of the iceberg against a rigid and an elastic glacier tongue. For a rigid glacier tongue ($k = (HE)/L_t = \infty$), the formulation in eq. 3.7 is not applicable. The straightforward method to calculate the dynamics of an iceberg in contact with the terminus is to fix the horizontal position of the iceberg corner to be equal to the position of the terminus during the capsize $x_c = x_t^0$. The contact force can then be calculated indirectly through Newton's second law, knowing the mass times horizontal acceleration of the iceberg and the other horizontal forces (the hydrodynamic forces acting on the iceberg). However, the limitation of this method is that the end of the capsize is not computed. It is necessary to artificially detach the iceberg from the wall, by relaxing the condition $x_c = x_t$. Because of this limitation, we did not use this method but two other methods described below: the *penalty method* and the *stiffness method*.

For a rigid wall

For integrating the contact force between a capsizing iceberg and a rigid wall, or a tongue with a high stiffness, we use the *penalty method*: a method used to solve constrained optimization problems. In the current problem, the constraint is the inequality between the position of the iceberg corner and the terminus corner $x_c \geq x_t$ (for an iceberg located on the right of the terminus). The penalty method consist of adding a force in the form of a multiplication between a penalty parameter and a measure of the violation of the constraint, here it is: $P_{pos} * |x_c - x_t|^Q$, with $Q = 1$ for a linear penalty method. Another constraint of the current problem is the time derivative of the condition on the position, that is: $\dot{x_c} = \dot{x_t}$. Using both constraints, the contact force writes:

$$\begin{aligned} &\text{if } x_c \leq x_t^0 \text{ , contact : } \ \boldsymbol{F}_c = -P_{pos}|x_c - x_t^0|^Q - P_{vel}|\dot{x_c} - \dot{x_t^0}|^P sign(\dot{x_c})\boldsymbol{e}_x \\ &\text{if } x_c > x_t^0 \text{ , no contact : } \ F_c = 0 \end{aligned} \tag{3.8}$$

the coefficient P_{pos} is in $\mathrm{N/m^{1-P}}$ and P_{vel} is in $\mathrm{N\ s/m^{1-P}}$. For a rigid wall, the terminus position is constant $x_t = x_t^0$, and the velocity of the terminus front is zero $\dot{x_t} = 0$ m/s.

To optimize Q, P, P_{pos}, P_{vel}, we test a large range of values of the coefficients. In the following simulations, we set the exponent values to $Q = P = 2$ (however similar results were obtained for $Q = 1$). For both high and low values of the coefficients P_{pos}, P_{vel}, the simulations yield noisy results, therefore we optimize the coefficients within an intermediate range of values. Due to the direct dependence of the force with the penetration, there is an inherent instability: at the beginning of the capsize, there is zero force and no penetration. While the iceberg rotates, there

is a penetration $x_c \leq x_t^0$, which implies an increase in the force which pushes the iceberg away from the terminus and thus decreases the penetration, in turn this leads to a decrease in the force which allows an increase in the penetration, and so on. The term $P_{vel}|\dot{x_c} - \dot{x_t^0}|^P sign(\dot{x_c})$ in the definition of the contact force eq.3.8 was added to dampen these oscillations.

In Fig. 3.3, we show the contact force for various sets of coefficients, not shifted in time (a), and shifted in time (b). On this plot, we compare the SAFCIM results with the simulation conducted with the finite element model Z-set for solid mechanics and contact dynamics. This model includes the same geometry, physical parameters and hydrodynamic fluid forces as in the SAFCIM model, but does not require penalty parameters. It is a flexibility method proposed by Francavilla and Zienkiewicz (1975) and improved by Jean (1995) (see description of the method and applications in Wronski, 1994). This Z-set solver is used in Sergeant et al. (2018, 2019) for a rigid glacier and will be used in the Chapters 4 and 5 with a deformable glacier. The error on the amplitude (*EOA* indicated in the legend) between the SAFCIM results and the reference Z-set results is < 1 %. With this small error, we validate the results of the contact force between the capsizing iceberg and the rigid terminus obtained with the penalty method in SAFCIM.

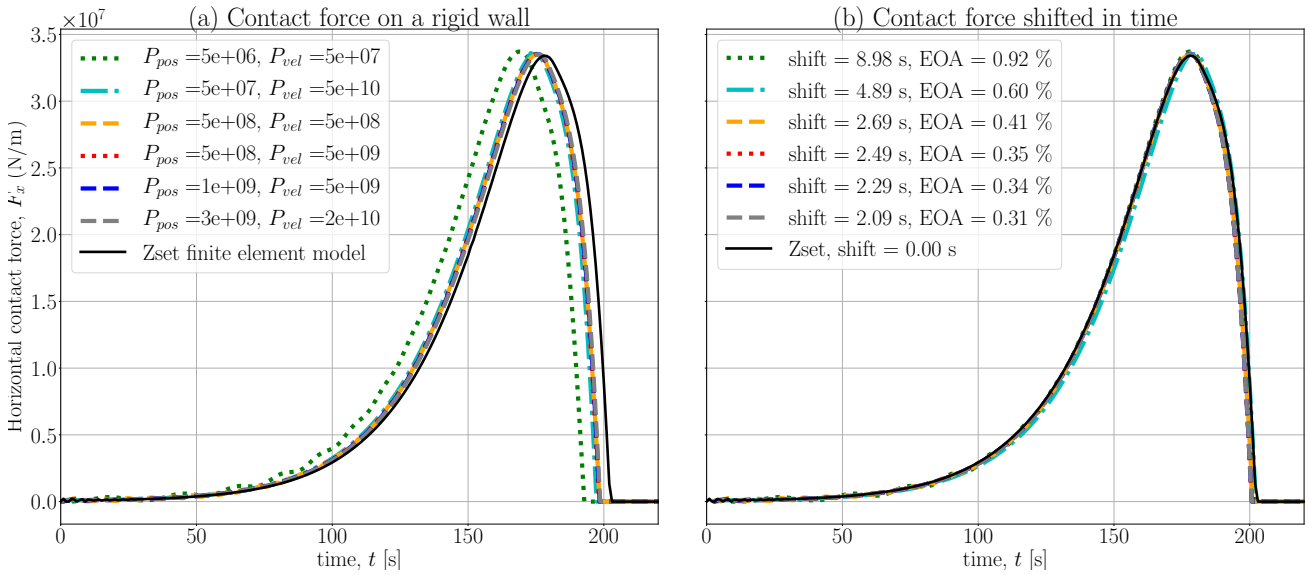

Figure 3.3: Horizontal force exerted by a capsizing iceberg of height $H = 800$ m, aspect ratio $\varepsilon = 0.23$, on a rigid wall. In panel (a) the forces are plotted with no shift in time, and in panel (b) the forces are shifted in time such that the maximum amplitude of the force matches the time of maximum of the Z-set simulation (in black). In the legend of caption (b), we indicate the shift in time and the error on the amplitude (EOA) with respect to the Z-set simulation.

For a field scale iceberg capsizing against a rigid wall, we use the following optimized values of the coefficients: $P_{pos} = 3\ 10^9$ N /m^{-1}, $P_{vel} = 2\ 10^{10}$ N /m^{-1}, $Q = P = 2$. These penalty coefficients are given for a field size iceberg. Note that for a laboratory size iceberg ($H \approx 0.1$ m), the coefficient for the penalty on the position is one order of magnitude smaller $P_{pos} = 5\ 10^7$ N /m^{-1}, as well as the coefficient for the penalty on the velocity $P_{vel} = 5\ 10^9$ N s/m^{-1}, and the power is kept equal to $Q = P = 2$.

For an elastic tongue

The penalty method can be used for the contact between an iceberg and a glacier tongue with a high stiffness and no inertia. In this case, at the time step $n+1$, the force is calculated using the position and velocity of time step n:

$$\boldsymbol{F}_c^{n+1} = P_{pos}|x_c^n - x_t^n|^P - P_{vel}|\dot{x_c^n} - \dot{x_t^n}|^P sign(\dot{x_c})\boldsymbol{e}_x \tag{3.9}$$

and the terminus position is updated at time $n+1$ according to the force and the glacier stiffness: $x_t^{n+1} = x_t^0 - L_t/(H_t * E) * \boldsymbol{F}_c^{n+1} \cdot \boldsymbol{e}_x$.

In Fig. 3.4, we show the contact force for various values of the glacier tongue stiffness for the penalty method with high values of the penalty coefficients in (a), and for lower values of the penalty coefficients (b). The values of the penalty coefficients are indicated in the titles of the captions. The smaller value of the stiffness showed is $k = 1.6\ 10^8$ N/m^2, and this corresponds to $E = 1$ GPa and $L_{tongue} = 4.9$ km, which is the value of the Young's modulus and the glacier tongue of the Helheim glacier as inverted by Murray et al. (2015a)[supplementary materials]. The highest value for the stiffness is $k = 2.7\ 10^{11}$ N/m^2 and this corresponds to $E = 10$ GPa and $L_{tongue} = 30$ m. For the rigid wall the value is $k = \infty$ which corresponds to $L_{tongue} = 0$ m. The penalty coefficients are sensitive to the stiffness: the optimized coefficients increase with the stiffness. As an example, we show in Fig. 3.4 a the results for a two small values of the stiffness $k = 1.6\ 10^8$ N/m^2 (gray dotted curve) and $k = 3.2\ 10^8$ N/m^2 (yellow dotted curves) and with the penalty coefficients fitted for higher values of the stiffness. In Fig. 3.4 b, with lower penalty coefficients, the results for these two small values of the stiffness is correct.

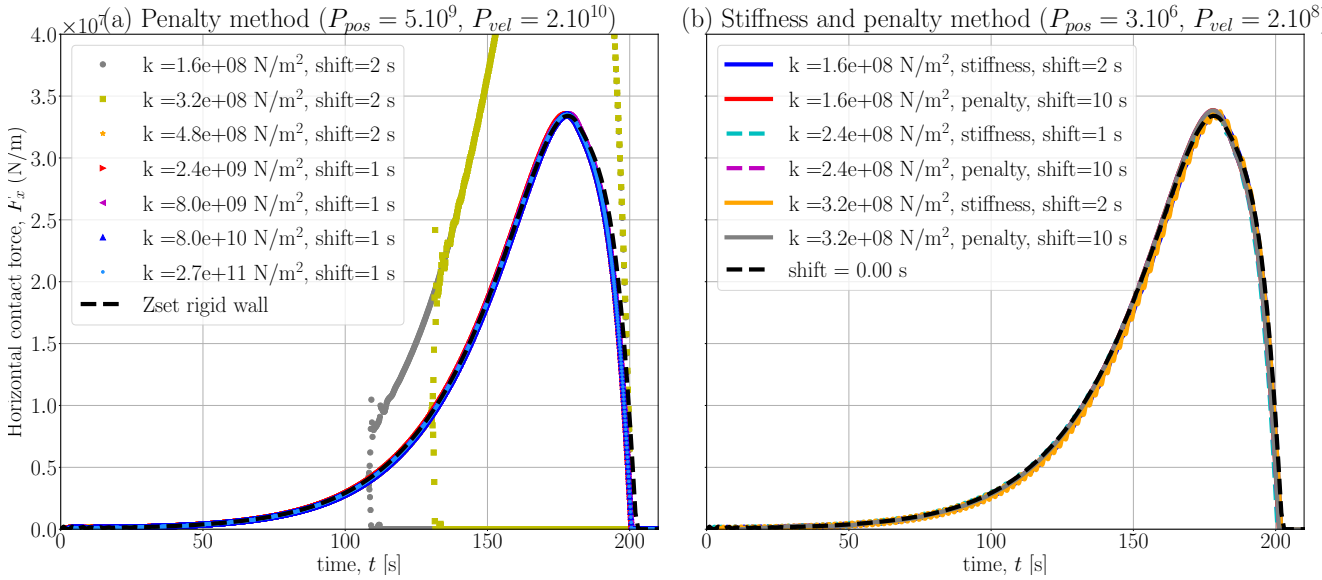

Figure 3.4: Horizontal force exerted by a capsizing iceberg of height $H = 800$ m and aspect ratio $\varepsilon = 0.23$, on an elastic glacier tongue (colored curves with SAFCIM), and for a rigid wall (black dotted lines with Z-set). In panel (a) the penalty force is used, in panel (b) the penalty and spring methods are compared. All curves are shifted in time relatively to the time of the force maximum. In the labels, we indicate the shift in time relatively to the Z-set simulations (black dotted curve).

To model the contact between an iceberg capsizing against a glacier tongue with a small stiffness and no inertia, there is the possibility to use the direct expression for the force as given in Eq. 3.7. This *stiffness method* gives a smooth force for low values of the stiffness, but produces oscillations at higher values of the stiffness (e.g. orange curve in Fig. 3.4 b), and cannot reproduce the contact force between a rigid glacier and an iceberg.

Choice of the method for the contact force

For the values of the aspect ratio for which both the penalty and stiffness methods are valid, the force given by the two methods are similar in amplitude (error <1 %) and in the overall integral $\int F dt$ (error <3 %). However, the time of the maximum differs for each set of parameters. We explain this by the fact that: (1) the contact force is slightly oscillating at the beginning of the capsize, (2) the duration of the initial steady phase is sensitive to the force amplitude at the beginning of the capsize. The oscillations of the force at the beginning of the capsize are due to the fact that the coefficients of the penalty method are constant throughout the simulation, so they cannot be perfectly adapted to both small amplitudes of the force (initial phase of the capsize) and the high amplitudes.

For high values of the stiffness, in particular for the limit case of a rigid terminus (that is an infinite stiffness k), the integration with the stiffness method provides oscillating results (the curves are not shown for clarity). We suggest here that the stiffness method is valid for stiffness lower than $k < 3\ 10^8$ N/m^2. When using the penalty method the coefficients decrease with the stiffness (as shown in Fig. 3.4). Note that for both a rigid and an elastic terminus, the contact force can be simulated with a finite element software. However, to change quickly the geometry and parameters, it is more convenient to use the SAFCIM model. Also the SAFCIM simulation takes ≈ 7 seconds while the Z-set simulations last ≈ 100 seconds (run in parallel on 2 threads). Note that independently of the values of the stiffness tested, the force is similar (after a shift in time): the error on the amplitude is < 1 % and the error on the integral $\int F dt$ is < 3 %.

3.3 Simulations of iceberg capsizing against a glacier terminus

3.3.1 Rigid glacier

Here, we choose the values of the parameters as observed at the Helheim glacier for one event of iceberg capsize presented in (Murray et al., 2015a): bottom-out capsize of an iceberg of aspect ratio $\varepsilon = 0.22$, with a glacier and iceberg height of $H = 790$m. The horizontal contact force $F_{x,contact}$ and the angle of inclination of the iceberg are shown in the Fig. 3.5 (a) for an initial angle of inclination of $\theta_0 = 0.06°$. We compare this simulation with the case of an iceberg of aspect ratio $\varepsilon = 0.45$ in Fig. 3.5 (b) (which is the aspect ratio that gives the highest force amplitude for a bottom-out capsize). The terminus is rigid (position fixed during capsize) and we use the penalty method. We run three simulations: one with $\alpha = 0$ which means there are no hydrodynamic effects in the model, one with the drag coefficient equal to $\alpha = 1$, and one with the optimized value $\alpha = 0.899$ for $\varepsilon = 0.22$ and $\alpha = 2.347$ for $\varepsilon = 0.45$, with the formula given in eq. 3.6. We observe that the amplitude and duration are affected by the value of the drag coefficient α. With $\alpha = 0$, the amplitude and duration of the contact force are underestimated compared to the simulation with the optimized drag coefficient, and the rotation is quicker (the iceberg reaches the horizontal position earlier). For $\varepsilon = 0.45$ (resp. $\varepsilon = 0.22$) and $\alpha = 1$ the force and duration are underestimated (resp. slightly overestimated). We made the same observations for a top-out capsize and for $\varepsilon = 0.22$ and $\varepsilon = 0.35$. However, the optimized values of the drag coefficient have been determined in the case of the capsize in open ocean by comparison with the ISIS-CFD reference model (Bonnet et al., 2020). In future work, it would be interesting to compare the results of SAFCIM with a reference model in fluid dynamics which is able to compute the motion of an iceberg capsizing in contact with a terminus. The ISIS-CFD model is not yet able to compute such a complex fluid-structure problem.

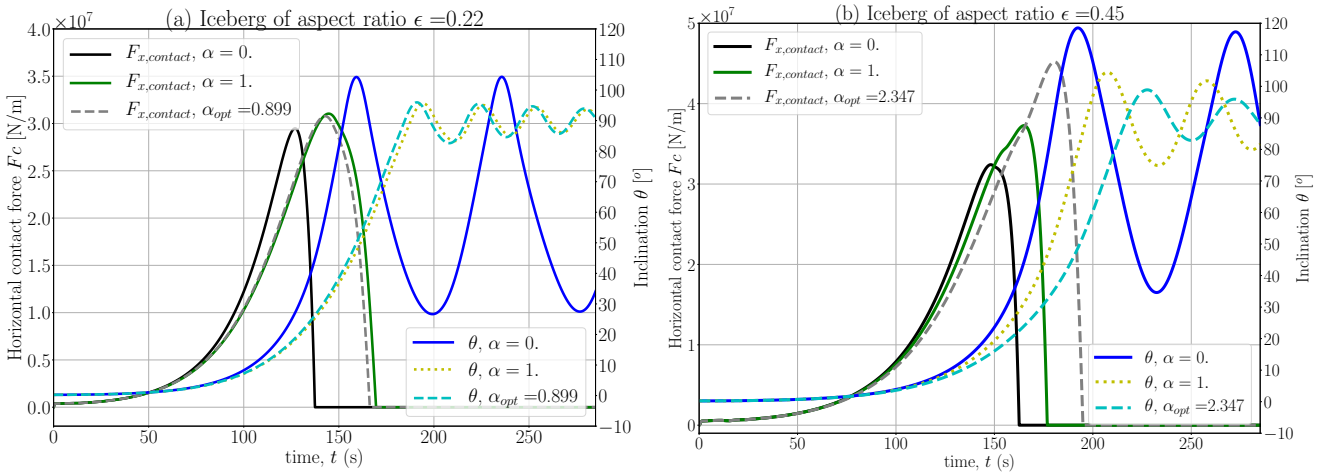

Figure 3.5: Horizontal contact force and angle of inclination with respect to the horizontal, for a bottom-out capsizing iceberg, for an aspect ratio $\varepsilon = 0.22$ (a), and $\varepsilon = 0.45$ (b).

3.3.2 Glacier tongue

We analyse the iceberg dynamics for various values of the stiffness of the glacier tongue, for a bottom-out capsizing iceberg. We use the same values of the parameters as estimated by (Murray et al., 2015a): glacier and iceberg height $H = 790$ m, iceberg aspect ratio $\epsilon = 0.22$, Young's modulus or the glacier tongue $E = 1$ GPa, tongue length 4.9 km. We show the contact force between the iceberg and the glacier for these parameters: red curve (F_1) in Fig. 3.6 and 3.7). We show the results for two other simulations with extrem values of the stiffness: one lower bound for the stiffness $k_2 = 7.9\ 10^7$ N/m^2, which corresponds to $E = 1$ GPa and $L_t = 10$ km (F_2, cyan doted curve), and a rigid terminus (F_0, $k_0 \approx$ inf yellow curve). The simulation with the infinite stiffness (yellow curve) is solved using the penalty method while the two other simulations with a smaller stiffness (red and cyan curves) are solved using the stiffness method. The force applied on the terminus is hardly affected (by less than 0.3 %) when varying the stiffness in this extreme range of values. These results suggests that the elastic compression of the glacier tongue does not affect the contact force.

An addition, we show the horizontal displacements of the terminus during capsize for these simulations in Fig. 3.7. When the iceberg capsizes against a rigid terminus there is no displacements (yellow curve). When it capsizes against an elastic tongue, there is a compression of the glacier (red and cyan curves). These curves are equal to the force divided by the tongue stiffness (dashed gray and magenta curves). Therefore the elastic compression of the glacier can be simply obtained with the SAFCIM model with a rigid glacier. In Fig. 3.8, we show the motion of the iceberg for a bottom-out capsize (a) and a top-out capsize in (b) against an elastic glacier tongue (blue vertical line) with a stiffness $k_1 = 1.6\ 10^8$ N/m^2. We show the snapshots of the position of the iceberg for the same times in the bottom-out and top-out capsize. These figures highlight the different dynamics of the iceberg in the two capsizes. In particular, when capsizing top-out, the iceberg moves away from the terminus much quicker than when capsizing bottom-out.

3.3.3 Coulomb friction at the iceberg glacier interface

In all previous simulations we assume there is no friction (vertical force) between the iceberg and the glacier. However, in practice a number of factors may produce a vertical force: the asperities on the glacier and iceberg surface, the inclination of the terminus front with respect to the vertical, the absence of lubrication by the liquid

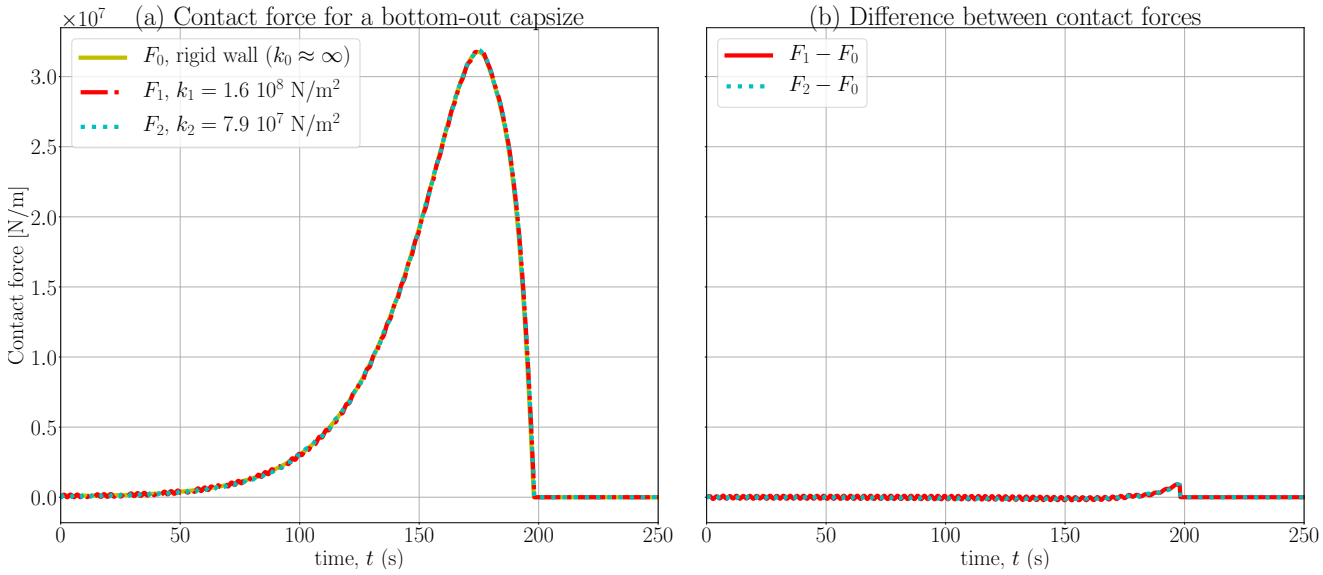

Figure 3.6: Horizontal force (a) exerted by a capsizing iceberg of height $H = 790$ m against a rigid wall (F_0, yellow curve), against an elastic wall with $k_1 = 1.6\ 10^8$ N/m^2 (F_1, red curve) which corresponds to ($E = 1$ GPa, $L_t = 4.9$ km) or ($E = 2$ GPa, $L_t = 10$ km), against an elastic wall with $k_2 = 7.9\ 10^7$ N/m^2 (F_2, cyan curve). In caption (b) the difference between two forces $F_1 - F_0$ and $F_2 - F_0$ are shown. Curves are not shifted in time.

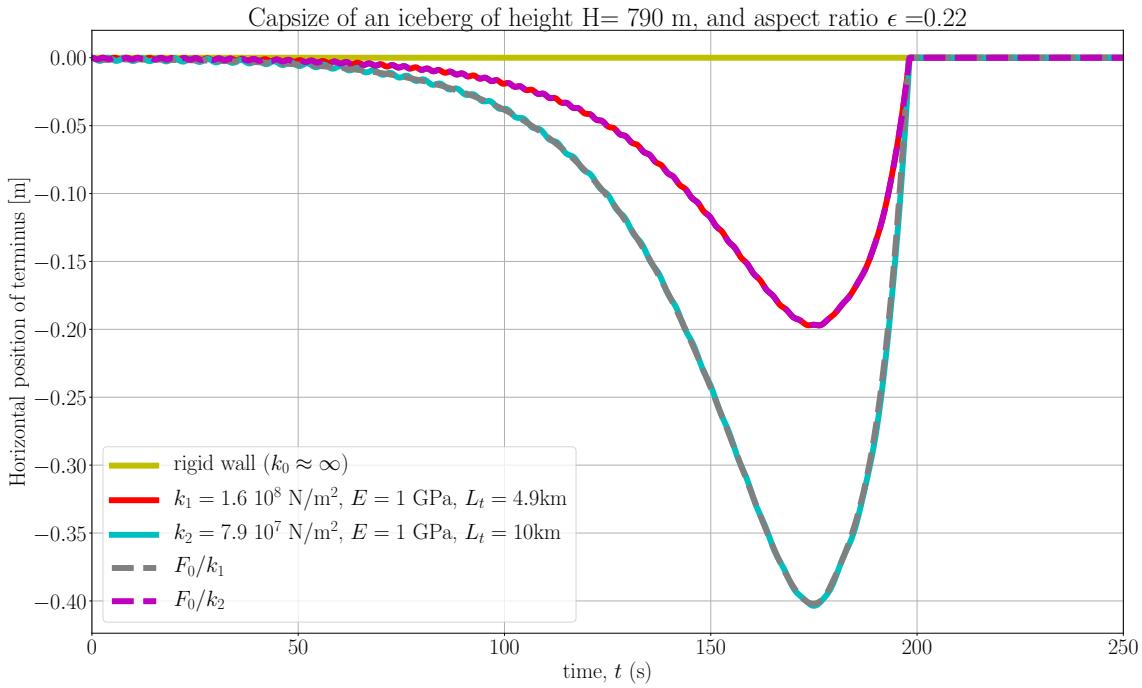

Figure 3.7: Displacement of the glacier terminus during the bottom-out capsize of an iceberg against the glacier front, for a rigid terminus (yellow curve), and an elastic terminus for two values of the stiffness $k_1 = 1.6\ 10^8$ N/m^2 (red curve) and $k_2 = 7.9\ 10^1$ N/m^2 (cyan curves). For comparison, we add the curves obtained by direct multiplication of the force times the inverse of the stiffness.

water, and a viscous drag induced by the interactions between the ice and the water layer. As discussed in Sergeant et al. (2018), the force at the origin of the glacial earthquakes is close to being horizontal, with an angle of inclination

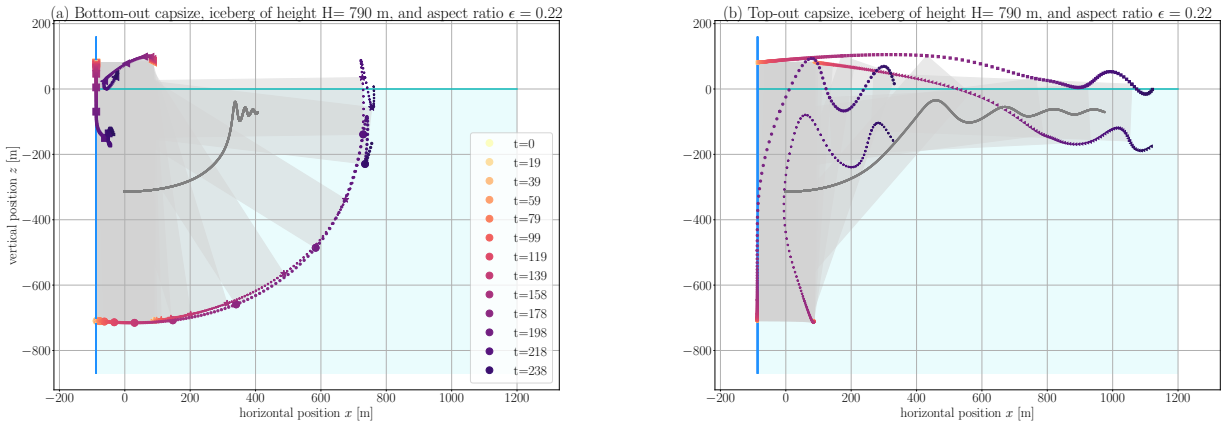

Figure 3.8: Motion of an iceberg capsizing bottom-out (a) and top-out (b) against an elastic glacier tongue (vertical blue line) with a stiffness $k_1 = 1.6\ 10^8$ N/m^2. The positions of the iceberg corners are shown in color varying in time (from yellow at $t = 0$ s to purple at $t = 238$ s): square for corner in the top left (in the initial position of the iceberg), circle for the bottom left corner, star for the bottom right corner and triangle for the top right corner. The position of the center of gravity is shown in gray.

smaller than 10° in most cases and always smaller than 30°. Fitting a Coulomb type friction to this observation, the coefficient of friction would be $\tan(10°) = 0.18$, or $\tan(30°) < 0.58$. We investigate the sensitivity of the contact force to a Coulomb force with various values of the friction coefficient using the Z-set software. In Fig. 3.9, we show the horizontal and vertical contact forces for four values of the Coulomb friction coefficient: $\mu = 0.0$ (no friction), $\mu = 0.1$, $\mu = 0.3$ and $\mu = 0.5$. The amplitude of the horizontal contact force reduces with increasing Coulomb friction coefficient: by < 1 % for $\mu = 0.1$, < 5 % for $\mu = 0.5$, compared to $\mu = 0.0$. The duration of the force and time of maximum of the force increases with increasing Coulomb friction coefficient: by 6s for $\mu = 0.5$, compared to $\mu = 0.0$. Therefore, when assuming no friction between the iceberg and the glacier, the amplitude of the horizontal force is slightly overestimated and the duration is slightly underestimated. The vertical force has an amplitude that increases with μ and reaches $1.6\ 10^7$N/m for $\mu = 0.5$. For a bottom-out capsize, the vertical force pushes the glacier terminus downward and for a top-out capsize, it pushes it upward.

3.3.4 Parametrization of the contact force

We seek a parametrization that can reproduce the shape of the contact force with few parameters. This parametrization is helpful since it allows to reproduce the contact force without requiring to solve the equations of the motion of the iceberg.

The analytical iceberg's force approximation we choose is:

$$F(t) = F_0 \left(\frac{t}{T}\right)^{\alpha} \left(1 - \frac{t}{T}\right)^{\beta} \tag{3.10}$$

The four parameters F_0 (in N/m), T (in seconds), α and β can be optimized for each aspect ratio of the iceberg ε, and its height H. In Fig. 3.10, we show the curves simulated with SAFCIM and the parametrized force with ($F_0 = 2.3\ 10^8$ N/m, $T = 7.7$ s, $\alpha = 6$ and $\beta = 0.6$) for $\varepsilon = 0.22$ and $H = 790$ m.

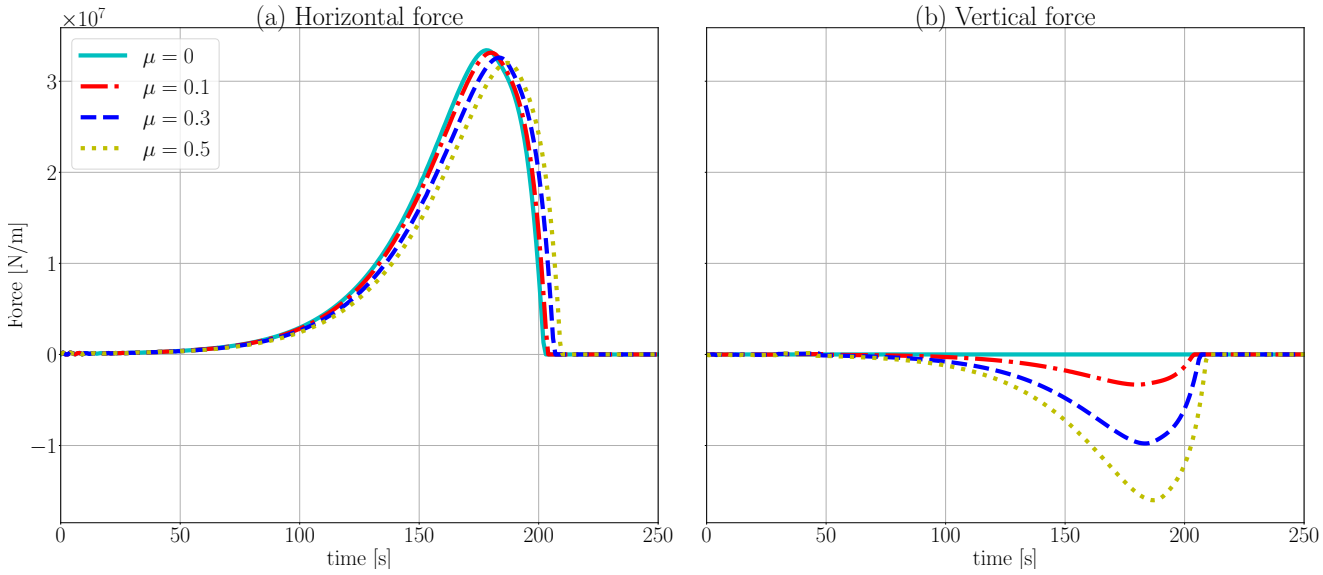

Figure 3.9: Horizontal (a) and vertical (b) contact force between a bottom-out capsizing iceberg and a glacier front. A negative vertical contact force means the iceberg is pushing the glacier downwards. The iceberg height is $H = 800$ m and the aspect ratio is $\varepsilon = 0.22$

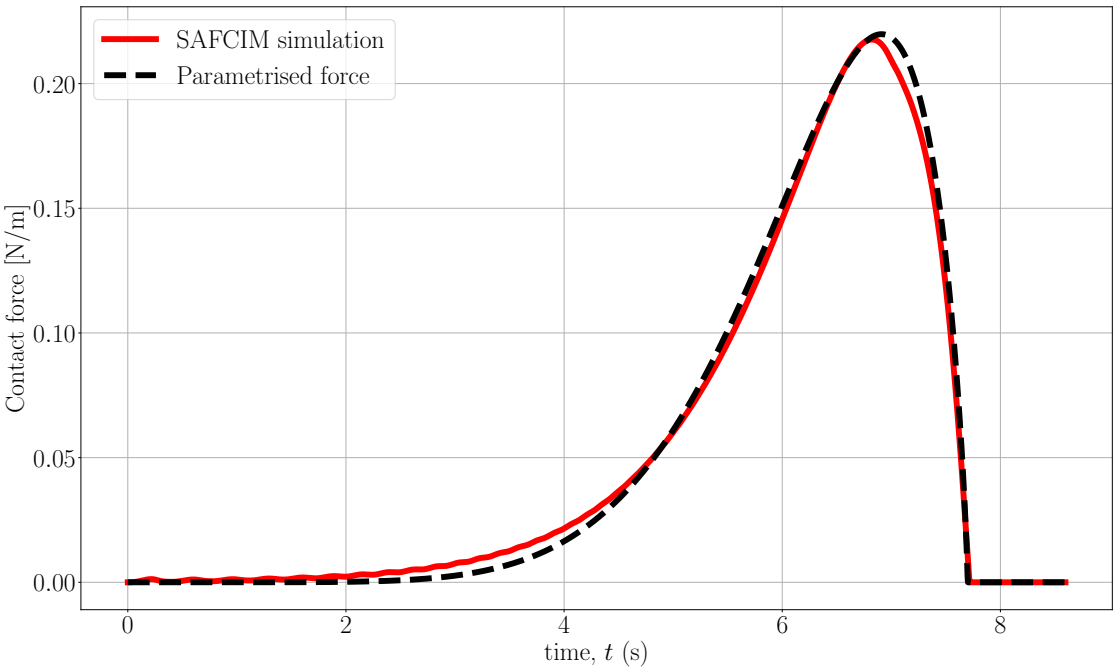

Figure 3.10: Simulated (red) and parametrized (black) contact force for $\varepsilon = 0.22$, and $H = 790$m.

3.4 Discussion

Elasticity and glacier motion

We observed that the stiffness of the glacier tongue hardly affects the iceberg dynamics. This conclusion implies that the contact force calculated in SAFCIM can be applied as a boundary condition, in a model for a two dimensional

glacier dynamics. However, it is also possible to model the capsize dynamics with the contact with a glacier, in the finite element solver Z-set (Sergeant et al., 2018, 2019). However, such simulations cannot include easily an initiation step (see section 4.3.2) which is necessary to initialize the motion of the glacier when considering a viscous behaviour of the glacier ice (as in Chapters 4 and 5).

Moreover, the iceberg in assumed rigid while the glacier tongue is elastic. However, the elasticity of the iceberg should have a little effect on the overall dynamics, due to its small width (deformation of the order of 4. 10^{-5} m). Also, the vertical motion of the glacier is neglected in this model. We expected that it would have a negligible impact on the contact force, since it would be smaller than the horizontal motion which we showed did not impact the contact force. Furthermore, the inertia of the glacier is not taken into account neither in this model, a simple analytical calculation (in section 4.6.1) suggests that it is negligible compared to the contact force.

Comparison with laboratory experiments

The SAFCIM model can reproduce the displacements of an elastic tongue without any viscous flow. Amundson et al. (2012) conducted laboratory experiments of capsizing icebergs in contact with a rigid terminus and measured the horizontal and vertical displacement of the center of gravity of the iceberg and its angle of inclination. In Fig. 3.11, we adapted their fig.2, and added the results of our SAFCIM simulations with the same parameters as used in their experiments: the height of the iceberg is $H = 0.103$ m, the aspect ratio $\varepsilon = 0.5$, the density of the iceberg is $\rho_i = 920$ kg/m, and the water density is $\rho_w = 997$ kg/m, the iceberg capsizes bottom-out. We show the results obtained with SAFCIM with the optimized drag coefficient (α) for a simulation with an initial angle of inclination of $\theta = 1°$ (magenta curve), and $\theta = 5°$ (cyan curve). The simulation with an initial angle of inclination of $\theta = 1°$ yields a duration of the capsize more consistent with the laboratory experiments. The vertical and angular displacement are also in agreement with the laboratory experiments. However the horizontal motion is much larger. Moreover, the initial angle of inclination of the laboratory experiments is closer to $\theta \approx 5°$ (Fig. 3.11 c). However, the SAFCIM simulation with this initial angle of inclination simulates a much quicker capsize than that observed with the laboratory experiments. The difference between our SAFCIM simulations and the laboratory experiments may be due to the influence of the initial conditions in the laboratory experiments: θ_0, dz, initial horizontal, vertical and angular velocities, and the three-dimensional nature of the problem. However, in future work, a comparison between our model and a reference model for fluid-structure interactions would help validated or modify, if needed, the formulation for the hydrodynamic forces in SAFCIM.

3.5 Conclusion

In this chapter, we extended the SAFIM model to include a contact between the iceberg and a rigid and an elastic glacier tongue and detailed the implementation methods for the contact force: the penalty method for a high stiffness, with coefficients depending on the stiffness and the scale, and the stiffness method for a smaller stiffness. We compared this contact force with that from a reference model for contact between solids, the Z-set software. We then showed the negligible influence of the glacier stiffness on the iceberg-glacier contact force. Extending this result to a two-dimensional visco-elastic glacier, it suggests that the coupling between a glacier and a capsizing iceberg does not influence the iceberg-glacier contact force. We then showed the small influence of the Coulomb friction on the horizontal contact force, and calculated the corresponding vertical force. The latter slightly pushes the glacier downward for a bottom-out capsize and upward for a top-out capsize.

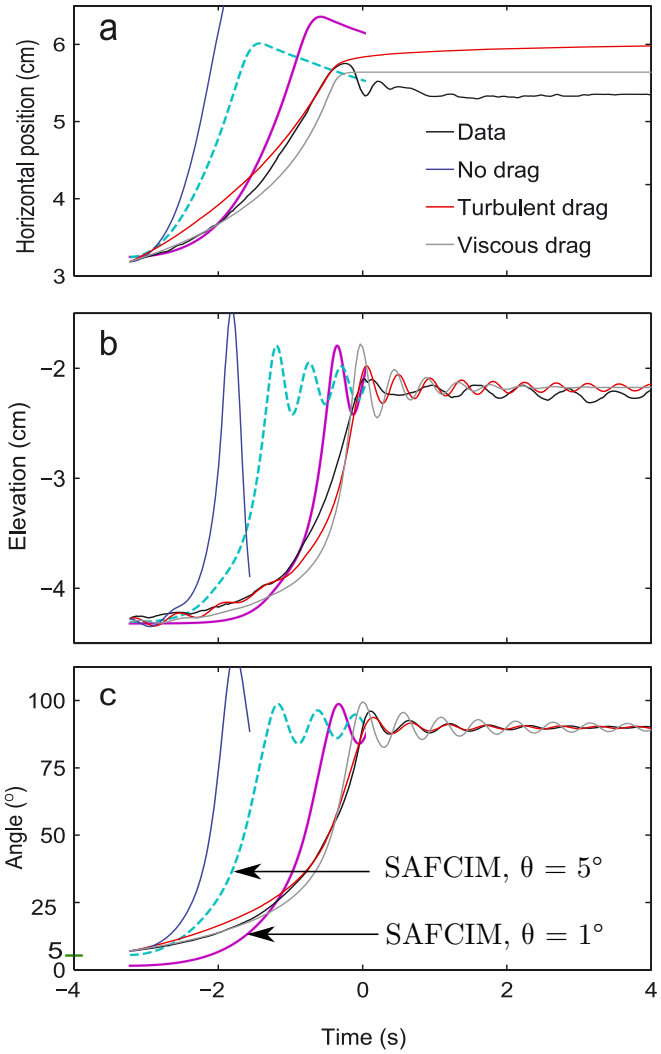

Figure 3.11: Horizontal displacement (a), vertical displacement (b) of the iceberg center of gravity, and angle position (c) for laboratory experiments, adapted from Amundson et al. (2012) fig.2: black curves show the laboratory data. The results using the model for iceberg capsize proposed by Amundson et al. (2012) are plotted in black (without drag), in red (turbulent drag) and in gray (viscous drag). We add the results obtained with a SAFCIM simulation with the initial angle of inclination $\theta = 1°$ (solid magenta curves) and $\theta = 5°$ (cyan dotted curve).

A preliminary comparison of the SAFCIM model with laboratory experiments from Murray et al. (2015a) suggests that the capsize is quicker in the SAFCIM model than in the laboratory experiments. This suggests that the contact force simulated with the SAFCIM model and then applied in the Z-set software will produce a deformation with a shorter duration than in the field. To further improve our SAFCIM model, the hydrodynamic forces could be compared to those calculated with a reference model for fluid-structure interactions and contact mechanics. This is ongoing work with our collaborators that develop the ISIS-CFD software.

To describe the response of the glacier to iceberg capsize, we should add complexity to the model: in the next two Chapters 4 and 5, we model the response of a two-dimensional visco-elastic glacier with various basal friction laws to the capsize of an iceberg against the terminus front.

CHAPTER 4

Modelling the response of a glacier on an inclined and smooth bedrock to iceberg capsize

4.1 Introduction

For future sea level rise predictions, it is crucial to understand the phenomenon contribute to the retreat, acceleration and thinning of glaciers. Iceberg capsize was observed to happen when such dynamic process occur (Veitch and Nettles, 2012). We wish to improve the understanding of tide-water glacier dynamics, at the short time scales of iceberg capsize. The information we have on these events comes from the recording of seismic signals emitted during capsize (Ekström et al., 2003; Tsai and Ekström, 2007; Tsai et al., 2008; Olsen and Nettles, 2017, 2019; Sergeant et al., 2016, 2018), and the measurements of the surface displacements (step-like change in the glacier-flow velocities, reverse horizontal motion and vertical motion of the terminus Nettles et al., 2008; Nettles and Ekström, 2010; Murray et al., 2015a,b; Cassotto et al., 2019). However, extracting information from these measurements is not straightforward. In particular because the short time response of tide-water glaciers to iceberg capsize depends on multiple intercorrelated parameters. Literature suggests that these measurements contain the signature of various processes: the existence or not of an ice tongue and its length, calving events (occurrence, iceberg size, capsize type), the ice-mélange characteristics, and the external forcing (climate variability, tides) (e.g. Veitch and Nettles, 2012; Murray et al., 2015b. These field measurements may also contain information son the ice properties (depending on temperature and damage), the bathymetry of the bedrock, the basal friction (the bedrock material properties, hydrology) and the upstream ice velocities. We analyse whether the surface displacements and the friction force that the glacier exerts on the bedrock (and that can be estimated using seismic data Sergeant et al., 2016) contain the signature of the basal friction laws, the iceberg size, the ice rheology, or glacier tongue length.

We propose a novel model for the response of a glacier to iceberg capsize. In the model, we include the viscous flow of the ice, the elastic deformation of the glacier in response to the force at the terminus, two tunable basal friction laws (the Coulomb friction law, and a viscous friction law), and an adjustable glacier geometry. To include this complexity, we use a finite element solver for solid mechanics *Z-set* developed at the Ecole des Mines de Paris and ONERA, cf http://www.zset-software.com/. In this chapter, we focus on a geometry with a constant slope bedrock.

4.2 Modelling glacier dynamics

The response of ice-sheet dynamics to iceberg calving happens on the time scale of minutes to days. Most models in the literature describe the dynamics of glaciers at rather longer time scales (months), and are not designed for iceberg capsize response. This is primarily because the elastic response of the ice is not included in these models. Only few models in the literature describe the glacier response to iceberg calving (Tsai et al., 2008; Amundson et al., 2012; Sergeant et al., 2018, 2019). These models use a simplified elastic behaviour for ice, with no viscous flow (see section 3.1 for more details on these models). Such assumption is justified by the relatively short time scale leading to smaller viscoplastic strain as compared to elastic strain. However, this does not allow to model the viscous response of the glacier to iceberg calving, nor the shearing of the glacier due to viscous flow under the driving stress.

4.2.1 Fluid and solid approaches

Most models in glaciology address the long time modelling of ice sheets. Here we focus on the short time response of a glacier. The long times are usually modelled with a fluid dynamics approach (Eulerian framework) whereas the short times are simulated with a solid mechanics approach (Lagrangian formulation). These two methods solve

Newton's second law of motion:

$$\rho \frac{d\boldsymbol{v}}{dt} = \nabla.\boldsymbol{\sigma} + \boldsymbol{f_v} \tag{4.1}$$

with $\boldsymbol{v}$ the velocity field, $\boldsymbol{f_v}$ the volumetric forces and $\boldsymbol{\sigma}$ the Cauchy stress tensor. These methods have some important differences:

1. The description of the problem:

   - with an Eulerian approach: the velocity of the material is defined as $\boldsymbol{v}(\boldsymbol{x}, t)$ with $\boldsymbol{x}$ the position of the material point at time t. The positions of the mesh nodes are fixed throughout the simulation, that is the nodes do not move with the material (unless there is a remeshing).
   - with a Lagrangien approach: the movement is defined for each point of the material by the position $\boldsymbol{x}(\boldsymbol{X}, t) = \boldsymbol{X} + \boldsymbol{u}(\boldsymbol{X}, t)$ with $\boldsymbol{X}$ the initial location, and $\boldsymbol{u}(\boldsymbol{X}, t)$ the displacement with regards to that initial position. In practice, one part of the glacier is followed during the simulation and the mesh deforms with the ice.

2. Isotropic elasticity is quantified with the Young's modulus E and the Poisson's ratio ν:

   - in a fluid mechanics model, glacier ice is usually assumed incompressible. This hypothesis is based on the estimation of the coefficient of compressibility $\gamma \approx 1.2 \cdot 10^{-10} Pa^{-1}$ (Cuffey and Paterson, 2010) compared to the inverse shear modulus. This compressibility means that the density increases linearly from 917 kg m^3 to 921 kg m^3 under 4 km of ice due to the *glaciostatic* pressure. This approximation yields a simplification in the mass conservation relation (continuity equation): $\boldsymbol{\nabla}.\boldsymbol{v} = \frac{\partial u}{\partial x} + \frac{\partial w}{\partial z} = tr(\dot{\boldsymbol{\epsilon}}) = 0$ (in a 2D setup). Note that this approximation is valid for glacier ice, but not for firn or snow (the ablation zone, there is no firn nor snow). Moreover, a model with an Eulerian approach does not allow to take into account the elasticity easily, but usually assumes a purely viscous ice. This means elastic responses to short time events, such as tide forcing or iceberg calving cannot be modelled.
   - in a solid mechanics model, ice is usually considered compressible. The ice rheology can be described by a Maxwell law, that is an elastic behaviour in series with a viscous dash pot. This allows to reproduce the non-linear visco-elastic ice response, although it does not include transient creep response of the ice (e.g. Ashby and Duval, 1985; Reeh et al., 2003).The typical value of the Poisson's ratio of ice is $\nu = 0.3$ (Cuffey and Paterson, 2010, p.88), and a summary of the literature on the Young's modulus of ice is given in section 3.1.

4.2.2 Viscous flow law

Microscopically the ice has a crystalline structure whose nature (size, orientation) depends on the local stresses, ice temperature, and the ice history. The rheology is a function of these physical properties. When modelling glacier dynamics, ice bulk properties are averaged in time and space. The typical viscous bulk law for ice is the *Generalized Glen's flow law* or the *Nye-Glen Isotropic Law*, also denoted *Norton-Hoff* law, which is an empirical law with adjustable coefficients relating the deviatoric-stress tensor $\boldsymbol{\tau'}$ and the viscous strain rate $\dot{\boldsymbol{\epsilon_p}}$.

The relationship writes (Cuffey and Paterson, 2010, p.59):

$$\dot{\boldsymbol{\epsilon_p}} = \lambda \boldsymbol{\tau'} \tag{4.2}$$

where, λ is defined as:

$$\lambda = \frac{\sigma_{vm}^{n-1}}{K_v^n}\frac{3}{2} \tag{4.3}$$

with the von Mises equivalent stress $\sigma_{vm} = \sqrt{\frac{3}{2}\tau'_{ij}\tau'_{ij}}$, where τ'_{ij} are the components of the deviatoric-stress tensor, and K_v is the coefficient of viscosity.

This is equivalent to the formulation in Huybrechts and Payne (1996); Huybrechts et al. (1998):

$$\lambda = B\tau^{n-1} \tag{4.4}$$

with $\tau = \sqrt{\frac{1}{2}\tau'_{ij}\tau'_{ij}} = \frac{1}{\sqrt{3}}\sigma_{VM}$ the octahedral stress, $B = f\ a\ e^{-Q/(RT^*)}$, $R = 8.3145$ J mol^{-1}K^{-1} the universal gas constant, Q the activation energy, f the enhancement factor, and $T^* = 273.15 - 8.7\cdot10^{-4}\times d$ (K) is the temperature corrected for the glaciostatic pressure, with d the depth in meter.

The link between the two formulations in equations 4.3 and 4.4 is given by the relationships:

$$B = \frac{3^{(n-1)/2}}{K_v^n}\frac{3}{2}, \quad K_v = \left(\frac{3^{(n+1)/2}}{2\ B}\right)^{1/n} \tag{4.5}$$

Note that the value of the exponent n ranges from 1.5 (at low stresses) to 4.2 (at higher stresses), with the mean value $n = 3$ usually used for glacier dynamic analysis (Cuffey and Paterson, 2010). Note that the flow of ice is *non-newtonian* ($n \neq 1$). The parameter a depends on the water content, the ice density, the grain size and the impurities of the ice (Cuffey and Paterson, 2010). The parameter f is an adjustable parameter that allows to modify equation 4.2 in order to roughly account for the viscous anisotropy associated with the ice fabric.

4.2.3 Elastic behaviour

To accurately model the response of the glacier on short time scales, the elasticity of the ice must be taken into account. That is, a spring is added in series with the above viscous damper, this is a Maxwell law. The total strain writes:

$$\boldsymbol{\epsilon_{tot}} = \boldsymbol{\epsilon_e} + \boldsymbol{\epsilon_p} \tag{4.6}$$

with $\boldsymbol{\epsilon_e}$ the elastic strain, and $\boldsymbol{\epsilon_p}$ the viscous strain.

The equation for the elastic response is: $\epsilon_{ekl} = C_{ijkl}\sigma_{ij}$, with $\boldsymbol{C}$ the stiffness tensor. For an isotropic material, in two dimensions, this equation writes:

$$\begin{vmatrix}\epsilon_{exx}\\ \epsilon_{ezz}\\ \epsilon_{exz}\end{vmatrix} = \begin{vmatrix}1/E & -\nu/E & 0\\ -\nu/E & 1/E & 0\\ 0 & 0 & (1+\nu)/E\end{vmatrix} \cdot \begin{vmatrix}\sigma_{xx}\\ \sigma_{zz}\\ \sigma_{xz}\end{vmatrix} \tag{4.7}$$

with the Young's modulus E and the Poisson's ratio ν. The Young's modulus of floating ice tongues has been estimated in the literature for visco-elastic models with measurements of glacier surface displacements. Rosier et al. (2017) modelled the flexural behaviour of the Ross ice shelf using a visco-elastic model (Maxwell law) and inverted the value of the Young's modulus of 3.2 GPa. The authors show that including basal crevasses (height 25 % H and opening angle 1°) in the grounded part of a glacier has a significant impact on the flexural mechanics, equivalent to reducing the Young's modulus by 40 %. The authors start with a control run with a homogeneous Young's modulus of $E = 3.2$ GPa and homogeneous density of 917 kg/m^3. Then they reduce the Young modulus on the upper 150 m

to 0.5 GPa, to account for a decrease of the ice density (to 350 kg/m^3) (Rosier et al., 2017 their Eq.12 and fig.3a). They find that this is equivalent to a simulation with a homogeneous Young's modulus reduced by 25 %. Moreover, the variation of the till stiffness is equivalent to a change of only 3 % in the effective Young's modulus.

These parameters determine the velocity of elastic waves.The velocity of P waves is $V_P = \sqrt{\frac{E(1-\nu)}{\rho(1+\nu)(1-2\nu)}}$, and the velocity of S waves is $V_S = \sqrt{\frac{E}{2\rho(1+\nu)}}$. In ice for a density of $\rho_i = 917$ kg.m^3 and a Poisson's ratio of $\nu = 0.3$, these velocities are $V_P = 3694$ km/s, $V_S = 1975$ km/s for $E = 9.3$ GPa, and $V_P = 2098$ km/s, $V_S = 1121$ km/s for $E = 3$ GPa.

4.2.4 Friction laws

One of the open questions in glacier modelling is the precise description of the shear stresses exerted at the base of the glacier. A basal friction law gives an equation for the tangential stresses applied on the basal surface.

The two main friction laws that have been proposed in the literature either assume that the basal stress depends on the basal velocity with a *viscous friction law* (also called *power-law* or *Weertman law*), or assume that the basal stress depends the effective pressure at the base with a *Coulomb type friction law*. With a Coulomb type basal friction close to the terminus, the glacier is more stable on positive slopes (going down towards the terminus) and more unstable on negative ones (going down in the upstream direction) than for a power-law basal rheology (Tsai et al., 2015). (Stearns and van der Veen, 2019a) analysed recent velocity data for 140 Greenland glaciers, whose discharge is mainly driven by basal rather than viscous flow, and that flow at > 50 m/day (mainly the 15 km upstream from the terminus). The authors invert for the basal drag using Newton's second law on a column of ice (assuming negligible inertial terms and horizontal velocities constant in depth), constrained with the measured surface velocities and the glacier geometry (*force budget approach*; Van Der Veen, 1989). The authors show a low correlation between the sliding velocity and the estimated basal drag. This suggests that a Weertman type friction law is not relevant for fast flowing glaciers. The authors show a correlation between the sliding velocity and the inverse of the square root of the effective pressure N. However, other studies in the literature suggest that this novel result should not be applied to all glaciers (Minchew et al., 2019). Stearns and van der Veen (2019b) argue that the low dependency between the basal drag and the sliding velocities may be explained by the fact that the grounding line is farther upstream than the documented position. Minchew and Joughin (2020) explain that basal drag is a combination of (1) the *form drag* which is due to the deformation of the ice-till and depends on the relative velocity at the basal interface $\boldsymbol{u_b}$ (Weertman's law, section 4.2.4) and (2) the *skin friction* which is the ability of two surfaces to slide past each other and is dependant on the effective normal stress $N = p_i - p_w$, with p_i the ice overburden pressure and p_w the water pressure (Coulomb's friction law).

Weertman's law

The first paper on the theory of basal sliding is Weertman (1957). In this paper, the authors assumes that no tangential force can be transmitted between two smooth surfaces: only the presence of asperities can explain the basal drag force. The author describes the two physical phenomena at the origin of basal resistance on a rigid bedrock with asperities: viscous creep due to stress concentration upstream from the asperity, and pressure melting due to the pressure upstream from the asperity.

The Weertman law prescribes a dependence of the basal drag $\boldsymbol{\tau_b}$ on the basal sliding velocity $\boldsymbol{u_b}$:

$$\boldsymbol{\tau_b} = C_W |\boldsymbol{u_b}|^M \boldsymbol{u_b} \tag{4.8}$$

with the coefficient C_W in Pa $(s/m)^M$.

Ritz et al. (2015) estimated the contribution of Antarctic ice to the future sea level rise (30 cm by 2100) using a statistical analysis on a large catalog of results of ice sheet simulations for various values of the retreat rate, the bedrock topography and the friction law (for a linear-viscous, nonlinear Weertman, and plastic friction law). This study showed that the uncertainty on the prediction is due in particular to the lack of the constraints on the basal friction law. Brondex et al. (2017) show the sensitivity of the grounding line position, and its retreat, to the choice of the spatial distribution of the coefficient C_W. Weertman (1957) demonstrated that for a simple geometry, $m = 2/(n+1)$ with n the exponent in the Glen's flow law. Later, it was commonly assumed that over rigid bedrock, the exponent is equal to $m = 1/n$, with n the exponent in eq. (4.3) (Gudmundsson et al., 2012; Joughin et al., 2010). For soft tills, due to the till deformation, there is a threshold for the exerted drag, in such case Joughin et al. (2010); Tsai et al. (2015); Gillet-Chaulet et al. (2016) suggest a Weertman law with $m \to 0$. In the case of the fast flowing Pine Island Glacier, Gillet-Chaulet et al. (2016) analysed surface velocities between 1996-2010 and used the Elmer Ice model to invert the value of the exponent to find $m = 1/20$, with an accuracy of 20 m/a for velocities varying between 25 m/a and $\approx$ 800 m/a. A linear relationship between $\boldsymbol{\tau_b}$ and $\boldsymbol{u_b}$, that is $m = 1$ in eq. (4.8), is also a commonly used approximation (Larour et al., 2012; Schäfer et al., 2012). Brondex et al. (2017) take a value of C_W decreasing to zero in the lowest $\approx$ 5 km before the grounding line to account for the observed acceleration of the glacier.

Coulomb friction law

The Coulomb friction law gives a dependence of the basal drag $\boldsymbol{\tau_b}$ on the effective pressure N at the glacier basal interface and a friction coefficient μ:

$$\begin{aligned} &\text{if } |\boldsymbol{\tau_b}| < |\mu N| : u_b = 0 : \text{stick condition} \\ &\text{if } |\boldsymbol{\tau_b}| = |\mu N| : \text{slip condition} \end{aligned} \tag{4.9}$$

To estimate the Coulomb friction coefficient Iverson et al. (1998) conducted shearing laboratory experiments on a confined layer of glacier till. They applied a normal force and measured the resisting shear stress. The authors showed a linear relationship between the shear stress and the normal stress with a friction angle of $\phi = 26.3°$ ($\mu = tan(\phi) = 0.49$) for a gravel rich till and a friction angle of $\phi = 17.8°$ ($\mu = tan(\phi) = 0.32$) for the finer clay rich till. Zoet et al. (2013) conducted shearing laboratory experiments between granite and ice samples of various nature: natural and synthetic, with various debris content (between $0 - 50$ %) and for temperatures between $-6°$ and $0°$. They estimated the friction coefficient $\mu = 0.55$ for $-2.5°$ C$< T < -2°$ C and showed a decrease of the coefficient down to $\mu = 0.1$ at the temperature $T = -0.5°$ C.

For tectonic events, the source of seismic waves is explained by a transition between a stick state and the slip state (e.g. Rice, 1983; Zoet et al., 2013), using a *rate-state friction laws*: a friction coefficient defined as a function of the velocity, a critical slip distance and a reference slip velocity. Similarly, the production of seismic waves at the base of a glacier could be explained by stick-slip events (e.g. Zoet et al., 2013; Wiens et al., 2008).

The transition between a stick and a slip situation may be due to a freezing/melting transition, a change in the hydrological system, a tidal forcing (e.g. Zoet et al., 2013; Wiens et al., 2008) or due to the force exerted by a capsizing iceberg opposite to the glacier flow direction.

A universal law

The following friction laws attempt to combine the two previous laws.

The following *Budd law* formulation (Budd et al., 1979; Brondex et al., 2017) relates the basal drag $\boldsymbol{\tau_b}$ to both the effective pressure N and the sliding velocity $\boldsymbol{u_b}$:

$$\boldsymbol{\tau_b} = C_B |\boldsymbol{u_b}|^{m-1} N^q \boldsymbol{u_b} \tag{4.10}$$

$C_B,\ m,\ q\ > 0$ are adjustable coefficients. This law does not relate the drag to the maximum bound: $\tau_b/N \leq \tan(\beta)$, with β the maximum slope between the bedrock and the flow direction. This bound was given by Iken (1981) on a simple geometry of a slope with asperities producing cavitation, and it was generalised to a more complex geometry by Schoof (2005). The following laws can be in agreement with this bound (depending on the choice of the coefficients).

Schoof (2005) gave a formulation that leads to the Weertman law for high values of the effective pressure N ($\tau_b = C_S u_b^m$), and to the Coulomb sliding law for low values of the effective pressure N (e.g. close to the grounding line) $\tau_b = C_{max} N$:

$$\tau_b = \frac{C_S u_b^m}{(1 + (C_S/(C_{max}\ N))^{1/m} u_b)^m} \tag{4.11}$$

Because of the independence of the two physical mechanisms described by the Weertman and the Coulomb law, Tsai et al. (2015) assumed a *minimum* condition to switch from one regime to the other. The authors explain that the Coulomb regime concerns only a small region close to the grounding line. The *Tsai law* writes:

$$\tau_b = \min(C_W u_b^m, \mu N) \tag{4.12}$$

with C_W and μ two adjustable parameters.

This Tsai law is also consistent with the laboratory experiments conducted by (Zoet and Iverson, 2020): measurements of shear stress between glacier ice and till of various composition, and confined in a ring shear device that allows to study a chosen normal stress and steady velocity. Zoet and Iverson (2020) proposed the following sliding rule (*Zoet law*), to reproduce approximately eq. 4.12 without a min condition:

$$\tau_b = N\mu \left(\frac{u_b}{u_b + u_t} \right)^{1/p} \tag{4.13}$$

with p the slip exponent, and u_t a transition velocity. The authors show that there exist a little variation of the exponent with the bedrock detailed geometry, and estimate the value to $p \approx 5$. The authors suggests the following physical interpretation for the transition velocity u_t: for $u_b < u_t$, the viscous deformation and regelation processes on the bedrock asperities dominate (form drag), and $u_b > u_t$, the glacier exerts a force on the bedrock asperities such that the bedrock drag force is limited by the till's Coulomb strength (skin friction). The authors show this law is consistent with their laboratory experiments and the Tsai law.

4.3 Modelling glacier dynamics and iceberg capsize at short time scales

In the literature, the models that compute the short time response of a glacier to the force of a capsizing iceberg assume a rigid and fixed terminus, or an elastic tongue fixed on the upstream side (see section 3.1). Here, we propose a two-dimensional model for a visco-elastic glacier sliding on an inclined bedrock with tunable friction laws

and with a floating tongue.

4.3.1 Finite element modelling equations

The Z-set software used here http://www.zset-software.com/ solves the equation of motion for deformable solids in contact. At each time step, the displacements at the nodes of the mesh are calculated through the resolution of the finite element formulation of the equations of motion for a visco-elastic material, with a geometry and boundary conditions described below. The strong form of the equation of motion is:

$$\rho \ddot{\boldsymbol{u}} = \boldsymbol{\nabla} \cdot \boldsymbol{\sigma} + \boldsymbol{f} \tag{4.14}$$

with $\ddot{\boldsymbol{u}}$ the acceleration, $\boldsymbol{\sigma}$ the stress tensor, $\boldsymbol{f}$ the density of volumetric forces.

The numerical calculation of the displacement field at each time step is done with a Newton-Raphson algorithm. We assume small deformations in all simulations.

Because the elasticity of the ice is taken into account, the solution of the equation of motion includes acoustic waves. The smallest period of these acoustic waves is constrained by the chosen time step of the simulation. It is possible to run the calculations with a *quasi-static* hypothesis which means ignoring the inertial term in Newton's second law. In this case acoustic waves are no longer solutions of the equation of motion. Therefore we define two types of resolution: the *dynamic* and the *quasi-static*. In the simulations of a glacier on an inclined smooth bedrock but no floating tongue, we observe that the dynamic effect is negligible.

Simulation parameters

Very preliminary results of simulations of a the dynamics of a glacier on a constant slope have been obtained by Sergeant (2016). Following recent studies (e.g. Tsai et al., 2015; Zoet and Iverson, 2020), we extended the model to include a Coulomb friction law close to the grounding line and a Weertman law upstream. We also added another complexity, presented in the next chapter 5: a temperature dependant viscosity and the geometry of the Helheim glacier.

Therefore, this model offers a range of options for the geometry, the friction law, the ice behaviour, the iceberg load application, and the numerical resolution options. We list the physical parameters for these options in Table 4.1. We have tested a number of combinations and we will present a few well selected simulations.

4.3.2 Numerical setup

As a first step in order to understand the response of a glacier to the force exerted by a capsizing iceberg, we model a glacier with a simple two-dimensional geometry: a glacier with an initially uniform thickness sliding down under gravity on a bedrock with a constant slope.

Geometry

The initial geometry of the model glacier with a constant bedrock slope is shown in Fig 4.1 (not to scale). This model glacier has a uniform height $H = 1$ km. Its grounded part is initially a parallelogram of length $L = 40$ km that extends from the upper (left) vertical boundary which is 510 m above water, to the grounding line which is at the hydrostatic equilibrium (that is the gravity force balances the buoyancy force). The floating tongue is modelled by a rectangular bloc of ice initially horizontal.

Component of the model	Parameters
Glacier geometry	
Grounded part of the glacier	H, θ, dz
Glacier tongue	H, L_{tongue}
Basal friction	
Weertman law	C_W, $L - L_C$
Coulomb law	μ, L_C
Glacier ice behaviour	
Elasticity	E, ν, ρ_i
Glen's law	$K_v(z, x)$
Loading	
Surface of application	z_0, z_1
Iceberg parameters	H, ε, ρ_i,
Water pressure	ρ_w

Table 4.1: Table of parameters in the finite element glacier simulations, with H the height of the model glacier, θ the angle of inclination of the bedrock, dz the vertical shift of the terminus position with respect to hydrostatic equilibrium, L_{tongue} the length of the glacier tongue, with C_W the Weertman coefficient, μ the Coulomb friction coefficient, L_C the length on which the Coulomb friction is applied, E the Young's modulus, ν the Poisson's ratio, ρ_i the ice density, K_v the coefficient of viscosity, n the exponent in the Glen's flow law, z_0 height of the lower extremity of the zone of application of the iceberg force, z_1 the height of the upper extremtiy of the zone of application of the iceberg force, H the height of the iceberg, ε the aspect ratio of the iceberg, ρ_w the water density.

The finite element mesh is shown in Fig 4.2 for the case without a floating tongue (a) and for the case with a floating tongue (b). It is made of quad elements of height $h = 77$ m, length $l = 134$ m on the whole glacier except for the last 1530 m before the grounding line and for the floating tongue, where the lengths of the elements are reduced to $l = 33$ m. A mesh convergence analysis was done and the error on the surface displacements due to mesh discretization is ≈ 1 %.

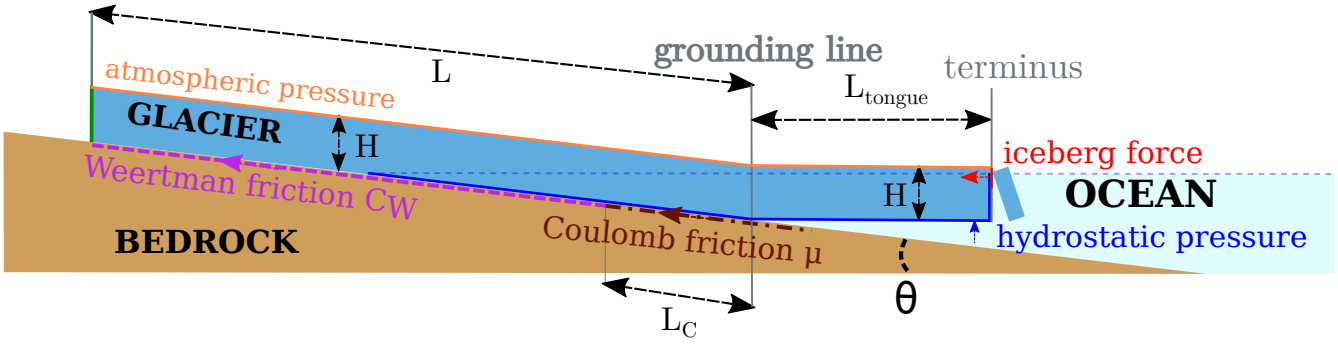

Figure 4.1: Schematic description of the model glacier.

Boundary conditions

The boundary condition at the free surface (orange line in Fig 4.1) of the glacier is a stress free condition. The boundary condition at the submerged part of the terminus (blue line in Fig 4.1) is the hydrostatic pressure $\boldsymbol{\sigma} \cdot \boldsymbol{n} = p_{hydro}(z)\boldsymbol{n} = \rho_w g z \boldsymbol{n}$. The left boundary (in green on Fig 4.1) was taken far enough from the terminus so that its motion is not affected by the capsize. The boundary condition (free or imposed displacements and tractions) on this left boundary was shown to have no effect on the glacier response to the capsize. We apply a Coulomb friction on a zone of the basal surface of length L_C close to the grounding line. Upstream of the Coulomb zone, we apply a Weertman basal friction, on a zone of length $L_W = L - L_C$. The Coulomb friction law was already implemented in the Z-set solver, whereas the Weertmann law was not. For the case of a simple basal geometry with a constant

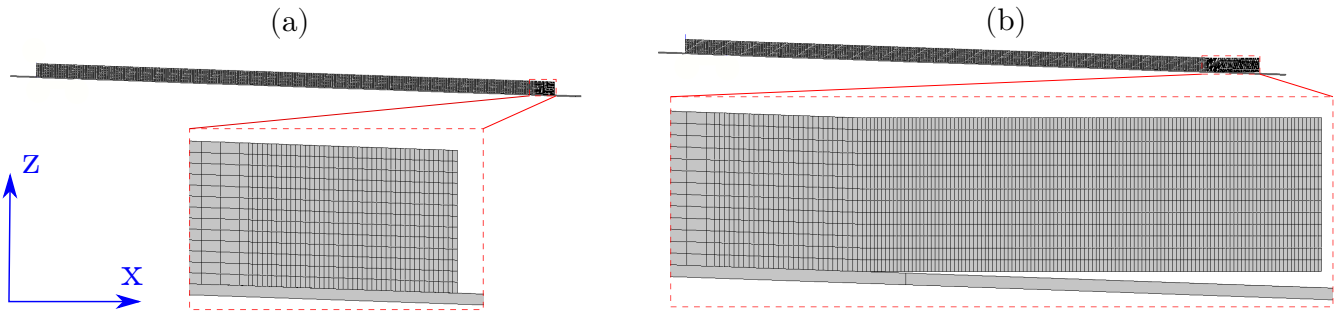

Figure 4.2: Mesh of the glacier: without a floating tongue (a) and with a floating tongue (b).

slope, we have validated the Weertman friction law against an analytical solution.We apply the horizontal force exerted by the iceberg on the terminus. This iceberg force is applied in a different part of the terminus whether it is a top-out or a bottom-out capsize, see paragraph 4.3.2.

Initiation phase

Before applying the capsize force, we initiate the motion of the glacier during 1000 seconds. At the end of this initiation phase, the glacier has a stabilised velocity and the total displacements with respect to the initial geometry are < 20 cm at the terminus of the grounded glacier, and < 60 cm at the terminus of the 3 km floating tongue.

Capsize force

When capsizing, the iceberg exerts a force, mainly horizontal (Sergeant et al., 2016) on a localized zone moving through time. This zone is approximatively a material point in the two-dimensional setup (and a horizontal line in the three-dimensional setup). This point moves vertically along the terminus during the capsize: towards the sky for a top-out capsize and in the opposite direction for a bottom-out capsize. The Z-set solver allows to model the motion of the iceberg in contact with the terminus. However, we wish to start the capsize after an initiation time ($\approx$ 1000s) during which the glacier almost reaches a steady state. Therefore, we must start the capsize after this initiation time, and this requires either to (1) artificially impose the displacements/position of the iceberg such that the iceberg would be at the right position with respect to the glacier at the end of the initiation or (2) to attach initially the iceberg to the glacier front, and to release it after some time. Both options require a modification of the solver that was not implemented during this thesis, but that could be investigated in future studies.

Another option is to apply the force of the iceberg calculated in a preliminary simulation, as a pressure force applied to the terminus of the glacier. In chapter 3, we show that the elastic response of the glacier does not affect the iceberg dynamics, nor the contact force of the iceberg on the glacier. Therefore, applying a force previously calculated is equivalent to including an iceberg moving in contact with the deformable glacier. This is true because the horizontal acceleration (due to the viscous flow and the basal sliding, not modelled in Chapter 3) of the glacier is negligible compared to that of the iceberg. However, for a full precision, the location of the force should be changed through time. As a first approximation, for the bottom-out capsize we apply the force on the upper part of the terminus ($\approx$ 300 m from $z_{0,bo} = -270.444$ m to $z_{1,bo} = 114.172$ m see Fig 4.3), and for the top-out capsize, we apply it on the lower part of the terminus front ($\approx$ 300 m from $z_{0,to} = -578.136$ m to $z_{1,to} = -885.828$ m). This approximation is consistent with the fact that, with a more realistic geometry, the zone of contact between the terminus and an iceberg is not exactly a point (in two-dimensions) but rather a line. To obtain these zones of the force spread, we ran a simulation with the SAFCIM model (chap 3). We show the trajectory of the corner of the

iceberg in contact with the terminus with the coloured line in Fig 4.3. The dark green color means a zero contact force and red color corresponds to the maximum amplitude of the force. For the bottom-out capsize, the force maximum is $7.46 \cdot 10^7$N/m at $t = 242$s after the beginning of the capsize and the total duration of the force is 259s (after that time the force is equal to 0.0N/m). For the top-out capsize, the maximum of the force is $6.69 \cdot 10^7$N/m at $t = 199$s, and the total duration of the force is 213s (see Fig. 4.4).

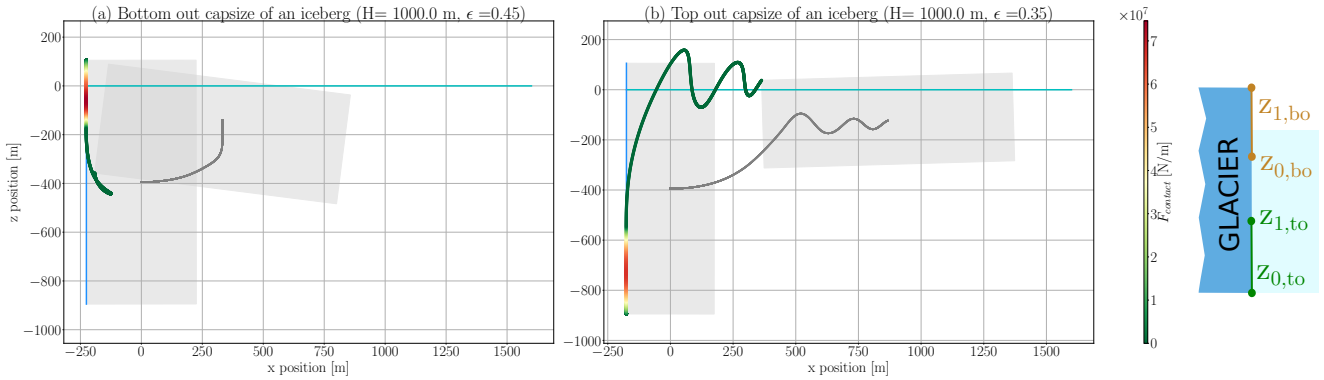

Figure 4.3: Iceberg (shaded gray rectangle) at the beginning of a capsize and at time $t = 300$s. The trajectories of the corner in contact with the glacier is shown in thick coloured line, and the trajectory of the center of gravity is given in gray. The capsize is bottom-out in (a) and top-out in (b), with the aspect ratio ($\varepsilon = 0.45$ for a bottom-out capsize, and $\varepsilon = 0.35$ for the top-out capsize) which provides the maximum amplitude of the force compared to other aspect ratios. On the right we schematically represent the zones of application of iceberg force on the terminus as used in the finite element model. The bottom-out force is applied on the brown line (between altitude $z_{0,bo}$ and $z_{1,bo}$), and the top-out force ont the green line (between altitude $z_{0,to}$ and $z_{1,to}$.)

In Fig. 4.4, we plot the contact force between an iceberg, initially at hydrostatic equilibrium and a (fixed) glacier front calculated with SAFCIM in Chapter 3. For thin icebergs with an aspect ratio $\varepsilon < 0.35$, the contact force has a higher amplitude and duration for the top-out capsize than for the bottom-out capsize. For larger icebergs with $\varepsilon > 0.35$ the force has a higher amplitude and duration for the bottom-out capsize than for the top-out. Note that the duration of the force is very sensitive to the initial angle of inclination (see discussion in Bonnet et al., 2020). In the following finite element simulations, we select the ε such that it yields a contact force with the maximum amplitude: $\varepsilon = 0.45$ for a bottom-out capsize, and $\varepsilon = 0.35$ for the top-out capsize. These values of the aspect ratio also correspond to the forces with the highest absolute time derivative (that is the highest positive slope before the peak) among all other aspect ratios.

Note that the slight change in the curvature of the force before the peak in the force amplitude occurs at the time when a third corner of the iceberg reaches the water level, thus there is an additional contribution to the hydrodynamic forces from one side of the iceberg (that was previously above the sea level) that increases the contact force.

4.4 Grounded glacier

We recall that the aim of this study is to simulate the effect of the characteristics of the system (geometry, bulk properties of the ice, basal friction laws, type of capsize) on the response of the glacier to the iceberg capsize, assess if this can have a measurable impact on the observed surface displacements and recorded seismic signals produced by the capsize, and ultimately constrain these characteristics using field measurements. In this context, the outputs of the model that we will focus on are: the displacements and velocities at the free surface (that can be measured

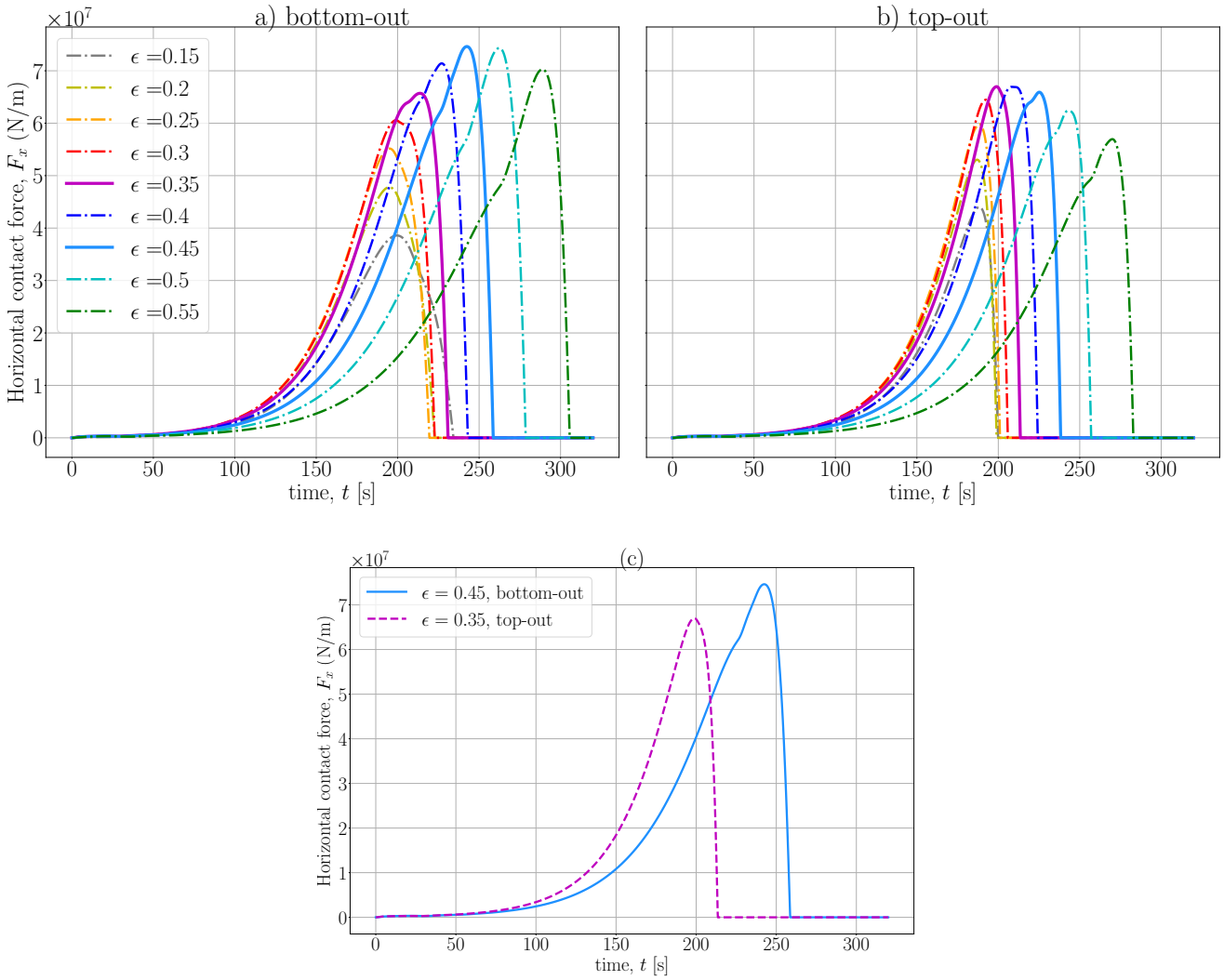

Figure 4.4: Horizontal contact force of a capsizing rigid iceberg against a vertical terminus front, for a bottom-out (a) and a top-out (b) capsize calculated for various aspect ratios ε, for a height $H = 1$ km, a water density $\rho_w = 1025$ kg/m^3, and an ice density of $\rho_w = 917$ kg/m^3. In panel (c), we plot the contact forces for the aspect ratios for which the force has the highest amplitude.

with GPS campaigns and teleseismic measurements) and the displacements and tangential stresses at the bed (to assess the influence of the glacier motion on the source of the seismic waves).

We choose the values of the parameters mentioned above according to the following constraints: (1) velocities should match the typical velocities of a fast flowing glacier such as the Helheim glacier, (2) the values of the parameters (rheology and friction) should be consistent with that inverted for the Helheim glacier with a state-of-the-art Ice-sheet and Sea-level System Model (ISSM) inversion (Chapter 5), (3) the geometry should be simple with similar dimensions as that of the Helheim glacier (the average slope on the last 25 km of the central flowline is $ang1 - ang2$). An additional constraint is that (4) the results should reproduce qualitatively the transitory motion that was measured at the surface of the Helheim glacier during capsize. We adjusted the parameters with an iterative (trial and error) process. One set of parameters that is consistent with the conditions above is: slope of the bedrock and initial slope of the free surface equal to $\theta = 2°$ (the glacier is assumed parallelogram shaped), viscosity coefficient (eq. 4.5) $k = 2\ 10^8$ Pa s$^{1/3}$ (which corresponds to a temperature of $\approx -7°$ C), Glen's flow law exponent $n = 3$, Young's modulus of pure ice $E = 9.3$ GPa, Poisson's ratio corresponding to an incompressible

material $\nu = 0.5$, Coulomb friction coefficient $\mu = 0.6$, Weertman friction coefficient $C_W = 5 \cdot 10^9$ Pa s/m, length of the Coulomb zone $L_C = 735$ m (or $L_C = 734.5$ m measured horizontally), height of the glacier $H = 1000$ m (measured on the vertical), water density $\rho_w = 1025$ kg/m^3, ice density $\rho_w = 917$ kg/m^3.

In this chapter the values of the slope of the basal interface, the aspect ratio, the water and ice densities and the length of the Coulomb friction zone are fixed throughout the simulations. We investigate the influence of a change in the values of the other parameters on the glacier dynamics during capsize.

In the following plots, vertical and horizontal displacements are shown. To obtain these values in a coordinate system rotated by the slope angle, the multiplication factor is $\cos(\theta)$, which is $\cos(2°) = 0.999 \approx 1$ because of the small angle of inclination of the bedrock.

4.4.1 Top-out capsize

Here, we analyse the response of a grounded glacier to a top-out capsize, for an iceberg of aspect ratio $\varepsilon = 0.35$. We apply the iceberg from time $t = 1000$ s as a homogeneous pressure on upper part of the terminus, between elevation $z_{0,to} = -578.136$ m and $z_{1,to} = -885.828$ m indicated in Fig. 4.3.

We represent the vertical and horizontal position through time, in the bed and free surface (Fig. 4.6). The points for which the displacements are plotted are shown schematically in Fig. 4.5 (a). We represent the displacements relative to the time of the beginning of capsize, which is $t = 1000$s.

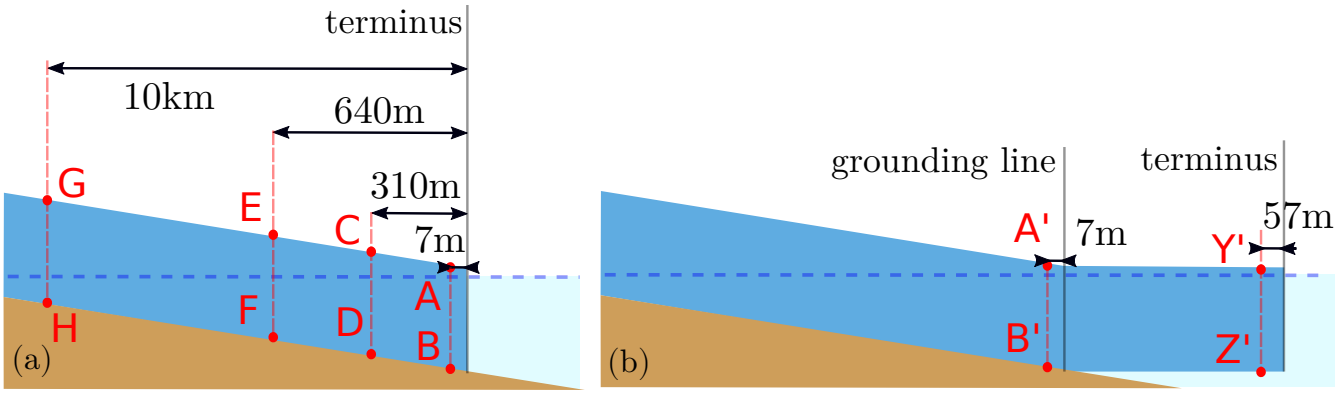

Figure 4.5: Schematic representation of the grounded glacier (a) with the points A, B, C, D, E, F, G and H, and the floating glacier (b) with the points A', B', Y' and Z'.

- at 7 m from the terminus, and at the base (point B, green curve on Fig. 4.6 d), the displacements do not change during the capsize. At the free surface (point A, blue curve on Fig. 4.6 c), there is a deceleration but no reverse motion. There is an upward vertical motion at the surface (point A, blue curve on Fig. 4.6 a).
- 310 m from the terminus is the closest point from the terminus for which the basal surface did not stop sliding (see point D, magenta curve on Fig. 4.6 d). At the free surface, the vertical and horizontal displacements (orange curves on Fig. 4.6 a and c) are similar to those closer to the terminus (blue curves on Fig. 4.6 a and c)
- at 640 m from the terminus, the deviation of the basal motion (point F, gray curve on Fig. 4.6 b and d) is approximately twice smaller than at the distance 310 m from the terminus (magenta curve on Fig. 4.6 b and d). At the free surface, the induced displacements (point E, black curve on Fig. 4.6 a and c) are similar to those at 7 m and 310 m from the terminus (blue and orange curves on Fig. 4.6 a and c), but the general velocity (the slope of the curve) is smaller at 640 m than at 310 m and 7 m.

- 10 km from the terminus is the closest point that is not affected by the capsize (at a precision of 10^{-2} mm). The horizontal and vertical velocities at the base and at the surface (points G and H, dotted lines on Fig. 4.6 a, b ,c and d) are smaller than those of points closer to the terminus.

The basal motion stops for a time interval for all the points located within 310 m from the terminus, the basal motion is affected by the capsize up to 5 km close to the terminus, and the motion at the free surface is affected up to 10 km upstream from the terminus. These observations suggest that, for a top-out capsize, the surface displacements observed during the capsize of an iceberg is the signature of a change in the basal sliding of the glacier and a visco-elastic response of the glacier. In the next sections, we investigate whether we can discriminate between the influence of the basal and bulk (viscous and elastic) properties.

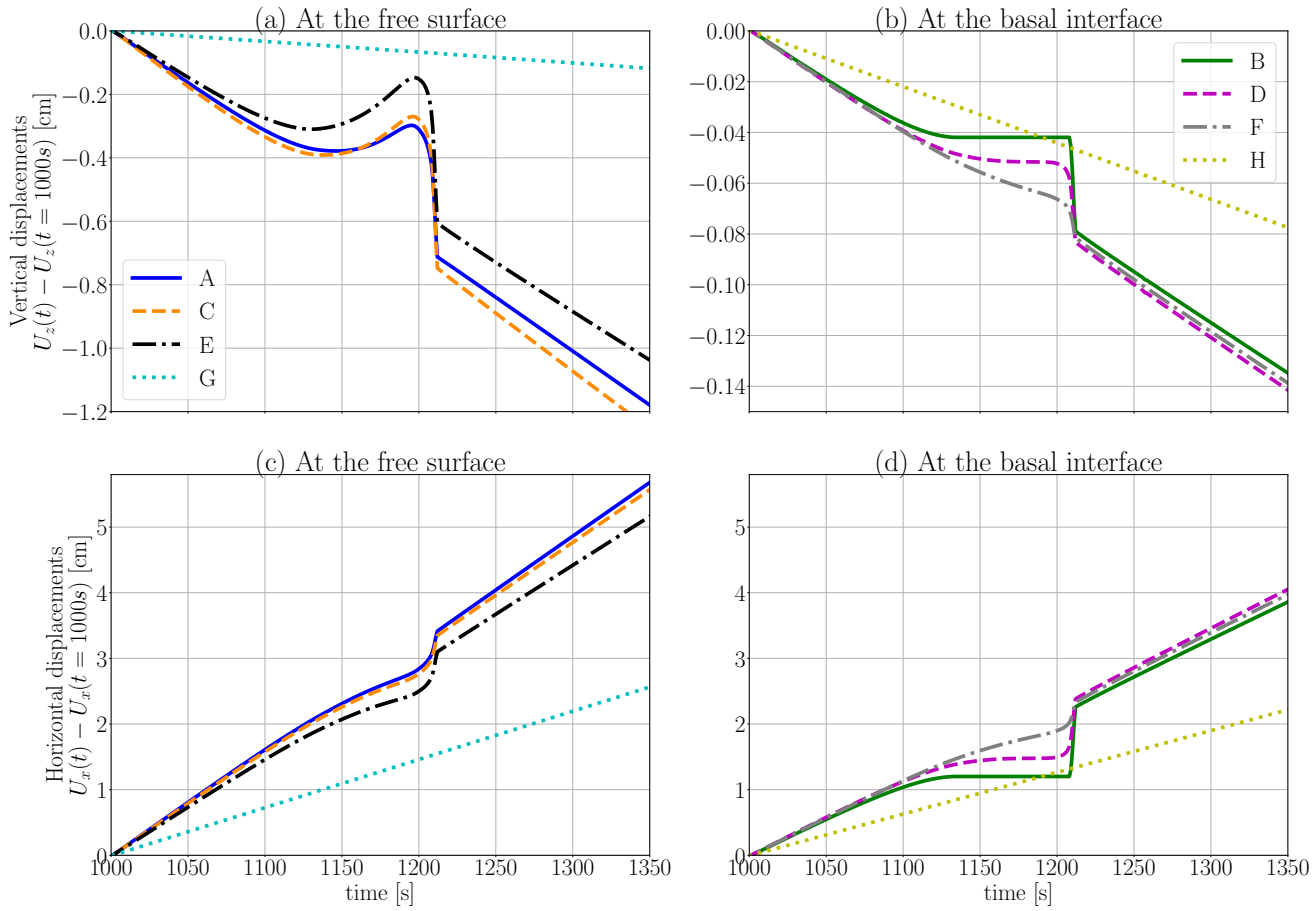

Figure 4.6: For a top-out capsize against a grounded glacier, we show the vertical displacements (a) and the horizontal displacements (c) at the glacier free surface. We also plot the vertical (b) and horizontal (d) displacements at the basal interface. The displacements are plotted at four distances from the terminus front: at 7 m from the terminus (points A and B), at 310 m (C and D), 620 m (E and F), and at 10 km from the terminus (point G and H).

4.4.2 Effect of the capsize type

In the previous simulation, we modelled the response of a glacier to the force of a top-out capsize applied on the bottom part of the terminus. Here, we compare this response to that due to a bottom-out force applied on the upper part of the terminus, between elevation $z_{0,bo} = -270.444$ m and $z_{1,bo} = 114.172$ m indicated on Fig. 4.3. We

recall that the aspect ratio of the iceberg is such that the amplitude and slope of the force is maximum: $\varepsilon = 0.45$ for a bottom-out capsize (amplitude 7.46 N/m and duration 259 s) and $\varepsilon = 0.35$ for the top-out capsize (amplitude 6.69 N/m and duration 213 s), see Fig. 4.4. These simulations are quasi-static.

Trajectories

The trajectories in the x-z plane with a color-coded time (from green at the beginning of the capsize to red at the end) are shown in Fig. 4.7. The trajectories for the simulations without iceberg capsize are shown in gray. All the time steps of the simulation are shown on the plots, that is every 0.1 s. For clarity, we have shifted the top-out curve horizontally (otherwise superimposed with the bottom-out curve), and we stretched the scale of the y-axis compared to the x-axis.

There is a slight absolute reverse motion for the bottom-out capsize (black arrow on Fig.4.7 a), but not for the top-out capsize. The horizontal and vertical displacements at the surface of the glacier are higher for a bottom-out capsizing iceberg than for a top-out capsize. At the basal surface, for the top-out capsize, there is a clear deceleration followed by an acceleration (cyan arrow on Fig.4.7 b) This plot can be compared to the figures 2.C and 2.D of Murray et al. (2015a): these plots show the map view of the GPS displacements measured at the surface of the Helheim glacier at ≈ 500 m from the terminus, during the capize of two icebergs (most probably bottom-out). We adapted the figure 2.C in Fig.4.8 (a), and highlight the reverse motion during capsize with the black arrow. This is qualitatively reproduced by our bottom-out simulations (black arrow on Fig.4.7 a).

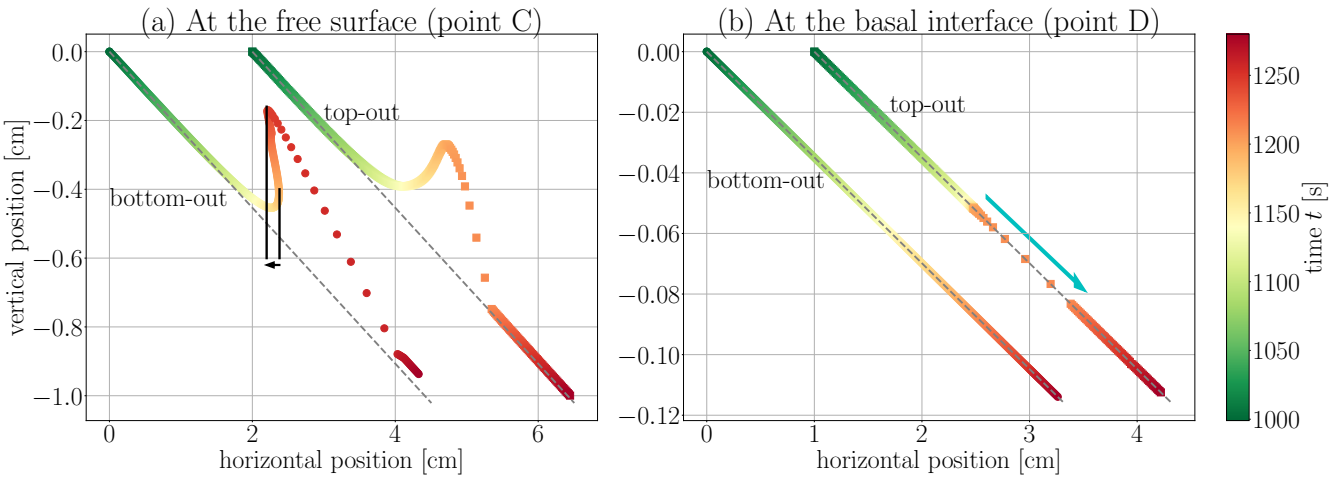

Figure 4.7: Side view trajectories of the point C (310 m from the terminus) at the free surface (a) and point D (310 m from the terminus) at the basal interface (b) for a grounded glacier. For clarity the curves for the top-out capsize are shifted to the right by 2 cm in (a) and 1 cm in (b), and the scale on the z-axis is strechted compared to the x-axis.

Displacements

To help with the interpretation of these motions, we plot the displacements through time, on Fig. 4.9, for the same locations on the glacier: point C at the free surface (a,b,c,d) and point D at the basal interface (e,f). The displacements for the simulations without iceberg capsize are shown in gray thin dashed lines on the plots a,c and e. On captions b, d and f, we show the results detrended relatively to the simulation without iceberg capsize. Fig. 4.9 (a) and (b) can be qualitatively compared to the figures 2.A and 2.B of (Murray et al., 2015a). We adapted the figure 2.A of (Murray et al., 2015a) in Fig.4.8 b. The amplitude of our simulated displacements for the bottom-

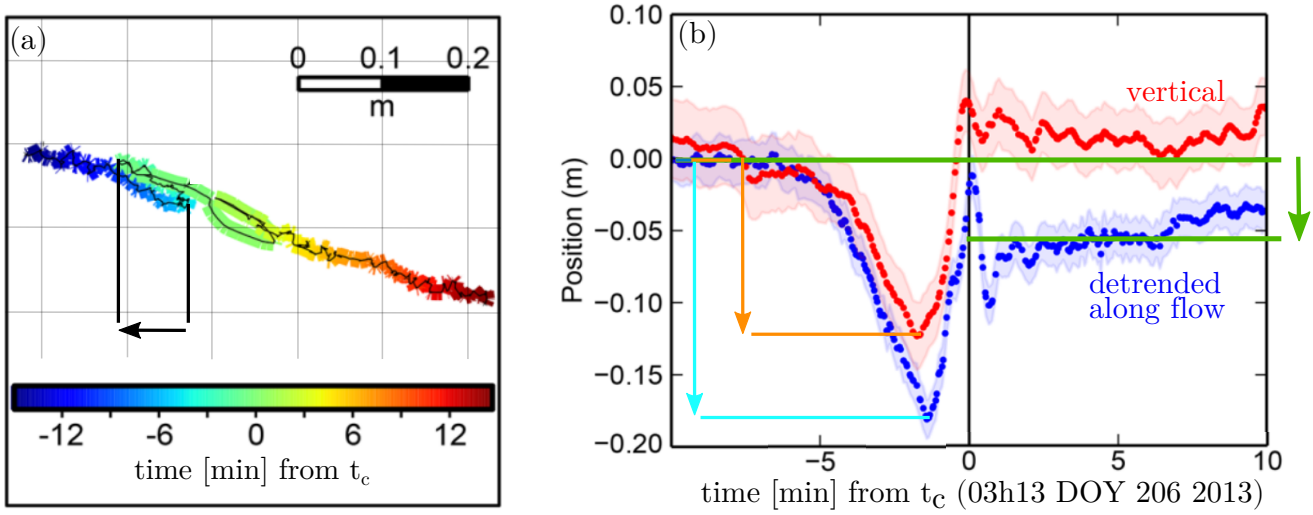

Figure 4.8: Side view of the GPS displacements (a) and time evolution of the vertical and along flow displacements measured at ≈ 500 m from the terminus of the Helheim glacier, during the capsize. Adapted from figure 2.C and 2.A in Murray et al. (2015a)

out capsize are: ≈ 0.7 cm on the vertical (orange arrow on Fig. 4.9 b) and ≈ 1.7 cm on the horizontal (light blue arrow on Fig. 4.9d). This is about one order of magnitude smaller than the detrended displacements measured in the field: on the vertical it is ≈ 12 cm (orange arrow on Fig.4.8 b) and on the horizontal ≈ 18 cm (light blue arrow on Fig.4.8 b). Later in this chapter we show that simulations with a floating tongue and a smaller Young's modulus (here $E = 9.3$ GPa) yields higher amplitudes of the detrended displacements.

When applying the bottom-out capsize force, point D at the base of the glacier moves slightly faster in the downstream direction than without any capsize (yellow curve on Fig. 4.9 f). The bottom-out force applied on the top part (pushing the glacier upstream) combined with the driving force (pulling the glacier downstream and through viscous flow) induces this apparent moment behaviour.

With the top-out capsizes, the reverse horizontal motion relative to the trend is higher at the base of the glacier ≈ 0.8 cm (orange curve in Fig 4.9 f) than at the free surface ≈ 0.4 cm (red curve in Fig 4.9 d). For a bottom-out capsize, the amplitude of the detrended horizontal motion (cyan curve on Fig. 4.9 d) is ≈ 1.7 cm which is about 2.5 times bigger than the detrended vertical motion ≈ 0.7 cm (cyan curve on Fig. 4.9 b). In the case of a two-dimensional elastic beam of height h and length l, the amplitude of the elastic vertical deformation is expected to be equal to that of the horizontal motion (direction of the force) times $\nu h/l$, with ν the Poisson's ratio. The value of the Poisson's ratio is $\nu = 0.5$ in the simulations. This suggests that close to the terminus in the upper meters (where the bottom-out force is applied), the glacier behaves like a rectangular elastic beam (with $l = 1.35h$) during capsize. For a top-out capsize, the amplitude of the detrended horizontal motion (red curve on Fig. 4.9 b) is similar to the amplitude of the vertical motion (red curve on Fig. 4.9 d) at the free surface (≈ 0.45 cm).

The ratio of the amplitude of the horizontal and vertical displacements is higher (≈ 2) for the bottom-out capsize than for the top-out capsize (≈ 1). This results from the fact that for the top-out capsize the deformations occur close to the basal interface, and this induces horizontal resisting forces. This suggests that close to the terminus in the lower meters (where the top-out force is applied), the glacier behaves like a thin elastic beam (with $h = 2\,l$) during capsize. Moreover, this observation is interesting since it can help to distinguish a top-out capsize from a bottom-out capsize at a grounded glacier given the ratio of the amplitude of the horizontal on vertical displacements, thus using only GPS measurements.

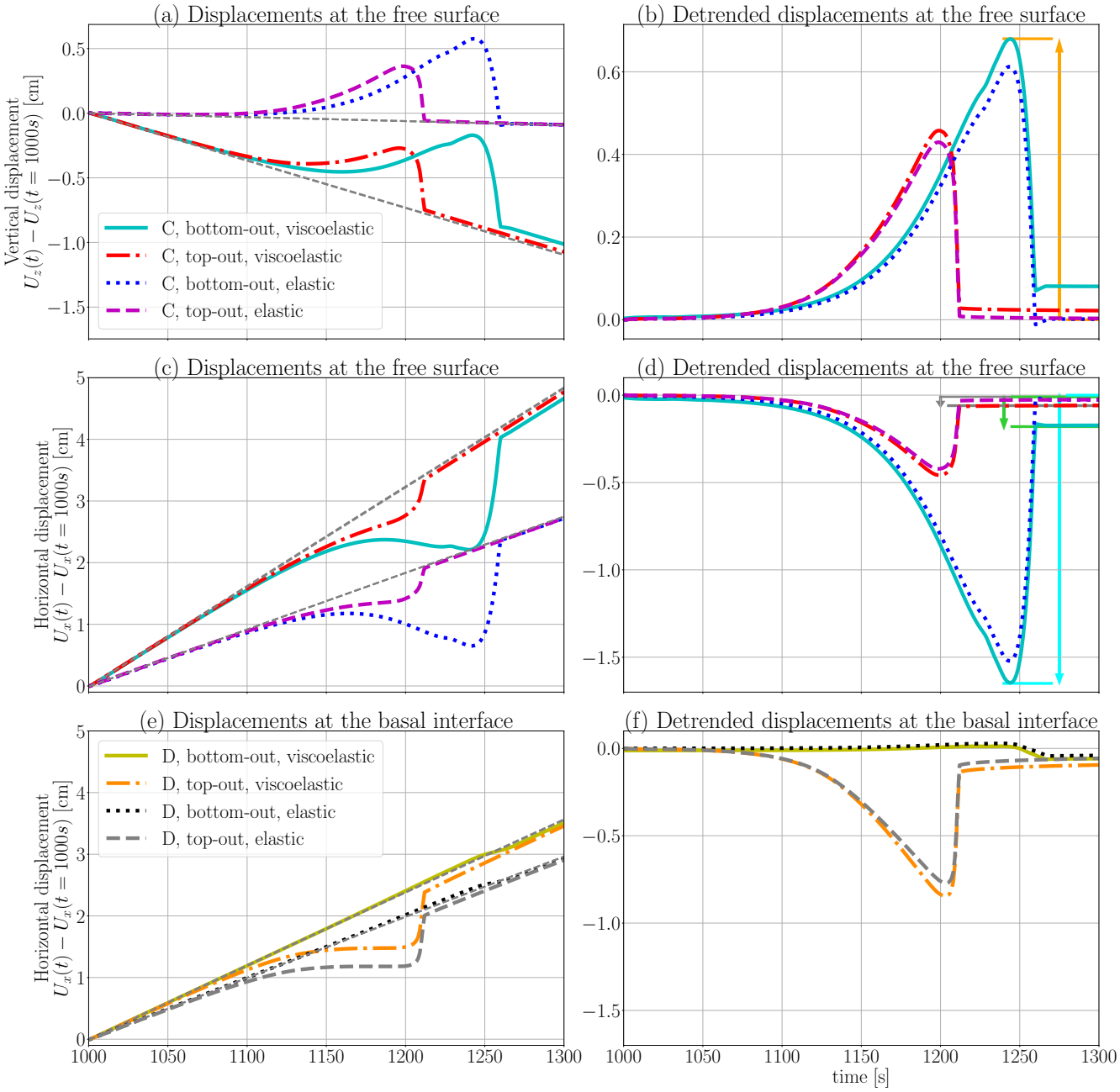

Figure 4.9: For a top-out capsize and a bottom-out capsize, we plot the displacements at 310 m from the terminus: vertical displacements at the free surface (a), the horizontal displacements at the free surface (c), and the horizontal displacements at the base of the glacier (e). The (b), (d) and (f) are the same as (a), (c), (e) but the displacements are calculated relatively to those obtained without a capsizing iceberg (dashed gray curves). Results are shown at 310 m from the terminus, for point C at the free surface and point D at the basal interface, and for a visco-elastic (cyan, red, yellow, orange curves) glacier and an elastic glacier (blue, magenta, black and gray curves). The amplitudes of the detrended motion are highlighted with the orange (b), gray, green and cyan (d) arrows.

Velocity field

In Fig. 4.10 we represent spatio-temporal maps of the velocities at the free surface and at the base of the glacier through time, for the 8 kilometers behind the terminus. The terminus front is located on the right hand side of the plots, the ice flows towards the right (cyan arrow). The initial instance ($t = 1000$s) and the final moment of application of the iceberg force (red curve on the left) on the terminus are represented with the dashed yellow lines. The red dashed vertical line indicates the transition between the applied Weertman friction (upstream) and the

Coulomb friction (downstream). The white contour line corresponds to a zero velocity, and the dark violet color correspond to negative velocities.

We notice a transitory change in the surface velocities during both types of capsize. In the last 75seconds of the bottom-out capsize, the free surface of the glacier (Fig. 4.10 a) located within the ≈ 500 m behind the terminus slows down: the velocities become negative (reverse motion). For the top-out capsize the decrease of the velocities at the free surface is not as strong as for the bottom-out capsize, and there is no zero velocities (Fig. 4.10 a). We notice that during this deceleration phase, at $t \approx 1230$ s, the velocities increase slightly and then decrease again. This coincides with the time of the change in the curvature of the iceberg force at that time (discussed in section 4.3.2). At the end of the capsize, there is a high increase in the velocities above 20 m/day for ≈ 20s for the bottom-out capsize and for ≈ 10s for the top-out capsize. This is due to the abrupt decrease of the capsize force.

The velocities at the basal interface are affected by the top-out capsize but are hardly affected by the bottom-out capsize. For the top-out capsize, the velocities in the Coulomb zone are greatly affected but not in the Weertman zone. Similar to the change in the velocities at the free surface during the bottom-out capsize, there is a decrease in the velocities down to negative values (absolute retreat) followed by a sharp increase in the velocities during the last ≈ 10 s before the end of the capsize.

The difference in the response of the glacier between the bottom-out and the top-out capsize is due to the difference in amplitude of the forces (higher for the bottom-out than for the top-out see Fig. 4.4 c), and the difference in the zone of application of the force (close to the free surface for the bottom-out capsize and close to the basal interface for the top-out capsize, see Fig. 4.3).

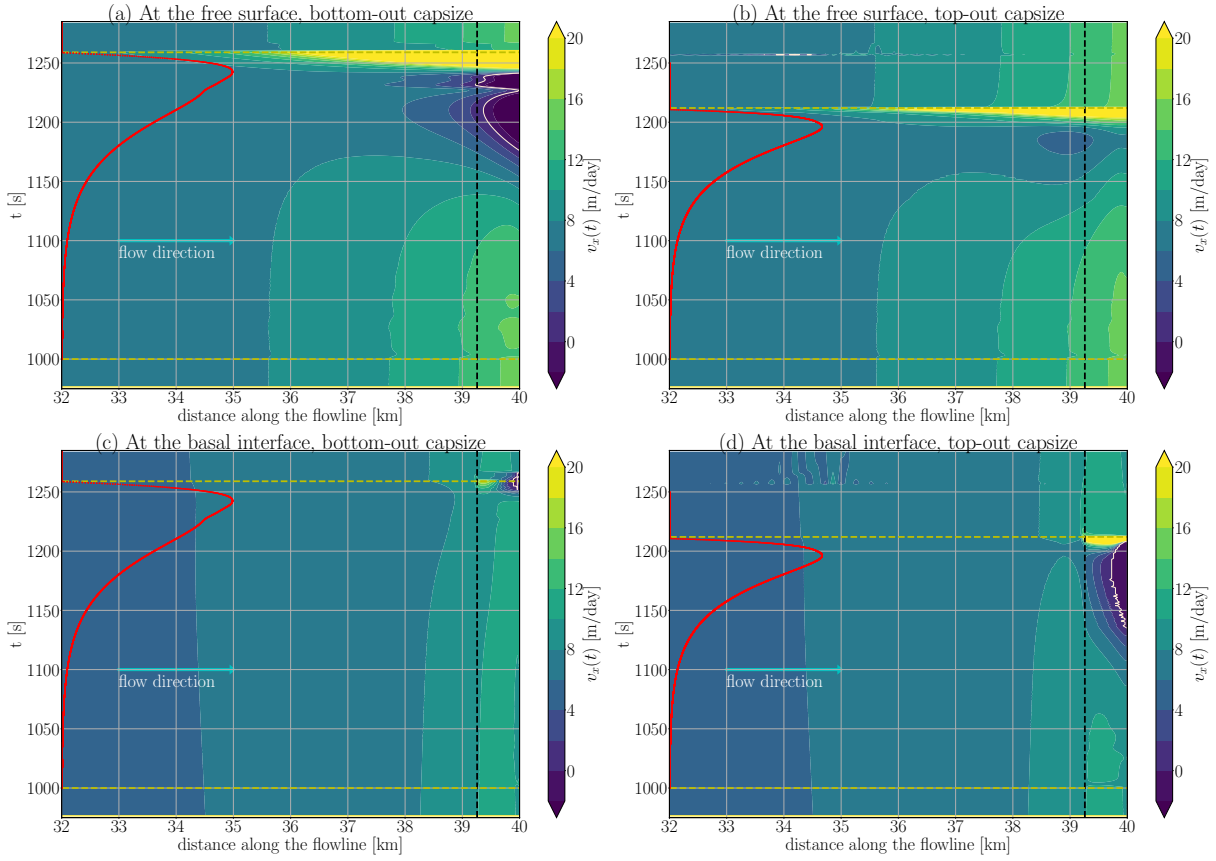

Figure 4.10: Horizontal velocities of the glacier along last 8 kilometres before the terminus, for a bottom-out capsize (a and c) and a top-out capsize (b and d), at the free surface (a and b) and at the basal surface of the glacier (c and d).

4.4.3 Effect of the ice rheology: purely elastic or visco-elastic

To analyse whether the response of the glacier is mainly elastic, or if there is also a significative part of the response which is due to the viscosity of the ice, we plot the results of a simulation with a purely elastic material, with all other parameters kept constant as in the previous simulation: blue curves (bottom-out, point C), magenta curves (top-out, point C), black curves (bottom-out, point D), and gray curves (top-out, point D) in Fig. 4.9. The velocity (slope of the gray curves) at the free surface (Fig. 4.9 a and c) is higher with a visco-elastic ice than with an elastic ice. This is due to the viscous flow under the *driving stress*, that is the component of gravity along the glacier slope.

The amplitude of the detrended displacements is about 10 % bigger with the visco-elastic ice (cyan and red curves in Fig. 4.9 b, d) than with a purely elastic ice (blue and magenta curves in Fig. 4.9 b, d). Therefore, ≈ 90 % of the deformation of the glacier is due to an elastic compression of the ice.

We observe that with the visco-elastic ice, the displacements at the free surface at the end of the capsize does not recover fully the background trend displacement: there is an *offset* after the end of the capsize compared to the simulation without capsize (see cyan and red curves in Fig. 4.9 b and d, highlighted with the gray and green arrows in d). A similar offset is visible on the horizontal displacements measured with GPS sensors at the surface of the Helheim glacier (Fig.4.8 b). However, there is about one order of magnitude of difference between the observed offset (≈ 5 cm, green arrow on Fig.4.8 b) and the simulated offset (≈ 0.3 cm, green arrow on Fig. 4.9 d). Relative to the amplitude of the horizontal motion, this offset is ≈ 25 % in the field GPS measurements and ≈ 10 % in the simulations. For the elastic material, this offset is much smaller (magenta and blue curves in Fig. 4.9 b and d). Note that there is no visible offset in the case of the laboratory experiments conducted by (Murray et al., 2015a) (see their figure 3A), for which the glacier was a rigid block without any viscous behaviour (designed to measure the force). The fact that the offset is observed on the visco-elastic simulations, and on the field measurements but hardly on the purely elastic simulations (and not on the laboratory experiments) suggests that this offset is produced by the viscous behaviour of the ice. During the capsize, the glacier ice is deformed in such a way that there is some residual deformation. At the end of the capsize, the elastic deformation that occurred during the capsize vanishes but there is a residual viscous deformation. According to Glen's flow law, this viscous deformation is dependent on the amplitude of the force, its duration and the value of the coefficient of viscosity. This suggests that the viscosity of the ice has a signature in the measured surface displacements. Note that such an offset is also visible on another event of iceberg capsize (Murray et al., 2015a, fig. S1B). However, for some events, the offset is not detectable, but it may be hidden by another phenomenon: a change in the background velocity (Murray et al., 2015a, fig. 2B and fig. S1A), or a noisy signal (Murray et al., 2015a, fig. S1C and fig. S1D).

We now assess the effect of a heterogeneous coefficient of viscosity K_v. This coefficient of viscosity depends on temperature which varies in time and space. Because of the short duration of our simulations, we can reasonably assume that the value of the viscosity K_v is constant in time. The values of the temperature and the viscosity field obtained with the ISSM inversion(collaboration with AWI, Bremerhaven, see Chapter 5) on the last 40 km of the central flowline of the Helheim glacier are plotted in Fig. 4.11. Because the height of the glacier varies along the flowline, we normalize the depth with the local height, and plot this value between 0 (at the base) and 1 (at the surface). The gray area shows the range of values of the temperature (a) and the viscosity (b) (maximum and minimum value at each depth along the flowline). In the Z-set simulations, we set the coefficient of viscosity as a function of depth: the profile is the same at each x-position. We recall that we are interested in the response of the glacier to the iceberg capsize, therefore we focus on the part close to the terminus. We fix the profile of the viscosity to that at the terminus of the Helheim glacier (red curve in Fig. 4.11 b), which corresponds to the temperature

profile plotted in black in Fig. 4.11 (a). Note that this profile is similar to the mean profile calculated on the lowest 10 km behind the glacier terminus (dashed green and blue curves in Fig. 4.11).

We plot the displacements obtained for a simulation with such a viscosity profile in Fig. 4.12. We observe that the horizontal velocities at the surface and at the base of the glacier (slope of the curves on the left column of Fig. 4.12) are higher than for the constant coefficient of viscosity. This is similar to what is observed when choosing a coefficient of viscosity constant but smaller than the value used before $K_v < 2\ 10^8$Pa s$^{1/3}$. We observe that the offset is higher for the simulations with the viscosity dependent on the depth (black and dark green arrows on Fig. 4.12 d) compared to the simulations with $K_v = 2\ 10^8$Pa s$^{1/3}$ (gray and light green arrows in Fig. 4.12 d). For the top-out capsize, the increase of offset is about five-fold, whereas for the bottom-out capsize, the increase is only two-fold. This is probably due to the fact that the top-out capsize force is applied on the lower part of the glacier terminus where the viscosity is lower than above (Fig. 4.11 b). This suggests the none negligible impact of a coefficient of viscosity dependent with the depth in the glacier. The higher value of the offset in the field measurements compared to the simulations can be explained by even lower values of the viscosity coefficient in the field. Moreover, a larger visco-elastic effect if expected with a constitutive law accounting for the transient creep regime (Reeh et al., 2003).

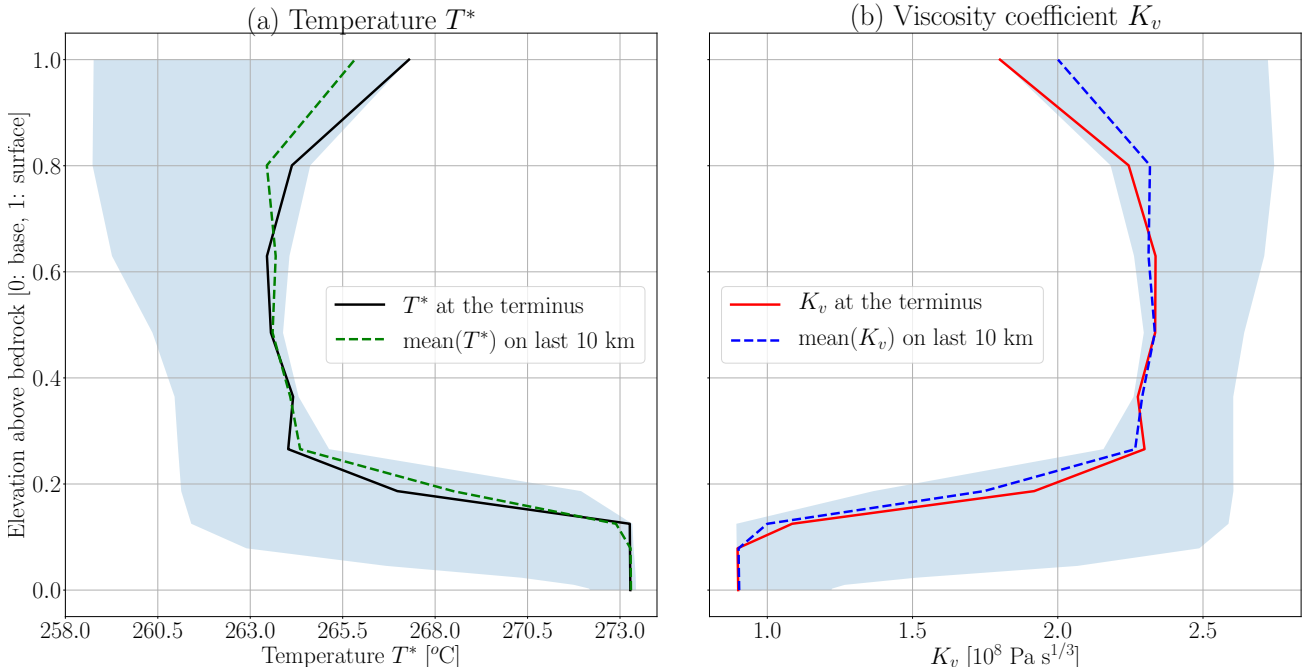

Figure 4.11: Temperature T^* and viscosity coefficient K_v in the Helheim glacier as inverted with ISSM inversion model (see Chapter 5). In shaded gray we show all the range of values in the last 40 km of the central flowline of the Helheim glacier. In (a) we show the profile of the temperature at the terminus (black curve) and the mean value on the T^* on the last 10 km before the terminus (dashed green curve). In (b) we show the viscosity coefficient at the terminus (red curve) and the mean value of the viscosity on the last 10 km before the terminus (dashed blue curve). In dashed

4.4.4 Terminus above or below hydrostatic equilibrium

In the previous simulations, the glacier was slightly grounded initially: it was 10 m higher than the elevation where it would have been at hydrostatic equilibrium (T_{ground} on Fig. 4.13 and solid green curve on Fig. 4.14). That is, the terminus front is upstream by 10/tan(2°)= 286 meters (measured on the horizontaly axis) relatively to the position

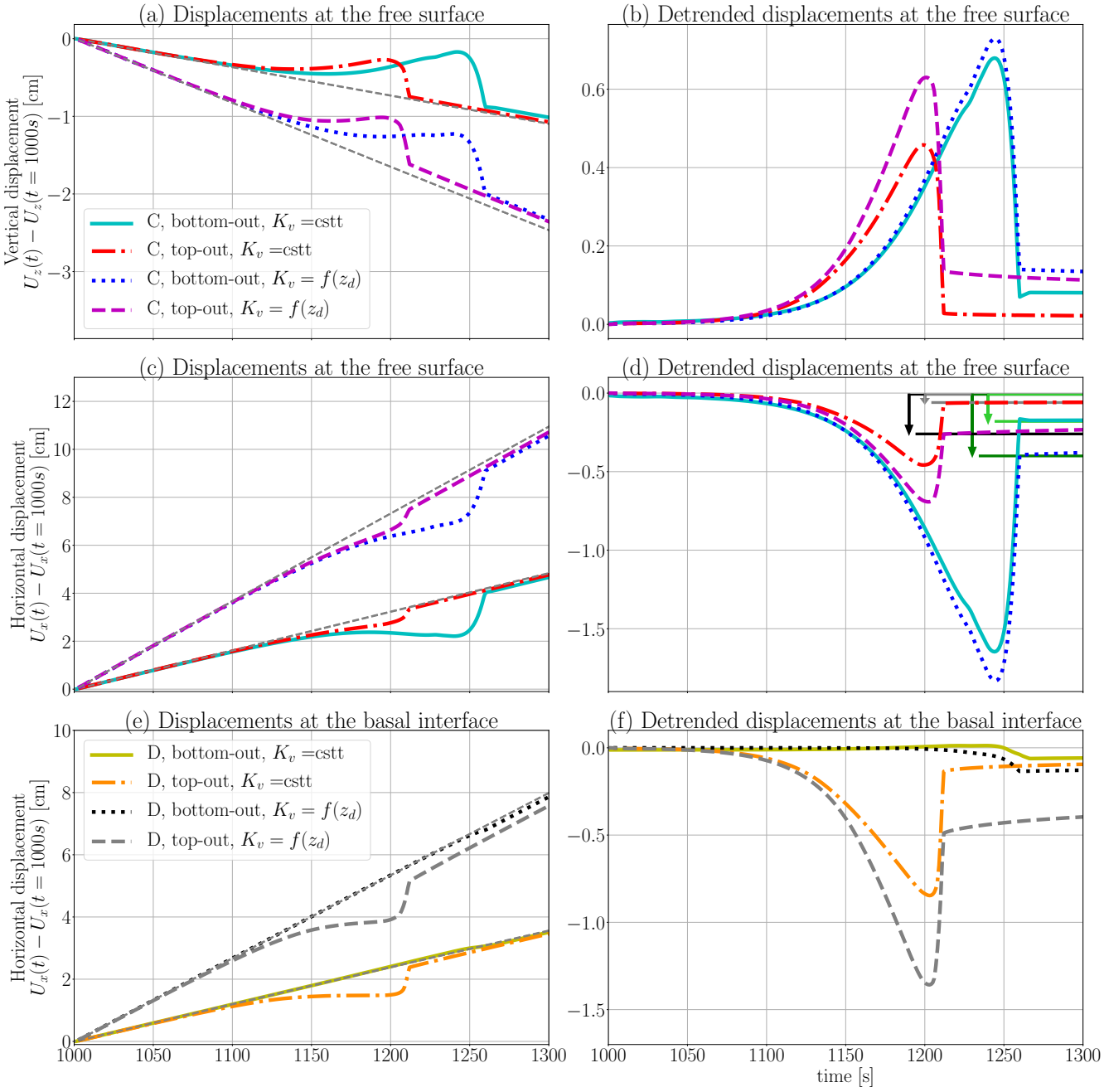

Figure 4.12: Same as Fig. 4.9 but where we replace the elastic simulations with the visco-elastic simulations with a coefficient of viscosity K_v that is a function of the depth z_d.

where the bedrock is such that, a glacier touching the ground would be at hydrostatic equilibrium. Note that if we change the ice density from 1025 kg/m^3 to 1028 kg/m^3 and the water density from 917 kg/m^3 to 910 kg/m^3 in the simulations, this would displace the equilibrium line by 10 meters upwards. Note that the values of the ocean water and ice densities in the field are usually within this range of values. Thus an uncertainty on the densities can lead to such a change (of $\pm$10 meters) in the height of the terminus relatively to its hydrostatic equilibrium.

To assess the sensitivity of the glacier dynamics to the position of the terminus relative to the hydrostatic equilibrium, we compare the results with two slightly different initial positions of the terminus. In the first geometry the terminus is initially at the hydrostatic equilibrium: T_{equi} on Fig. 4.13 and dashed red curve in Fig. 4.14. In the second geometry, the terminus is initially slightly under the hydrostatic equilibrium (initially 10 m below

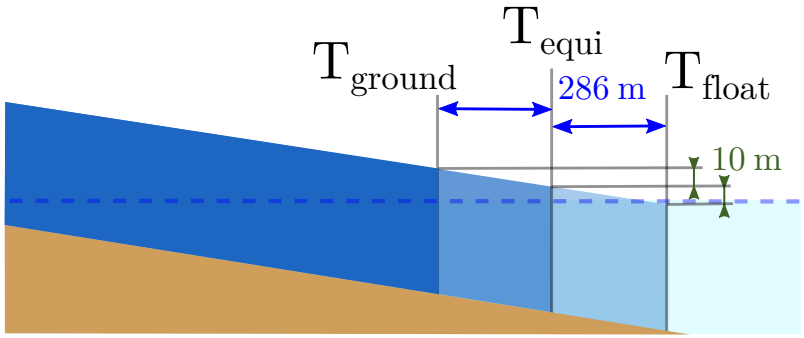

Figure 4.13: Schematic view of the terminus position for the sligthly grounded glacier (T_{ground}), for the terminus position at hydrostatic equilibrium (T_{equi}, 286 m downstream) and the terminus position below hydrostatic equilibrium (T_{float}, again 286 m downstream).

equilibrium, T_{float} in Fig. 4.13 and dotted blue curve in Fig. 4.14). The velocity for a slightly grounded glacier (horizontal velocity of 14.1 m/day) is higher than for a glacier at equilibrium (horizontal velocity of 12.9 m/day), which is higher than for a floating glacier (horizontal velocity of 11.7 m/day). The detrended displacements are similar: the amplitude of the reverse motion and the displacements after the end of the capsize differ by only < 5 % (see Fig. 4.14). This shows that the detrended response of the glacier to the capsize of an iceberg is not sensitive to a change of ± 10 m around the hydrostatic position of the glacier terminus.

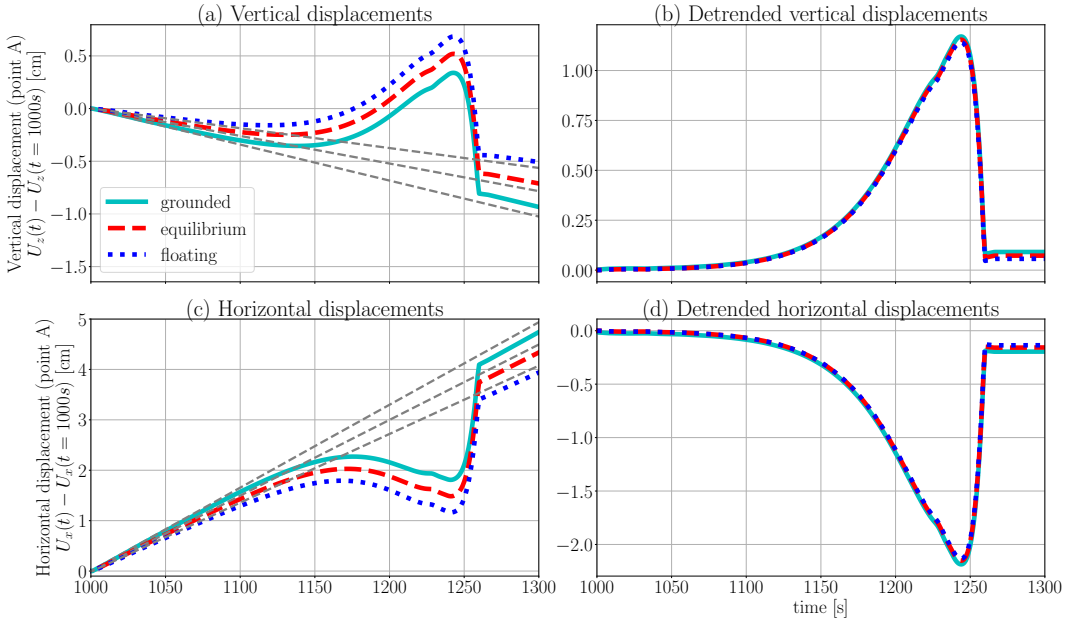

Figure 4.14: For a bottom-out capsize, horizontal and vertical displacements of point A (7 m from the terminus) for a geometry with the terminus slightly grounded (10 m higher, in cyan), at equilibrium (in dashed red) and slightly floating (10 m lower in dotted blue)

4.4.5 Influence of the friction law on the glacier dynamics

Displacements

We now investigate the influence of the friction parameters on the glacier response. The force of a bottom-out capsize hardly affects the basal sliding as shown on Fig. 4.7 b and Fig. 4.9e, thus we consider here a top-out capsize only. We analyse qualitatively the effect of a change in the parameters describing the basal friction: the Weertman

friction coefficient and the Coulomb friction coefficient. In the next Chapter 5, we investigate the influence of a change in the length of the Coulomb friction zone.

As before, we show the curves with and without the background trend Fig. 4.15. We observe that the horizontal displacements are doubled when reducing the Weertman coefficient by a factor of5 (from $5 \cdot 10^9$ Pa s/m to $1 \cdot 10^9$ Pa s/m) and again doubled when reducing it further by a factor of 2 (from $1 \cdot 10^9$ Pa s/m to $5 \cdot 10^8$ Pa s/m). The horizontal displacements also depend on the Coulomb friction coefficient. In Fig 4.16 we show the maximum horizontal displacement (relative to the case with no iceberg) for three values of the Weertman coefficient ($5 \cdot 10^9$ Pa s/m , $1 \cdot 10^9$ Pa s/m and $5 \cdot 10^8$ Pa s/m) and four values of the Coulomb friction coefficient 0, 0.2, 0.4 and 0.6 (range of values within that indicated in the literature, see section 4.2.4). We observe the higher variation of the maximum horizontal displacement with the Weertman friction coefficient than with the Coulomb friction coefficient. This may be linked with the higher extension of the Weertman zone compared to the Coulomb zone, and the higher values of the stresses in this zone (see section 4.4.5). Therefore, in this study, with all other parameters kept constant, the measurement of the maximum horizontal displacement at the surface of the glacier is a proxy for the Weertman friction coefficients. However, in practice the field values of the other parameters of the system -length of the Coulomb friction zone, viscosity, geometry, iceberg aspect ratio, type of capsize, length of the glacier tongue- are not strongly constrained. In order to estimate these parameters using the measurements of surface displacements, it would be necessary to make a more systematic parametric study.

Basal stresses during capsize

In order to investigate the possible signature of the capsize on the transmitted seismic waves, we calculate the sum of the stresses on the bedrock during capsize. We compare the horizontal component of this force ($F_{bedrock}$) to the horizontal iceberg force applied on the terminus $F_{iceberg}$. We plot the relative difference between these two forces $(F_{bedrock} - F_{iceberg})/\max(F_{iceberg})$ in Fig 4.17 (a) for a quasi-static simulation and in Fig 4.17 b for a dynamic simulation. In the simulations presented previously, we used a quasi-static approximation, that is we neglected the influence of the inertial term in the equation of motion eq. 4.14. In the quasi-static approximation, $F_{bedrock} - F_{iceberg}/\max(F_{iceberg})$ is negligible: < 0.1 % (with a maximum amplitude of the iceberg force of $\max(F_{iceberg} = 7\ 10^7$ N/m). For the dynamic simulation (Fig 4.17 b) there are some oscillations with an amplitude < 5 % due to numerical artefacts. there is no visible influence of the Coulomb friction coefficient on $(F_{bedrock} - F_{iceberg})/max(F_{iceberg})$ (Fig 4.17 b). The horizontal force applied by the iceberg on the terminus is directly transmitted to the bedrock. We discuss this results in section 4.6.1.

We investigate the local variations of the stresses transmitted to the bedrock during the capsize. To do so, we plot the shear stress σ_{xz} at the bed close to the terminus on Fig. 4.18: for the simulation with a Coulomb friction coefficient $\mu = 0.0$, without capsize (that is no resistance tangential to the bedrock) (a), with a top-out capsize (b), with a Coulomb friction coefficient $\mu = 0.2$ without capsize (c), with a top-out capsize (d), with a Coulomb friction coefficient $\mu = 0.6$ without capsize (e), with a top-out capsize (f). We plot the shear traction along two last kilometers behind the terminus, which is on the right side of the figure, at the position 40 km. The position of the transition between the Weertman and the Coulomb zone (750 m behind the terminus) is shown with the vertical black dotted line. We observe an effect of the capsize on the shear stress in particular around the time $t \approx 1200$ s (cyan, blue and black curves on Fig. 4.18 b, c and d). The local distribution of basal stresses is affected by the iceberg forcing and depends on the Coulomb friction coefficient: there exists a slight changes in the curves between Fig. 4.18 b, c, and d. To see these differences better, we show the shear stresses relative to the simulations without capsize in Fig. 4.19 for $\mu = 0.0$ in (a), $\mu = 0.2$ in (b) and $\mu = 0.6$ in (c). There is a local signature of the

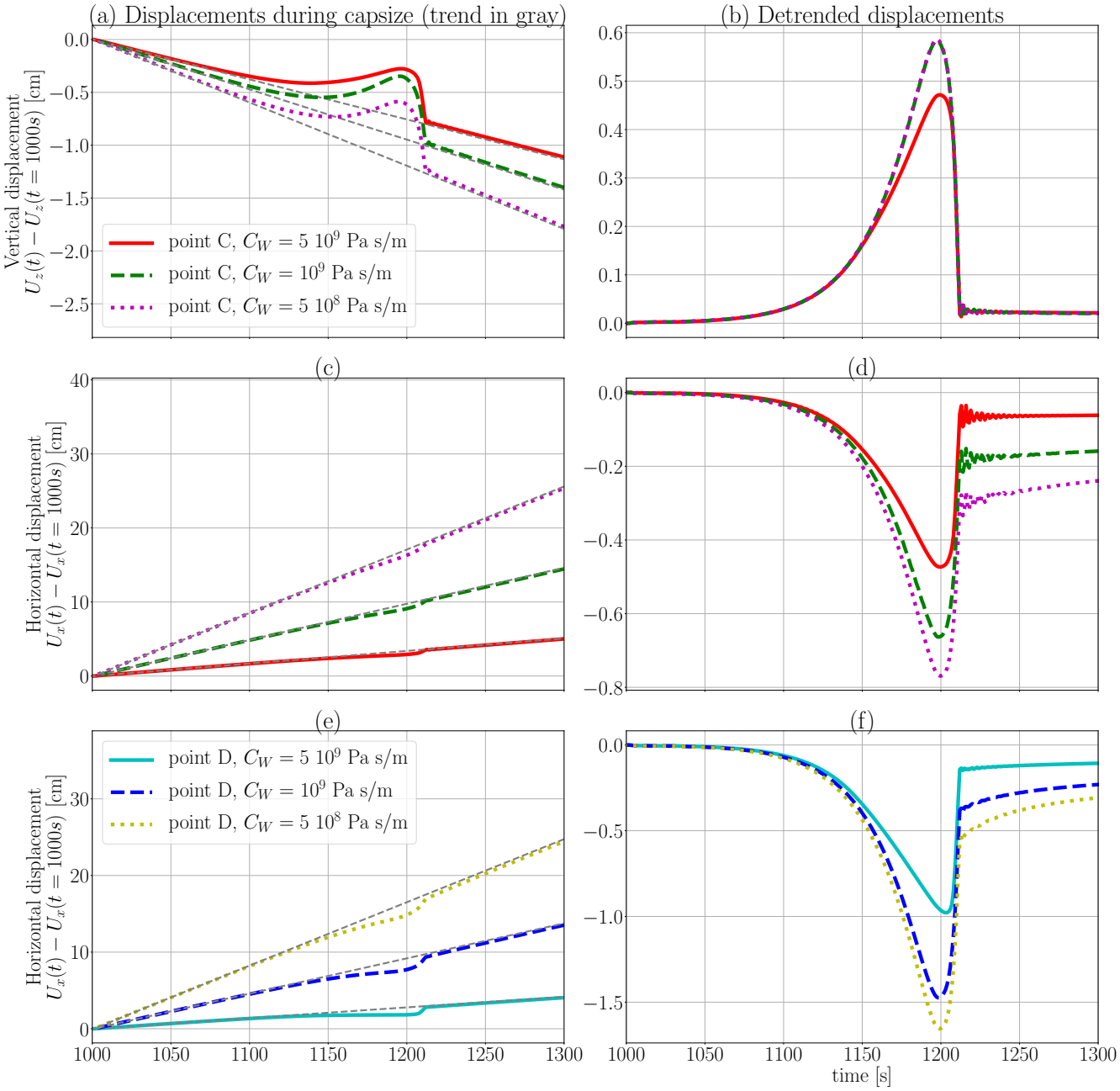

Figure 4.15: Displacements at point A (a-d) and point B (e-f) for a top-out capsize, with a Coulomb friction coefficient $\mu = 0.4$, and a Weertman friction coefficient $C_W = 5 \cdot 10^9$ Pa s/m (red and cyan), $C_W = 1 \cdot 10^9$ Pa s/m (dashed green and blue), and $C_W = 5 \cdot 10^8$ (dotted magenta and yellow).

Coulomb friction coefficient in the force transmitted to the bedrock during the capsize. Whether this signature is also detectable in the emitted on the seismic waves is had to say. This depends on the proximity of the station: the closer the station will be from the terminus front the more likely it may detect the elastic waves produced at the basal interface and distinguish them from those produced at the glacier terminus. This will also depend on the amplitude of the variations of the tangential stresses. This change in the tangential forces is produced by the force of the capsizing iceberg applied on the terminus front. The amplitude of the iceberg force is dependent on the iceberg height and aspect ratio (see Fig 4.4).

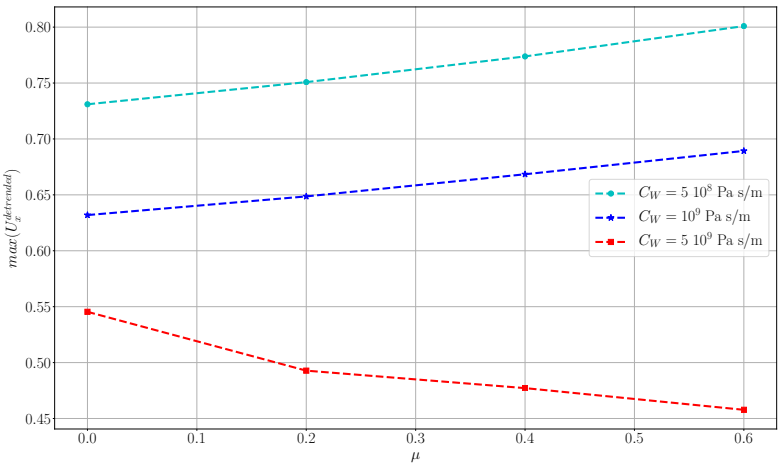

Figure 4.16: Maximum detrended horizontal displacements at the free surface (y-axis) for various Coulomb friction coefficients μ (x-axis) and for various Weertman coefficients C_W (indicated in the label).

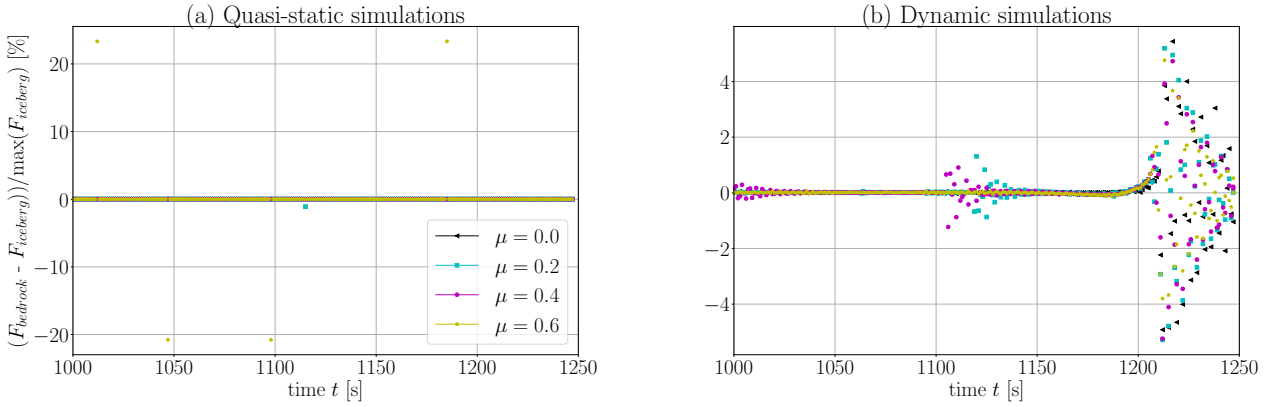

Figure 4.17: Relative difference between the external force applied on the terminus and the force transmitted in the bedrock $(F_{iceberg} - F_{bedrock})/max(F_{iceberg})$ for a top-out capsize, a grounded glacier, a Weertman coefficient of $5 \cdot 10^9$ Pa s/m, and for a Coulomb friction coefficient of $\mu = [0, 0.2, 0.4, 0.6]$.

4.5 Glacier with a floating tongue

In addition to the iceberg aspect ratio, the capsize type, the friction parameters, the temperature (viscosity) field, the other unknown parameters are the tongue's length and the crevasse field which affect the effective elastic modulus and the effective bending stiffness. In our model, the crevasse field is indirectly accounted for in the elasticity. We investigate here the sensitivity of the glacier response to the length of the floating tongue and its elasticity.

4.5.1 Effect of the type of capsize

We simulate a glacier with a floating tongue as shown in Figs. 4.2 and 4.1. In particular, we show the displacements of the point close to the grounding line (points A' and B') and close to the terminus front (points Y' and Z') as shown in Fig. 4.5 (b).

We plot the displacements at the surface of the glacier (points A' and Y') and at the base of the glacier (points B' and Z') for a 3 km long tongue, for a bottom-out and a top-out capsize in Fig 4.20. We compare these displacements

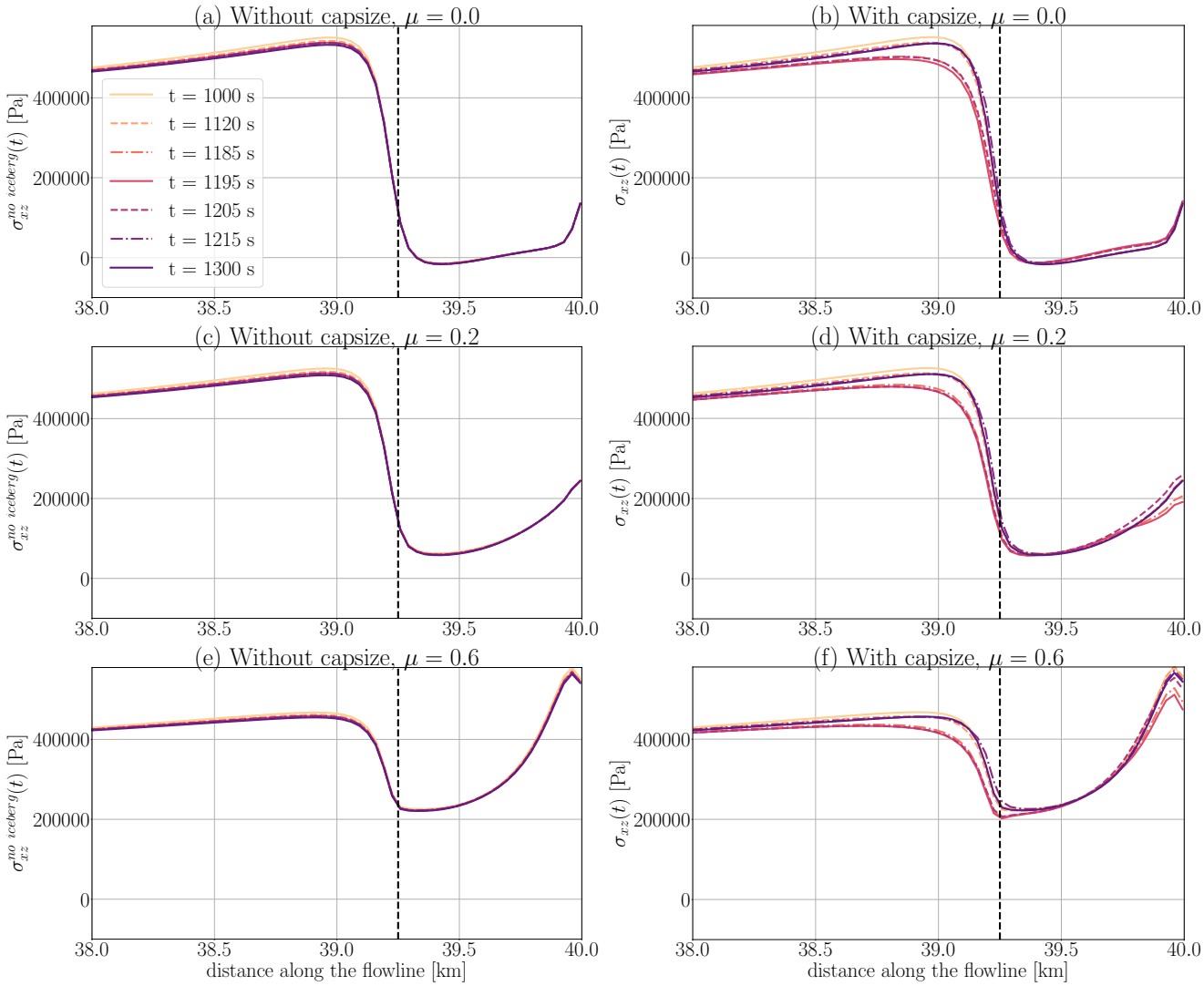

Figure 4.18: For a grounded glacier, and a Weertman coefficient of $5 \cdot 10^9$ Pa s/m, shear stresses $\sigma_{12}^{no\ iceberg}$ on the basal surface for a simulation without iceberg capsize (a,c,e), shear stresses σ_{12} on the basal surface for a simulation with iceberg capsize (b,d,f). For $\mu = 0.0$ (a,b), $\mu = 0.2$ (c,d), and $\mu = 0.6$ (e,f).

to those obtained with a glacier with no tongue (cyan and red curves) close to the terminus, at points A and B (Fig 4.20 a, c and e). For a glacier with a floating tongue, we observe that during a bottom-out capsize, the terminus moves upwards ($\approx$ 15 cm, dotted blue curve on Fig 4.20 b), whereas during a top-out capsize it moves downwards ($\approx$ 10 cm, dashed magenta curve on plot Fig 4.20 b). The vertical displacements during capsize are more than 10 times bigger at the terminus than at the grounding line for the bottom-out capsize (dotted blue curve on Fig 4.20 a and b). During the bottom-out capsize, the terminus retreats by $\approx$ 5 cm during capsize (blue curve on Fig 4.20d), whereas it advances by $\approx$ 1 cm for a top-out capsize. Close to the grounding line, the glacier free surface moves upwards and has a reverse horizontal motion for both the bottom-out and the top-capsize with or without tongue (Fig 4.20 a and b).

In Fig. 4.21, we show the position of the glacier free surface and basal interface in the two kilometers behind the terminus during capsize. The surface is shown at the time of the maximum of the force (that is $t = 1242$ s for the bottom-out capsize and $t = 1199$ s for the top-out capsize). For the glacier with a 3 km floating tongue, we show a zoom on the two kilometers behind the grounding line in Fig. 4.22 (a) and (c) and the last 5 kilometers before the terminus in Fig. 4.22 (b) and (d). We summarize these plots schematically in Fig. 4.21 (c) and Fig. 4.22 (e).

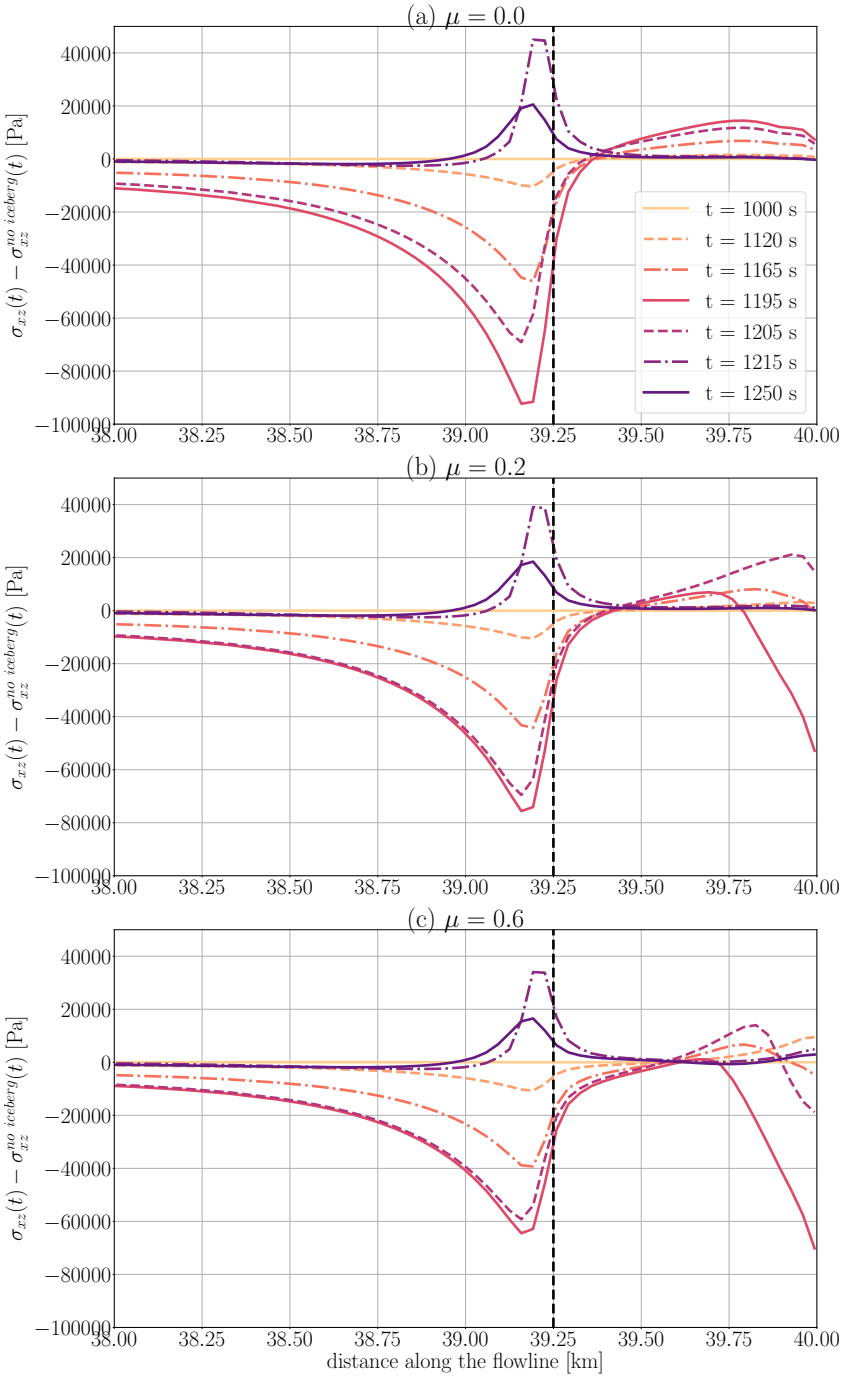

Figure 4.19: For a grounded glacier, and a Weertman coefficient of $5 \cdot 10^9$ Pa s/m, difference between the shear stresses σ_{12} on the basal surface for a simulation with iceberg capsize and the shear stresses $\sigma_{12}^{no\ iceberg}$ on the basal surface for a simulation without iceberg capsize. For $\mu = 0.0$ (a), $\mu = 0.2$ (b), and $\mu = 0.6$ (c).

Field measurements of the vertical and horizontal displacements at the surface of the glacier close to the terminus can constrain the type of capsize (top-out or bottom-out), and the length of the glacier tongue.

4.5.2 Effect of the Young's modulus

In Fig 4.23 we show four simulations with a Young's modulus of 9.3 GPa, 6 GPa, and 3 GPa for a 3 km long glacier tongue and a 1.5 km long glacier tongue. As expected, the most extreme displacements at the surface of the glacier are obtained for the simulation with the smaller value of the Young's modulus ($E = 3$ GPa) and the

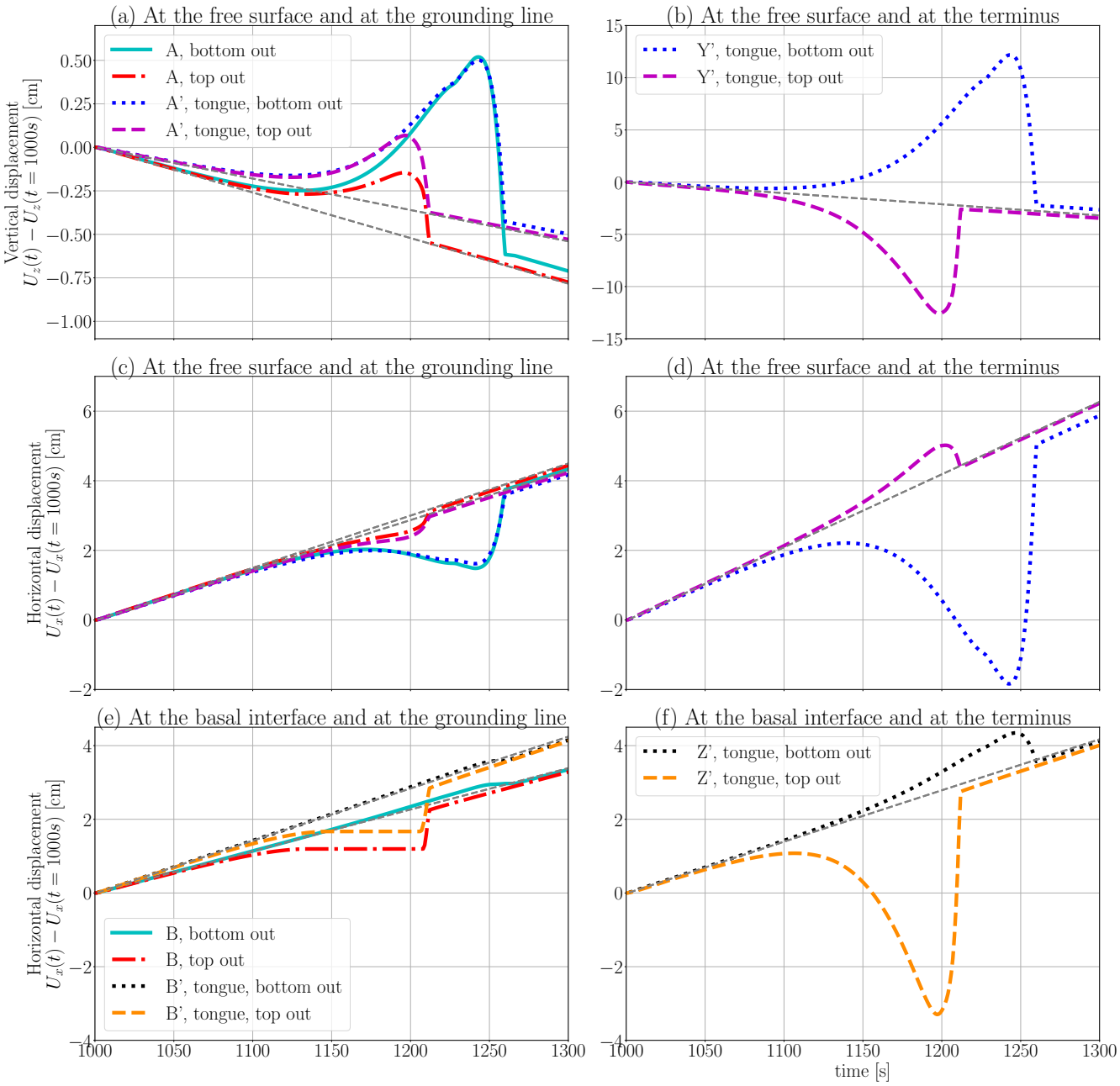

Figure 4.20: Vertical displacements at the free surface of the glacier (top), horizontal displacements at the free surface (middle) and at the base (bottom), 7 m upstream from the grounding line (left) and 57 m upstream from the terminus (right).

longer glacier tongue (3 km). We plot the variation of the detrended reverse motion with respect to the Young's modulus for a glacier without a floating tongue, for a glacier with a 1.5 km tongue and a 3 km tongue in Fig 4.24. We observe in Fig 4.24 (a) and (b) that the amplitudes of the horizontal and vertical displacements increase with the tongue length and the Young's modulus. Interestingly, the ratio between the vertical and the horizontal motion (Fig 4.24 c) is weakly dependent on the Young's modulus. This suggests that using only GPS measurements on the glacier during capsize, and without knowing the Young's modulus of the ice, one can estimate the length of the glacier tongue.

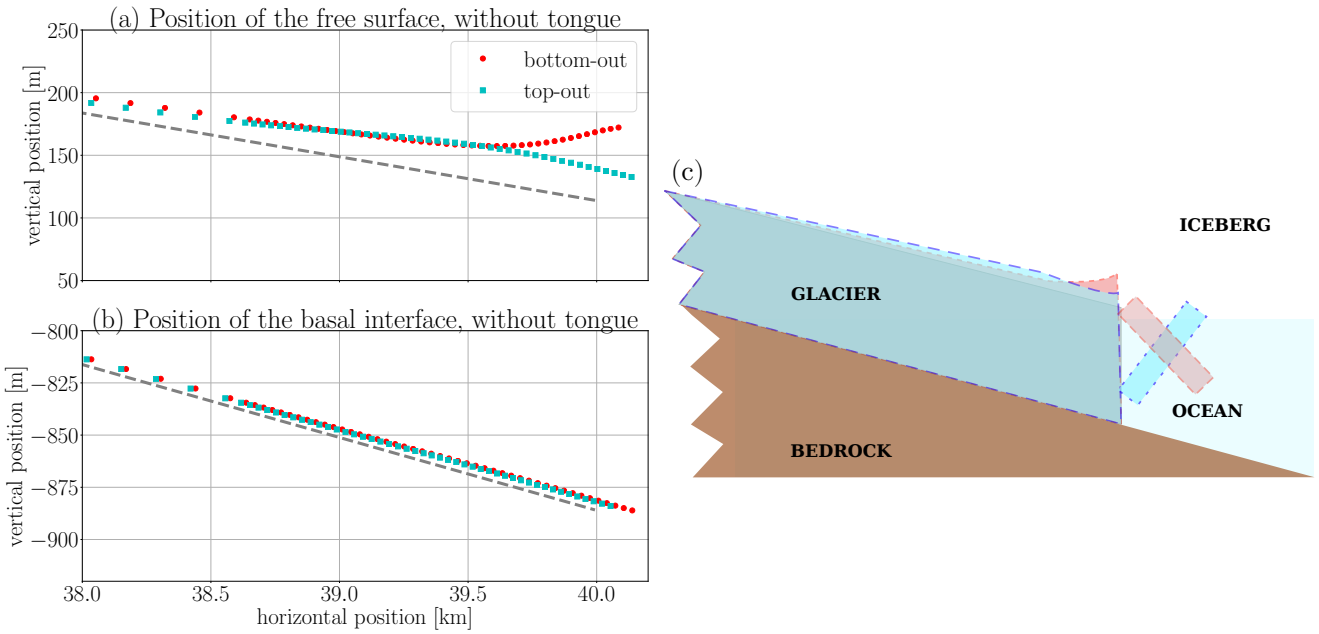

Figure 4.21: For a glacier without a glacier tongue, position of the free surface in a and the basal interface in (b). The gray dashed lines corresponds to the undeformed surface (without capsize) X. The red and blue lines represent the deformed surface X'. In order to visualised clearly the deformation, we plot the deformed surface such that the displacements relatively to the simulation without capsize are amplified by a factor 5000, that is $X' = X + 5000\ dX$. Schematic view of the displacements in (c).

4.6 Discussion

4.6.1 Glacier dynamics and effect on the force transmitted to the bedrock

We showed that the iceberg force exerted on the terminus is directly transmitted to the bedrock, although locally the shear stresses are affected by the capsizing iceberg and sensitive to the friction coefficient. In the simple case of a one-dimensional elastic glacier tongue, the inertial term in the equation of motion eq. 4.14 can be estimated by integrating the inertia of a column of ice over the whole glacier tongue:

$$I = \int_{L_free} \rho_i \ddot{u}(x,t) H dx \tag{4.15}$$

with L_{free} the length of the glacier tongue, ρ_i the ice density, $\ddot{u,}t$ the second time derivative of the displacements at the position x, H the height of the glacier tongue. The displacement at the terminus $u(x_{term}, t)$ is directly proportional to the force of the capsizing iceberg applied on the terminus $F(t)$: $u_{term} = F/k$, with $k = (HE)/L_{free}$ the stiffness of the glacier tongue, with E the Young's modulus of the ice. For a one dimensional elastic beam, the displacements along the glacier tongue decrease linearly with the distance to the terminus, thus $u(x) = u(x_{term})x/L_{free}$. This yields to an estimation of the inertia of the glacier tongue $I(x)$. In the case of a glacier tongue of length $L_{free} = 5$ km, a height $H = 1000$ m, and a Young's modulus $E = 3$ GPa, the maximum amplitude of $I(x)$ is $\approx 8\ 10^5$ N/m (per unit of length in the third dimension). That is ≈ 0.1 % of the iceberg force amplitude (per unit of length in the third dimension), therefore, the inertial term is negligible. In the case of a glacier without a floating tongue, it is expected to be even smaller because of the resisting forces at the basal surface. This is consistent with the observation made in section 4.4.5 that the force transmitted to the bedrock is similar to the iceberg force exerted on the terminus.

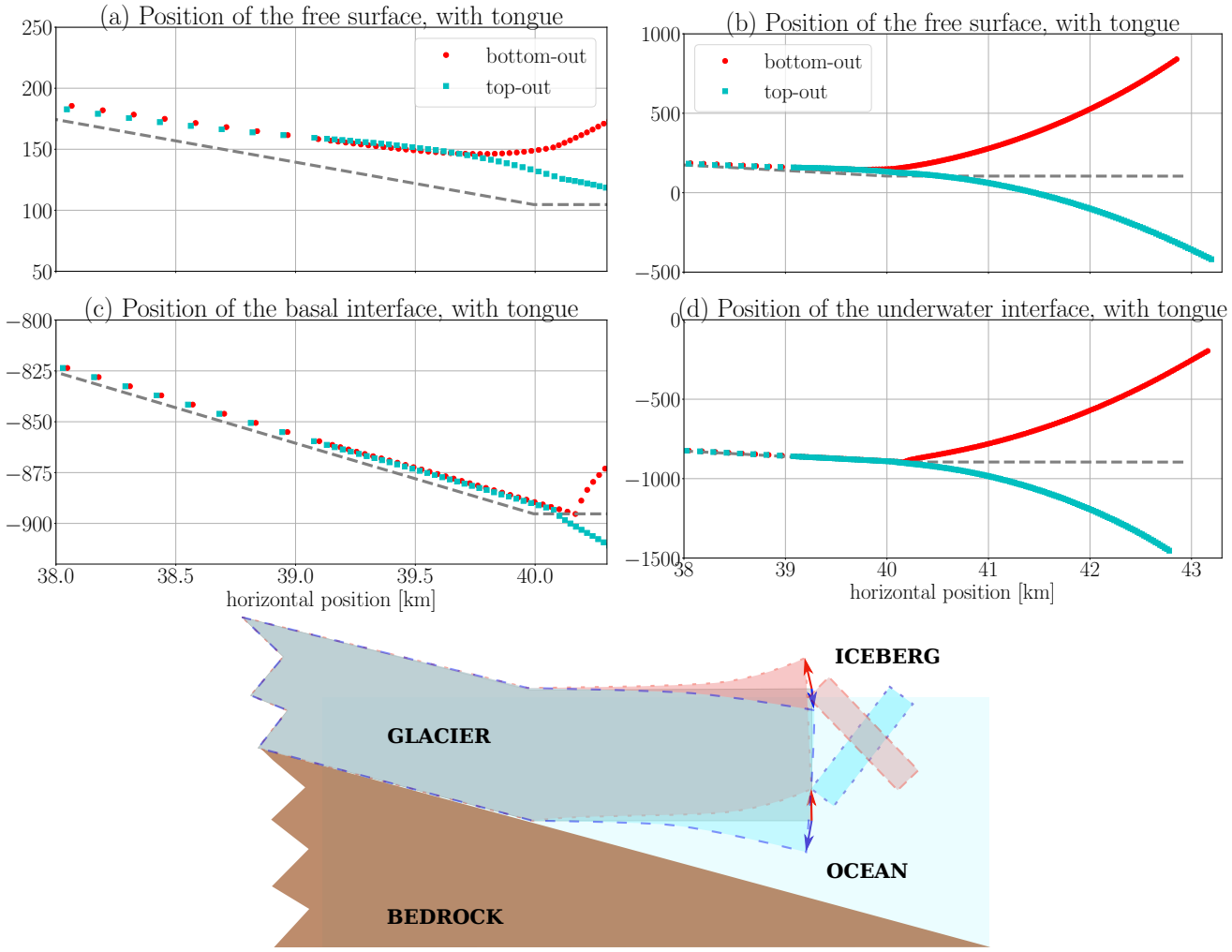

Figure 4.22: Same as Fig. 4.21, for a glacier with floating tongue. The gray dashed lines corresponds to the undeformed surface (without capsize). Position of the free surface in (a) and (b) and the basal interface in (c) and (d). Caption (a) is a zoom of the caption (b) in order to see the deformed surface at the grounding line (at 40 km) and caption (c) is a zoom of caption (d). The terminus is at 43 km (in b and d). Schematic view of the displacements in (e).

4.6.2 Vertical motion during capsize

Measurements of the displacements at the surface of the Helheim glacier during the capsize of an iceberg show a reverse horizontal motion and a downward vertical motion (Murray et al., 2015a, fig. 2) adapted in Fig 4.8. These displacements are consistent with their laboratory experiments (Murray et al., 2015a, fig. 3) for a bottom-out capsize. The authors suggest that the downward vertical motion is due to a drop in the hydrodynamic pressure.

In our simulations with a bottom-out capsize against a glacier with a floating tongue, we observe a reverse horizontal motion and an upwards vertical motion close to the grounding line (blue dotted curves in Fig. 4.20 a and b) and close to the floating terminus (blue dotted curves in Fig. 4.20 b and d). For a top-out capsize, we observe a similar trend close to the groundind line: a reverse horizontal motion and an upwards motion (red curve in Fig. 4.20 a and b). However, for the top-out capsize, and close to the terminus, we observe a small horizontal accelerated motion and a downward vertical motion (purple dashed curve in Fig. 4.20 a and b). This result suggests that the top-out capsize would more likely explain the reverse and downward motion (somewhere between the grounding line and the terminus) as observed by (Murray et al., 2015a)To investigate more precisely the hydrodynamic effects, one

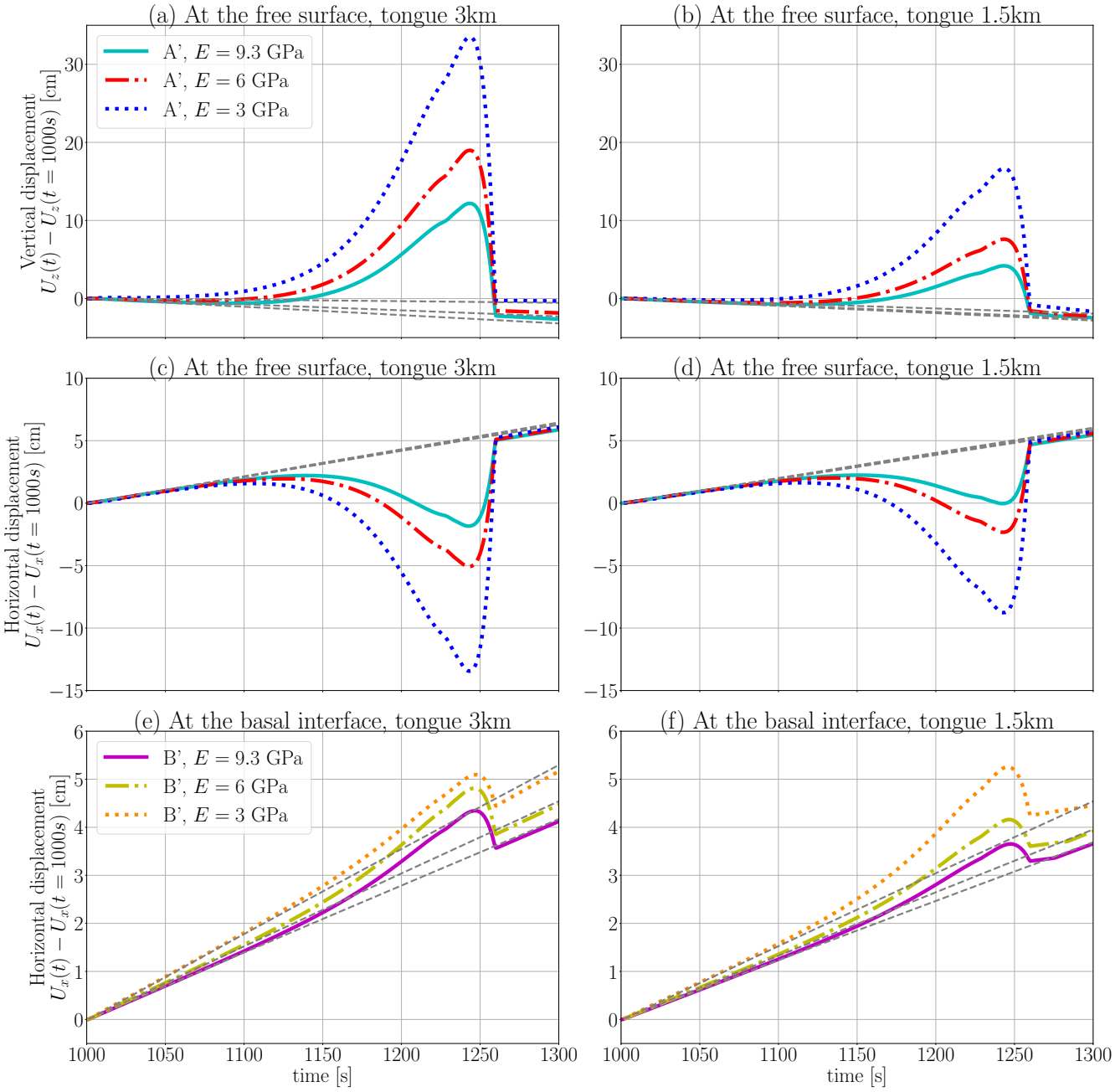

Figure 4.23: Displacements at point A', for a bottom-out capsizing iceberg, and a glacier with a long (3 km long) floating tongue (left) or a short (1.5 km long) floating tongue, and the Young's modulus of the glacier $E = 9.3$GPa, $E = 6$GPa or $E = 3$GPa. Displacements for a simulation with no capsize are plotted in gray.

perspective would be to couple the two state-of-the-art solvers used in this PhD: the solid mechanics Z-set solver and the Computational-Fluid-Dynamics solver ISIS-CFD. As a first step before a full coupling, we could apply on the underwater part of the glacier tongue a downwards force to reproduce the drop in the hydrodynamic pressure measured in (Murray et al., 2015a).

Moreover, it this study we assume a purely horizontal contact force. In practice, there is a small vertical force component (Sergeant et al., 2016, 2018). In the case of a bottom-out capsize, this tangential force pushes the glacier tongue downwards. However, we ran such simulations with a downward vertical force. With this vertical downward force on the terminus, the upwards motion was reduced. However, even for an extreme amplitude of the vertical force with the same amplitude as the horizontal force, the induced vertical motion is still upwards.

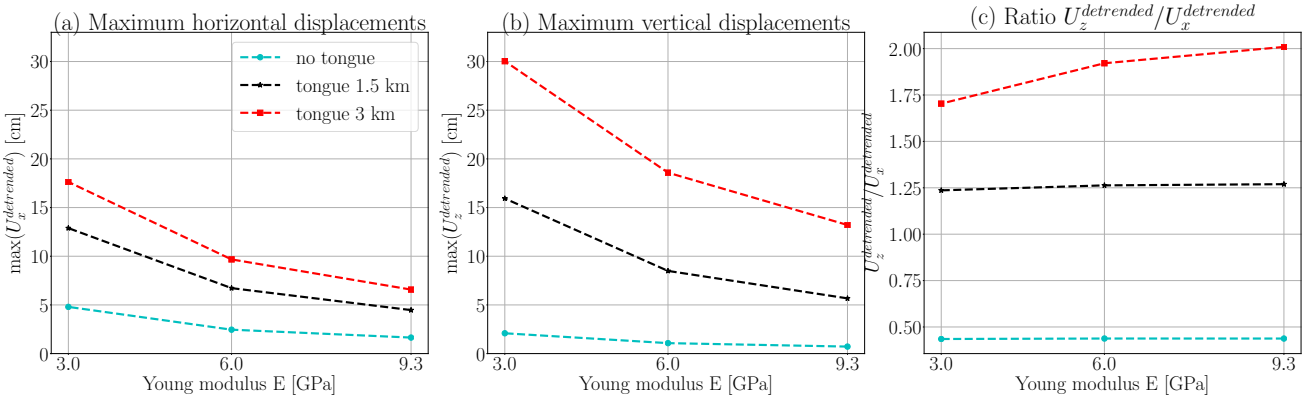

Figure 4.24: Maximum amplitude of the detrended horizontal (a) and vertical (b) reverse motion, and the ratio between the maximum amplitude of the vertical and the horizontal detrended motion (c)

4.7 Conclusion

Here we investigated the physical process at play during the capsize of an iceberg at the glacier front, through several sensitivity analyses of the response of the glacier to a capsize, for the parameters of the rheology, the friction laws, the geometry and the capsize type. For a grounded glacier, for both the top-out and the bottom-out capsize, there is a reverse horizontal motion and an upward vertical motion. In the case of a bottom-out capsize, the vertical displacements are twice smaller than the horizontal displacements, whereas in the case of a top-out capsize, horizontal and vertical displacements are similar. This observation is also valid in the case of a glacier with a floating tongue, and in the part of the glacier upstream from the grounding line. This suggests a possible way to invert for the type of capsize, using only the GPS measurements on the glacier.

We compared the response of a visco-elastic glacier and the response of a purely elastic glacier. We showed that the displacements of the glacier during capsize are mainly explained by the elastic compression of the ice. The viscous deformation also explains part of the amplitude of the displacements. In the field measurements, a shift of the displacements at the end of the capsize compared to the background trend was observed. This is qualitatively explained by a viscous deformation of the ice during capsize, however it is underestimated in our model. A more precise rheology for the ice that includes the transient creep response could help to explain the higher amplitude of the observed residual.

The motion of the floating tongue is upwards and backwards for the bottom-out capsize and downwards and backwards for a top-out capsize. In the field, a backwards and downwards motion was observed for capsize, that was identified, most probably as a bottom-out capsize. In future work, a downwards force on the underwater surface of the glacier could be applied in our model, in order to assess the impact of hydrodynamic forces on the glacier tongue motion.

In the case of a top-out capsize without a glacier tongue, the force transmitted to the entire bedrock surface is equal to the capsize force applied on the terminus. This suggests that the force integrated on the whole basal surface does not contain any information on the glacier motion and basal friction. However, during the capsize, the basal shear stresses close to the terminus are locally affected. In the Coulomb zone, these stresses are governed by the Coulomb friction coefficient. This suggests that the locally integrated force on the basal surface, close to the terminus, contains the signature of the Coulomb friction coefficient.

In the next Chapter 5, we model a glacier with the geometry of the Helheim glacier in a recent year (2007), and a heterogeneous ice viscosity associated with the temperature field within the glacier.

CHAPTER 5

Modelling the response of the Helheim glacier to the capsize of an iceberg

5.1 Introduction

In the previous Chapter 4, we investigated the response of a glacier with a simple geometry: the surface of the bedrock and the glacier were initially parallel and slightly sloping down by 2° in the ice flow direction (*positive bed slope*).

However, bedrock below Greenland glaciers has an irregular shape (e.g. see bathymetry of the Helheim glacier in Fig. 5.4 a). Theoretical studies in literature describing the behaviour of ice at the basal interface define the bathymetry by giving its roughness: the ratio between the size of an asperity and the distance between two asperities of the same size (e.g. Weertman, 1957). At the scale of hundreds of meters, the slope changes its sign along the glacier flowlines. In particular, the central part of Greenland ice sheet is lying on a bedrock which is below sea level. Moving towards the coasts, the bedrock elevation rises to reach elevations above sea level (Morlighem et al., 2017): in these parts, the ice sheets flows along *negative bed slopes* (sloping up in the ice flow direction).

The geometry of the bedrock has an influence on the glacier dynamics, especially at short time scales and close to the terminus (e.g. Durand et al., 2011). When a grounding line is located on a negative bed slope, it may be unstable and retreat to reach a new stable position (Marine Ice Sheet Instability (MISI) (e.g. Weertman, 1974; Gudmundsson et al., 2012). This instability is a major concern in estimations of future sea level rise (e.g. Ritz et al., 2015; Robel et al., 2019; Feldmann and Levermann, 2015). Similarly, a *pinning point*, which is a submarine mount in contact with a glacier, will have a stabilising effect. If the glacier looses contact with the pinning point, the glacier will accelerate its retreat (Favier et al., 2012, 2014). Due to tidal forcing, a pinning point can periodically be in contact with the glacier tongue: at high tide, the glacier moves upwards, and can lose contact with a pinning which reduces the stabilising buttressing forces (Robel et al., 2017; Tsai and Gudmundsson, 2015). Walter et al. (2010) observed a significative change in the style of calving and its occurrence when the terminus of the Columbia glacier changed from being grounded to being floating.

The time scale of the response of a glacier to the capsize of an iceberg is a few minutes, which is short compared to the seasonal or yearly variations of glacier dynamics widely studied in the context of long term mass losses estimations. The few studies in literature that investigated the interactions between a capsizing iceberg and a glacier front considered a purely elastic or rigid terminus (Tsai et al., 2008; Sergeant et al., 2019; Murray et al., 2015a). At the time scale of days, a number of studies have proposed mechanical models to investigated the impact of tidal forcing on the grounding line position and the stability of tide water glaciers: e.g. Sayag and Worster (2013); Tsai and Gudmundsson (2015) used an elastic model, e.g. Brunt and Macayeal (2014); Robel et al. (2017) used a visco-elastic model. A review of ice sheet dynamic models at long time scales is given by (Schoof and Hewitt, 2013). To model the flow of ice sheets at long times, Navier-Stokes equations are usually solved with a few assumptions in order to get reasonable computational costs. In most models, the Stokes equations are used: this means that the inertial terms in the equations of motion are neglected. The ice behaviour is usually described by a non-linear viscous rheology with various degrees of complexity (section 4.2.2). Time and space are discretized, and a finite difference, finite volume, finite element method or spectral method is used (see the comparison of models done by Pattyn et al., 2008, 2012). The spatial extent can be reduced to one or two dimensions, provided some simplifications.

Other approximations are usually added to simplify the equations. The Shallow Ice Approximation (MacAyeal, 1989) is used when modelling a zone with a horizontal span larger that the glacier height.The Blatter-Pattyn approximation (Blatter et al., 1998; Pattyn, 2003) assumes a simplification in the gradients of velocity and a simplified vertical component of the stress balance equation as explained in section 5.2.

In this Chapter we investigate the response of a glacier with visco-elastic behaviour and with the geometry of the Helheim glacier, to the force of a capsizing iceberg on the glacier front. In particular, we aim to better understand the transitory motion observed at the surface of the Helheim glacier during a few capsize events (Nettles et al., 2008; Nettles and Ekström, 2010; Murray et al., 2015a,b).

To simulate the response of the Helheim glacier to the capsize of an iceberg, we run two-dimensional finite element simulations, with the Z-set software described previously in section 4. To initiate the simulation, we include the precise geometry along the central flowline, the value of the temperature dependent rheology of the ice at each point. On this complex geometry, the implementation of the Weertman friction law has given numerical challenges, thus it is not yet implemented. Therefore, we apply the Coulomb friction law on the whole basal surface. This is a first step in the study of the response of the Helheim glacier to the capsize.

The Helheim glacier is near grounded according to observation of the response of the glacier to the tides forcing (Kehrl et al., 2017). However, the length of and height of the floating tongue is not well monitored and varies in time. Here, we consider two different geometries for the Helheim glacier: a grounded geometry and a Helheim glacier with a floating tongue.

In this Chapter, we investigate the impact of the Coulomb friction law on the response of the grounded Helheim glacier. Because of the significative impact of this coefficient on the response, and on the background velocities we investigate whether this is still the case when the Coulomb friction zone does not cover the whole basal interface. To do so, we switch to the model geometry, for which we can include a Weertman law and a Coulomb friction law with adjustable lengths. Then we analyse the response of the Helheim glacier with a floating tongue to a capsize at the glacier front.

5.2 Results of the ISSM inversion

To initiate the behaviour of the Helheim glacier using the Z-set software, we use results from a state-of-the-art for ice flow modelling. Collaborators at AWI (Martin Rueckamp and Angelika Humbert) who develop and run this model, have produced a visco-elastic Helheim ice flow model setup. This setup makes use of a basal friction coefficient, k^2_{inv} and temperature distribution that are retrieved by an inversion method based on velocities and measured temperatures at the glacier surface for a three-dimensional modelling of the Helheim glacier drainage basin.

The Ice-Sheet and Sea-level System Model (ISSM Morlighem et al., 2010; Larour et al., 2012), an open source finite element ice flow model (purely viscous) that simulates the thermodynamics of ice sheets and outlet glaciers.

The surface temperature values are a multiyear mean from the period 2000-2015 taken from RACMO2.3 (Noël et al., 2018). The geometry is taken from the latest BedMachine v3 database (Morlighem et al., 2017). The surface velocities used as target during the inversion process for each individual capsize events are taken from the Rosenau et al. (2015) database (available on the webpage `https://data1.geo.tu-dresden.de/flow_velocity/index.shtml`) that was calculated using Landsat 1 to 8 satellite images. The ice sheet front position was manually clipped using this dataset.

The ice flow model solves the thermo-mechanical steady-state flow of an ice sheet. The solution is an iterative calculation, until convergence is achieved for the friction coefficient, the velocity and enthalpy (i.e. temperature and water content) and the thermo-mechanical equilibrium. Model calculations are performed on a structured finite element grid with a horizontal resolution of 0.25 km. The domain is vertically extruded with 15 layers refined to the base.

In practice, the model solves the full-Stokes equation, but they employ the Blatter-Pattyn higher order approximation (Blatter et al., 1998; Pattyn, 2003), to allow reasonable model accuracy and computational costs.

The Blatter-Pattyn approximation includes two assumptions:

- the horizontal gradients of the vertical velocity are small compared with the vertical gradients of the horizontal velocities

$$|\frac{\partial w}{\partial x}| \ll |\frac{\partial u}{\partial z}|$$

and

$$|\frac{\partial w}{\partial y}| \ll |\frac{\partial v}{\partial z}|$$

which yields to $\dot{\epsilon_{xz}} = \frac{1}{2}\frac{\partial u}{\partial z}$ and $\dot{\epsilon_{yz}} = \frac{1}{2}\frac{\partial v}{\partial z}$. This is an assumption that is valid for most of the ice sheet domain (Pattyn, 2003).

- the hydrostatic approximation is assumed on the vertical component of the force balance, that is:

$$|\frac{\partial \sigma_{xz}}{\partial x}| \ll |\frac{\partial \sigma_{zz}}{\partial z}|$$

and

$$|\frac{\partial \sigma_{yz}}{\partial y}| \ll |\frac{\partial \sigma_{zz}}{\partial z}|$$

, that yields $\frac{\partial \sigma_{zz}}{\partial z} \approx \rho g$

The constitutive equation governing the creep of the ice is the generalized Glen's flow law with $n = 3$ (Glen, 1958; Steinemann, 1954):

$$t^D = 2\eta D = 2(1/2A^{-1/n}\dot{\epsilon}_{\text{eff}}^{(1-n)/n})D, \tag{5.1}$$

with t^D deviatoric part of the Cauchy stress tensor, $D = 1/2(\nabla \mathbf{v} + (\nabla \mathbf{v})^T)$ the train rate tensor, $\dot{\epsilon}_{\text{eff}}$ the effective strain rate (2^{nd} invariant of the strain-rate tensor, Pattyn (2003, Eq. 13 therein)), and $A(\omega, T^*)$ the flowrate factor. This law is equivalent to that used in Z-set (eq. 4.2 and eq. 4.3), with the coefficient of viscosity being simply a factor of $A^{-1/n}$:

$$K_v = \frac{3^{(1/6+1/2)}}{2^{(1/3)}}A^{-1/n} \tag{5.2}$$

The flow rate factor is assumed to be dependent on the temperature T^* (temperature relative to the pressure melting point T_{pmp}) and liquid water fraction ω

$$A(\omega, T^*) = \begin{cases} A_0 e^{-Q_a/(RT)} & \text{for } T^* < T_{\text{pmp}}, \\ A_0^t(1 + 181.25\omega) & \text{for } T^* = T_{\text{pmp}}, \end{cases}$$

T^* is the absolute temperature corrected for the pressure melting point $T^* = T + \beta P$, with $\beta = 7.910^{-8}\,\text{K}\,\text{Pa}^{-1}$ the Clausius-Clapeyron constant, and P the pressure in Pa, positive in compression. Note that $T^* = T_{\text{pmp}} = 273.15\,\text{K}$ at the pressure melting point. The upper bound of the water fraction ω is 0.01 to ensure validity of the flow rate factor parameterization in the temperate part with the experimental dataset (Duval et al., 1977; Lliboutry and Duval, 1985).

The coefficient A_0 is defined as:

$$A_0 = \begin{cases} 3.61\ 10^{-13}\ \mathrm{Pa}^{-3}\ \mathrm{s}^{-1} & \text{if } T^* < 263.15\ \mathrm{K} \\ 1.73\ 10^{3}\ \mathrm{Pa}^{-3}\ \mathrm{s}^{-1} & \text{if } T^* > 263.15\ \mathrm{K} \end{cases}$$

and $A_0^t = A(T^* = T_{\mathrm{pmp}}, \omega = 0)$, for the continuity of the flowrate factor A.

At the base, basal sliding is allowed everywhere and the basal drag, τ_b, is written:

$$\tau_b, i = -k^2 N^{1/p} |v_b|^{1/p-1}\ v_{b,i} \tag{5.3}$$

where $v_{b,i}$ is the basal velocity component in the horizontal plane and $i = x, y$ and k^2 the friction coefficient. The effective pressure is parameterized as $N = \rho_i\ g\ h - \rho_w\ g\ \max(0, z_{\mathrm{sealevel}} - z_b)$. The parametrisation accounts for full water-pressure support from the ocean wherever the ice sheet base is below sea-level, even far into its interior where such a drainage system may not exist (see cyan dotted line in Fig. 5.4c). The friction exponent p is set to $p = 1$ (linear).The boundary conditions are a stress-free condition at the glacier upper surface, and a hydrostatic water pressure at the ice-seawater interface. At lateral boundaries observed velocities are used as Dirichlet boundary conditions.

For the thermal model, we impose a Dirichlet condition at the surface such as the $T(x, y)$ is set to the measured dataset.

The unknown parameter k^2 in the friction law is retrieved by an inverse problem. Within the inverse problem a cost function (J), that measures the misfit between observed, v^{obs}, and modelled velocities, v_{x}, is minimised. They use the observed velocities from the MEaSUREs project (Joughin et al., 2016, 2018) as target within the inversion. The cost function is composed of two terms which fit the velocities in fast- and slow-moving areas. A third term is a Tikhonov regularisation to avoid oscillations. The cost function is defined as follows:

$$J(\mathbf{v}, k_{\mathrm{inv}}) = J_0(\mathbf{v}) + J_{\mathrm{reg}}(k_{\mathrm{inv}}), \tag{5.4}$$

$$J_0(\mathbf{v}) = \gamma_1 \frac{1}{2} \int_{d\Gamma_s} (v_x - v^{\mathrm{obs}})^2 d\Gamma_s + \gamma_2 \frac{1}{2} \int_{d\Gamma_s} \left(\ln \left(\frac{\sqrt{v_x^2 + \varepsilon}}{\sqrt{v^{\mathrm{obs}}{}^2 + \varepsilon}} \right) \right) d\Gamma_s, \tag{5.5}$$

$$J_{\mathrm{reg}}(k_{\mathrm{inv}}) = \gamma_t \frac{1}{2} \int_{\Gamma_b} \nabla k_{\mathrm{inv}} \cdot \nabla k_{\mathrm{inv}}\ d\Gamma_b, \tag{5.6}$$

where ε is a minimum velocity used to avoid singularities and Γ_s and Γ_b are the ice surface and ice base, respectively. An L-curve analysis was performed to pick the Tikhonov parameter γ_t (not shown). The inverse problem is run for the linear and non-linear friction types (eq. 5.3).

The outputs of this model are an estimation of: the velocity field in the glacier, the temperature field, the viscosity field (coefficient A in eq. 5.1), and the friction coefficient (k in eq. 5.3).

5.3 Steady-state of the Helheim glacier

In Fig. 5.1 we show a top view of the Helheim glacier modified from (Nettles et al., 2008, fig.1). The background satellite image is a LANDSAT image from 2001, the blue dotes are the locations of the GPS sensors used in (Nettles et al., 2008), the yellow lines are the glacier velocities (averaged on the 2007 campaign) the two black dotted lines show the locations of the terminus front. We added to this map the central flowline (magenta line) of the Helheim used in this Chapter for the two-dimensional modelling of Helheim glacier. Note that the terminus position in our

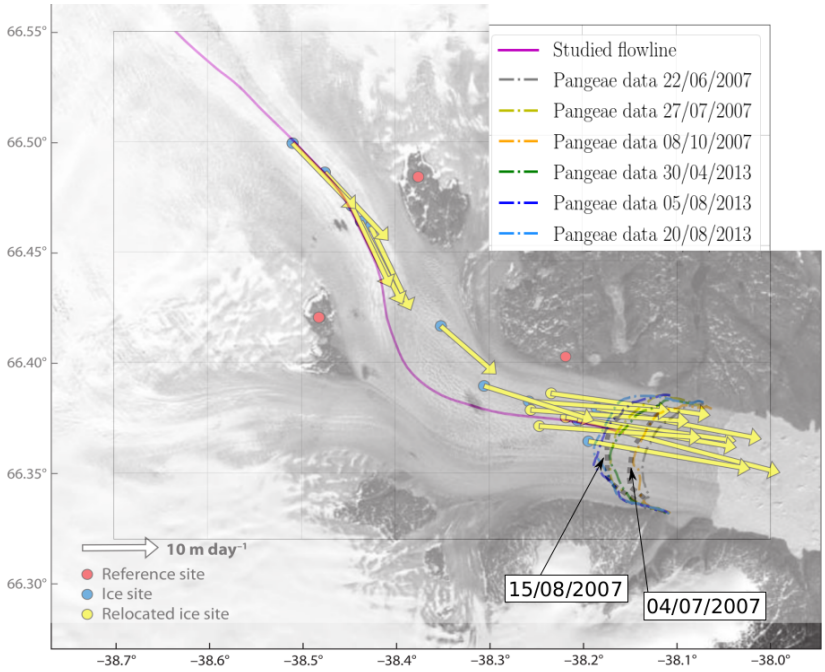

Figure 5.1: Top view of the Helheim glacier with a 2001 LANDSAT image in the background, the position of the GPS sensors used in the 2007 campaign (blue circles), and position of the terminus front (black dotted lines) on 15/08/2007 and 04/07/2007 (adapted from Nettles et al. (2008, fig.1)). The flowline used in the 2D model for the Helheim glacier this Chapter is indicated with the magenta line. The location of the terminus front position from the (Zhang et al., 2020) database are indicated in gray, yellow, orange, green, blue, cyan (dates indicated in the legend *Pangeae*).

model is located at the extremity of the magenta flowline on the right. As a comparison, we also add the position of the terminus front (label *Pangeae data*) estimated by (Zhang et al., 2020; Zhang et al., 2021) (available on the webpage `https://doi.pangaea.de/10.1594/PANGAEA.923272?format=html#download`) for the three dates when the terminus positions are available close to the dates of capsize events that we study in the summer 2007 and 2013.

We analyse the steady-state behaviour of the Helheim glacier (2007 geometry), that is its behaviour without capsize, obtained with the ISSM inversion. We plot the characteristics of the velocity fields along the central flowline in Fig. 5.2 and at each depth z ($z = 0$ m is the sea level).

The horizontal velocity in Fig. 5.2(a) is ≈ 0.4 m/day at ≈ 60 km from the terminus along the flowline, and increases towards the terminus up to ≈ 26 m/day. The vertical velocities in Fig. 5.2 (b) are one or two orders of magnitude smaller than the horizontal velocities, and change sign before and after the subglacial hill (see black dotted line in Fig. 5.4). We show the velocity vectors with a magnification of the vertical scale in Fig. 5.2. On the last ≈ 15 km before the terminus, the horizontal and vertical velocities are almost homogeneous on the vertical (d).

The viscosity coefficient K_v (as defined in eq. 5.2) ranges from 8.6 10^7 Pa $s^{1/3}$ to 6.4 10^8 Pa $s^{1/3}$. We show the Pressure P (assumed positive in compression) in Fig. 5.3 (a). We plot the absolute temperature T^* corrected for the pressure melting point $T^* = T + \beta P$, with $\beta = 7.910^{-8}$K Pa^{-1} the Clausius-Clapeyron constant in Fig. 5.3 (b). The temperature T^* is such that $T^* = 273.15°$ C corresponds to the pressure melting point, no matter the value of the pressure P. The mass fraction ω is shown in Fig. 5.3 (c). The upper bound of the water fraction ω is 0.01 to ensure validity of the flow rate factor parameterization in the temperate part with the experimental dataset (Duval et al., 1977; Lliboutry and Duval, 1985).

We show in Fig. 5.4 the glacier geometry: (a) the top view, (b) the distance along the flowline and (c) the

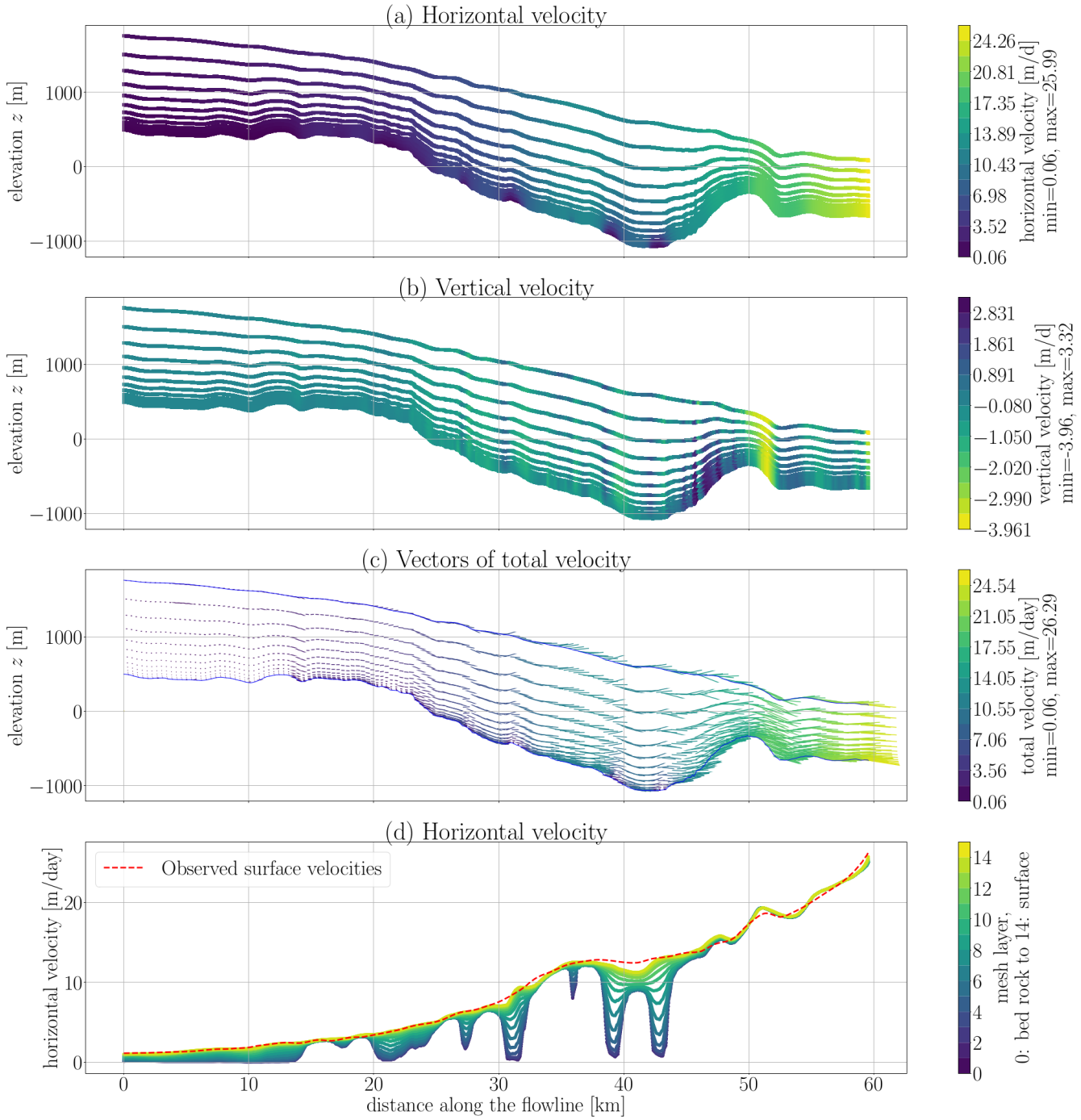

Figure 5.2: Color maps of the horizontal velocities (a), vertical velocities (b), and velocity vectors (c) along the central flowline. In (d) we show the total velocity along the central flowline, for each of the layers. This velocity field was inverted with the ISSM inversion. On caption (d) we show the total velocities measured in the field at the surface of the Helheim glacier that was used to constrain the inversion.

bedrock (in shaded orange) and glacier (in shaded blue) and the sea level (cyan line).

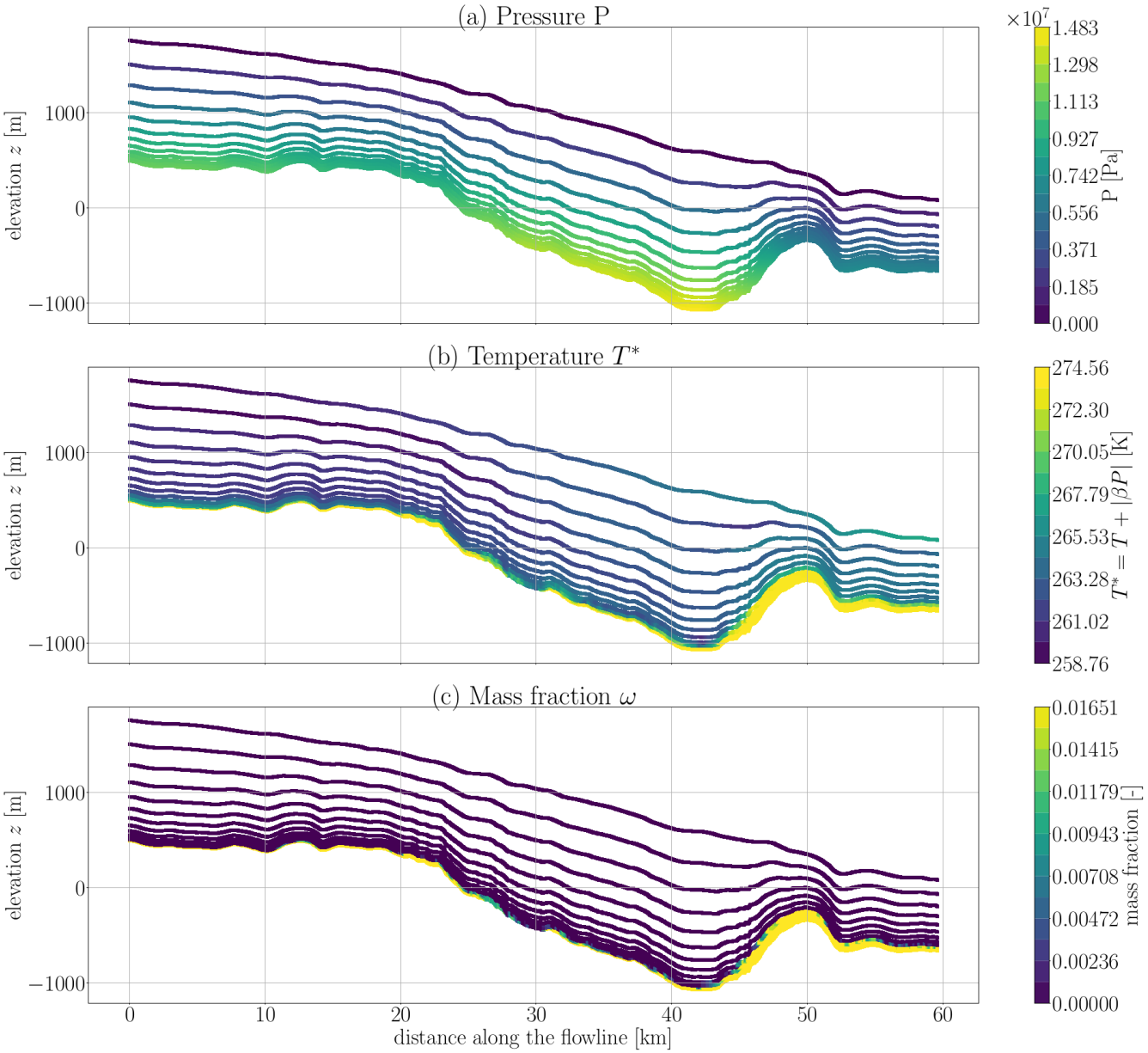

Figure 5.3: Pressure P, temperature T^* (corrected for the pressure effect), and mass fraction ω obtained with the ISSM inversion

5.4 Finite element simulations setup and initiation

5.4.1 Geometry and boundary conditions

The boundary conditions we apply are similar than in Chapter 4: stress free condition on the surface of the glacier above sea level, hydrostatic pressure on the surface of the glacier below sea level. We model the last ≈ 26 km of the Helheim glacier before the terminus. The length was chosen long enough to see the whole part of the glacier that is affected by the capsize and such as there is no boundary effects (i.e. that the boundary on the left is not affecting the capsize). The length was chosen small enough to reduce computational costs.

The geometry used in ISSM inversionis the grounded geometry (latest BedMachine v3 database Morlighem et al., 2017). However, other field observations show the Helheim glacier has a floating tongue about $3-5$ km long between 2008-2016 (Kehrl et al., 2017). Therefore, we investigated the response of the glacier with two different

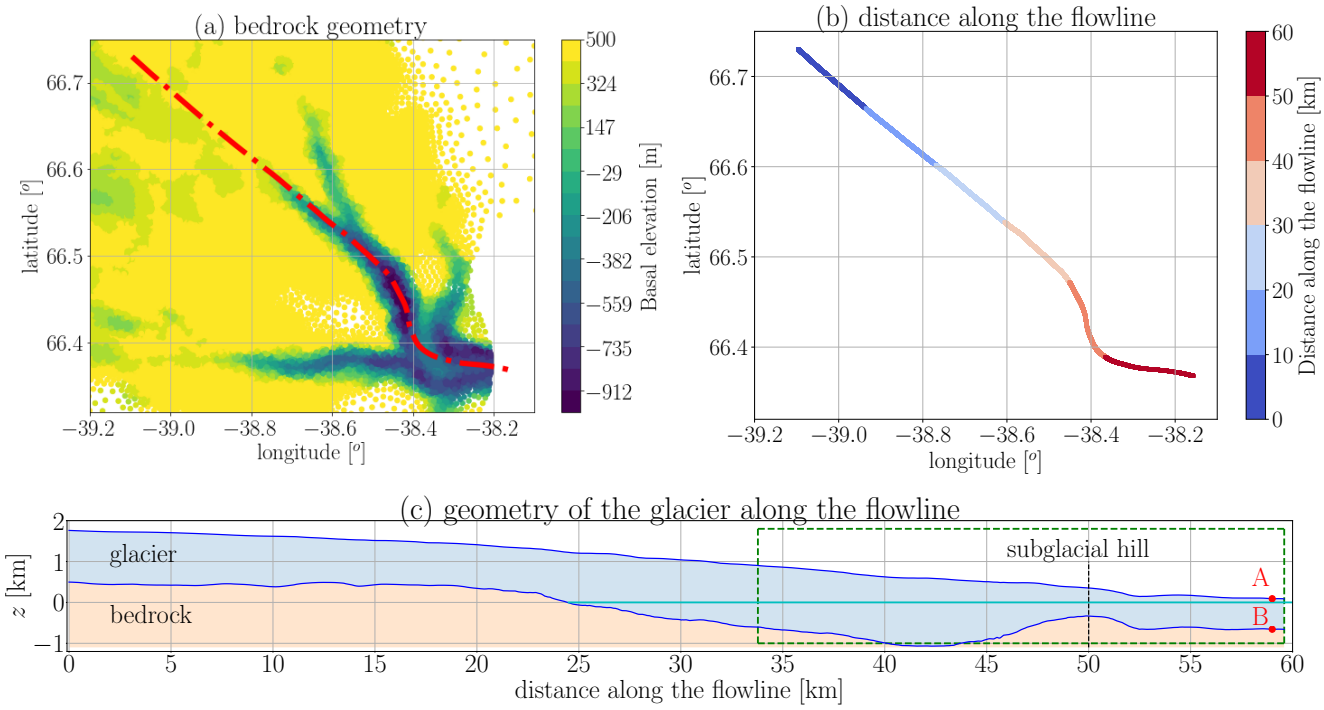

Figure 5.4: (a) Color map of the bathymetry, and the flow line that we model is shown in red, (b) distance along the flowline relatively to the top-view geometry of the glacier and (c) geometry of the bedrock and the glacier along the flowline, for clarity, one unit of length (1 km) is two times longer on the y-axis than on the x-axis. The green dotted box indicates the zone that is modelled in the Z-set simulations.

geometries: a grounded glacier or a glacier with a floating tongue. In Fig. 5.5, we show the mesh used for the Helheim glacier: (a) for the grounded glacier and (b) for the floating tongue.

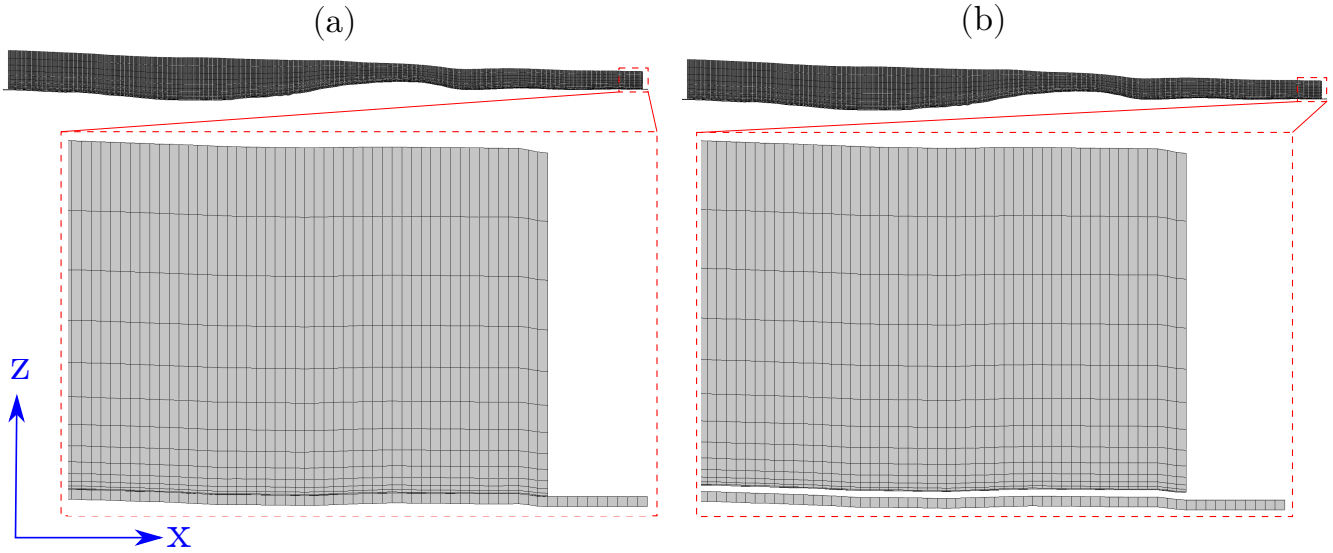

Figure 5.5: Mesh used in the Z-set simulations of the Helheim glacier: (a) for a grounded Helheim glacier, and (b) for a floating tongue

The geometry with the floating tongue was modified from the geometry of the grounded Helheim glacier, keeping the bedrock at the same elevation but shrinking the height of the Helheim glacier. The transformation is done in the following way: the ten last kilometers are shrinked with a geometric factor with a bilinear relationship proportional to both the distance along the flowline and the elevation. This transformation is such the upper point of the

terminus is moved downwards by 40 m and, at the terminus, all the points located closer than 200 m from the basal surface are moved upwards, all the points located above 200 m from the basal surface are moved towards, proportionally to the distance to the point at 200 m above the basal interface. In future work, the geometry of the Helheim glacier with a floating tongue could be included in the ISSM inversion, in order to adjust the geometry to fit the observed velocities.

In Fig. 5.6, we show the grounded mesh (green), and the modified floating mesh (red). The sea level in shown in cyan, and the flotation line in black.

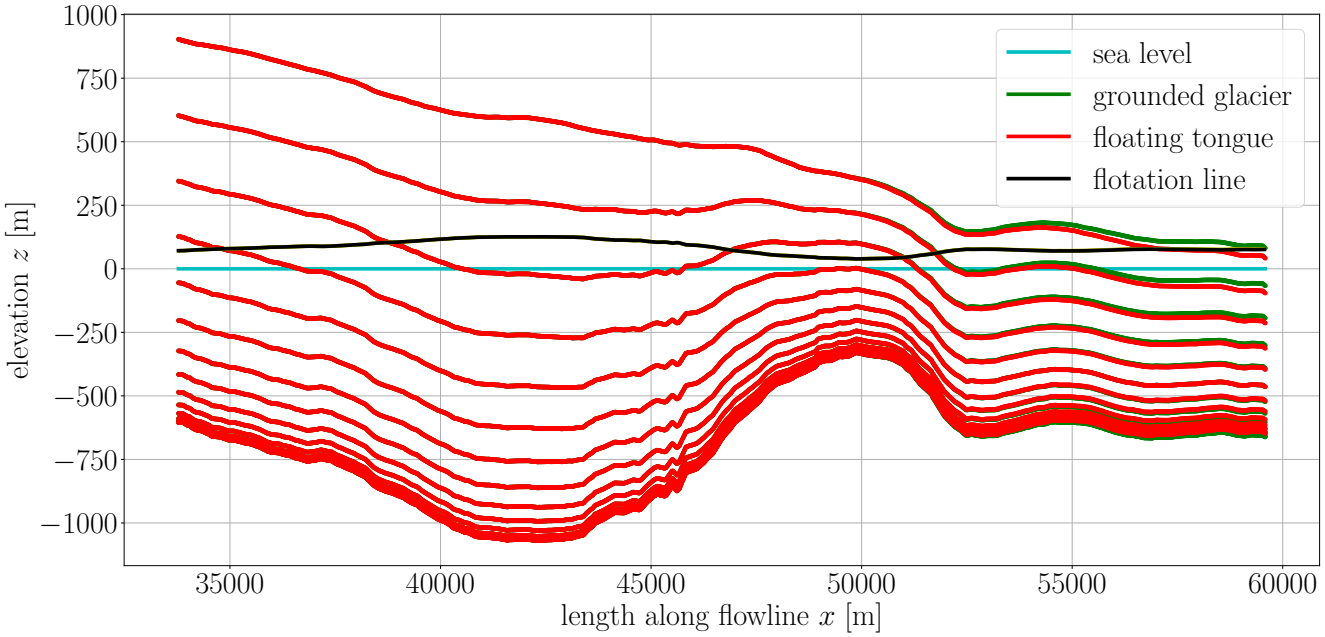

Figure 5.6: Original and modified Heleim mesh

One simulation lasts typically 35 h, when run in parallel on two Intel Core i7-8550U 1.80 GHz CPU.

5.4.2 Ice Rheology

The rheology is the same as in Chapter 4: a Maxwell law, that is an elastic spring in series with a non-linear viscous damper (dash pot). In the Z-set simulations, we set the values of the viscosity coefficient K_v at each node to that calculated with the ISSM inversion(eq. 5.2). With the Z-set software, the viscosity coefficient K_v is a function of the initial position (x,z) of the nodes of the mesh, and is unchanged through time. As will be detailed later, the Young modulus of the ice is fixed to $E = 9.3$ GPa or $E = 3$ GPa, and the Poisson's ratio to $\nu = 0.499$.

5.4.3 Friction

The friction law used in ISSM inversionis a function of the effective pressure N and the basal velocity u_b. In the Z-set software, for the complex geometry, only the Coulomb friction law is implemented. Because these laws are significantly different, we investigate the values of the friction coefficient in next section 5.4.4 that allow to best reproduce the observed surface velocities (Fig. 5.2 d).

5.4.4 Initiation

We investigated how to initiate the calculation. With the small strain formalism used here, the strains are calculated relatively to the initial mesh. Therefore, the choice of the initial mesh might influence the strains and thus the velocities throughout the calculation. Ideally one should initialize the model by simulating the long time history of the glacier dynamics. This would require to include snow accumulation, melting and calving of icebergs, and the thermo-mechanical behaviour of ice. Therefore, we investigated how to initiate the model using results from a state-of-the-art solver in glacier flow modelling, the ISSM setup presented in section 5.3.

It is possible to impose the deformation of the mesh at the first time step, and thus to impose an initial velocity. However, calculations have shown that the velocity field is highly governed by the geometry. Our calculations have consisted in two steps. First, we initiated a simulation A with an undeformed mesh, and after some time, the mesh deformed and the velocity field converged. Second, we initiated a simulation B with the deformed mesh obtained in the converged state in simulation A. After some initiation time, simulation B reaches the same velocity field as in simulation A. Therefore, we initiate the Helheim simulations using the mesh and geometry from the ISSM inversion. For a simulation with a Poisson's ratio of the ice of $\nu = 0.3$ (Cuffey and Paterson, 2010) the initiation time was ≈ 1 day whereas when the ice was considered as incompressible, i.e. for a Poisson's ratio $\nu = 0.5$ the initiation time is reduced to ≈ 1000 s. In this PhD, we take $\nu = 0.5$, that is we consider the ice as an incompressible material. Note that this approximation is used in most ice flow models (when using a fluid dynamics approach). In the next simulations, we fix the Poisson's ratio to $\nu = 0.499$ (with $\nu = 0.5$ the Z-set software would require more degrees of freedom, thus a more costly calculation). At the end of the 1000 s long initiation phase, we apply the force of a capsizing iceberg on the terminus front.

The observed velocities at the surface of the glacier are shown in Fig. 5.7, as well as the velocities of the glacier obtained with the ISSM inversion, and the velocities at the surface simulated with the Z-set model with various values of the Coulomb friction coefficient μ indicated in the legend. The surface velocities increase with decreasing values of the Coulomb friction coefficient (in Z-set). For a friction coefficient $0.15 < \mu < 0.2$ the velocities are coherent with the observed values close to the terminus. Note that the high discrepancy between the velocities simulated with Z-set far from the terminus and the observed velocities could be corrected with further developments in the Z-set software. Possible developments could include a Coulomb friction law with a coefficient dependent on the location, or a Weertman friction law (but numerically challenging for a complex geometry and a small Weertman coefficient). The current configuration still allows to qualitatively assess the response of the glacier to an iceberg capsize.

5.5 Response of the Helheim glacier to iceberg capsize: grounded geometry

5.5.1 Surface and basal velocities

We investigate the response of the grounded Helheim glacier to a model capsize. We set the Young's modulus of the glacier ice to $E = 9.3$ GPa. As explained in Chapter 4, this values is an upper bound for the Young's modulus of the ice (the lower bound is $E \approx 1$ GPa), and the displacements during the capsize are approximately proportional to the Young's modulus. We apply a Coulomb friction law on the whole basal interface. As mentioned above, it does not allow to model accurately velocities of the glacier upstream, but it can still help to qualitatively assess the

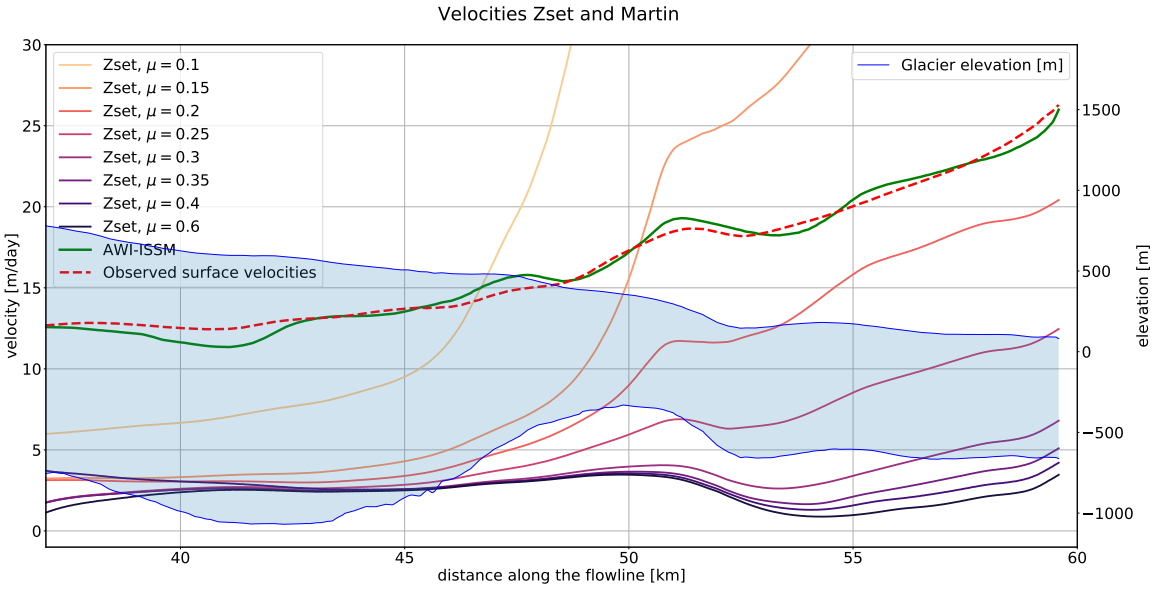

Figure 5.7: Velocities at the surface of the glacier: measured data, values obtained with the ISSM inversion, and values obtained with the Z-set model for various values of the Coulomb friction coefficient, and velocities in the glacier

response of the glacier (close to the terminus) to the capsize of an iceberg.

We apply the force of the top-out capsize of an iceberg of the same height as the glacier front ($H = 739$ m), with an aspect ratio $\varepsilon = 0.35$. This value of the aspect ratio gives a force with the highest amplitude. Note that the amplitude of the capsize force would be $\approx 1/4$ smaller for a value of the aspect ratio of $\epsilon = 0.23$ (as inverted by (Murray et al., 2015a) in their fig. 3 for an event on July 25th 2013). The force is applied as a uniform pressure force on the whole terminus front. If the force is applied on the top part of the terminus (bottom-out capsize), the displacements are higher at the free surface and smaller at the basal interface. If the force is applied on the bottom part of the terminus (top-out capsize), the displacements are higher at the basal interface and smaller at the free surface (section 4.4.2). Thus, applying the force on the whole terminus front means that in terms of displacements of the glacier during the capsize, it gives an intermediate response between the two local zones of application of the force. Thus, this simulation will yield rather a lower bound for the surface displacements during capsize.We set the Coulomb friction coefficient to $\mu = 0.2$ in order to have coherent surface velocities close to the terminus (see Fig. 5.7)

In Fig. 5.8, we plot the colormap of the velocities during capsize at the free surface in (a) and at the basal interface in (b). Before the beginning of the capsize (below the horizontal dotted yellow line at $t = 1000$ s), the velocities (at the surface and at the basal interface) are steady in time and increase towards the terminus. However, upstream (on the left) of the position 51 km, the basal velocities are ≈ 0 m/day. This is not a realistic steady-state basal condition. However, the portion of glacier between 51 km has realistic velocities (see Fig. 5.7). Furthermore, these last kilometers are located after the rotation of the flowline (si Fig. 5.4b). Therefore, focusing on these last kilometers is more appropriate relatively to the two-dimensional approximation used here. Further developments in the Z-set software could be done in the future to improve the behaviour of the glacier upstream (Weertman friction law). During the capsize, the velocities decrease until approximately the peak of the iceberg force $t \approx 1165$ s (zone in dark blue), and then accelerate brutally until $t \approx 1175$ s (zone in yellow) in the last ≈ 23 km before the

terminus. We observe that between time $t = 1115$ s and time $t = 1160$ s, and close to the terminus (white line in Fig. 5.8) up to a distance of ≈ 3 km from the terminus), the velocities drop below zero, at the free surface and at the basal interface. This means that there is an absolute reverse motion. The switch between a downstream-upstream-downstream direction of sliding at the basal interface implies a change of the basal stresses (not plotted here). In the previous Chapter 4, a similar local variation on the basal stresses was observed. However, the total force transmitted in the bedrock was exactly that applied on the terminus front. This result was consistent with a simple analytical calculation of the inertia of a beam in compression.

5.5.2 Displacements for various Coulomb friction coefficients

We assess the effect of a change of the Coulomb friction coefficient from $\mu = 0.2$, to $\mu = 0.4$ and up to $\mu = 0.6$. We show in Fig. 5.9 (a), the displacements at the free surface (a-c) and at the basal interface (e) of the glacier during capsize, at 150 m from the terminus (point A at the surface and point B at the bottom see Fig. 5.4c). The detrended evolutions are also shown in Fig. 5.9b, d, f: these curves are obtained by running the simulation without the capsize of an iceberg.

We observe an absolute reverse horizontal motion for all three values of the Coulomb friction coefficient: at the free surface it is ≈ 0.5 cm (e.g. brown arrow in Fig. 5.9c) and at the basal interface it is ≈ 0.1 cm (e.g. red arrow in Fig. 5.9e). This reverse horizontal motion corresponds to the negative values of the velocities observed in Fig. 5.8. In terms of detrended displacements: the amplitude of the vertical detrended displacements (Fig. 5.9b) is hardly affected by a change of the Coulomb friction coefficient, whereas the amplitude of the detrended horizontal reverse motion (Fig. 5.9d) is highly sensitive to a change in the Coulomb friction coefficient. The amplitude decreases with increasing values of the friction coefficient: it is ≈ 2.3 cm for $\mu = 0.2$ and it drops to ≈ 0.9 cm for $\mu = 0.4$, and then to ≈ 0.7 cm for $\mu = 0.6$. When increasing the friction twofold (by 100 %) from $\mu = 0.2$ to $\mu = 0.4$ the amplitude decreases by 60 % (orange arrow in Fig. 5.9d), and when increasing again the friction coefficient (by 50 %) from $\mu = 0.4$ to $\mu = 0.6$, the amplitude decreases by 20 % (green arrow in Fig. 5.9d). Therefore, the displacements are highly dependent on the Coulomb friction coefficient (in particular for values of the Coulomb friction coefficient that give reasonable surface velocities $\mu \approx 0.2$). This result is interesting because it suggests that the horizontal surface displacements are a good proxi for the Coulomb friction coefficient. In this simulation, we used a Coulomb friction law on the whole basal surface. It would be interesting to assess the validity of this results in the case where the Coulomb friction zone is smaller and close to the terminus (as suggested by Tsai et al., 2015). To do so we cannot used the geometry of the Helheim glacier (for which only the Coulomb friction is available), but we can conduct the analysis with the geometry of the glacier on a constant slope. Thus, we present results with the geometry with a constant slope without a floating tongue, in the next section.

5.6 Comparison with the geometry of a grounded glacier on a constant slope

5.6.1 Velocities and displacements during capsize

Following the analysis of the effect of the Coulomb friction coefficient, we investigate whether the geometry has an important role in this analysis.

To do so, we compare the previous simulations with the simulations for a grounded glacier with a constant slope.

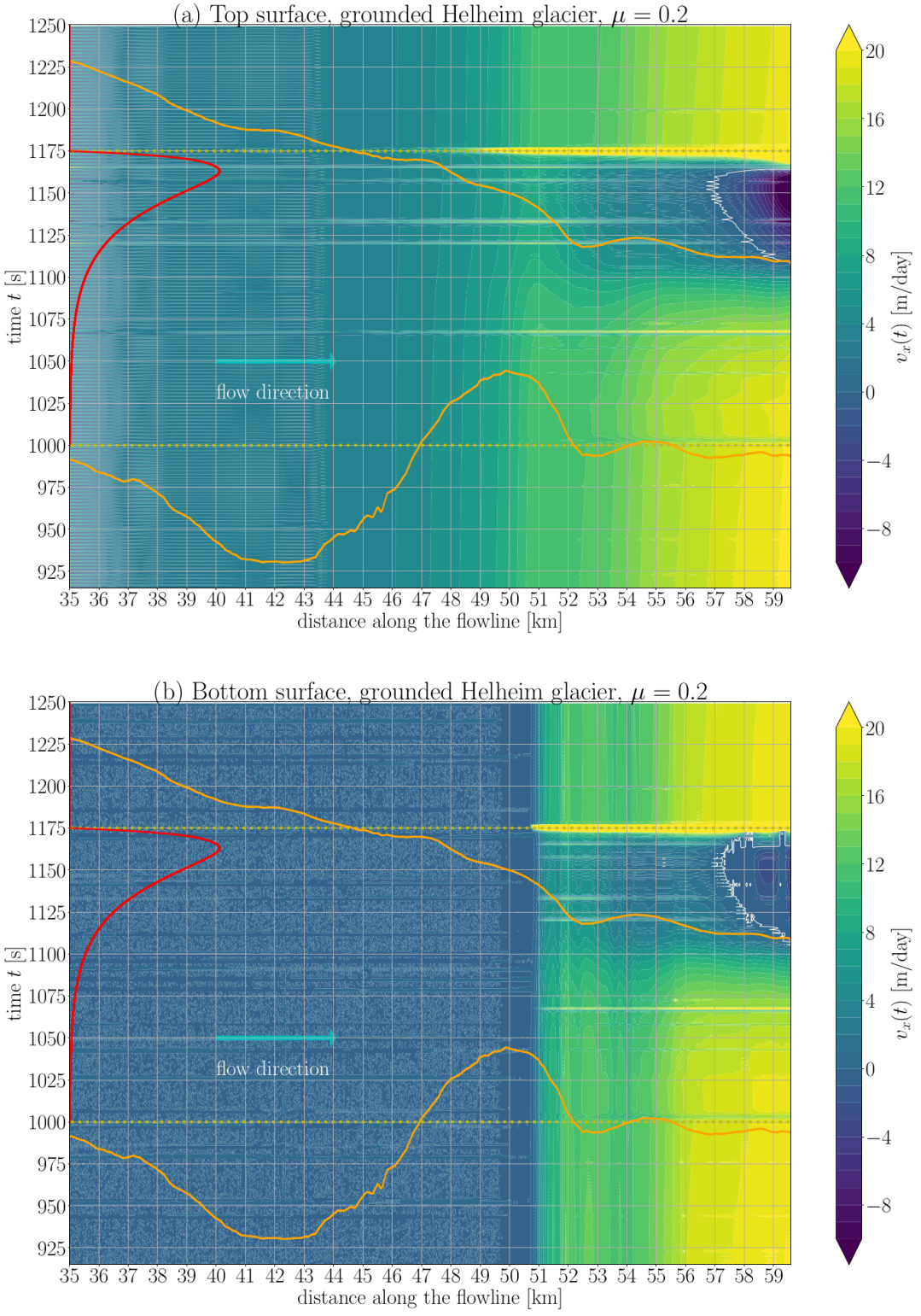

Figure 5.8: For a grounded Helheim glacier: horizontal velocities at the free surface (a) and at the basal interface (b), along the flowline (terminus on the right), and through time (y-axis). The red curve shows the iceberg force applied on the terminus front, the start and end time are indicated with the yellow dotted horizontal lines. The Coulomb friction coefficient is $\mu = 0.2$. The orange lines indicate the geometry of the glacier along the flowline. The zero velocities (for the last 5 km before the terminus) are indicated with the white line.

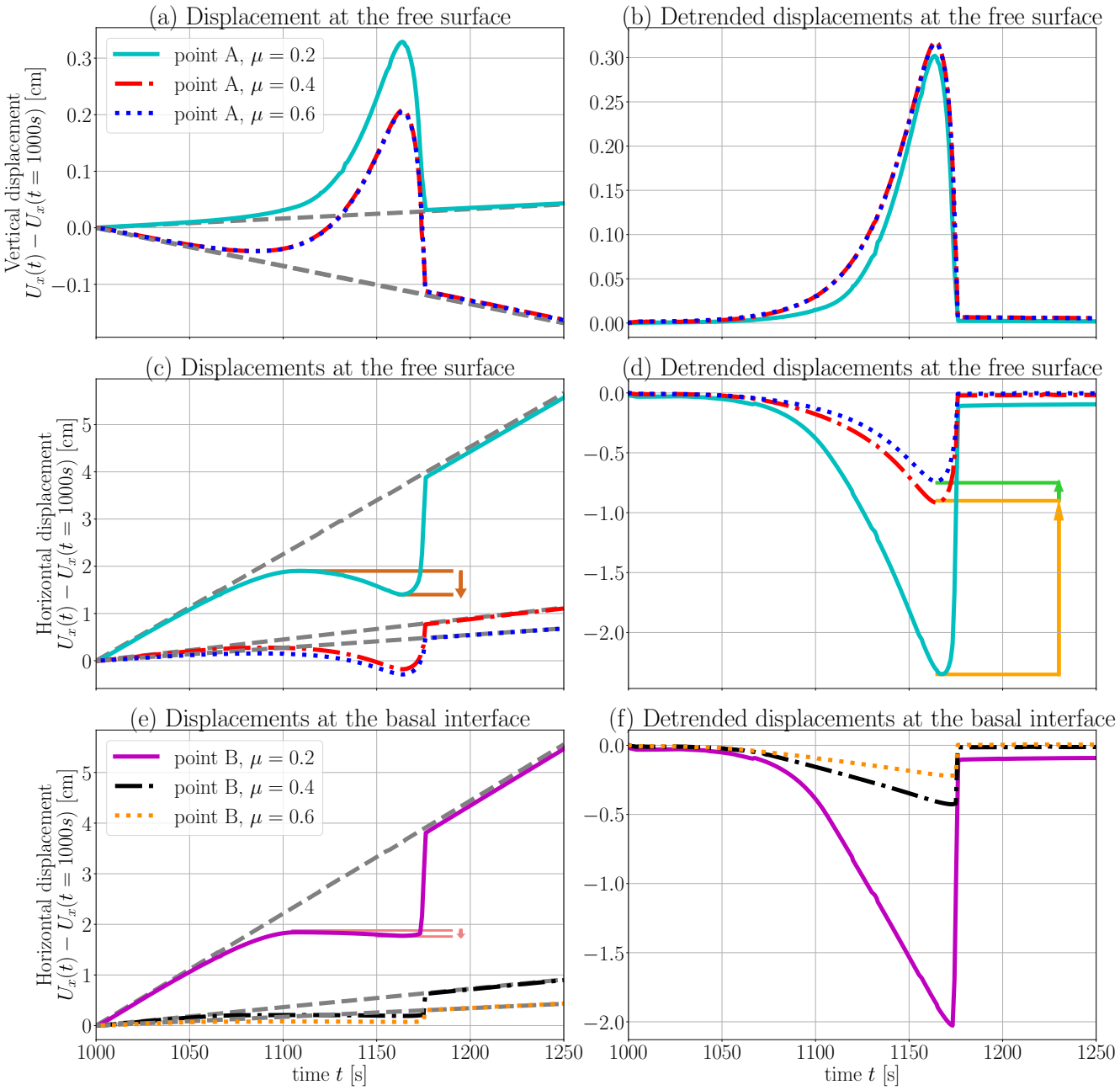

Figure 5.9: For a grounded Helheim glacier: vertical displacements at the free surface (point A) (a) and corresponding detrended displacements (b), horizontal displacements at the free surface (point A) (c) and corresponding detrended displacements (d), horizontal displacements at the basal interface (point B) (e) and corresponding detrended displacements (f). The results are shown for three values of the Coulomb friction coefficient $\mu = 0.2$ (cyan and magenta curves), $\mu = 0.4$ (red and black curves), $\mu = 0.6$ (blue and orange curves).

It is almost the same setup as in Chapter 4 except for two parameters that we adapted for the comparison with the Helheim glacier: we changed the height of the glacier from $H = 1000$ m in Chapter 4, to $H = 764$ m here, and we apply a Coulomb friction law on the whole basal surface. The other parameters are: angle of inclination of the glacier and the bedrock $\theta = 2°$, homogeneous viscosity coefficient $K_v = 2\ 10^8$ Pa s$^{1/3}$, terminus at the hydrostatic equilibrium, top-out capsize of an iceberg of height $H = 764$ m, aspect ratio 0.35, and force applied on the whole terminus front. Note that with this geometry, the first point of the bedrock reaching the sea level is located at 20 km from the terminus.

We plot the velocities at the free surface (a) and at the basal interface (b) for a glacier with a constant slope in Fig. 5.10, and for $\mu = 0.2$.

The displacements observed during capsize for the grounded Helheim glacier are similar qualitatively to that obtained for a model glacier on a constant slope: during capsize the velocities decrease (below zero) in a ≈ 3 km zone before the terminus, at the free surface and at the basal interface.

We show in Fig. 5.11, the horizontal displacements close to the terminus in the case of the geometry with a constant slope for $\mu = 0.2$, $\mu = 0.4$, and $\mu = 0.6$. The amplitude of the horizontal retreat is similar to that obtained with the Helheim geometry.

This similarity (in the surface and basal displacements during capsize between the Helheim geometry and the model geometry) suggests that the results obtained in the previous Chapter 4 can help to understand the displacements of glaciers during capsize observed in the field.

5.6.2 Effect of the length of the Coulomb friction zone

In this section, we use the geometry with the constant slope (described above), because with this simple geometry our model can handle a Weertman friction law and a Coulomb friction law on tunable lengths. We choose the following lengths for the zone of application of the Coulomb friction law (counted from the terminus as shown in Fig. 4.1): $L_C = 40$ km (that is equal to the whole length), $L_C = 5$ km, $L_C = 2$ km and $L_C = 750$ m. We choose the same values of the friction coefficient as above: $\mu = 0.2$, $\mu = 0.4$, $\mu = 0.6$. In Fig. 5.12, we show the displacements relatively to the time of beginning of capsize ($t = 1000$s). On the column on the right (b, d, f), we show the detrended displacements (obtained by removing the linear trend joining the positions at time $t = 1000$ s and time $t = 1250$ s. This shows the high influence of the amplitude of the horizontal surface displacements with the Coulomb friction coefficient, especially for longer Coulomb friction zones $L_C > 2$ km (Fig. 5.11 and Fig.5.12 a-d). For small Coulomb friction zones ($L_C \leq 2$ km, Fig.5.12c-f), the amplitude of the horizontal retreat increases linearly with the Coulomb friction coefficient, whereas, for longer Coulomb friction zones ($L_C \geq 5$ km, Fig. 5.11 and Fig.5.12 a-b), the amplitude of the horizontal retreat increases non linearly with the Coulomb friction coefficient. One possible source of non linearity is the non-linear ice rheology (non-newtonian fluid). When we use a linear rheology (newtonian fluid, exponent $n = 1$ in the Glen's flow law eq. 4.3), we observe a smaller non linear effect.

In Fig. 5.13, we plot the values of the amplitude of the detrended horizontal retreat (a) and the horizontal velocities (b) during capsize, with respect to the Coulomb friction coefficient μ (x-axis) and the length of Coulomb friction zone L_C (squares for $L_C = 40$ km, stars for $L_C = 5$ km, triangles for $L_C = 2$ km and circles for $L_C = 750$ m). We observe in caption (a) the sensitivity of the horizontal retreat to the value of the Coulomb friction coefficient and the length of the Coulomb zone. The horizontal retreat increases with decreasing values of the Coulomb friction coefficient μ, especially for high values of L_C and low values of μ. However, the variations of the amplitude of the displacements are similar to the variations of the velocities. We investigate in more details whether there is a direct correlation between the amplitude of the displacements, the Coulomb friction coefficient and the velocities. For this, we show in Fig. 5.14 (a), the variations of the horizontal displacements with respect to the horizontal velocities. We show the results for various values of the Coulomb friction coefficient (colors of the symbols indicated in the legend) and for various lengths of the Coulomb friction zone (shape of the symbols indicated in Fig. 5.13 a). There is a correlation between the velocities and the amplitude of the horizontal displacement (similar lines for various lengths of the Coulomb friction zone in Fig. 5.14 a). The fact that the correlation is not exact means that for a given value of the velocity there is various possible horizontal retreat that correspond to different values of

the friction coefficient μ and length L_C. This is illustrated in Fig. 5.14b where we show in the amplitude of the horizontal displacements (coloured circles) with respect to the friction coefficient (μ in x-axis) and the length of the Coulomb friction zone (L_C in y-axis). In practice, such database of simulations can help to invert for (μ, L_C) given the horizontal velocity and amplitude of the horizontal retreat.

5.7 Response of the Helheim glacier to iceberg capsize: geometry with a floating tongue

One of the objectives of this Chapter is to qualitatively reproduce the observed displacements during the capsize of an iceberg at the Helheim glacier. Moreover, by tuning the parameters of our model to fit measured displacements, we can help to constrain the unknown physical parameters of the Helheim glacier during the capsize event (e.g. July 25 2013 Murray et al., 2015a). We have put in place a simulation for the geometry of the Helheim glacier with a floating tongue. As explained in section 5.5, this is a geometry artificially modified from the grounded geometry: based on measurements of the elevation of the glacier free surface, the bedrock elevation, and the estimation of the length of the glacier tongue.

In this simulation, we fix the Coulomb friction coefficient to $\mu = 0.6$, this yields reasonable values of the horizontal surface velocities of ≈ 15 m/day. Compared to the previous simulation with a grounded Helheim glacier, we decrease the Young's modulus to $E = 3$ GPa, and we apply the force of a bottom-out capsizing iceberg of aspect ratio $\varepsilon = 0.45$ on the whole basal surface (this gives the highest amplitude of the force amongst all aspect ratios).

The surface velocities are plotted in Fig. 5.15: the background horizontal velocities (before the capsize) at the glacier free surface are ≈ 15 m/day close to the terminus. This value is much higher than the surface velocities of ≈ 3 m/s obtained for a simulation with a grounded Helheim geometry with the same friction coefficient $\mu = 0.6$. This is due to the fact that there is no resisting force on the floating part. There is a sharp increase in the velocities at the position 55 km along the flowline. Here the basal interface in the grounded part of the glacier is not sliding and is not affected by the capsize. Such a no-slip condition can be seen here as an end-member behaviour in basal sliding (such as in the benchmark presented in Pattyn et al., 2008). However, we analyse the response of the glacier close to the terminus where the surface velocities are consistent with the observed velocities. In the floating tongue, we observe a decrease of the velocities followed by a sharp increase of the velocities. In a zone close to the terminus (≈ 4 km long) the velocities become negative (absolute retreat) for ≈ 45 s until $t \approx 1163$ s, and then the velocities brutally increase until the end of the capsize (at time $t = 1175$ s).

To further analyse the response of the glacier to the capsize force, and the effect of the floating tongue, we plot the surface horizontal displacements in Fig. 5.17. We observe a reverse motion at 500 m from the terminus of ≈ 12 cm (green curve). This is coherent with the displacements of ≈ 15 cm measured during the 2013 events, at ≈ 500 m from the terminus, see Fig.5.16, adapted from fig. 2A in Murray et al. (2015a). However, the duration of the reverse motion measured in the field is longer $\approx$ 5 min, compare to the duration of $\approx$ 3 min in our simulations. This may be due to the short duration of the contact force (SAFCIM) or to additional resisting forces that apply on the iceberg (ice-mélange) or on the floating tongue (fluid forces, lateral friction on the fjord sides) during the capsize at the Helheim glacier. As for the simulations with the constant slope, the vertical displacements during the bottom-out capsize of an iceberg is upwards, whereas it is downwards for the events monitored by Murray et al. (2015a). We simulated the response of the Helheim glacier to a capsize with a Coulomb friction force, and this did not allow to simulate the downward motion.

As discussed in the Chapter 4, the displacements at the surface of the floating tongue are mainly explained by an elastic compression of the floating tongue. In the case of an elastic spring of length L (Chapter 3), $F = ku(x)$, with F the normal efforts on a section of the glacier, $k = H \cdot E/L$, H the glacier height and L the length of the glacier tongue. Therefore, there is a direct relation between the displacements at the terminus $u_{terminus}$ and the displacements $u(x)$ at a distance x from the terminus:$u(x) = u_{terminus}(L - x)/L$.

We investigate whether our current geometry could simply be approximated as an elastic tongue (fixed on one side and with the capsize force on the other side). To do so, we plot (Fig. 5.17) the displacements at several distances from the terminus: curves C_i, for $i = 1 - 5$ for a point at the terminus (solid green curve), for a point at the distance $d_2 = 973$ m from the terminus (solid cyan curve), $d_3 = 1943$ m (solid black curve), $d_4 = 3894$ m (solid red curve), and $d_5 = 5847$ m(solid orange curve) from the terminus. To compare with the hypothesis of a purely elastic tongue, we add plot the curves obtained by the following formulation:

$$(L - d_i)/LC_1(t)\cdot \tag{5.7}$$

for $i = 2 - 5$, with $C_1(t)$ the displacements at the terminus ($d_1 = d_{terminus} = 0$), see non solid curves on Fig. 5.17.

For each distance d_i, we tune the length L to match the solid curves C_i.

We observe that the fitted values of L (3500 m$\leq L \leq$ 6050 m) increase with the distance to the terminus. This may be due to the fact that moving upstream, the height H of the glacier increases. In the above explanation, we adjust L, and considered the height fix H, but the stiffness is a function of the ratio H/L ($k = H \cdot E/L$). Moreover, the grounded part of the glacier is also under elastic compression, and the basal velocity decreases during capsize. Therefore, the geometry cannot be precisely approximated by an elastic spring. However, the fitted values of the length L are close to the length between the terminus and the grounding line $L \approx 4.5$ km. Therefore, such observation can help to constrain the length of the glacier tongue.

5.8 Discussion

We discuss here the hypothesis used for the simulations with the Z-set model with the Helheim geometry.

5.8.1 Three dimensional effects

For a two dimensional model to be representative of the three dimensional setup, several approximations are made.

Greenland glaciers are confined in fjords, the lateral friction of the glaciers in these fjords plays a stabilising effect. In our study, we assume that the effects of the lateral friction is negligible on the central flowline. (Gagliardini et al., 2010; Krug et al., 2014b) take into account this effect through an additional body force including a lateral friction coefficient k:

$$\boldsymbol{f} = -k|\boldsymbol{u}|^{1/n-1}\boldsymbol{u} \tag{5.8}$$

with $k = \frac{(n+1)^{1/n}}{W^{\frac{n+1}{n}}(2A)^{1/n}}$ with n and A the Glen's flow law parameters (eq. 5.1), and W the channel width.

In the case of the Helheim glacier, a tributary glacier joins the main stream a few kilometers before the terminus (see Fig. 5.4 a). This smaller ice stream is narrower and slower than the bigger one. However, this additional ice advected in the main ice stream may increase the speed of its discharge, compared to the case where the main ice stream would be in contact with a lateral bedrock.

These three-dimensional effects mainly affects the simulated background motion. We do not expect that they are significant in simulations for the transitory response of the glacier to the capsize.

5.8.2 Calving process and calved icebergs (ice-mélange)

In this model, we do not include the calving, that is the detachment of the iceberg from the glacier tongue, and we do not include crack opening (Krug et al., 2014b). Crack opening and iceberg calving are the source of seismic signals (Podolskiy and Walter, 2016; Walter et al., 2013), this suggests that there is a dynamic phenomenon in the glacier during these events. With buttressing forces close to the terminus (resisting forces due to the contact between the glacier and the fjords sides or the bedrock), the calving of an iceberg yields a change in the boundary conditions and thus a potential destabilisation of the glacier (Goldberg et al., 2009). In future work, it could be interesting to assess the response of a glacier to a change in the boundary conditions at the terminus front.

There is no ice-mélange in our simulations. A dense ice-mélange induces buttressing forces, which stabilize the glacier. The seasonality of the ice-mélange, denser in the winter then in the summer, is one of the reasons given for the observed seasonality in iceberg calving. Therefore, ignoring the ice-mélange for modelling the capsize of iceberg in summer in Greenland is a reasonable approximation. The presence of ice-mélange would probably decelerate the motion of the iceberg by applying a resisting force higher than the hydrodynamic forces (in absence of ice-mélange). In future work an ice-mélange could be included in the model to analyse its influence on the glacier response to the iceberg capsize.

5.8.3 Basal hydrology

In our model, we do not include surface nor basal melting. Summer melts varies between 1 and 17 m/day (Krug et al., 2014a). At the time scale of a capsize (maximum duration of ≈ 300 s) it corresponds to an average melt of 3 mm to 6 cm, which is negligible with respect to the height of the glacier. (Gagliardini et al., 2010) discuss how the melting of the ice shelf affects the position of the grounding line, and show, that in absence of buttressing, the variations in the melt rate does not change the grounding line.

Subglacial hydrology affects the basal stresses. The increase in surface melting during the summer season induces an increase in the runoff, thus an increase of the basal hydrology. During the summer season, the glacier velocity is known to increase, and this velocity change has been correlated to the rate of runoff (Vijay et al., 2019). If the subglacial drainage system is not *efficient*, the effective pressure increases and the glacier will slide quicker. However, as the water discharge increases, the drainage system evolves from an inefficient *cavity* drainage mode to an efficient *channel* mode, which reduced the effective pressure and the glacier sliding velocity (Schoof, 2010).

A step-like increase in the Helheim glacier surface velocities during the capsize of an iceberg was observed by (Nettles et al., 2008). This could be related to a brutal change in the basal properties that would be triggered during capsize: such as an increase in the subglacial runoff with an inefficient hydrological system. However, followed later by a switch to an efficient hydrological system, and thus a slowdown of the velocities.

5.9 Conclusion and Perspectives

In this Chapter we analysed the response of the Helheim glacier to the capsize of an iceberg, for a two-dimensional geometry, along the central flowline. For the ice rheology, we used a visco-elastic behaviour, we a heterogeneous field for coefficient of viscosity. In the Z-set simulations of the Helheim glacier, there is a Coulomb friction law on

the whole basal surface. This is due to the challenging implementation of the Weertman friction coefficient (for low values of the friction coefficient).

The values of the Coulomb friction coefficient that yield reasonable surface velocities close to the terminus, in absence of a floating tongue, is $0.1 < \mu < 0.2$. However, further upstream the basal surface is in a stick state. To improve the description of the basal laws with this complex geometry, we could include a Coulomb friction coefficient varying along the flowline.

We showed the high dependence of the horizontal displacements with the Coulomb friction coefficient. This results is qualitatively the same for the glacier with a constant slope, which suggests the little effect of the geometry. In order go further in this study, we investigated the effect of the length of the Coulomb friction zone. To do so we used the geometry of the constant slope that allows a zone with a Weertman friction law. This study suggests that for low values of the Coulomb friction coefficient ($\mu \approx 0.2$), the surface displacements are highly dependent on the friction coefficient μ. For a given value of the velocities, different values of the friction coefficient μ and length L_C gives slightly different amplitudes of the horizontal retreat. This study gives a possible way to invert for basal parameters using surface measurements.

Then we investigated the response of the Helheim glacier with a floating tongue, to the capsize of an iceberg. The horizontal reverse motion is qualitatively coherent with the amplitude of the measurements by Murray et al. (2015a), but the amplitude and duration are under-estimated. The comparison of the displacements at various distances from the terminus can give an estimate of the glacier tongue length.

The Jakobshavn Isbrae glacier and the Kangerdlussuaq glacier lie on negative bed slopes which makes them unstable in the long term (Beckmann et al., 2019, fig.7). It would be interesting to assess the short term response of these glaciers to capsize events. However, there are no measure surface displacements at these glaciers during capsize. Our model may give insights on the expected response.

Similarly to the simulations with a simple geometry, we do not reproduce the vertical downwards motion during capsize with the Helheim geometry (observed for several events at the Helheim glacier). (Murray et al., 2015a) suggests it is due to a drop in the hydrostatic pressure below the glacier tongue. We did not include a hydrodynamic pressure below the glacier tongue which might allow to reproduce such vertical motion.

Moreover, a step-like increase in the velocities was observed during capsize by (Nettles et al., 2008). the brutality of the capsize event might affect the basal interface in such a way that friction law can be changed during the capsize. In future work, we could include in the Z-set software a time dependent Coulomb friction coefficient, and investigate whether a brutal change in the Coulomb friction coefficient during the capsize might reproduce the observed change in the velocities.

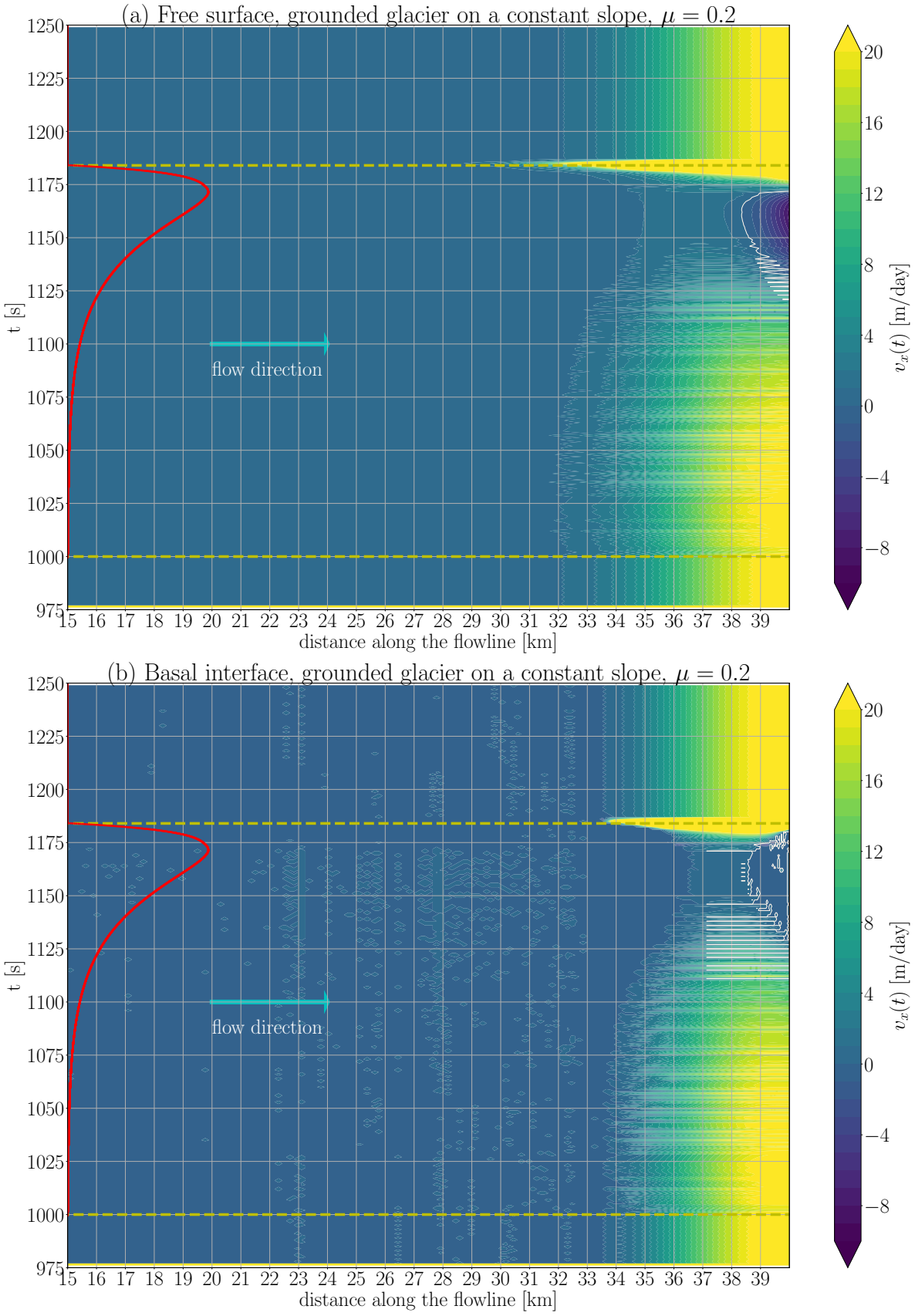

Figure 5.10: For a grounded glacier on a constant slope, and a Coulomb friction law on the whole basal surface: horizontal velocities at the free surface (a) and at the basal interface (b), along the 25 km before the terminus (on the right), and through time (y-axis). The red curve shows the iceberg force applied on the terminus front, the start and end time are indicated with the yellow dotted horizontal lines. The Coulomb friction coefficient is $\mu = 0.2$. The zero velocities (for the last 5 km before the terminus) are indicated with the white line.

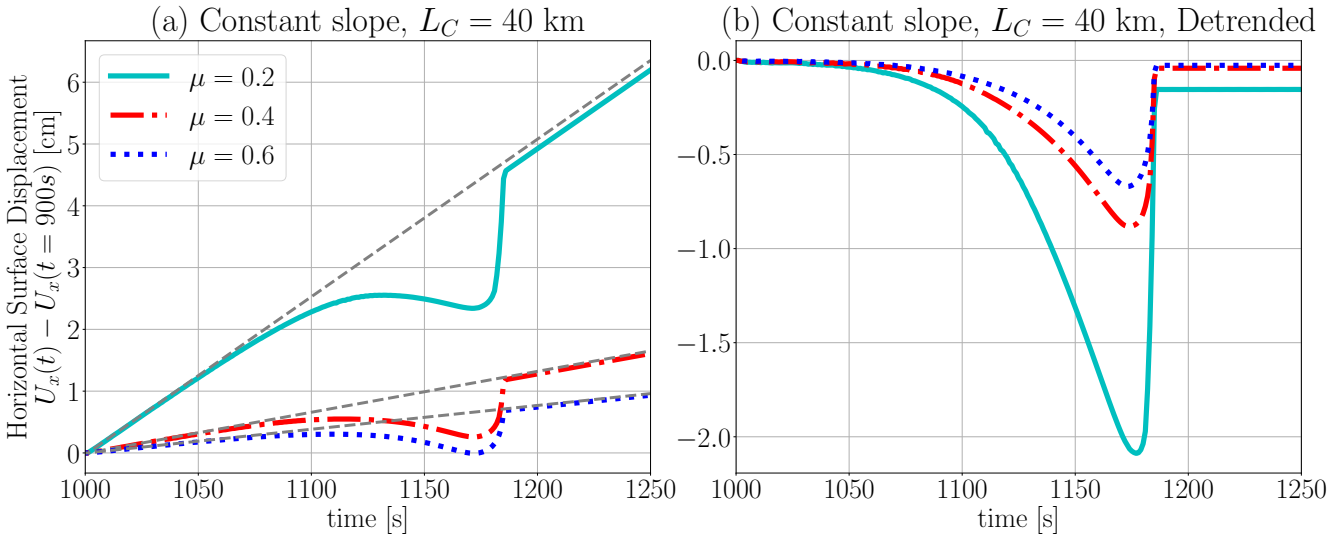

Figure 5.11: For a glacier on a constant slope, and a Coulomb friction law on the whole basal surface: horizontal displacements (a) and detrended horizontal displacements (b), at the free surface, for three values of the Coulomb friction coefficient μ.

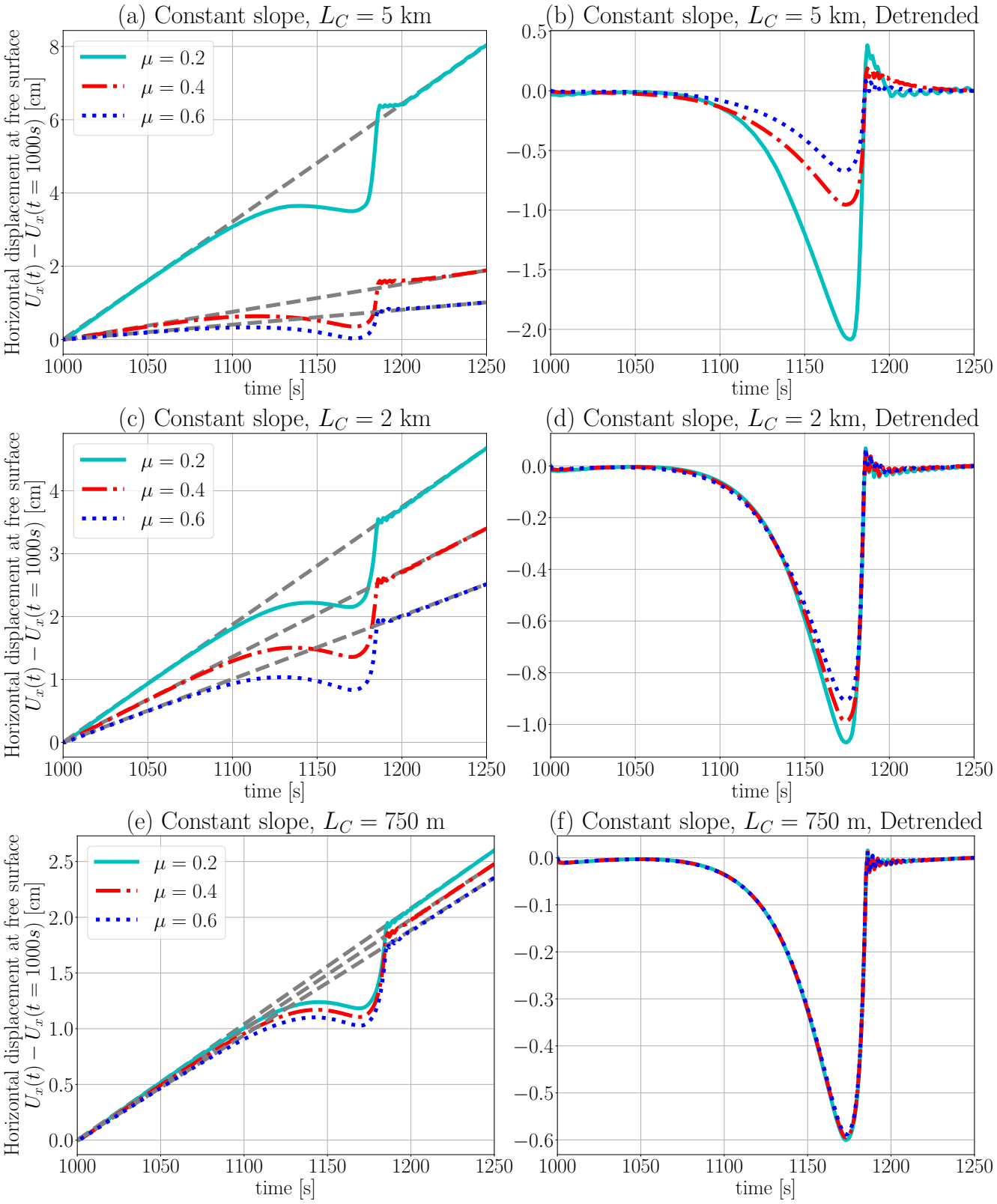

Figure 5.12: For a glacier on a constant slope, horizontal displacements at the free surface, for three values of the Coulomb friction coefficient μ and for various lengths of the Coulomb friction zone: (a-b) $L_C = 5$ km, (c-d) $L_C = 2$ km, (e-f) $L_C = 750$ m.

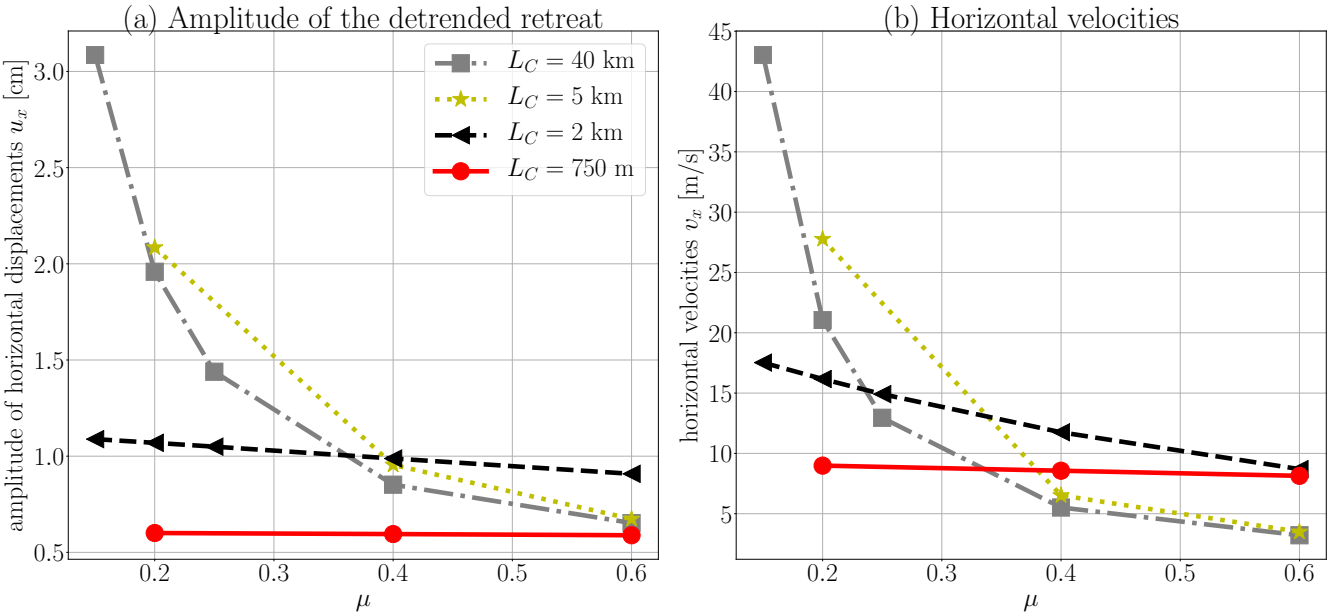

Figure 5.13: Horizontal displacements with respect to the Coulomb friction coefficient and horizontal velocities (between time $t = 900$ s and time $t = 1000$ s), for various lenghts of the Coulomb friction zone

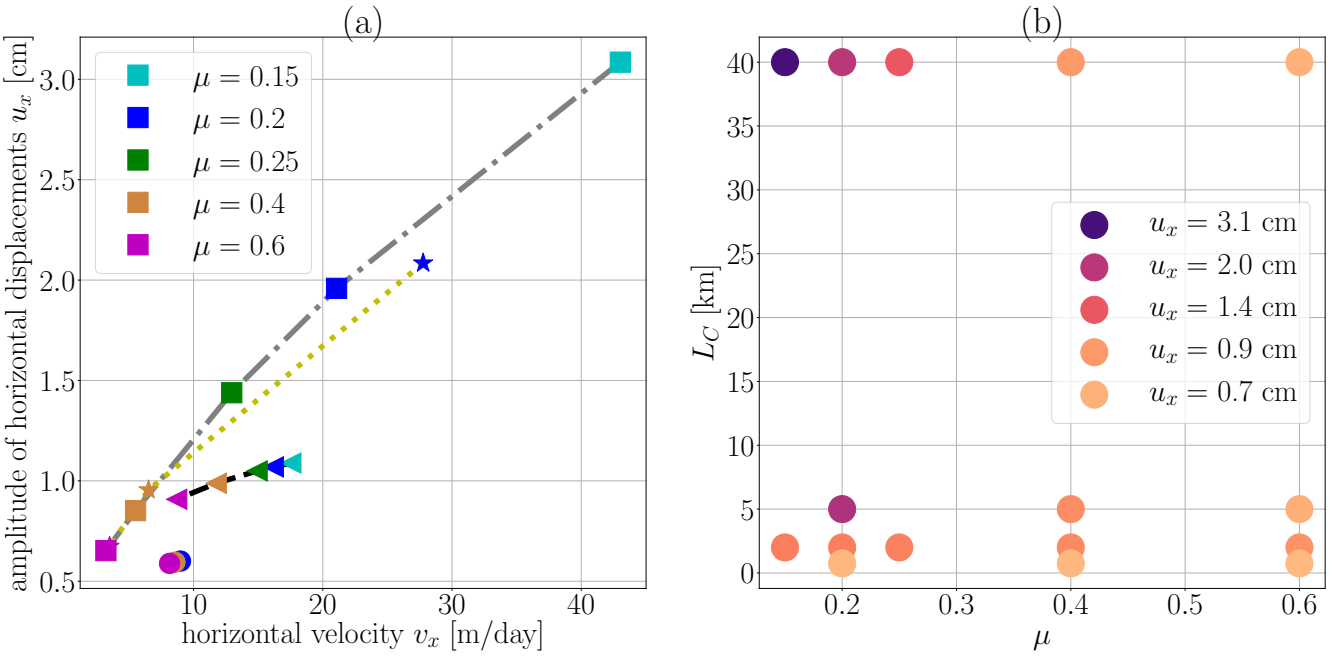

Figure 5.14: Horizontal displacements with respect to the Coulomb friction coefficient and horizontal velocities, for various lenghts of the Coulomb friction zone

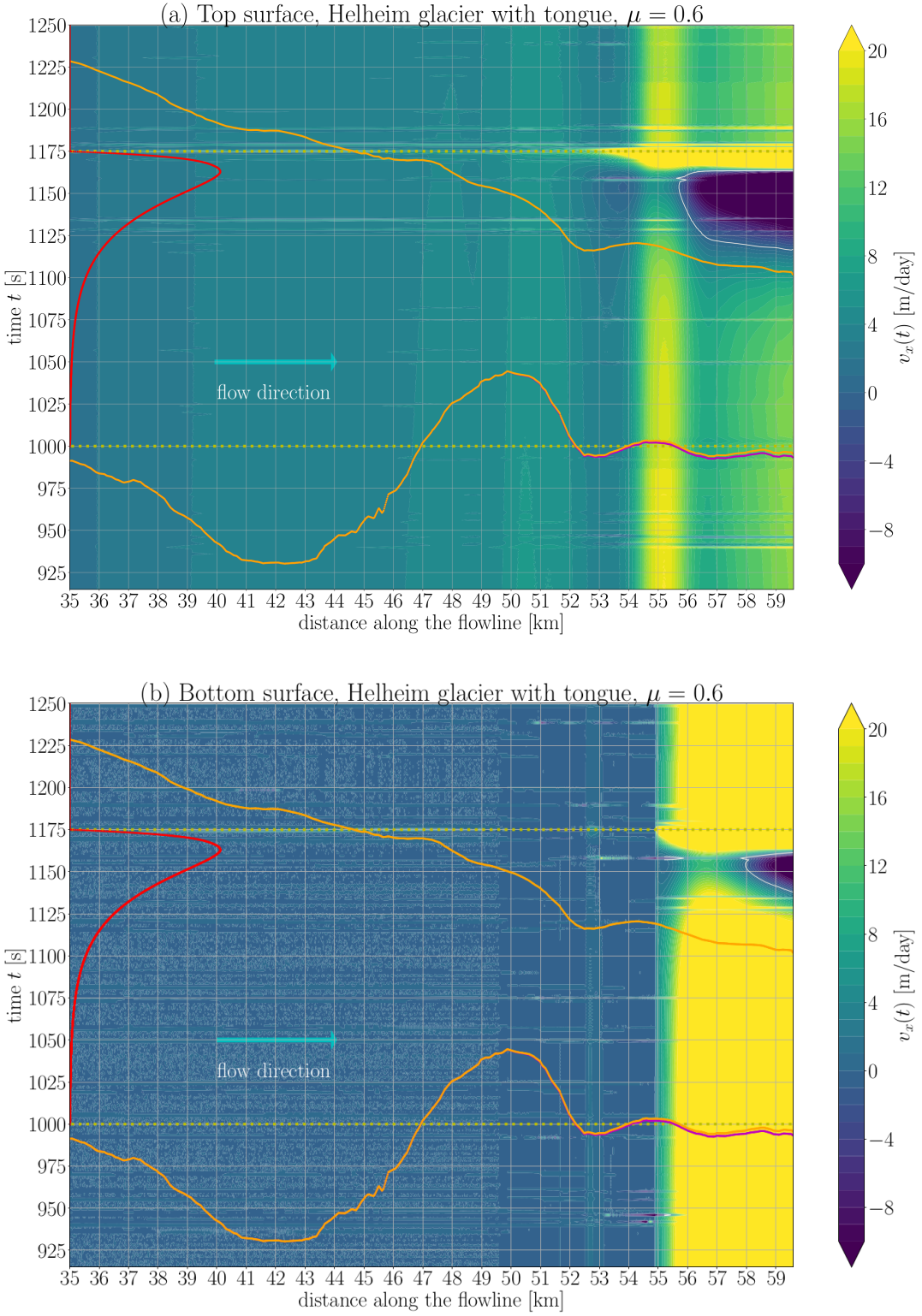

Figure 5.15: Helheim glacier with a floating tongue: surface (top) and basal (bottom) velocities during capsize at the terminus of the Helheim glacier with a floating tongue. The Coulomb friction coefficient is $\mu = 0.6$. The red curve shows the iceberg force applied on the terminus front. The orange lines indicates the initial position of the mesh along the flowline, the cyan line is the sea level, and the yellow solid line is the flotation line, the bedrock is shown in magenta, which is almost superimposed with the glacier basal surface in orange.

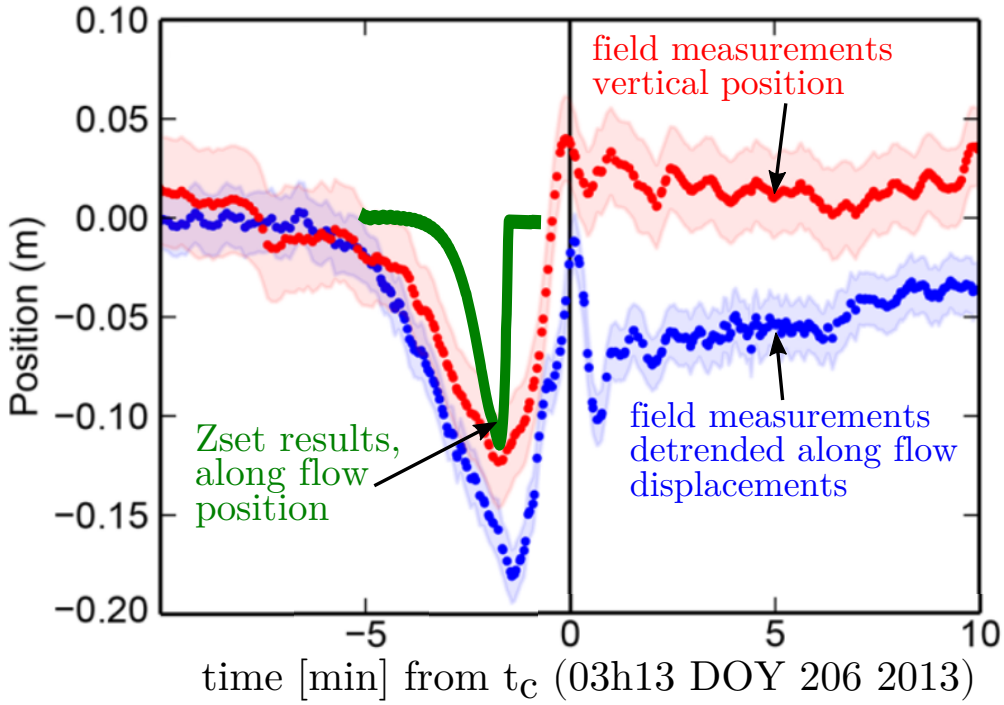

Figure 5.16: Field measurements measured at the Helheim glacier during capsize: horizontal detrended displacements (blue) and vertical displacements (red) during capsize, at 500 m from the terminus front (adapted from Murray et al., 2015a). In green we added, the horizontal detrended displacements obtained with the Z-set simulations of a Helheim glacier with a floating tongue, with $E = 3$ GPa, and $\varepsilon = 0.45$.

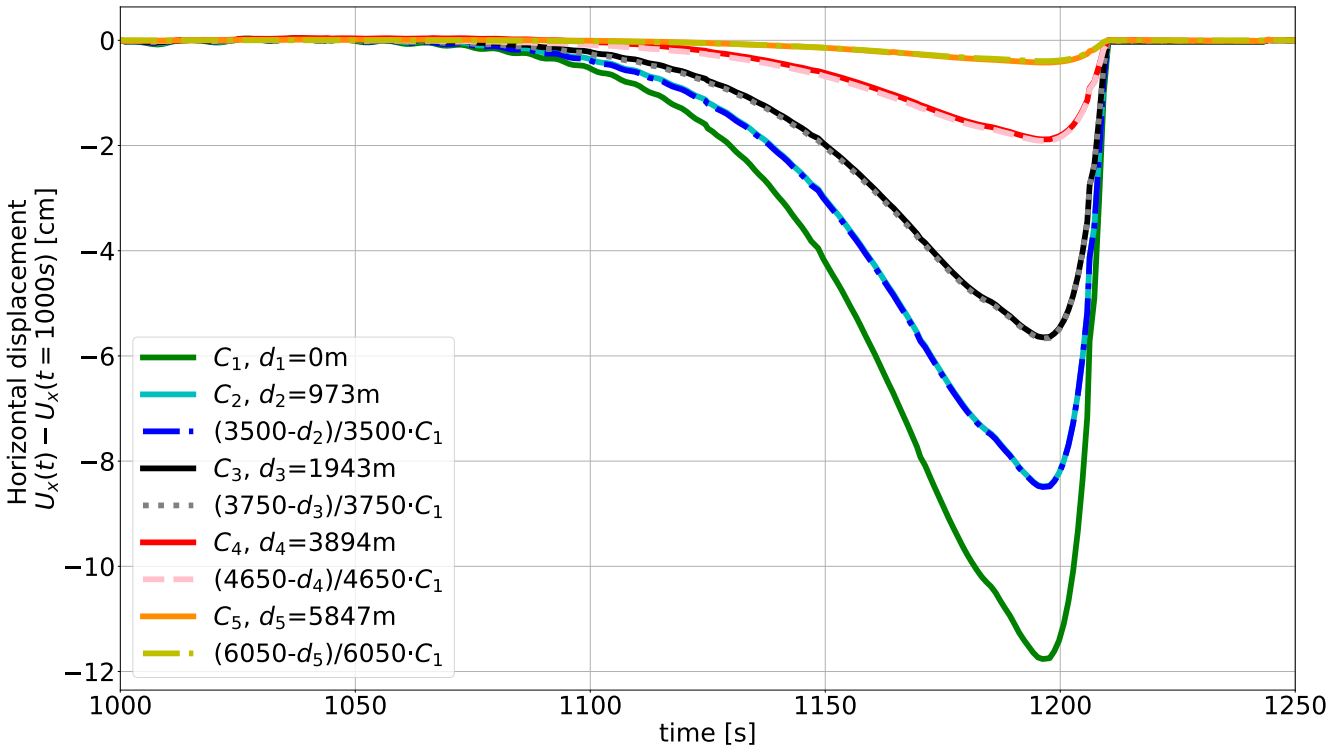

Figure 5.17: Helheim glacier with a floating tongue: horizontal displacements at various distances d_i $(i = 1 - 5)$ from the terminus.

CHAPTER 6

Conclusions and Perspectives

This PhD allowed to improve the physical understanding of the source of glacial earthquakes due to the capsize of an iceberg close to the terminus of a marine terminating glacier. In this work, the response of a visco-elastic glacier (with a Weertman and a Coulomb friction law) to the capsize of an iceberg was modelled for the first time. We summarize the important results and the possible perspectives.

We improved the physical understanding of the processes at play during the capsize of an iceberg in the open ocean. ISIS-CFD model highlighted the intense motion of the fluid around the capsizing iceberg. ISIS-CFD simulations showed the effect of the scale on the normalised force, especially for large aspect ratios of the iceberg. The ISIS-CFD simulations also showed the impact of a change in the water and ice densities on the modelled hydrodynamic forces on the capsizing iceberg. We validated a semi-analytical model for the hydrodynamic forces acting on the iceberg. We pointed out the sensitivity of the initial angle of inclination of the iceberg on the duration of the initiation of the capsize, that is when the iceberg slowly starts rotating and when the hydrodynamic forces have a negligible amplitude. In the case where the duration of the initiation of the capsize should be well modelled, we suggest to use a drag force and added-masses, however the amplitude is underestimated in that case. In the case where the amplitude of the force should be well modelled (but not duration of initiation of the capsize), we suggest to use a formulation for the hydrodynamic effects (horizontal and vertical forces and the torque) which requires only one parameter, the drag coefficient. We optimize this drag coefficient for various aspect ratios of the iceberg by minimizing the error on the horizontal force compared to the ISIS-CFD model. This work was published in (Bonnet et al., 2020).

Using results of ISIS-CFD simulations on a field scale iceberg capsizing close to the sea floor, we estimated the time evolution of the pressure force on the sea floor during capsize. This preliminary study suggests that these efforts are at least 10% smaller in amplitude than the iceberg-glacier contact force. To model a more realistic geometry, we could include a glacier tongue close to the capsizing iceberg in the ISIS-CFD. This is ongoing work conducted by our collaborators developing the ISIS-CFD solver.

We then extended the SAFIM model to include the contact between the iceberg and a rigid terminus or an elastic glacier tongue. With this SAFCIM model, we showed the little impact of the stiffness of the glacier tongue on the contact force. This observation implies that we can use a pre-calculated iceberg-glacier contact force in the Z-set model. Although the Z-set model is able to model the dynamics of a capsizing iceberg, it is challenging to release the iceberg after an initiation time, using a precalculate contact force makes it computationaly easier to initiate the motion of the glacier before the capsize of the iceberg. We estimated the zone of application of the top-out and bottom-out capsize force which is then used in the Z-set model. Using the Z-set software, we calculated the horizontal and the vertical contact force applied on the terminus in the case where there is a Coulomb friction law at the glacier-iceberg interface. Such calculation showed the negligible influence of the Coulomb friction parameter on the horizontal force. A preliminary comparison of the SAFCIM model with laboratory experiments from Amundson et al. (2012) suggests that the duration of the capsize is slightly under-estimated using the SAFCIM model.

Then we modelled the response of a two-dimensional visco-elastic glacier to the capsize of an iceberg at the terminus front using the Z-set finite element software and the iceberg contact force precalculated with SAFCIM. We investigated the impact of the parameters of the geometry, the ice rheology, the friction laws and the type of capsize on the response of the glacier to a capsize force at the terminus. First, we analysed the behaviour of a glacier with a model geometry: a glacier with a constant height, a bedrock with a constant slope, and a glacier tongue in a rectangular horizontal shape. At the basal interface, assume a Weertman type friction law upstream, and a Coulomb friction law close to the terminus, with adjustable coefficients.

Concerning the ice rheology, the displacements during the capsize are mainly explained by the elastic behaviour

of the ice, but are also slightly affected by the viscous behaviour of the ice. The viscous behaviour of the ice explains the observed shift of the detrended displacements at the end of the capsize compared to the detrended displacements before the capsize. However, this residual displacement is underestimated with our model (compared to the field measurements). Integrating the transient creep of ice in our rheology could help explain the higher amplitude of these residual displacements.

For both a top-out and bottom-out capsize, the glacier surface moves upwards and the horizontal velocity decreases. This observation was done for a grounded glacier (without a floating tongue), and in the case of a glacier with a floating tongue, in the part of the glacier upstream from the grounding line. Moreover, the ratio of the amplitude of the horizontal displacements on the amplitude vertical displacements is equal to 2 for a bottom-out capsize and to 1 for a top-out capsize, due to the different in the zone of application of the force on the terminus. This suggests that, using only GPS measurements, the type of capsize can be known.

On the floating tongue, close to the terminus, the surface of the glacier moves upwards and backwards for a bottom-out capsize and downwards and slightly forwards for a top-out capsize. However, this does not fit with the following field measurements: at the surface of the Helheim glacier a downward and reverse horizontal motion was observed during a bottom-out capsize. A vertical force of the same amplitude of the horizontal force applied on the terminus front does not produce a downward motion. However, this downward motion may be explained by a depression below the glacier tongue due to the fluid motion during capsize (Murray et al., 2015a). To investigate this hypothesis we could include a pressure force on the submarine surface on the glacier tongue. The amplitude of such a depression could be estimated a priori, using the ISIS-CFD solver with an iceberg capsizing close to a glacier tongue. The ISIS-CFD model should able to model an iceberg capsizing close to a rigid glacier tongue, but not yet for an iceberg capsizing in contact with the terminus.

Our simulations suggest that the capsize force applied on the terminus is transmitted in the bedrock without being affected by response of the two-dimensional visco-elastic glacier. The basal shear stresses close to the terminus are affected by the capsize and are sensitive to the Coulomb friction coefficient. However, whether such local and small variations are detectable is difficult to say.

Then we modelled the response of the Helheim glacier, totally grounded or near-grounded, to the capsize of an iceberg. In this case we fixed the coefficient of the viscous law to that obtained from a state-of-the-art model for glacier and ice sheet flow the ISSM inversion model, constrained with surface velocities and temperatures. We applied the Coulomb friction law on the whole basal surface because of the challenging implementation of the Weertman law (for low values of the friction coefficient in the case of the complex basal geometry). We adjusted the Coulomb friction coefficient to obtain velocities close to the terminus similar to that in the state-of-the-art simulations (between 20m/day and 25 m/day in the last 5 km before the terminus). With the grounded Helheim glacier, the values of the Coulomb friction coefficients are set to $0.1 < \mu < 0.2$. For the simulations with a Helheim glacier with a floating tongue, a coefficient of $\mu = 0.6$ yield consistent velocities of the floating tongue. More constraints on the floating or grounded state of the glacier could help discriminate between both of these values of the Coulomb friction coefficient.

For a grounded Helheim glacier, we showed a high dependence of the amplitude of the reverse horizontal motion to the Coulomb friction coefficient: when the Coulomb friction coefficient decreases from 0.4 to 0.2, the amplitude of the reverse motion is more than two times bigger.

For a Helheim glacier with a floating tongue, we suggest that the ratio of the displacements at various distances from the terminus can help estimate of the length of the glacier tongue. We showed that the amplitude of horizontal displacements at the surface of the glacier that were measured at the Helheim glacier are well predicted in the case

of a glacier with a floating tongue of length ≈ 3 km and with a Young's modulus of 3 GPa. However, the duration of the force is underpredicted. This may be due to a too short duration of the SAFCIM force, or to an additional resisting force that may slow down the capsize (from the ice-mélange or lateral friction on the fjord). In future work, we could include the ice-mélange dynamics by considering additional blocks of ice in the capsize model (SAFCIM) or a continuous viscous medium (Peters et al., 2014; Cassotto et al., 2015) in contact with the terminus in the finite element model (in the Z-set software).

In our model glacier, the geometry of the floating tongue is a rectangle. We could adjust the shape of the glacier tongue in our model to a more realistic shape: either using the theoretical estimation with elastic beam equations (e.g. Wagner et al., 2016), or by running longer time simulations with Z-set. Moreover, it could be interesting to investigate the effect of a inverse sloping bedrock at the grounding line. It might allow a greater retreat of the glacier during capsize. This could be investigated with a model glacier (constant slope) or with the geometry of a Greenland glacier lying on a retrograde slope (such at the Jakobshavn Isbrae glacier and the Kangerdlussuaq glacier).

In our simulations with the simple geometry, we used a Weertman law upstream, and a Coulomb friction law close to the grounding line, with constant coefficients. In order to obtain a smooth transition between the Weertman and the Coulomb friction zone, we could consider a variation of these coefficient in space, or a hybrid law where the basal stress that is a proportional to both a power of the velocity and a power of the effective basal pressure (Budd et al., 1979). Moreover, the step-like change of the velocities of the Helheim glacier observed during a capsize event (Nettles et al., 2008), could be explained by a change in time of the friction coefficients. Such hypothesis is investigated to explain the brutal change in velocities in surging glaciers (e.g. Jay-Allemand et al., 2011). Moreover, such brutal and short live acceleration was also observed at the marine-terminating Bowdoin glacier prior to the appearance of a plume (release of basal water forming a ice-free zone close to the terminus) by (Jouvet et al., 2018). The authors suggest that it may be due to the collapse of a subglacial lake. Glacier speedup can also occur after the calving of a tabular iceberg (without capsize), as observed Petermann glacier in northern Greenland (Rückamp et al., 2019).

To improve our understanding of the response of a glacier to the capsize of an iceberg, a one dimensional analytical model of a glacier with a Coulomb friction force or a Weertman friction force has been developed recently by Vladislav Yastrebov (co supervisor of this PhD). This model could give further insights on the effect of both friction laws without considering the two-dimensional effects.

In our simulations we did not take into account the three dimensional effects. Thus we neglected the lateral friction on the glacier, the variation of the width of the glacier along the flowline, the three-dimensional motion of the water around the capsizing iceberg. We could extend our simulations to three dimensional simulations to investigate the impact of these effects on the response of the glacier to the capsize of an iceberg. However, such simulations would be computationally costly.

APPENDIX A

Discussion on the formulation for the relative position station-event used for the calculation of Green's functions

Introduction

An inversion methodology was designed and used previously in the team (Sergeant et al., 2016, 2018, 2019). The seismic inversion consists in removing the propagation effect from the seismic data in order to retrieve the seismic source. The inversion methodology in divided into three steps, (1) download of the data and removal of the instrumental response, (2) calculation of the propagation effects (Green's function), (3) processing of the seismic data and the Green's functions and inversion of the source force.

In this appendix, we suggest a minor correction on step (2) the calculation of the Green's functions. However, this is preliminary work and it would require to estimate the impact of this correction on the inverted source force.

To calculate the Green's function, we solve the linear equation for wave propagation in an elastic medium (Aki and Richards, 2002)[p. 28], using the discrete wave number method (Bouchon, 2003, 1981). To solve numerically these equations, we use the code developed by (Favreau et al., 2010). Compared to other codes in the litterature (e.g. Herrmann, 2013; Cotton and Coutant, 1997) it has the advantage of being able to model event with a force source located at the earth surface, however it is not documented.

For each station, the inputs for this code that calculate the Green's function are:

- the velocity model
- the relative position of the stations and the event
- the number of sources: 1 here
- the type of source i.e. a force or a moment: a force here
- the time step: 1 s here

The Green's function are calculated by solving the equation of elastodynamics for an impulse source force. There are 9 Green's functions: Si_Fj with $i = E$ or N or Z, the component of the source, and $j = E$ or N or Z, the component of the seismic trace.

The velocity model of the Earth is the one used in (Sergeant et al., 2016; Sergeant, 2016) and written in Table A.1.

A sensitivity analysis of the Green's function with the velocity model was conducted by (Sergeant, 2016).

Correction in the calculation of the relative position between the station and the event

The calculation of the Green's functions requires the relative position of the event and the stations.

Given the event latitude and longitude, and using the law of cosines, we calculate:

- the azimuth az: oriented angle between the direction $event - N$ and the direction $event - station$, with N the North pole, positive clock-wise.
- δ: oriented angle between the direction $center - event$ and the direction $center - station$, with $center$ the center of the earth.

The angles δ and az_{tmp} (the angle between the direction $event - N$ and the direction $event - station$ such as $0 < az_{tmp} < 180$) are given by the law of cosines:

depth [m]	VP [m/s]	VS [m/s]	rho [kg / m^3]
0.00	6200.0	3600.0	2800.0
3000	6200.0	3600.0	2800.0
16000	6400.0	3600.0	2850.0
28000	6800.0	3800.0	2950.0
40000	8200.0	4700.0	3400.0
80000	8076.250	4470.520	3374.710
220000	8558.950	4643.900	3435.780
400000	9133.920	4932.490	3723.750
600000	10157.76	5516.020	3975.820
670000	10751.32	5945.130	4380.740
771000	11065.59	6240.390	4443.200
1500000	12293.16	6725.48	4897.83
2200000	13015.79	7010.53	5207.13
2741000	13680.44	7265.970	5491.480
2891000	8064.790	0100.000	9903.440
3600000	9050.15	0100.000	10853.21
4400000	9834.96	0100.000	11654.78
5149500	11028.26	3504.310	12763.61

Table A.1: PREM model

$$\begin{aligned} \delta &= \text{acos}\big(\ \cos(coLat_{event})\cos(coLat_{station}) + \sin(coLat_{event})\sin(coLat_{station})\cos(Lon_{event}\text{-}Lon_{station})\ \big) \\ az_{tmp} &= \text{acos}\big(\ (\ \cos(coLat_{station}) + \cos(\delta)\cos(coLat_{event})\ )\ /\ (\sin(\delta)\cos(coLat_{event})\ )\ \big) \end{aligned}$$

$$\begin{aligned} \text{if } Lon_{station} > Lon_{event}: &\quad az = az_{tmp} \\ \text{else:} &\quad az = 2\pi - az_{tmp} \end{aligned}$$

The azimuth angle az is defined as a positive clockwise angle, thus:
We define the coordinates :

$$X = D * cos(az) \tag{A.1}$$

$$Y = D * sin(az) \tag{A.2}$$

with D the distance in meters between the event and the station along the surface of the Earth.
Let us now compare the previous code and the new code.

1. Concerning the if-condition "if $Lon_{station} > Lon_{event}$" written above:

previous code The if-condition was wrong: it was "if $mod(Lon_{station}, 2\pi) > mod(Lon_{event}, 2\pi)$", with *mod* the modulo function. For a station and event with $-2\pi < Lon_{station} < 0$ and $-2\pi < Lon_{event} < 0$ or $0 < Lon_{station} < 2\pi$ and $0 < Lon_{event} < 2\pi$, it is equivalent. However, for a station with a positive longitude and an event with a negative longitude, the modulo will shift the event longitude by $2pi$ to a positive value. The $mod(Lon_{event}, 2pi)$ becomes bigger than $Lon_{station}$ if $Lon_{event} > Lon_{station} - 2pi$, in particular, it is the case for KBS $Lon_{station} = 11.9385$ and events on Greenland. In that case the azimuth is wrong, and the X (defined bellow) has the wrong sign.

new code The values of δ and az are now calculated with the python function obspy.geodetics.base.gps2dist_azimuth based on (Karney, 2013), which doesn't have the error on X.

2. The distance D can be calculated with various levels of approximation:

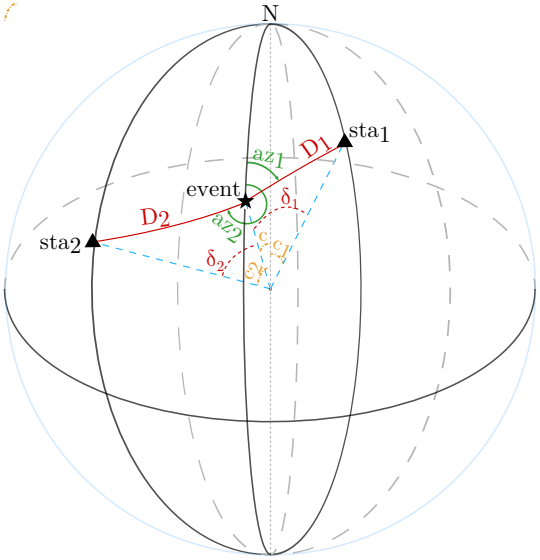

Figure A.1: Schematic view of an event and two stations sta_1 and sta_2 with c the colatitude of the event, $c1$ and $c2$ the colatitude of station 1 and 2, $az1$ and $az2$ the azimuth angles, $D1$ and $D2$ the distances from the event to stations along the earth surface, and the corresponding angle $\delta 1$ $\delta 2$

previous code For a spherical earth with radius r, this distance is $D = r\delta$ with δ in radians. An additional approximation was used : the factor to convert δ in degrees to D in meter is $pi/180 * 6371 = 111.194927$ m, it was approximated to 111 m.

new code For an ellipsoid earth, the python function obspy.geodetics.base.gps2dist_azimuth, takes in input the event latitude and longitude and the station latitude and longitude and returns the distance D in meters for a spheroid of radius r and flattening f. The default radius and flattening are those from the WGS84 ellipsoid (reference system used by the Global Positioning System): $r = 6378137.0$ m and $f = 0.0033528106647474805$.

The error on the sign of X yields an error in the Green's function: some Green's functions have the wrong sign. This error also impacts the inversion. Also, the spherical earth approximation yields a small error. The corresponding errors on the Green's functions are given for a specific seismic event in the next section.

Discussion

In this section we give an example of the Green's function for the 13 August 2007 event at Helheim glacier. The latitude and longitude of the event (Tsai and Ekström, 2007) are given in table A.2 and Fig. A.2:

$$\text{event latitude } Lat_{event} = 66.40$$
$$\text{event longitude } Lon_{event} = -38.34.$$

For this event, four closest active stations are used for the inversion. In table A.2, for each station we give the name of the station and network, the country where the station is located, the station latitude $Lat_{station}$, station longitude $Lon_{station}$, and the azimuth az (defined above).

In the next figures we plot the Green's function for the station KBS for various approximations described above. The previous code (black curves) gives different results than the new code, see Figs. A.3. When changing for a spherical Earth with radius 6371 m, the Green's function fit with that of the previous code for some of the

network.station	Country	$Lat_{station}$ [°]	$Lon_{station}$ [°]	D [m]	az [°]
II.BORG	Iceland	64.7474	−21.3268	803.9387	95.3544
CN.FRB	Canada	63.7469	−68.5451	1436.3733	272.2638
IU.KBS	Norway	78.9154	11.9385	2062.4161	27.8297
IU.SFJD	Greenland	66.9961	−50.6207	545.4695	282.6046

Table A.2: Information on stations used for the inversion of the Helheim glacier event on 13 August 2007

Figure A.2: Stations in orange (CN.FRB, IU.SFJD, II.BORG, IU.KBS) and event location in blue (Helheim glacier)

components only, see Figs. A.4. When changing the sign of the X coordinate (as in the previous code), the Green's function fit perfectly with that of the previous code, see Figs. A.5. Note that changing the sign of the X component (KBS was taken to be on the west of the event instead of being on the east) has the following effect on the Green's function: the time and frequency amplitude are also of the wrong sign for only some of the Green's functions: E-E, E-Z, N-N, Z-N (the first letter is the component of the Trace, the second letter in the component of the Force)

The new code is more precise and does not have the error on the Green's function, thus is used hereafter.

Conclusion

This preliminary work on the seismic inversion code suggests a small mistake in the inversion code. Further investigation are required to estimate the impact of such an error on the force inversion. However, this mistake should only concern station KBS, therefore it is damped by the number of stations in the calculation.

The code used for calculating Green's functions is not well documented. In future work, another code could be used such as the codes developed by (Herrmann, 2013) or (Cotton and Coutant, 1997). However, these codes may require some adaptations in order to model a source force located at the earth surface.

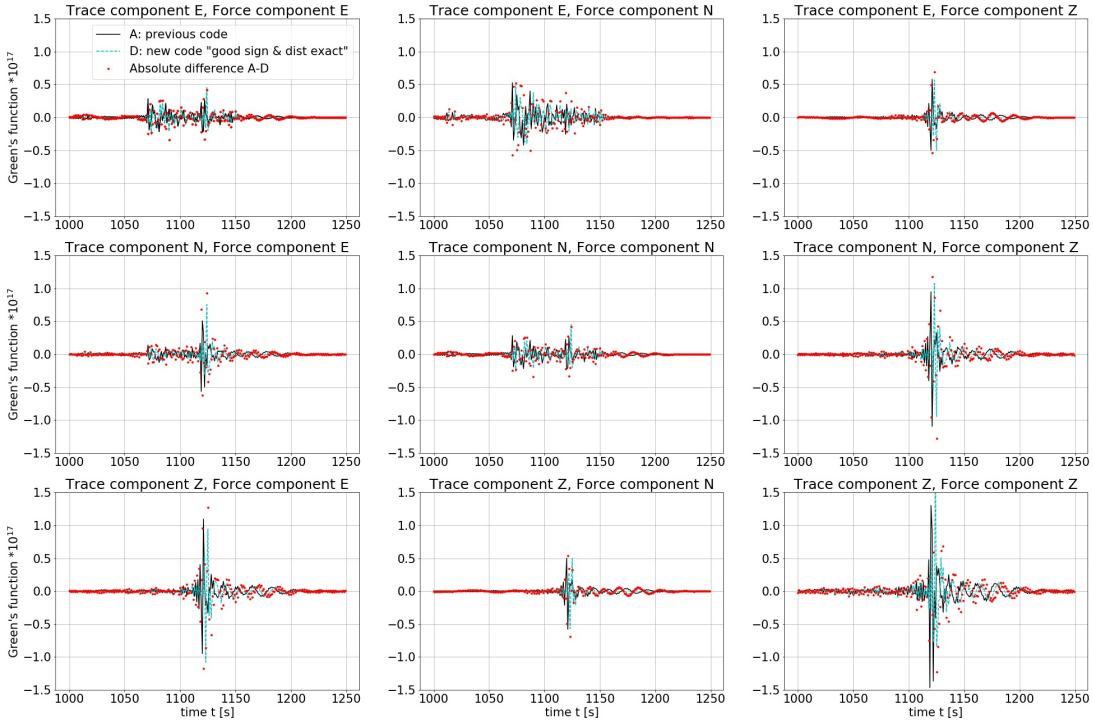

Figure A.3: KBS, Time evolution of the Green's functions, calculated with the previous code (A) and with the new code (B)

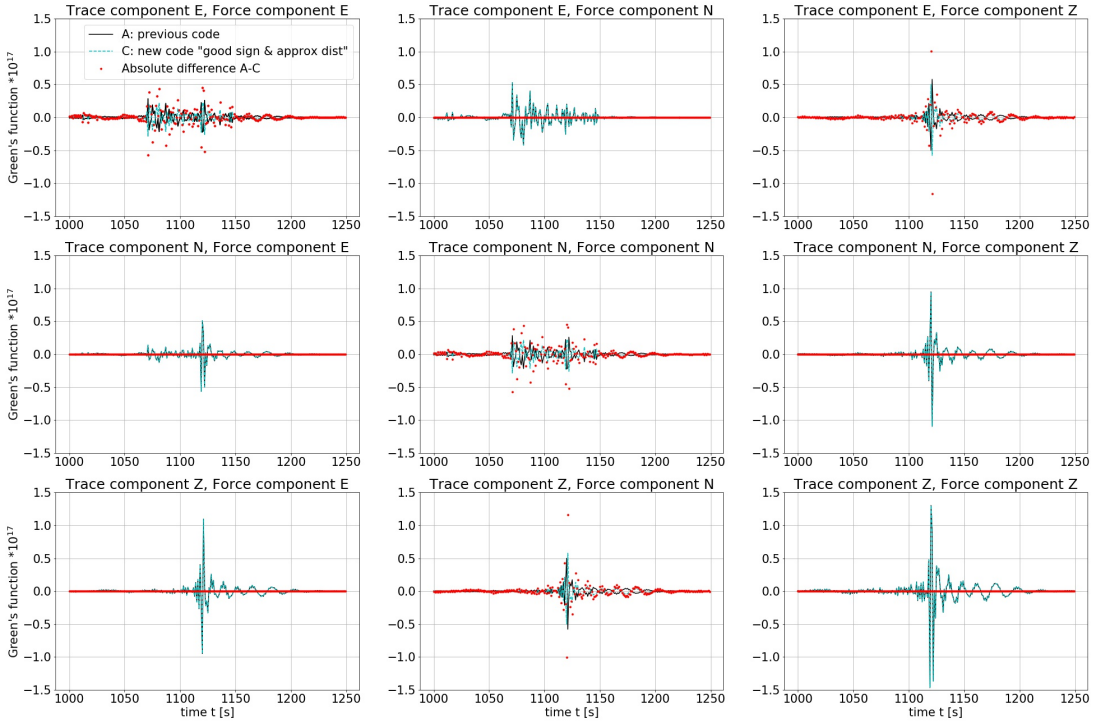

Figure A.4: KBS, Time evolution of the Green's functions, calculated with the previous code (A) and with the new code with the spherical earth assumption with radius $R = 6371$ m (C)

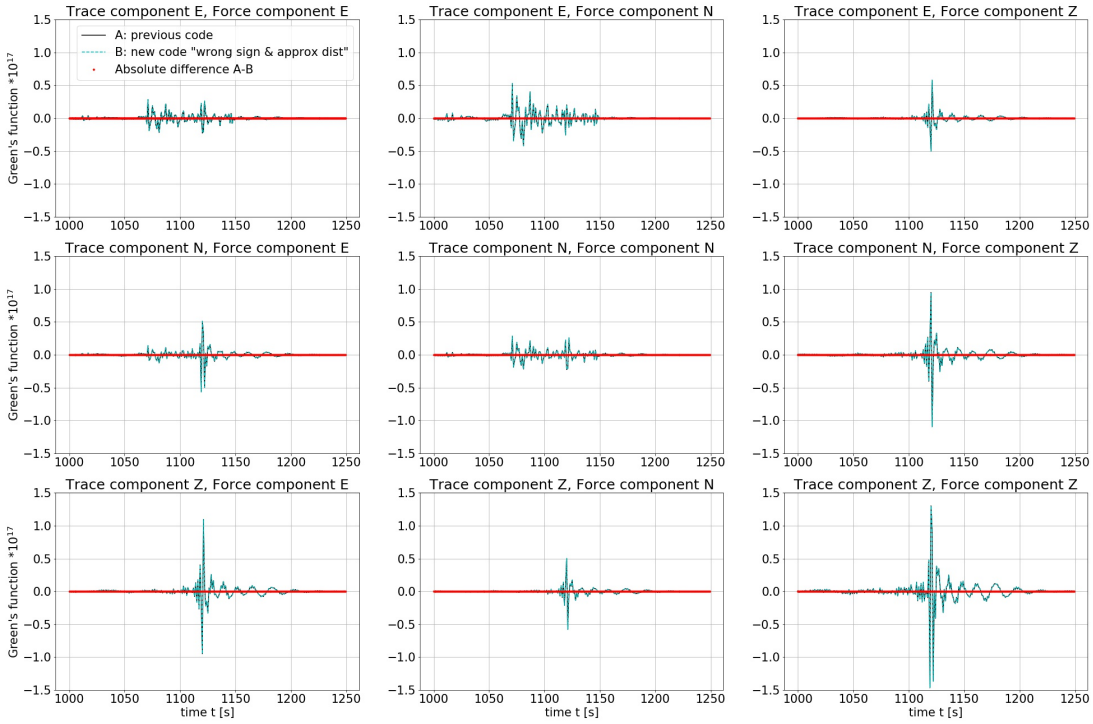

Figure A.5: KBS, Time evolution of the Green's functions, calculated with the previous code (A) and with the new code with the spherical earth assumption with radius $R = 6371$ m and taking the same sign for X then in the previous code (C)

Bibliography

Aki, K. and Richards, P. G. (2002). *Quantitative seismology*. University Science Books.

Amundson, J. M., Burton, J. C., and Correa-Legisos, S. (2012). Impact of hydrodynamics on seismic signals generated by iceberg collisions. *Annals of Glaciology*, 53(60):106–112.

Amundson, J. M., Fahnestock, M., Truffer, M., Brown, J., Lüthi, M. P., and Motyka, R. J. (2010). Ice mélange dynamics and implications for terminus stability, Jakobshavn Isbrse, Greenland. *Journal of Geophysical Research: Earth Surface*, 115(1).

Amundson, J. M., Truffer, M., Lüthi, M. P., Fahnestock, M., West, M., and Motyka, R. J. (2008). Glacier, fjord, and seismic response to recent large calving events, Jakobshavn Isbræ, Greenland. *Geophysical Research Letters*, 35(22):2–6.

Ardhuin, F., Gualtieri, L., and Stutzmann, E. (2015). How ocean waves rock the Earth: Two mechanisms explain microseisms with periods 3 to 300s. *Geophysical Research Letters*, 42(3):765–772.

Ardhuin, F., Stutzmann, E., Schimmel, M., and Mangeney, A. (2011). Ocean wave sources of seismic noise. *Journal of Geophysical Research: Oceans*, 116(C9).

Arthern, R. J., Hindmarsh, R. C., and Williams, C. R. (2015). Flow speed within the Antarctic ice sheet and its controls inferred from satellite observations. *Journal of Geophysical Research F: Earth Surface*, 120(7):1171–1188.

Ashby, M. and Duval, P. (1985). The creep of polycrystalline ice. *Cold Regions Science and Technology*, 11(3):285–300.

Aster, R. C. and Winberry, J. P. (2017). Glacial seismology. *Reports on Progress in Physics*, 80(12):126801.

Ballinger, T., Overland, J., Wang, M., Bhatt, U., Hanna, E., Hanssen-Bauer, I., Kim, S.-J., Thoman, R., and Walsh, J. (2020). Arctic report card 2020: Surface air temperature.

Bartholomaus, T., Larsen, C. F., O'Neel, S., and West, M. (2012). Calving seismicity from iceberg–sea surface interactions. *Journal of Geophysical Research: Earth Surface*, 117(F4).

Beckmann, J., Perrette, M., Beyer, S., Calov, R., Willeit, M., and Ganopolski, A. (2019). Modeling the response of greenland outlet glaciers to global warming using a coupled flow line–plume model. *The Cryosphere*, 13(9):2281–2301.

Blatter, H., Clarke, G. K., and Colinge, J. (1998). Stress and velocity fields in glaciers: Part ii. sliding and basal stress distribution. *Journal of Glaciology*, 44(148):457–466.

Bonnet, P., Yastrebov, V. A., Queutey, P., Leroyer, A., Mangeney, A., Castelnau, O., Sergeant, A., Stutzmann, E., and Montagner, J. P. (2020). Modelling capsizing icebergs in the open ocean. *Geophysical Journal International*, 223(2):1265–1287.

Bouchon, M. (1981). A simple method to calculate Green's functions for elastic layered media. *Bulletin of the Seismological Society of America*, 71(4):959–971.

Bouchon, M. (2003). A review of the discrete wavenumber method. *Pure and Applied Geophysics*, 160(3-4):445–465.

Brondex, J., Gagliardini, O., Gillet-Chaulet, F., and Durand, G. (2017). Sensitivity of grounding line dynamics to the choice of the friction law. *Journal of Glaciology*, 63:854–866.

Brunt, K. M. and Macayeal, D. R. (2014). Tidal modulation of ice-shelf flow: A viscous model of the Ross Ice Shelf. *Journal of Glaciology*, 60(221):500–508.

Budd, W. F., Keage, P. L., and Blundy, N. A. (1979). Empirical studies of ice sliding. *Journal of Glaciology*, 23(89).

Burton, J. C., Amundson, J. M., Abbot, D. S., Boghosian, A., Cathles, L. M., Correa-Legisos, S., Darnell, K. N., Guttenberg, N., Holland, D. M., and MacAyeal, D. R. (2012). Laboratory investigations of iceberg capsize dynamics, energy dissipation and tsunamigenesis. *Journal of Geophysical Research: Earth Surface*, 117(1):1–13.

Burton, J. C., Cathles, L. M., and Wilder, W. G. (2013). The role of cooperative iceberg capsize in ice-shelf disintegration. *Annals of Glaciology*, 54(63):84–90.

Calov, R., Beyer, S., Greve, R., Beckmann, J., Willeit, M., Kleiner, T., Rückamp, M., Humbert, A., and Ganopolski, A. (2018). Simulation of the future sea level contribution of greenland with a new glacial system model. *The Cryosphere Discussions*, pages 1–37.

Cassotto, R., Fahnestock, M., Amundson, J. M., Truffer, M., Boettcher, M. S., De La Peña, S., and Howat, I. (2019). Non-linear glacier response to calving events, Jakobshavn Isbræ, Greenland. *Journal of Glaciology*, 65(249):39–54.

Cassotto, R., Fahnestock, M., Amundson, J. M., Truffer, M., and Joughin, I. (2015). Seasonal and interannual variations in ice melange and its impact on terminus stability, jakobshavn isbræ, greenland. *Journal of Glaciology*, 61(225):76–88.

Castelnau, O., Shoji, H., Mangeney, A., Milsch, H., Duval, P., Miyamoto, A., Kawada, K., and Watanabe, O. (1998). Anisotropic behavior of grip ices and flow in central greenland. *Earth and planetary science letters*, 154(1-4):307–322.

Catania, G. A., Stearns, L. A., Moon, T. A., Enderlin, E. M., and Jackson, R. H. (2020). Future Evolution of Greenland's Marine-Terminating Outlet Glaciers. *Journal of Geophysical Research: Earth Surface*, 125(2):1–28.

Chauché, N. (2016). *Glacier-Ocean interaction at Store Glacier (West Greenland)*. PhD thesis, Aberystwyth University, UK.

Chouet, B., Saccorotti, G., Martini, M., Dawson, P., De Luca, G., Milana, G., and Scarpa, R. (1997). Source and path effects in the wave fields of tremor and explosions at stromboli volcano, italy. *Journal of Geophysical Research: Solid Earth*, 102(B7):15129–15150.

Clinton, J. F., Nettles, M., Walter, F., Anderson, K., Dahl-Jensen, T., Giardini, D., Govoni, A., Hanka, W., Lasocki, S., Lee, W. S., McCormack, D., Mykkeltveit, S., Stutzmann, E., and Tsuboi, S. (2014). Seismic network in Greenland monitors earth and ice system. *EOS*, 95(2):13–14.

Copland, L. and Mueller, D. (2017). *Arctic ice shelves and ice islands*. Springer.

Cotton, F. and Coutant, O. (1997). Dynamic stress variations due to shear faults in a plane-layered medium. *Geophysical Journal International*, 128(3):676–688.

Cuffey, K. M. and Paterson, W. S. B. (2010). *The Physics of Glaciers Fourth Edition*. Elsevier.

Deshayes, J., Curry, R., and Msadek, R. (2014). Cmip5 model intercomparison of freshwater budget and circulation in the north atlantic. *Journal of Climate*, 27(9):3298–3317.

Durand, G., Gagliardini, O., Favier, L., Zwinger, T., and Le Meur, E. (2011). Impact of bedrock description on modeling ice sheet dynamics. *Geophysical Research Letters*, 38(20).

Duval, P. et al. (1977). The role of the water content on the creep rate of polycrystalline ice. *IAHS Publ*, 118:29–33.

Ekström, G. (2006). Global detection and location of seismic sources by using surface waves. *Bulletin of the Seismological Society of America*, 96(4A):1201–1212.

Ekström, G., Nettles, M., and Geoffrey, A. A. (2003). Glacial Earthquakes. *Science*, 622(2003):10–13.

Enderlin, E. M., Howat, I. M., Jeong, S., Noh, M.-J., van Angelen, J. H., and van den Broeke, M. R. (2014). An improved mass budget for the Greenland ice sheet. *Geophysical Prospecting*, 41(9):3307–3314.

Favier, L., Durand, G., Cornford, S. L., Gudmundsson, G. H., Gagliardini, O., Gillet-Chaulet, F., Zwinger, T., Payne, A. J., and Le Brocq, A. M. (2014). Retreat of Pine Island Glacier controlled by marine ice-sheet instability. *Nature Climate Change*, 4(2):117–121.

Favier, L., Gagliardini, O., Durand, G., and Zwinger, T. (2012). A three-dimensional full Stokes model of the grounding line dynamics: Effect of a pinning point beneath the ice shelf. *Cryosphere*, 6(1):101–112.

Favreau, P., Mangeney, A., Lucas, A., Crosta, G., and Bouchut, F. (2010). Numerical modeling of landquakes. *Geophysical Research Letters*, 37(15):1–5.

Feldmann, J. and Levermann, A. (2015). Collapse of the West Antarctic Ice Sheet after local destabilization of the Amundsen Basin. *Proceedings of the National Academy of Sciences of the United States of America*, 112(46):14191–14196.

Francavilla, A. and Zienkiewicz, O. (1975). A note on numerical computation of elastic contact problems. *International Journal for Numerical Methods in Engineering*, 9:913–924.

Fretwell, P., Pritchard, H. D., Vaughan, D. G., Bamber, J. L., Barrand, N. E., Bell, R., Bianchi, C., Bingham, R., Blankenship, D. D., Casassa, G., et al. (2013). Bedmap2: improved ice bed, surface and thickness datasets for antarctica. *The Cryosphere*, 7(1):375–393.

Gagliardini, O., Cohen, D., Råback, P., and Zwinger, T. (2007). Finite-element modeling of subglacial cavities and related friction law. *Journal of Geophysical Research: Earth Surface*, 112(F2).

Gagliardini, O., Durand, G., Zwinger, T., Hindmarsh, R. C., and Le Meur, E. (2010). Coupling of ice-shelf melting and buttressing is a key process in ice-sheets dynamics. *Geophysical Research Letters*, 37(14):1–5.

Gagliardini, O. and Zwinger, T. (2008). The ismip-hom benchmark experiments performed using the finite-element code elmer. *The Cryosphere*, 2(1):67–76.

Gagliardini, O., Zwinger, T., Gillet-Chaulet, F., Durand, G., Favier, L., de Fleurian, B., Greve, R., Malinen, M., Martín, C., Råback, P., Ruokolainen, J., Sacchettini, M., Schäfer, M., Seddik, H., and Thies, J. (2013). Capabilities and performance of Elmer/Ice, a new-generation ice sheet model. *Geoscientific Model Development*, 6(4):1299–1318.

Gillet-Chaulet, F., Durand, G., Gagliardini, O., Mosbeux, C., Mouginot, J., Rémy, F., and Ritz, C. (2016). Assimilation of surface velocities acquired between 1996 and 2010 to constrain the form of the basal friction law under pine island glacier. *Geophysical Research Letters*, 43(19):10,311–10,321.

Glen, J. (1958). The flow law of ice: A discussion of the assumptions made in glacier theory, their experimental foundations and consequences. *IASH Publ*, 47(171):e183.

Goelzer, H., Nowicki, S., Payne, A., Larour, E., Seroussi, H., William, H., Gregory, J., Abe-ouchi, A., Shepherd, A., Simon, E., and Agosta, C. (2020). The future sea-level contribution of the Greenland ice sheet : a multi- model ensemble study of ISMIP6. *The Cryosphere Discussions*, (January):1–43.

Goldberg, D., Holland, D. M., and Schoof, C. (2009). Grounding line movement and ice shelf buttressing in marine ice sheets. *Journal of Geophysical Research: Earth Surface*, 114(4):1–23.

Golledge, N. R., Keller, E. D., Gomez, N., Naughten, K. A., Bernales, J., Trusel, L. D., and Edwards, T. L. (2019). Global environmental consequences of twenty-first-century ice-sheet melt. *Nature*, 566(7742):65–72.

Greve, R. and Blatter, H. (2009). Constitutive equations for polycrystalline ice. In *Dynamics of Ice Sheets and Glaciers*, pages 49–60. Springer.

Gudmundsson, G. H. (2013). Ice-shelf buttressing and the stability of marine ice sheets. *Cryosphere*, 7(2):647–655.

Gudmundsson, G. H., Krug, J., Durand, G., Favier, L., and Gagliardini, O. (2012). The stability of grounding lines on retrograde slopes. *Cryosphere*, 6(6):1497–1505.

Gudmundsson, G. H. and Raymond, M. (2008). On the limit to resolution and information on basal properties obtainable from surface data on ice streams. *The Cryosphere Discussions*, 2(3):413–445.

Hasselmann, K. (1963). A statistical analysis of the generation of microseisms. *Reviews of Geophysics*, 1(2):177–210.

Herrmann, R. B. (2013). Computer programs in seismology: An evolving tool for instruction and research. *Seismological Research Letters*, 84(6):1081–1088.

Hoegh-Guldberg, O., Jacob, D., Bindi, M., Brown, S., Camilloni, I., Diedhiou, A., Djalante, R., Ebi, K., Engelbrecht, F., Guiot, J., et al. (2018). Impacts of 1.5°C global warming on natural and human systems. *Global warming of 1.5° C. An IPCC Special Report*.

Hulbe, C. (2017). Is ice sheet collapse in West Antarctica unstoppable? *Science*, 356(6341):910–911.

Huybrechts, P., Abe-Ouchi, A., Marsiat, I., Pattyn, F., Payne, T., Ritz, C., and Rommelaere, V. (1998). Intercomparison Of Ice-Shelf Models: In Report of the Third EISMINT Workshop on Model Intercomparison. *European Science Foundation (Strasbourg)*, pages 69–81.

Huybrechts, P. and Payne, T. (1996). The EISMINT benchmarks for testing ice-sheet models. *Annals of Glaciology*, 23:1–12.

Iken, A. (1981). The effect of the subglacial water pressure on the sliding velocity of a glacier in an idealized numerical model. *Journal of Glaciology*, 27(97):407–421.

Iverson, N. R., Hooyer, T. S., and Baker, R. W. (1998). Ring-shear studies of till deformation: Coulomb-plastic behavior and distributed strain in glacier beds. *Journal of Glaciology*, 44(148):634–642.

Jay-Allemand, M., Gillet-Chaulet, F., Gagliardini, O., and Nodet, M. (2011). Investigating changes in basal conditions of variegated glacier prior to and during its 1982–1983 surge. *The Cryosphere*, 5(3):659–672.

Jean, M. (1995). Frictional contact in collections of rigid or deformable bodies: numerical simulation of geomaterial motions. *Studies in Applied Mechanics*, 42:463–486.

Joughin, I., Shean, D. E., Smith, B. E., and Dutrieux, P. (2016). Grounding line variability and subglacial lake drainage on pine island glacier, antarctica. *Geophysical Research Letters*, 43(17):9093–9102.

Joughin, I., Smith, B. E., and Holland, D. M. (2010). Sensitivity of 21st century sea level to ocean-induced thinning of pine island glacier, antarctica. *Geophysical Research Letters*, 37(20).

Joughin, I., Smith, B. E., and Howat, I. M. (2018). A complete map of Greenland ice velocity derived from satellite data collected over 20 years. *Journal of Glaciology*, 64(243):1–11.

Jouvet, G., Weidmann, Y., Kneib, M., Detert, M., Seguinot, J., Sakakibara, D., and Sugiyama, S. (2018). Short-lived ice speed-up and plume water flow captured by a VTOL UAV give insights into subglacial hydrological system of Bowdoin Glacier. *Remote Sensing of Environment*, 217(August):389–399.

Karney, C. F. (2013). Algorithms for geodesics. *Journal of Geodesy*, 87(1):43–55.

Kawakatsu, H. (1989). Centroid single force inversion of seismic waves generated by landslides. *Journal of Geophysical Research: Solid Earth*, 94(B9):12363–12374.

Kehrl, L. M., Joughin, I., Shean, D. E., Floricioiu, D., and Krieger, L. (2017). Seasonal and interannual variabilities in terminus position, glacier velocity, and surface elevation at Helheim and Kangerlussuaq Glaciers from 2008 to 2016. *Journal of Geophysical Research: Earth Surface*, 122(9):1635–1652.

King, M. D., Howat, I. M., Candela, S. G., Noh, M. J., Jeong, S., Noël, B. P., van den Broeke, M. R., Wouters, B., and Negrete, A. (2020). Dynamic ice loss from the greenland ice sheet driven by sustained glacier retreat. *Communications Earth & Environment*, 1(1):1–7.

Krug, J., Durand, G., Gagliardini, O., and Weiss, J. (2014a). Modelling the impact of submarine frontal melting and ice mélange on glacier dynamics. *Cryosphere*, 9(3):989–1003.

Krug, J., Weiss, J., Gagliardini, O., and Durand, G. (2014b). Combining damage and fracture mechanics to model calving. *The Cryosphere*, 8(6):2101–2117.

Langleben, M. P. (1962). Young's Modulus For Sea Ice. *Canadian Journal of Physics*, 40(1):1–8.

Larour, E., Seroussi, H., Morlighem, M., and Rignot, E. (2012). Continental scale, high order, high spatial resolution, ice sheet modeling using the Ice Sheet System Model (ISSM). *Journal of Geophysical Research: Earth Surface*, 117(1).

Lenaerts, J. T., Le Bars, D., Van Kampenhout, L., Vizcaino, M., Enderlin, E. M., and Van Den Broeke, M. R. (2015). Representing greenland ice sheet freshwater fluxes in climate models. *Geophysical Research Letters*, 42(15):6373–6381.

Lenssen, N. J., Schmidt, G. A., Hansen, J. E., Menne, M. J., Persin, A., Ruedy, R., and Zyss, D. (2019). Improvements in the gistemp uncertainty model. *Journal of Geophysical Research: Atmospheres*, 124(12):6307–6326.

Lliboutry, L. and Duval, P. (1985). Various isotropic and anisotropic ices found in glaciers and polar ice caps and their corresponding rheologies. *Annales Geophysicae*, 3(2):207–224.

Longuet-Higgins, M. S. (1950). A theory of the origin of microseisms. *Phil. Trans. R. Soc. Lond. A*, 243(857):1–35.

MacAyeal, D. R. (1989). Large-scale ice flow over a viscous basal sediment: Theory and application to ice stream b, antarctica. *Journal of Geophysical Research: Solid Earth*, 94(B4):4071–4087.

Macayeal, D. R. (1992). The basal stress distribution of ice stream E, Antarctica, inferred by control methods. *Journal of Geophysical Research*, 97(B1):595–603.

MacAyeal, D. R. and Scambos, T. A. (2003). Catastrophic ice-shelf break-up by an ice-shelf-fragment-capsize mechanism. *Journal of Glaciology*, 49.

Mangeney, A. and Califano, F. (1998). The shallow ice approximation for anisotropic ice: formulation and limits. *Journal of Geophysical Research: Solid Earth*, 103(B1):691–705.

Mangeney, A., Califano, F., and Hutter, K. (1997). A numerical study of anisotropic, low reynolds number, free surface flow for ice sheet modeling. *Journal of Geophysical Research: Solid Earth*, 102(B10):22749–22764.

Minchew, B. and Joughin, I. (2020). Toward a universal glacier slip law. *Science*, 368(6486):29–30.

Minchew, B. M., Meyer, C. R., Pegler, S. S., Lipovsky, B. P., Rempel, A. W., Hilmar Gudmundsson, G., and Iverson, N. R. (2019). Comment on "Friction at the bed does not control fast glacier flow". *Science*, 363(6427).

Moon, T., Heide-Jørgensen, M. P., Dietz, R., Laidre, K. L., Hudson, B., McGovern, R., and Hauser, D. D. W. (2016). Use of glacial fronts by narwhals (Monodon monoceros) in West Greenland . *Biology Letters*, 12(10):20160457.

Morlighem, M., Rignot, E., Seroussi, H., Larour, E., Ben Dhia, H., and Aubry, D. (2010). Spatial patterns of basal drag inferred using control methods from a full-Stokes and simpler models for Pine Island Glacier, West Antarctica. *Geophysical Research Letters*, 37(14):1–6.

Morlighem, M., Williams, C. N., Rignot, E., An, L., Arndt, J. E., Bamber, J. L., Catania, G., Chauché, N., Dowdeswell, J. A., Dorschel, B., Fenty, I., Hogan, K., Howat, I., Hubbard, A., Jakobsson, M., Jordan, T. M., Kjeldsen, K. K., Millan, R., Mayer, L., Mouginot, J., Noël, B. P., O'Cofaigh, C., Palmer, S., Rysgaard, S., Seroussi, H., Siegert, M. J., Slabon, P., Straneo, F., van den Broeke, M. R., Weinrebe, W., Wood, M., and Zinglersen, K. B. (2017). BedMachine v3: Complete Bed Topography and Ocean Bathymetry Mapping of Greenland From Multibeam Echo Sounding Combined With Mass Conservation. *Geophysical Research Letters*, 44(21):11,051–11,061.

Mouginot, J., Rignot, E., Bjørk, A. A., Van den Broeke, M., Millan, R., Morlighem, M., Noël, B., Scheuchl, B., and Wood, M. (2019). Forty-six years of greenland ice sheet mass balance from 1972 to 2018. *Proceedings of the National Academy of Sciences*, 116(19):9239–9244.

Mouginot, J., Rignot, E., Scheuchl, B., and Millan, R. (2017). Comprehensive annual ice sheet velocity mapping using landsat-8, sentinel-1, and radarsat-2 data. *Remote Sensing*, 9(4):364.

Murray, T., Nettles, M., Selmes, N., Cathles, L. M., Burton, J. C., James, T. D., Edwards, S., Martin, I., O'Farrell, T., Aspey, R., Rutt, I., and Baugé, T. (2015a). Reverse glacier motion during iceberg calving and the cause of glacial earthquakes. *Science*, 349(6245):305–308.

Murray, T., Selmes, N., James, T. D., Edwards, S., Martin, I., O'Farrell, T., Aspey, R., Rutt, I., Nettles, M., and Baugé, T. (2015b). Dynamics of glacier calving at the ungrounded margin of helheim glacier, southeast greenland. *Journal of Geophysical Research: Earth Surface*, 120(6):964–982.

Nettles, M. and Ekström, G. (2010). Glacial Earthquakes in Greenland and Antarctica. *Annual Review of Earth and Planetary Sciences*, 38(1):467–491.

Nettles, M., Larsen, T. B., Elósegui, P., Hamilton, G. S., Stearns, L. A., Ahlstrøm, A. P., Davis, J. L., Andersen, M. L., De Juan, J., Khan, S. A., Stenseng, L., Ekström, G., and Forsberg, R. (2008). Step-wise changes in glacier flow speed coincide with calving and glacial earthquakes at Helheim Glacier, Greenland. *Geophysical Research Letters*, 35(24):1–5.

Noël, B., van de Berg, W. J., van Wessem, J. M., van Meijgaard, E., van As, D., Lenaerts, J. T. M., Lhermitte, S., Kuipers Munneke, P., Smeets, C. J. P. P., van Ulft, L. H., van de Wal, R. S. W., and van den Broeke, M. R. (2018). Modelling the climate and surface mass balance of polar ice sheets using RACMO2 – Part 1: Greenland (1958–2016). *The Cryosphere*, 12(3):811–831.

Oerlemans, J. and Nick, F. (2005). A minimal model of a tidewater glacier. *Annals of Glaciology*, 42:1–6.

Olsen, K. G. and Nettles, M. (2017). Patterns in glacial-earthquake activity around Greenland , 2011 – 13. *Journal of Glaciology*, 63:1077–1089.

Olsen, K. G. and Nettles, M. (2019). Constraints on Terminus Dynamics at Greenland Glaciers From Small Glacial Earthquakes. *Journal of Geophysical Research: Earth Surface*, 124(7):1899–1918.

Pattyn, F. (2003). A new three-dimensional higher-order thermomechanical ice sheet model: Basic sensitivity, ice stream development, and ice flow across subglacial lakes. *Journal of Geophysical Research*, 108(B8):1–15.

Pattyn, F., Perichon, L., Aschwanden, A., Breuer, B., de Smedt, B., Gagliardini, O., Gudmundsson, G. H., Hindmarsh, R., Hubbard, A., Johnson, J. V., Kleiner, T., Konovalov, Y., Martin, C., Payne, A. J., Pollard, D., Price, S., Rückamp, M., Saito, F., Souček, O., Sugiyama, S., and Zwinger, T. (2008). Benchmark experiments for higher-order and full Stokes ice sheet models (ISMIP-HOM). *The Cryosphere Discussions*, 2(1):111–151.

Pattyn, F., Schoof, C., Perichon, L., Hindmarsh, R. C., Bueler, E., De Fleurian, B., Durand, G., Gagliardini, O., Gladstone, R., Goldberg, D., Gudmundsson, G. H., Huybrechts, P., Lee, V., Nick, F. M., Payne, A. J., Pollard, D., Rybak, O., Saito, F., and Vieli, A. (2012). Results of the marine ice sheet model intercomparison project, MISMIP. *Cryosphere*, 6(3):573–588.

Payne, A. J., Huybrechts, P., Abe-Ouchi, A., Calov, R., Fastook, J. L., Greve, R., Marshall, S. J., Marsiat, I., Ritz, C., Tarasov, L., and et al. (2000). Results from the eismint model intercomparison: the effects of thermomechanical coupling. *Journal of Glaciology*, 46(153):227–238.

Peters, I., Cassotto, R., Amundson, J. M., Fahnestock, M., and Darnell, K. (2014). Dynamic jamming of iceberg-choked fjords. *Geophysical Research Letters*, 42:1–8.

Podolskiy, E. A., Sugiyama, S., Funk, M., Walter, F., Genco, R., Tsutaki, S., Minowa, M., and Ripepe, M. (2016). Tide-modulated ice flow variations drive seismicity near the calving front of bowdoin glacier, greenland. *Geophysical Research Letters*, 43(5):2036–2044.

Podolskiy, E. A. and Walter, F. (2016). Cryoseismology. *Reviews of geophysics*, 54(4):708–758.

Reeh, N., Christensen, E. L., Mayer, C., and Olesen, O. B. (2003). Tidal bending of glaciers: A linear viscoelastic approach. *Annals of Glaciology*, 37:83–89.

Rice, J. R. (1983). Constitutive relations for fault slip and earthquake instabilities. pages 443–475.

Rist, M. A., Sammonds, P. R., Murrell, S. A., Meredith, P. G., Oerter, H., and Doake, C. S. (1996). Experimental fracture and mechanical properties of Antarctic ice: preliminary results. *Annals of Glaciology*, 23:284–292.

Ritz, C., Edwards, T. L., Durand, G., Payne, A. J., Peyaud, V., and Hindmarsh, R. C. (2015). Potential sea-level rise from antarctic ice-sheet instability constrained by observations. *Nature*, 528(7580):115–118.

Robel, A. A., Seroussi, H., and Roe, G. H. (2019). Marine ice sheet instability amplifies and skews uncertainty in projections of future sea-level rise. *Proceedings of the National Academy of Sciences*, 116(30):14887–14892.

Robel, A. A., Tsai, V. C., Minchew, B., and Simons, M. (2017). Tidal modulation of ice shelf buttressing stresses. *Annals of Glaciology*, 58(74):12–20.

Rosenau, R., Scheinert, M., and Dietrich, R. (2015). A processing system to monitor Greenland outlet glacier velocity variations at decadal and seasonal time scales utilizing the Landsat imagery. *Remote Sensing of Environment*, 169:1–19.

Rosier, S. H., Marsh, O. J., Rack, W., Gudmundsson, G. H., Wild, C. T., and Ryan, M. (2017). On the interpretation of ice-shelf flexure measurements. *Journal of Glaciology*, 63(241):783–791.

Rückamp, M., Falk, U., Frieler, K., Lange, S., and Humbert, A. (2018). The effect of overshooting 1.5 °C global warming on the mass loss of the Greenland ice sheet. *Earth System Dynamics*, 9(4):1169–1189.

Rückamp, M., Goelzer, H., and Humbert, A. (2020). Sensitivity of Greenland ice sheet projections to spatial resolution in higher-order simulations: the Alfred Wegener Institute (AWI) contribution to ISMIP6 Greenland using the Ice-sheet and Sea-level System Model (ISSM). *The Cryosphere*, 14(10):3309–3327.

Rückamp, M., Neckel, N., Berger, S., Humbert, A., and Helm, V. (2019). Calving Induced Speedup of Petermann Glacier. *Journal of Geophysical Research: Earth Surface*, 124(1):216–228.

Sayag, R. and Worster, M. G. (2013). Elastic dynamics and tidal migration of grounding lines modify subglacial lubrication and melting. *Geophysical Research Letters*, 40(22):5877–5881.

Schäfer, M., Zwinger, T., Christoffersen, P., Gillet-Chaulet, F., Laakso, K., Pettersson, R., Pohjola, V. A., Strozzi, T., and Moore, J. C. (2012). Sensitivity of basal conditions in an inverse model: Vestfonna ice cap, Nordaustlandet/Svalbard. *The Cryosphere*, 6(4):771–783.

Schoof, C. (2005). The effect of cavitation on glacier sliding. *Proceedings of the Royal Society A: Mathematical, Physical and Engineering Sciences*, 461(2055):609–627.

Schoof, C. (2010). Ice-sheet acceleration driven by melt supply variability. *Nature*, 468(7325):803–806.

Schoof, C. and Hewitt, I. (2013). Ice-sheet dynamics. *Annual Review of Fluid Mechanics*, 45:217–239.

Sergeant, A. (2016). *Analysis and Modelling of Glacial Earthquakes and Iceberg Calving*. PhD thesis, Seismology team, Institut de Physique du Globe de Paris.

Sergeant, A., Mangeney, A., Stutzmann, E., Montagner, J. P., Walter, F., Moretti, L., and Castelnau, O. (2016). Complex force history of a calving-generated glacial earthquake derived from broadband seismic inversion. *Geophysical Research Letters*, 43(3):1055–1065.

Sergeant, A., Mangeney, A., Yastrebov, V. A., Walter, F., Montagner, J.-p., Castelnau, O., Bonnet, P., Ralaiarisoa, V. J.-l., Bevan, S., and Luckman, A. (2019). Monitoring Greenland ice-sheet buoyancy-driven calving discharge using glacial earthquakes. *Annals of Glaciology*, 60(000):75–95.

Sergeant, A., Yastrebov, V., Mangeney, A., Castelnau, O., Montagner, J.-P., and Stutzmann, E. (2018). Numerical Modeling of Iceberg Capsizing Responsible for Glacial Earthquakes. *Journal of Geophysical Research: Earth Surface*, 123(11):3013–3033.

Shepherd, A., Ivins, E., Rignot, E., Smith, B., van Den Broeke, M., Velicogna, I., Whitehouse, P., Briggs, K., Joughin, I., Krinner, G., et al. (2020). Mass balance of the greenland ice sheet from 1992 to 2018. *Nature*, 579(7798):233–239.

Stearns, L. A. and van der Veen, C. (2019a). Friction at the bed does not control fast glacier flow. *Science*, 363(6427):273–277.

Stearns, L. A. and van der Veen, C. (2019b). Response to Comment on "Friction at the bed does not control fast glacier flow". *Science*, 363(6427):273–277.

Steinemann, S. (1954). Results of preliminary experiments on the plasticity of ice crystals. *Journal of Glaciology*, 2(16):404–416.

Todd, J. and Christoffersen, P. (2014). Are seasonal calving dynamics forced by buttressing from ice mélange or undercutting by melting? Outcomes from full-Stokes simulations of Store Glacier, West Greenland. *The Cryosphere*, 8(6):2353–2365.

Truffer, M., Echelmeyer, K. A., and Harrison, W. D. (2001). Implications of till deformation on glacier dynamics. *Journal of Glaciology*, 47(156):123–134.

Tsai, V. C. and Ekström, G. (2007). Analysis of glacial earthquakes. *Journal of Geophysical Research: Earth Surface*, 112(3):1–13.

Tsai, V. C. and Gudmundsson, G. H. (2015). An improved model for tidally modulated grounding-line migration. *Journal of Glaciology*, 61(226):216–222.

Tsai, V. C., Rice, J. R., and Fahnestock, M. (2008). Possible mechanisms for glacial earthquakes. *Journal of Geophysical Research: Earth Surface*, 113(3):1–17.

Tsai, V. C., Stewart, A. L., and Thompson, A. F. (2015). Marine ice-sheet profiles and stability under Coulomb basal conditions. *Journal of Glaciology*, 61(226):205–215.

Tulaczyk, S., Kamb, W. B., and Engelhardt, H. F. (2000). Basal mechanics of Ice Stream B, West Antarctica 1. Till mechanics. *Journal of Geophysical Research: Solid Earth*, 105(B1):463–481.

Van Den Broeke, M. R., Enderlin, E. M., Howat, I. M., Kuipers Munneke, P., Noël, B. P., Jan Van De Berg, W., Van Meijgaard, E., and Wouters, B. (2016). On the recent contribution of the Greenland ice sheet to sea level change. *The Cryosphere*, 10(5):1933–1946.

Van Der Veen, C. (1989). Force budget: I. theory and numerical methods. *Journal of Glaciology*, 35(119):53–60.

Vaughan, D. G. (1995). Tidal flexure at ice shelf margins. *Journal of Geophysical Research: Solid Earth*, 100(B4):6213–6224.

Vaughan, D. G., Comiso, J., Allison, I., Carrasco, J., Kaser, G., Kwok, R., Mote, P., Murray, T., Paul, F., Ren, J., et al. (2014). Observations: cryosphere.

Veitch, S. A., Karplus, M., Kaip, G., Gonzalez, L. F., Amundson, J. M., and Bartholomaus, T. C. (2021). Ice thickness estimates of lemon creek glacier, alaska, from active-source seismic imaging. *Journal of Glaciology*, page 1–9.

Veitch, S. A. and Nettles, M. (2012). Spatial and temporal variations in Greenland glacial-earthquake activity, 1993-2010. *Journal of Geophysical Research: Earth Surface*, 117(4):1993–2010.

Vijay, S., Khan, S. A., Kusk, A., Solgaard, A. M., Moon, T., and Bjørk, A. A. (2019). Resolving Seasonal Ice Velocity of 45 Greenlandic Glaciers With Very High Temporal Details. *Geophysical Research Letters*, 46(3):1485–1495.

Wagner, T. J., James, T. D., Murray, T., and Vella, D. (2016). On the role of buoyant flexure in glacier calving. *Geophysical Research Letters*, 43(1):232–240.

Walter, F., Amundson, J. M., O'Neel, S., Truffer, M., Fahnestock, M., and Fricker, H. A. (2012). Analysis of low-frequency seismic signals generated during a multiple-iceberg calving event at Jakobshavn Isbr, Greenland. *Journal of Geophysical Research: Earth Surface*, 117(1):1–11.

Walter, F., Olivieri, M., and Clinton, J. F. (2013). Calving event detection by observation of seiche effects on the Greenland fjords. *Journal of Glaciology*.

Walter, F., O'Neel, S., McNamara, D., Pfeffer, W. T., Bassis, J. N., and Fricker, H. A. (2010). Iceberg calving during transition from grounded to floating ice: Columbia Glacier, Alaska. *Geophysical Research Letters*, 37(15):1–5.

Weertman, J. (1957). On the Sliding of Glaciers. *Journal of Glaciology*, 3(21):33–38.

Weertman, J. (1974). Stability of the Junction of an Ice Sheet and an Ice Shelf. *Journal of Glaciology*, 13(67):3–11.

Wiens, D. A., Anandakrishnan, S., Winberry, J. P., and King, M. A. (2008). Simultaneous teleseismic and geodetic observations of the stick–slip motion of an antarctic ice stream. *Nature*, 453(7196):770–774.

Winberry, J. P., Anandakrishnan, S., Alley, R. B., Bindschadler, R. A., and King, M. A. (2009). Basal mechanics of ice streams: Insights from the stick-slip motion of whillans ice stream, west antarctica. *Journal of Geophysical Research: Earth Surface*, 114(F1).

Winberry, J. P., Anandakrishnan, S., Wiens, D. A., Alley, R. B., and Christianson, K. (2011). Dynamics of stick–slip motion, whillans ice stream, antarctica. *Earth and Planetary Science Letters*, 305(3):283–289.

Winberry, J. P., Huerta, A. D., Anandakrishnan, S., Aster, R. C., Nyblade, A. A., and Wiens, D. A. (2020). Glacial Earthquakes and Precursory Seismicity Associated With Thwaites Glacier Calving. *Geophysical Research Letters*, 47(3).

Wronski, M. (1994). *Couplage du contact et du frottement avec la mécanique non linéaire des solides en grandes déformations*. PhD thesis, Université de Technologie de Compiègne, France. Sc. advisor G. Touzot.

Yvin, C., Leroyer, A., Visonneau, M., and Queutey, P. (2018). Added mass evaluation with a finite-volume solver for applications in fluid–structure interaction problems solved with co-simulation. *Journal of Fluids and Structures*, 81:528–546.

Zhang, E., Liu, L., Huang, L., and Ng, K. S. (2020). Network delineated calving fronts at Jakobshavn Isbræ, Kangerlussuaq, and Helheim. https://doi.org/10.1594/PANGAEA.923272.

Zhang, E., Liu, L., Huang, L., and Ng, K. S. (2021). An automated, generalized, deep-learning-based method for delineating the calving fronts of greenland glaciers from multi-sensor remote sensing imagery. *Remote Sensing of Environment*, 254:112265.

Zoet, L. K., Carpenter, B., Scuderi, M., Alley, R. B., Anandakrishnan, S., Marone, C., and Jackson, M. (2013). The effects of entrained debris on the basal sliding stability of a glacier. *Journal of Geophysical Research: Earth Surface*, 118(2):656–666.

Zoet, L. K. and Iverson, N. R. (2020). A slip law for glaciers on deformable beds. *Science*, 368(6486):76–78.

Zwally, J. H., Li, J., Brenner, A. C., Beckley, M., Cornejo, H. G., Marzio, J. D., Giovinetto, M. B., Neumann, T. A., Robbins, J., Saba, J. L., Yi, D., and Wang, W. (2011). Greenland ice sheet mass balance: Distribution of increased mass loss with climate warming; 2003-07 versus 1992-2002. *Journal of Glaciology*, 57(201):88–102.

Modélisation mécanique de la source des séismes glaciaires en régions polaires

par Pauline Bonnet

L’estimation du bilan de masse des calottes polaires est un enjeu actuel pour appréhender l’évolution rapide de ces masses glaciaires sous l’effet du changement climatique. Le vêlage d’icebergs représente une part importante de la perte de masse des glaciers du Groenland. Leur retournement proche du terminus déstabilise les glaciers.

A l'aide d'un modèle de référence de dynamique des fluides, nous avons quantifié et caractérisé l’interaction entre l’eau et un iceberg qui se retourne, et validé et amélioré un modèle simplifié de retournement d'iceberg. Puis nous avons construit et validé un modèle éléments finis qui reproduit la réponse d’un glacier à la force de contact d’un retournement d’iceberg au terminus et qui inclut plusieurs rhéologies de l’interface glacier/lit rocheux et une loi de comportement élasto-viscoplastique de la glace. A l'aide de ce modèle complet, nous avons reproduit les déplacements en surface et les efforts à la base du glacier et analysé l’influence des paramètres sur la réponse du glacier. Nous avons d’abord modélisé un glacier avec une géométrie idéalisée. Puis nous avons modélisé un glacier réel, le glacier Helheim, et pour cela nous avons ajusté les paramètres du modèle à l’aide de résultats d’un modèle de référence pour l’écoulement des glaciers. On observe une dépendance forte de l’amplitude des déplacements en surface avec le module d’Young de la glace et la longueur de la langue flottante, mais également une signature des paramètres des lois de frictions sur ces déplacements. Notre modèle suggère que la force de l’iceberg appliquée au terminus est retransmise au lit rocheux sans modification malgré le mouvement induit du glacier.

Le résultats obtenus avec le modèle complet ouvre des perspectives intéressantes sur l’estimation des paramètres de la rhéologie, de la géométrie et des lois de frottement basales à l’aide de comparaison avec des observations sur le terrain.

Glaciers, iceberg, retournement, modélisation mécanique, Groenland, icequakes

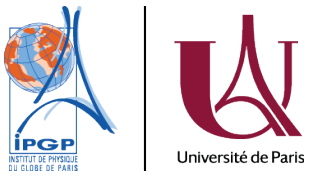

Mechanical modelling of the source of glacial earthquakes in polar regions

by Pauline Bonnet

Estimating the mass balance of the polar ice caps is a current challenge to understand the rapid evolution of these ice masses under the effect of climate change. The calving of icebergs represents a significant part of the mass loss of Greenland's glaciers. Their overturning near the terminus destabilises the glaciers.

Using a reference model in fluid dynamics, we quantified and characterised the interaction between water and a capsizing iceberg, and validated and improved a simplified iceberg overturning model. Then we built and validated a finite element model that reproduces the response of a glacier to the contact force of a capsizing iceberg at the terminus and that includes several rheologies of the glacier/rock interface and an elasto-viscoplastic behaviour law of the ice. Using this comprehensive model, we reproduced surface displacements and stresses at the base of the glacier and analysed the influence of the parameters on the glacier response. We first modelled a glacier with an idealised geometry. Then we modelled a real glacier, the Helheim glacier, and for this we adjusted the model parameters using results from a reference glacier flow model. A strong dependence of the amplitude of the surface displacements on the Young's modulus of the ice and the length of the floating tongue is observed, but also a signature of the friction law parameters on these displacements. Our model suggests that the iceberg force applied at the terminus is transmitted back to the bedrock unchanged despite the induced glacier motion.

The results obtained with the full model open interesting perspectives on the estimation of the parameters of the rheology, geometry and basal friction laws through comparison with field observations.

Glaciers, iceberg, capsize, mechanical modelling, Greenland, icequakes

IPGP
INSTITUT DE PHYSIQUE DU GLOBE DE PARIS

Université de Paris